

# Composition and geometric structure of ultrathin oxide films

Dissertation

zur Erlangung des  
Doktorgrades der Naturwissenschaften (Dr. rer. nat.)

am Institut für Physik  
der Naturwissenschaftlichen Fakultät II  
der Martin-Luther-Universität  
Halle-Wittenberg

vorgelegt von

Herrn Alireza Bayat  
geb. am 04.08.1986 in Teheran, Iran



Gutachter:

1. PD Dr. Karl-Michael Schindler (Martin-Luther-Universität Halle-Wittenberg)
2. Prof. Dr. Kathrin Dörr (Martin-Luther-Universität Halle-Wittenberg)
3. Prof. Dr. Andreas Stierle (Universität Hamburg)

Tag der Verleihung: 19.12.2018



To dream of my father

Hamid Bayat

To my dear mother

Efat Zandevakili

and

my sweet love

Maryam



# Contents

|          |  |           |
|----------|--|-----------|
| <b>1</b> | <b>Introduction</b>  | <b>13</b> |
| <b>2</b> | <b>Investigated materials</b>                                    | <b>15</b> |
| 2.1      | Barium titanate . . . . .  | 15        |
| 2.2      | Strontium titanate . . . . .                                     | 17        |
| 2.3      | Pt(111) single crystal substrate . . . . .                       | 17        |
| 2.4      | Barium titanate derived oxide quasicrystal . . . . .             | 17        |
| <b>3</b> | <b>Experimental Techniques</b>                                   | <b>21</b> |
| 3.1      | The X-ray radiation source . . . . .                             | 21        |
| 3.2      | X-ray absorption spectroscopy (XAS) . . . . .                    | 21        |
| 3.2.1    | The X-ray absorption spectrum . . . . .                          | 24        |
| 3.2.2    | The X-ray absorption data analysis . . . . .                     | 25        |
| 3.2.3    | Detection methods . . . . .                                      | 26        |
| 3.3      | X-ray photoelectron spectroscopy (XPS) . . . . .                 | 29        |
| 3.4      | Synchrotron beam lines . . . . .                                 | 31        |
| 3.4.1    | The KMC-1 beamline at BESSYII . . . . .                          | 31        |
| 3.4.2    | The SuperESCA beamline at Elettra . . . . .                      | 32        |
| 3.5      | Extended X-ray absorption fine structure (EXAFS) . . . . .       | 32        |
| 3.5.1    | Physical principles . . . . .                                    | 32        |
| 3.5.2    | The EXAFS data analysis . . . . .                                | 38        |
| <b>4</b> | <b>Projection Analysis of EXAFS Modulations of STO</b>           | <b>41</b> |
| 4.1      | The projection method . . . . .                                  | 41        |
| 4.2      | Experimental procedures . . . . .                                | 43        |
| 4.3      | XAS measurements . . . . .                                       | 44        |
| 4.4      | Data analysis . . . . .  | 45        |
| 4.4.1    | Projection method: Oxygen . . . . .                              | 45        |
| 4.4.2    | Projection method: Strontium . . . . .                           | 47        |
| 4.4.3    | Projection method: Titanium . . . . .                            | 49        |
| <b>5</b> | <b>Structural determination of BTO-derived OQC on Pt(111)</b>    | <b>51</b> |
| 5.1      | Barium titanate single crystal . . . . .                         | 51        |
| 5.1.1    | Structure determination of the BTO single crystal . . . . .      | 52        |
| 5.2      | Structural determination of BTO-derived OQC on Pt(111) . . . . . | 55        |
| 5.2.1    | Sample preparation of OQC on Pt(111) . . . . .                   | 56        |
| 5.2.2    | X-ray absorption measurements . . . . .                          | 58        |
| 5.2.3    | X-ray photoemission measurements . . . . .                       | 61        |
| 5.2.4    | OQC EXAFS data analysis . . . . .                                | 70        |
| 5.2.5    | Summary . . . . .  | 91        |
| <b>6</b> | <b>Growth and decay of BTO-derived OQC on Pt(111)</b>            | <b>95</b> |
| 6.1      | Experimental procedures . . . . .                                | 95        |

## Contents

|                 |   |            |
|-----------------|---|------------|
| 6.2             | Binding energy calibration . . . . .                                | 97         |
| 6.3             | X-ray photoemission spectroscopy . . . . .                          | 98         |
| 6.3.1           | Investigation of satellites in the Ti $2p$ emission lines . . . . . | 104        |
| 6.4             | Stoichiometry . . . . .   | 105        |
| 6.5             | X-ray absorption spectroscopy . . . . .                             | 107        |
| 6.6             | UHV annealing of the reduced 4 ML BTO on Pt(111) . . . . .          | 110        |
| 6.7             | Oxidation of 4 ML BTO on Pt(111) . . . . .                          | 112        |
| 6.8             | Reduction of 4 ML BTO on Pt(111) . . . . .                          | 119        |
| <b>7</b>        | <b>Summary</b>  | <b>127</b> |
| <b>8</b>        | <b>Appendix</b>   | <b>143</b> |
| <b>Appendix</b> |   | <b>143</b> |
|                 | Erklärung . . . . .   | 153        |
|                 | Acknowledgement . . . . .   | 157        |



# List of Figures

|      |   |    |
|------|---|----|
| 2.1  | A perovskite unit cell with the elemental composition of $ABO_3$ in the cubic phase . . . . .   | 15 |
| 2.2  | BTO phases with changes of the lattice parameters during heating (dot lines) and cooling (solid lines) with their hysteresis behaviors at their phase transition temperatures [8, 9, 10].   | 16 |
| 2.3  | Domains and domain walls in BTO, taken from [14] . . . . .  | 17 |
| 2.4  | Niizeki-Gähler tiling [23, 24] consists of squares, triangles and rhombs, the image courtesy of S. Förster. . . . .   | 18 |
| 2.5  | (a) STM image of the dodecagonal structure of the BTO-derived oxide quasicrystal, which is tiled according to Niizeki-Gähler tiling. The STM image was taken with a tunneling voltage of 0.1 V. The structure exhibits 12-fold diffrational symmetry, as given by the LEED image (b) taken at 66 eV electron energy. The (10) spot of the Pt substrate is illustrated in the image. Both measurements were performed at in 77 K [40]. . . . . | 19 |
| 2.6  | (a) STM image of the $BaTiO_3$ -derived Kepler-approximant, taken at a tunneling voltage of 1 V. Different domains of the Kepler-approximant around BTO-derived OQC are shown in Fig. (b). (c) The LEED pattern of the Kepler-approximant on Pt(111) at an electron beam energy of 20 eV. The LEED pattern shows the 6 different domains of the BTO-derived Kepler-approximant [44]. . . . .  | 20 |
| 2.7  | Top view and side view of structural model for the Kepler-approximant from a DFT calculation [44]. . . . .  | 20 |
| 3.1  | X-ray absorption process and excitation of the core electron to unoccupied states, derived from [53]. . . . .   | 23 |
| 3.2  | Fluorescence decay, Auger electron emission and X-ray photoelectron ejection processes, derived from [53]. . . . .  | 24 |
| 3.3  | Different XAS transition processes [54]. . . . .  | 24 |
| 3.4  | Background subtraction in an arbitrary $L_{2,3}$ spectrum. . . . .  | 26 |
| 3.5  | The energy level diagram and the schematic photoemission spectra at different energies [56]. . . . .  | 28 |
| 3.6  | The universal curve of the inelastic mean free path of electrons (MFP) taken from [58] according to [59]. . . . .   | 29 |
| 3.7  | Energy diagram in the XPS process [61] . . . . .  | 30 |
| 3.8  | (a) XAS spectrum at the Ti $K$ -edge in a STO(001) crystal and corresponding modulation functions (b). . . . .  | 33 |
| 3.9  | Fourier transformation of $\chi(k) \times k^2$ of the Ti $K$ -edge in STO(001) crystal . . . . .  | 34 |
| 3.10 | The schematic of the single scattering and important collinear and triangular multiple scatterings taken from [85] according to [84] . . . . .  | 37 |
| 3.11 | (a) Subtracted background of the experimental Ti $K$ -edge spectrum from a STO single crystal, in normal incidence, together with fitted lines in the pre-edge and the post-edge regions. The resulted normalized spectrum is shown in Fig. (b). . . . .  | 40 |
| 4.1  | (a) X-ray absorption spectra of the Ti $K$ -edge of STO(001) crystal in normal incidence in TEY and FY detection mode and (b) the corresponding XANES regions. The pre-edge transition A is in agreement with reported data [101, 108, 109, 110]. . . . .   | 44 |

|      |   |    |
|------|---|----|
| 4.2  | (a) Modulation function and (b) Fourier transformations of single scattering processes from first shells of neighboring atoms of Ti in STO bulk [16], as is calculated by FEFF6 using DEMETER software package [86]. . . . .  | 46 |
| 4.3  | SrTiO <sub>3</sub> : Projection coefficient $c_{trans}$ of the Ti <i>K</i> -edge EXAFS modulations as function of Ti-O distance $r$ . . . . .   | 47 |
| 4.4  | SrTiO <sub>3</sub> : Projection coefficient $c_{trans}(r)$ of the Ti <i>K</i> -edge EXAFS modulations as function of Ti-Sr distance $r$ . . . . .   | 48 |
| 4.5  | SrTiO <sub>3</sub> : Projection coefficient $c_{trans}(r)$ of the Ti <i>K</i> -edge EXAFS modulations as function of Ti-Ti distance $r$ . . . . .   | 49 |
| 5.1  | X-ray absorption spectra of BTO(001) crystal at the Ti <i>K</i> -edge (a) and the Ba <i>L</i> <sub>3</sub> -edge (c) in normal incidence in TEY and FY detection mode. (b,d) The zoomed XANES regions.  | 52 |
| 5.2  | Directional anisotropy of FY measurements of a BTO(001) crystal at the Ti <i>K</i> -edge (a) and the Ba <i>L</i> <sub>3</sub> -edge (c) in 2° and 72° from the surface normal, together with the XANES regions (b,d). . . . .   | 53 |
| 5.3  | Illustration of labels of the atoms in a BTO unit cell, used in Tab. 5.1. . . . .   | 54 |
| 5.4  | The FEFF analysis results of bulk BTO(001) crystal ( $R$ -factor= 0.14) in $k$ -space (a) and $R$ -space (b). The window in $k$ -space corresponds to the selected region for Fourier transformation, while the fitting has been done in $R$ -space in the specified region. . . . .  | 55 |
| 5.5  | SPALEED pattern of 3 Å BTO on Pt(111), taken at an electron kinetic energy, $E_{kin}$ of 66 eV. . . . .   | 56 |
| 5.6  | (a) The LEED image of the reduced 1 ML BTO sample was taken at 66 eV electron kinetic energy, was prepared as at KMC-1 beamline. (b) The same sample after 14 hours in an UHV chamber with a base pressure of $5.6 \times 10^{-8}$ mbar. . . . .  | 57 |
| 5.7  | AFM image of the oxidized sample of 1 ML BTO on Pt(111), measured in tapping mode with a cantilever with a spring constant of 43 N/m. (a,b) The topography and the phase images, measured with a drive amplitude of 0.3 V and a drive frequency of 300 kHz. Scan size and scan speed are $1.5 \times 1.5 \mu\text{m}^2$ and $1.5 \mu\text{m/s}$ . (c) The topography of a zoomed region, measured with a drive amplitude of 0.6376 V and a drive frequency of 288 840 Hz and a scan speed of $1 \mu\text{m/s}$ . (d) Corresponding line profile analysis. . . . . | 58 |
| 5.8  | (a) The Ti <i>K</i> -edge absorption spectrum of the OQC (the reduced 1 ML BTO) in normal and grazing incidence in FY and the absorption spectrum of BTO single crystal in normal incidence in FY. (b) Zoomed XANES region. . . . .   | 60 |
| 5.9  | X-ray absorption spectrum of the Ba <i>L</i> <sub>3</sub> -edge of the OQC (the reduced 1 ML BTO) in normal and grazing incidence and bulk BTO in normal incidence. All the spectra have been recorded in FY. . . . .   | 61 |
| 5.10 | X-ray absorption spectra at the Ti <i>K</i> -edge (a) and the zoomed region (b) of 1 ML BTO in the reduced (OQC) and the oxidized (oxidized OQC) state, recorded in FY mode in grazing incidence. . . . .   | 62 |
| 5.11 | X-ray absorption spectra at the Ba <i>L</i> <sub>3</sub> -edge of 1 ML BTO in the reduced (OQC) and the oxidized (oxidized OQC) states, recorded in FY mode in grazing incidence. The absorption spectrum of BTO(001) crystal in FY in normal incidence is presented. . . . .   | 63 |
| 5.12 | XPS spectra of the Pt 4 <i>f</i> (a) and the C 1 <i>s</i> emission lines of 1 ML BTO in the reduced (OQC) and the oxidized (oxidized OQC) states, recorded in normal emission. FWHMs of the C spectra are given in the parenthesis. . . . .   | 64 |
| 5.13 | XPS spectra of the Ti 2 <i>p</i> emission line of 1 ML BTO in (a) the reduced (OQC) and (b) the oxidized (oxidized OQC) states, recorded in normal emission. . . . .  | 65 |

|      |   |    |
|------|---|----|
| 5.14 | O 1s emission line of 1 ML BTO in the reduced (OQC) and the oxidized (oxidized OQC) states (a,b) and comparison with the 4 ML BTO (c,d) in the reduced (OQC) and the oxidized (oxidized OQC) states. FWHM of every component has been given in parenthesis below the peak position. . . . .   | 66 |
| 5.15 | (a,b) The Ba $3d_{5/2}$ emission line of 1 ML BTO in (a) the reduced (OQC) and (b) the oxidized (oxidized OQC) states, recorded in normal emission. . . . .   | 67 |
| 5.16 | $k^2$ weighted modulation function of 1 ML BTO at the Ti $K$ -edge in the reduced (OQC) and the oxidized (oxidized OQC) state, at the Ti $K$ -edge in normal and grazing incidence (a) and the corresponding Fourier transformations (b). . . . .   | 71 |
| 5.17 | (a) $k^2$ weighted modulation function of 1 ML BTO in the reduced (OQC) state at the Ti $K$ -edge in normal incidence and the modulation function of a single scattering process from an O atom at a distance of 2.6 Å and (b) the Fourier transformations. . . . .   | 72 |
| 5.18 | (a) $k^2$ weighted modulation function of 1 ML BTO in the reduced (OQC) state at the Ti $K$ -edge in normal incidence and the modulation function of a single scattering process from a Pt atom at a distance of 2.7 Å (a) and (b) the corresponding Fourier transformations. . . . .   | 73 |
| 5.19 | Results of fitting in a system composed of a Ti atom as the emitter and an O atom and a Pt atom as scatterers with the initial distances from Ti as 2.6 and 2.3 Å (colored as blue) and 2.6 and 2.7 Å (colored as red). Only single scattering processes have been considered. The Top: $R$ -factor as a function of the shifts in the edge energy. Bottom: Calculated distances of O and Pt from Ti with the above mentioned initial values. . . . . | 74 |
| 5.20 | The side view of the models with four (a) and six (b) scattering atoms around a Ti atom as the emitter. The electric fields of the incoming beams are show in red for normal incidence (along $x$ axis) and blue for grazing incidence ( $70^\circ$ from $x$ axis). . . . .   | 75 |
| 5.21 | (a) $k^2$ weighted modulation function of 1 ML BTO at the Ti $K$ -edge in the reduced state (OQC) and results of FEFF structural analysis of the model in Fig. 5.20 (b) in normal incidence and (b) the Fourier transforms. The pink bars correspond to O atoms, the light brown bars to Pt atoms. . . . .  | 77 |
| 5.22 | (a) $k^2$ weighted modulation function of 1 ML BTO at the Ti $K$ -edge in the reduced state (OQC) and results of FEFF structural analysis of the model in Fig. 5.20 (b) in grazing incidence and (b) the Fourier transforms. The pink bars correspond to O atoms, the light brown bars to Pt atoms. . . . .   | 78 |
| 5.23 | The modulation function (a) and the Fourier transform (b) of 1 ML BTO in the reduced state (OQC) at the Ti $K$ -edge and the calculations resulting from all single and multiple scattering processes in a model composed of one Ti atom 2.28 Å above the Pt surface at close to fcc 3-FH site, in $70^\circ$ incidence angle. . . . .  | 79 |
| 5.24 | The modulation function (a) and the Fourier transform (b) of 1 ML BTO in the reduced state (OQC) at the Ti $K$ -edge and the calculations resulting from all single and multiple scattering processes in a model composed of Ti atom 2.28 Å above the Pt surface at close to fcc 3-FH site, in normal incidence angle. A presumable distance of a Ba atom at 3.15 Å is illustrated as a green bar. . . . .  | 80 |
| 5.25 | Top and side view of the cluster model for BTO-derived OQC. Due to the possibility of presence of different orientations of Ba and O atoms around Ti, two orientations have been considered (a,b), rotated by $90^\circ$ . . . . .  | 81 |
| 5.26 | The modulation function (a) and the Fourier transform (b) of 1 ML BTO in the reduced state (OQC) at the Ti $K$ -edge and FEFF calculations on the cluster model (Fig. 5.25) after optimization of distances of a model with six scatterers (Fig. 5.22) in normal incidence. The bars correspond to distances of atoms from Ti: pink (O), light brown (Pt) and green (Ba). . . . .   | 83 |

|      |  |    |
|------|--|----|
| 5.27 | The modulation function (a) and the Fourier transform (b) of 1 ML BTO in the reduced state (OQC) at the Ti <i>K</i> -edge and FEFF calculations on the cluster model (Fig. 5.25) after optimization of distances of a model with six scatterers (Fig. 5.22) in grazing incidence. The bars correspond to distances of atoms from Ti: pink (O), light brown (Pt) and green (Ba). . . . .  | 84 |
| 5.28 | Top view of the cluster model for BTO-derived OQC with defects. Due to the possible presence of different orientations of Ba and O atoms around Ti, two orientations have been considered (a,b), rotated by 90°. . . . .   | 85 |
| 5.29 | Experimental and calculated modulation functions and FFT of EXAFS at the Ti <i>K</i> -edge in normal incidence, calculated with model of Fig. 5.28. . . . .  | 87 |
| 5.30 | Experimental and calculated modulation functions and FFT of EXAFS at the Ti <i>K</i> -edge in grazing incidence, calculated with model of Fig. 5.28. . . . .   | 88 |
| 5.31 | (a) An extreme example of lateral site distribution of Ti atoms in BTO-derived OQC on Pt(111) surface, leads to the height variation of atoms, shown in (b), due to the constant Ti-Pt distance. . . . .   | 89 |
| 5.32 | (a) The region of the lateral mesh of Ti atoms with steps of 0.1 Å and the corresponding height difference distribution (b). (c) The illustration of the asymmetry in the height distribution. . . . .   | 90 |
| 5.33 | (a) An STM image of a large area of BTO-derived OQC sample taken with -1 V tunneling voltage at 77 K. (b) The comparison of the corresponding height variation of the atoms in the image (a) and the calculated one, shown in Fig. 5.32. . . . .   | 91 |
| 5.34 | (a) The individual modulation functions of the lateral mesh, discussed in the text, at the Ti <i>K</i> -edge in grazing incidence starting from on top position to fcc 3-FH site. (b) The comparison of $k^2$ -weighted modulation functions of the superposition of the sites in the lateral mesh (Fig. 5.32), the cluster model with Ti at close to fcc 3-FH site (5.25) and the experiment (OQC) at the Ti <i>K</i> -edge in grazing incidence. . . . . | 92 |
| 5.35 | The selected area of the Pt surface to back-fold Ti atoms in the QC structure, as discussed in the text. . . . .   | 92 |
| 5.36 | (a) The result of back-folding Ti atoms in different generations of the QC structure on the selected Pt area, shown in Fig. 5.35. The Pt-Pt and Ti-Ti bond distances are set to 2.775 Å [20] and 6.85 Å [40]. The arrows show the selected Pt area, as shown in Fig. 5.35. (b) The zoomed region. . . . .  | 93 |
| 5.37 | The result of back-folding Ti atoms in different generations of the QC structure on the selected area of Pt(111) surface, shown in Fig. 5.35. The Pt-Pt bond distance is set to 2.775 Å [20] and the Ti-Ti bond distance is assumed to be 6.873 309 Å (a) and 22.315 023 7 Å (b). . . . .  | 93 |
| 6.1  | (a) Topography of 4 ML BTO on Pt(111) measured by AFM (MFP-3d) under ambient air in tapping mode. (b) PFM measurements on the islands in contact mode in remanence. Top: The phase difference of the applied alternating voltage to the piezo and the tip responses (in degree). Bottom: Island oscillation amplitude (in pm). See text for the measurements parameters. . . . .   | 97 |
| 6.2  | Fermi level of Pt, corrected in the binding energy by referring to the Pt $4f_{7/2}$ line in the overview spectrum, taken at 1000 eV. The black bar shows the zero binding energy, while the point of inflection of the spectrum is at 0.15 eV. . . . .  | 98 |
| 6.3  | High resolution XPS spectrum of the Ti $2p$ emission lines, taken in normal emission at room temperature, at a photon energy of 670 eV for 4 ML BTO sample (a) in the reduced state, annealed in UHV and (b) oxidized state, annealed in $5 \times 10^{-7}$ mbar O <sub>2</sub> . . . . .  | 99 |

|      |  |     |
|------|--|-----|
| 6.4  | High resolution XPS spectrum of the O 1s and Ba 3d <sub>5/2</sub> emission lines, taken in normal emission at RT, at a photon energy of 670 (O 1s) and 1000 eV (Ba 3d <sub>5/2</sub> ) for 4 ML BTO sample (a,b) in the reduced state, annealed in UHV and (c,d) in the oxidized state, annealed in 5 × 10 <sup>-7</sup> mbar O <sub>2</sub> . . . . .   | 100 |
| 6.5  | High resolution XPS spectrum of (a) the Ti 2p and (b) the O 1s (taken at 670 eV) and (c) the Ba 3d <sub>5/2</sub> (taken at 1000 eV) emission lines of 4 ML BTO sample in the further annealed state, annealed in 1 × 10 <sup>-5</sup> mbar O <sub>2</sub> , taken at normal emission at room temperature. . . . .   | 101 |
| 6.6  | High resolution XPS spectrum of the O 1s emission line of 4 ML BTO sample in the reduced state, taken at (a) room temperature and (b) annealed at 999 K in UHV at a photon energy of 670 eV in normal emission. . . . .  | 102 |
| 6.7  | High resolution XPS spectrum of the Ti 2p emission lines, taken in normal emission at room temperature, at a photon energy of 670 eV for 4 ML BTO sample in the reduced state, annealed in UHV, recorded at a position labeled as (a) z = 197 mm and (b) z = 191 mm. . . . .   | 103 |
| 6.8  | High resolution XPS spectrum of the Ti 2p emission lines, taken in normal emission at room temperature at a photon energy of 670 eV for the 4 ML BTO sample in (a) the reduced, (b) the oxidized and (c) the further annealed state. . . . .   | 105 |
| 6.9  | X-ray absorption spectrum at the Ti L-edge of the reduced, the oxidized and the further annealed state of 4 ML BTO on Pt(111) in normal and 70° off normal incidences and the BTO(001) in normal incidence. The spectra of the 4 ML (bulk) BTO sample were recorded in AEY (TEY) measurement mode. The peaks are labeled according to [171]. . . . .   | 107 |
| 6.10 | X-ray absorption spectrum at the O K-edge of the reduced, the oxidized and the further annealed state of 4 ML BTO on Pt(111) in normal and 70° off normal incidences and bulk BTO(001) in normal incidence. The spectra of the 4 ML (bulk) BTO sample were recorded in AEY (TEY) measurement mode. The peaks are labeled according to [171]. . . . .   | 108 |
| 6.11 | X-ray absorption spectrum at the Ba M-edge of 4 ML BTO sample in the reduced and the oxidized state in normal and 70° off normal incidences and bulk BTO(001) in normal incidence. The spectra of the 4 ML (bulk) sample were recorded in AEY (TEY) measurement mode. . . . .  | 109 |
| 6.12 | The binding energy shifts of the green Ti <sup>4+</sup> (in Fig. 6.3) and the blue O 1s components (in Fig. 6.13) during heating the 4 ML BTO sample in UHV up to 950 K and cooling down to RT, taken at a photon energy of 670 eV, in normal emission (Fig. 8.5). . . . .   | 111 |
| 6.13 | High resolution XPS spectrum of the O 1s emission lines, taken in normal emission at (a) RT and (b) 999 K for 4 ML BTO sample in the reduced state at a photon energy of 670 eV. . . . .   | 111 |
| 6.14 | High resolution XPS spectrum of the Ti 2p emission lines of the 4 ML BTO sample in normal emission, (a) taken in the reduced state at 301 and 999 K (UHV annealed) and (b) taken in the oxidized state at 320 and 828 K (oxygen annealed at 5 × 10 <sup>-7</sup> mbar O <sub>2</sub> ), at a photon energy of 670 eV. . . . .  | 112 |
| 6.15 | High resolution XPS spectrum of the 4 ML BTO sample of (a) the O 1s and (b) the Ba 3d <sub>5/2</sub> emission lines, taken at RT (sample in the oxidized state) and at 826 K (oxidizing at 5 × 10 <sup>-7</sup> mbar O <sub>2</sub> ) with a photon energy of 670 eV for the O 1s line and 1000 eV for the Ba 3d <sub>5/2</sub> line in normal emission. . . . .   | 113 |
| 6.16 | Binding energy shifts of the Ti <sup>4+</sup> components in Fig. 6.14 via heating in UHV, referenced to the green Ti <sup>4+</sup> component at 549.25 eV at 301 K in the reduced state, shown as green squares and are fitted with a line. The blue circles indicate the shifts in the blue Ti <sup>4+</sup> component, referenced to its binding energy at 548.2 eV (at 320 K) in the oxidized state, while oxidizing of the 4 ML BTO sample at 5 × 10 <sup>-7</sup> mbar O <sub>2</sub> . . . . . | 114 |

|      |  |     |
|------|--|-----|
| 6.17 | The Ti $2p$ emission lines of 4 ML BTO on Pt(111), taken in normal emission during oxidation in $5 \times 10^{-7}$ mbar $O_2$ . The binding energy of every individual spectrum has been corrected by referring to the Pt $4f$ spectrum. . . . .   | 115 |
| 6.18 | Temperature, relative areas and binding energies of individual components of the Ti $2p$ emission lines of 4 ML BTO on Pt(111) versus time, taken in normal emission during oxidation in $5 \times 10^{-7}$ mbar $O_2$ , shown in Fig. 6.17. The color codings of the components are the same as Fig. 6.3. . . . .   | 116 |
| 6.19 | Relative areas of the total $Ti^{3+}$ and the total $Ti^{4+}$ contributions of the Ti $2p$ emission lines of 4 ML BTO on Pt(111) versus time, during oxidation in $5 \times 10^{-7}$ mbar $O_2$ , shown in Fig. 6.17, taken in normal emission. The total Ti and Pt areas normalized to the mirror current (Pt footpoints) are appended to the right (left) axis. . . . .  | 117 |
| 6.20 | The O $1s$ emission line of 4 ML BTO sample during oxidation in $5 \times 10^{-7}$ mbar $O_2$ , taken at a photon energy of 670 eV in normal emission. Temperature, relative areas and binding energies of individual components are plotted versus time. The color codings of the components are the same as in Fig. 6.4 (a,b). The total spectrum areas normalized to the mirror current (O footpoints) are appended to the right (left) axis. . . . .   | 118 |
| 6.21 | The Ti $2p$ spectra while reducing the 4 ML sample in UHV by heating up to 1029 K, taken in normal emission. The binding energies of the spectra were corrected by referencing to the Pt $4f$ lines. . . . .   | 120 |
| 6.22 | Temperature, relative areas and binding energies of individual components of the Ti $2p$ emission lines of 4 ML BTO on Pt(111) versus time, taken in normal emission during reduction in UHV, shown in Fig. 6.21. The color codings of the components are the same as Fig. 6.3 (a,b) and 6.5 (a). . . . .  | 121 |
| 6.23 | High resolution XPS spectrum of the Ti $2p$ emission lines of the 4 ML BTO sample, taken at 871 K (while annealing in UHV) at a photon energy of 670 eV, in normal emission. . . . .   | 122 |
| 6.24 | Relative areas of the total $Ti^{3+}$ and the total $Ti^{4+}$ contributions of the Ti $2p$ emission lines of 4 ML BTO on Pt(111) during reduction in UHV, shown in Fig. 6.21, versus time, taken in normal emission. The total Ti and Pt areas are normalized to the mirror current and Pt footpoints and are appended to the right and left axis. The relative surface to bulk area of the Pt $4f$ emission lines, recorded simultaneously in the reduction ramp (Fig. 6.25) is given, as well. . . . . | 123 |
| 6.25 | The Pt $4f$ spectra while reducing the 4 ML sample in UHV by heating up to 1029 K, taken in normal emission. . . . .   | 124 |
| 6.26 | High resolution XPS spectra of the Pt $4f$ emission lines of 4 ML BTO on Pt(111) in normal emission in (a) the reduce and (b) the oxidized state, taken at a photon energy of 140 eV [41]. The Pt $4f$ emission lines are shown while reducing the sample in UHV, recorded (c) at 302 K (beginning of the reduction) and (d) at 517 K, taken at a photon energy of 670 eV in normal emission. . . . .  | 126 |
| 8.1  | (a) Ternary phase diagram of $BaO-TiO_{2-x}$ systems above 1573 K [128]. The blue lines specify phases with the Ba:Ti ratios 1:1, 1:2 and 1:3. (b) Pseudo-binary phase diagram of $BaO-TiO_2$ systems under ambient air condition [130]. . . . .   | 145 |
| 8.2  | The typical spectrum of an undulator, taken from [47]. . . . .   | 146 |
| 8.3  | High resolution XPS spectrum of the Ti $2p$ emission lines, taken in $70^\circ$ off normal emission at RT at a photon energy of 670 eV for 4 ML BTO sample (a) in the reduced state, annealed in UHV and (b) in the oxidized state, annealed in $5 \times 10^{-7}$ mbar $O_2$ and (c) in the further annealed state, annealed in $1 \times 10^{-5}$ mbar $O_2$ . . . . .   | 147 |

|     |   |     |
|-----|---|-----|
| 8.4 | High resolution XPS spectrum of the O $1s$ and the Ba $3d_{5/2}$ emission lines, taken in $70^\circ$ off normal emission at RT at a photon energy of 670 for the O- $1s$ and 1000 eV for the Ba $3d_{5/2}$ emission line for 4 ML BTO sample (a,d) in the reduced state, annealed in UHV, (b,e) in the oxidized state, annealed in $5 \times 10^{-7}$ mbar $O_2$ and (c,f) in the further annealed state, annealed in $1 \times 10^{-5}$ mbar $O_2$ . . . . . | 148 |
| 8.5 | (a) The O $1s$ and (b) the Ti $2p$ spectra during reducing the 4 ML BTO sample in UHV, by heating up to 950 K. The spectra were taken at a photon energy of 670 eV, in normal emission. . . . .   | 149 |
| 8.6 | XPS spectra of (a) the Ti $2p$ and (b) the O $1s$ emission lines, taken at RT at the start and the end of heating 4 ML BTO sample in the reduced state in UHV up to 950 K, at a photon energy of 670 eV, taken in normal emission, shown in Fig. 8.5. . . . .   | 149 |
| 8.7 | The combined plot of Fig. 6.12 and 6.16. . . . .  | 150 |
| 8.8 | High resolution XPS spectrum of the Ti $2p$ emission lines of the 4 ML BTO sample in the reduced state, taken in normal emission at 402 K at a photon energy of 670 eV. . . .   | 150 |
| 8.9 | The O $1s$ emission line of 4 ML BTO sample during oxidation in $5 \times 10^{-7}$ mbar $O_2$ , taken at a photon energy of 670 eV in normal emission. Temperature, relative areas and binding energies of the individual components are plotted versus time. The color codings of the components are the same as in Fig. 6.4 (a,b). . . . .  | 151 |





# List of Tables

|     |   |     |
|-----|---|-----|
| 5.1 | The results of the structure determination of bulk BTO, using FEFF6 calculations. Values are given in Å. . . . .  | 54  |
| 5.2 | The stoichiometry of 1 ML BTO in the reduced and the oxidized states, calculated from relative step heights in the absorption spectra at the Ti <i>K</i> -edge and the Ba <i>L</i> <sub>3</sub> -edge. . .  | 68  |
| 5.3 | The values of $\sigma_A$ and the calculated values of $\lambda_{m,E}$ and $S'$ according to Eq. 5.2 calculated for different elements at a photon energy of 2003 eV. . . . .  | 69  |
| 5.4 | The stoichiometry of 1 ML BTO in the reduced and the oxidized states, as well as bulk BTO, determined by different experimental techniques. The presented measurement angles are the incidence angles in XAS and the emission angles in XPS from the normal of the sample surface. . . . .  | 70  |
| 5.5 | The results of FEFF6 calculations of the model presented in Fig. 5.20 (b). The distances are given in Å and the shift in the edge position, $\Delta E$ in eV. <i>cn</i> stands for the coordination number of each atom. . . . .  | 76  |
| 5.6 | The results of FEFF6 calculations on the cluster for BTO-derived OQC (Fig. 5.25), with distances of atoms from Ti in Å and the shift in the edge position, $\Delta E$ in eV. <i>x</i> and <i>y</i> positions of Ti are referred to Pt <sub>1</sub> , while <i>z</i> (in Å) is referred to Pt <sub>4</sub> , since Pt <sub>1,2,3</sub> can have a relaxation of $\Delta z_{Pt}$ . <i>no</i> <sub>3</sub> refers to the number of O <sub>3</sub> atoms. The corresponding distance of the Kepler-approximant, derived from surface X-ray diffraction and density functional theory calculations are included for comparison [44]. . . . . | 82  |
| 5.7 | The results of FEFF6 calculations on the cluster model in Fig. 5.28 ( <i>R</i> -factor: 0.18). The distances are given in Å, the shift in the edge position, $\Delta E$ , in eV. <i>x</i> and <i>y</i> positions of Ti are referred to Pt <sub>1</sub> and have been set to 1.35 and $-0.75$ Å, while <i>z</i> of Ti and $\Delta z_{Pt}$ of Pt <sub>1,2,3</sub> are referred to Pt <sub>4</sub> . The coordination number of O <sub>1,3</sub> are determined through the fit. . . . .   | 86  |
| 6.1 | The values of $\sigma_A$ and the calculated values of $\lambda_{m,E}$ and $S'$ according to Eq. 5.2 calculated for the Ti <i>2p</i> and the O <i>1s</i> emission lines at 670 eV and for the Ba <i>3d</i> at 1000 eV photon energies. . . . .   | 106 |
| 6.2 | The stoichiometry of 4 ML BTO on Pt(111) in the reduced, the oxidized and the further annealed state, determined by XPS, taken in normal and grazing emission angles. O1 stands for O values resulting from subtracting only the contamination peaks from the total O area, while O2 values result from subtracting the broad feature, assigned to O in OH or surface defects, in addition. . . . .   | 106 |

8.1 The line shapes of the components, employed for fitting the XPS spectra of 4 ML BTO on Pt(111) in the reduced state, presented in Sec. 6.3. In case of a modification in the corresponding peaks in the oxidized or the further annealed states, new parameters are given. The line shapes have been defined by using Eq. 5.1. In the table,  $E_B$  (eV) stands for the binding energy of the peak,  $M$ , the mixing ratio (0: pure Gaussian; 1: pure Lorentzian),  $\Gamma$  (eV), the FWHM of the peak, SOS (eV), the spin orbit splitting of the Ti doublet and AR and IR, the area and the intensity ratios of the peak in the Ti  $2p_{3/2}$  region to those in the Ti  $2p_{1/2}$  region. The peaks in Ti  $2p_{1/2}$  are Gaussian with the FWHM calculated so that they full fill the conditions of AR and IR. . . . . 144

# 1 Introduction

Ultrathin oxide films play a crucial role in industry due to their special electronic and photonic properties. Ultrathin BaTiO<sub>3</sub> films are a class of oxide films, which also show ferroelectric behavior and therefore are promising for further interesting applications.

In the reference books of crystallography, materials are usually categorized as crystals and amorphous. The introduction of quasicrystals opened a new category in crystallography as well as in material science. Quasicrystals have self-similarity instead of crystalline long-range order. This makes tiling of a surface by quasicrystals still possible. The discovery of BaTiO<sub>3</sub>-derived oxide quasicrystals (OQC) on Pt(111) surface in 2013 created a new class in quasicrystalline structures. This has revealed enormous questions about the geometrical structure, oxidation states, interaction between the OQC layer and the crystalline substrate and the possible applications of OQCs. BaTiO<sub>3</sub>-derived OQC layer is extensively described in Sec. 2.4.

The lateral arrangement of Ti atoms in a OQC layer has been determined by scanning tunneling microscopy (STM). However, no further information about the geometry of other atoms in the OQC layer has been obtained by STM. In addition, no information could be obtained by STM about the relation of the OQC layer to the Pt substrate. The quasicrystalline nature of the layer makes the study of the system even more complex since the system must be investigated with local methods.

One of the main contributions of the current work is the investigation of the OQC layer using extended X-ray absorption fine structure (EXAFS), which probes the local coordination of atoms. Understanding the geometry of the system, in particular the bond lengths, results in information about the atomic interactions within the layer and the interaction of the layer and the substrate and therefore, paves the path to introduce new applications.

To perform the EXAFS data analysis, approximate pre-knowledge about the bond lengths leads to more accurate data analysis. This is usually done by a Fourier transform of EXAFS modulations. However, this transformation does not lead to any information about the elemental species of neighbors. In addition, it leads to uncertainties up to 0.8 Å in distances of neighbors. Developments in the EXAFS data analysis overcome these problems and lead to more accurate pre-knowledge about the distances of atoms in the system.

The oxidation states of the OQC system are linked to the coordination of atoms in the system. Monitoring the changes in the oxidation states and coordination during the formation of the OQC layer plays a key role for this purpose, which can be obtained through high resolution X-ray photoemission spectroscopy. In addition, this technique permits monitoring the processes of dewetting and rewetting of the Pt surface during growth and decay of OQCs. Therefore, it leads to a deeper understanding of interactions between the OQC layer and the crystalline Pt substrate.

The present thesis consists of 7 chapters. The next two chapters describe the investigated ma-

## *1 Introduction*

materials, as well as the physical fundamentals of the main experimental techniques. Developments in the EXAFS data analysis are presented in Ch. 4 and are applied to EXAFS modulations of a SrTiO<sub>3</sub> single crystal. Within the framework of this work, the local geometries of recently discovered BaTiO<sub>3</sub>-derived OQCs, as well as single crystal BaTiO<sub>3</sub> are investigated using EXAFS, as discussed in Ch. 5. The local structure of OQCs are further investigated by studying their growth and decay using X-ray absorption and X-ray photoemission spectroscopy, as presented in Ch. 6. Finally, the conclusions are summarized in Ch. 7, together with outlooks for future investigations.

## 2 Investigated materials

Materials investigated in this thesis are introduced in this chapter briefly. The physical properties of them are discussed, as was required within the scope of the current work. The investigated systems are barium titanate derived quasicrystal as well as single crystalline barium titanate and strontium titanate.

### 2.1 Barium titanate

Barium titanate (BTO) is an oxide with the elemental composition  $\text{BaTiO}_3$  and a perovskite structure. Fully oxidized stoichiometric barium titanate is light yellow. It is ferroelectric at room temperature with a large dielectric constant [1, 2]. These properties suggest interesting applications for  $\text{BaTiO}_3$  in semiconductors [3], thin film storage devices [4] and catalysts [5, 6].

The unit cell of BTO consists of 8  $\text{Ba}^{2+}$  ions at the cubic corners and 6  $\text{O}^{2-}$  at the face center positions. Therefore, every Ba is coordinated by 12 O and Ti is octahedrally coordinated by 6 O [7]. The schematic of a perovskite unit cell with the general elemental composition of  $\text{ABO}_3$  is given in Fig. 2.1.

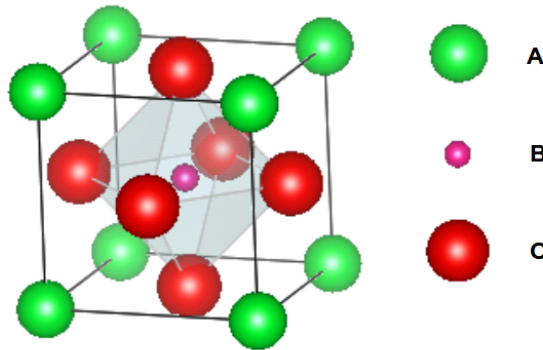


Figure 2.1: A perovskite unit cell with the elemental composition of  $\text{ABO}_3$  in the cubic phase

Barium titanate undergoes several phase transitions. Below 193.15 K it has a rhombohedral structure. Between 193.15 K and 278.15 K the structure is orthorhombic. It is tetragonal between 278.15 K and 393.15 K and changes to cubic at 393.15 K. The temperature dependence of the different phases of BTO, as well as the changes in the unit cell parameters are shown in Fig. 2.2 ([8], Ch. 11 of [9]).

As mentioned, between 278.15 K and 393.15 K BTO has a tetragonal structure with  $a = 399.05$  pm and  $c = 404.12$  pm. In this unit cell Ti is not at the center and has two distances from O atoms along

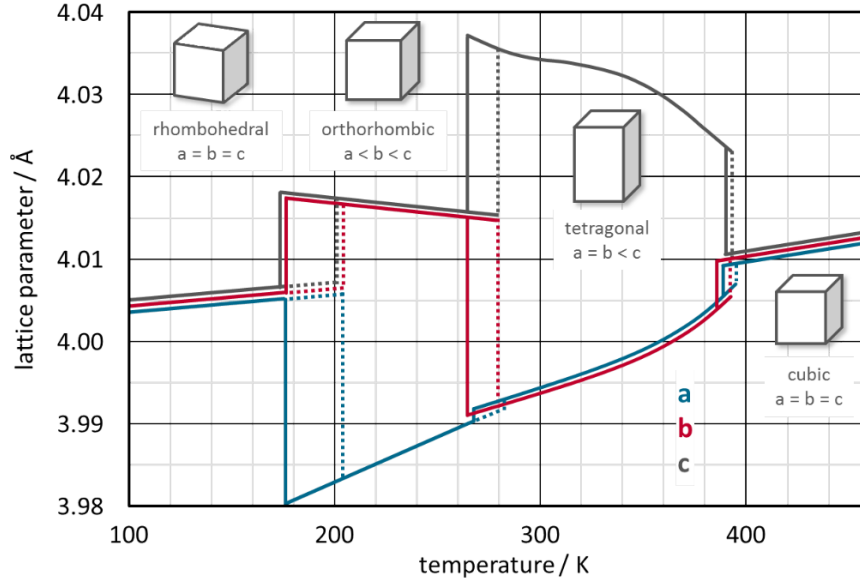


Figure 2.2: BTO phases with changes of the lattice parameters during heating (dot lines) and cooling (solid lines) with their hysteresis behaviors at their phase transition temperatures [8, 9, 10].

z direction, which are 175 pm and 229 pm, while 4 equatorial O atoms are at 200.9 pm [7]. That results in a polarization and therefore, the ferroelectricity of tetragonal phase. BTO is investigated in the ferroelectric phase in the current work.

Similar to the transition from ferromagnetic to paramagnetic, there is also the ferroelectric to the paraelectric transition at the corresponding *Curie Temperature*  $T_C$ .  $T_C$  for barium titanate is 393.15 K, above which it is cubic with a lattice constant of  $a = 401.8$  pm.

In this work, the BTO(001) surface is investigated, which can have two terminations. The top layer of BTO(001) surface can either be barium oxide (BaO) or titanium dioxide ( $\text{TiO}_2$ ). Pancotti *et al.* and Berlich *et al.* have reported BaO termination of the surface with their preparation methods [11, 12]. In addition, Kolpak *et al.* have proposed a phase diagram for the termination of the BTO(001) surface as a function of sample preparation [13]. According to their findings, after annealing at 970 K under ultra high vacuum (UHV) condition the surface has mostly BaO termination.

There are ferroelectric domains, which are similar to ferromagnetic domains. In the ferroelectric domains unit cells have the same polarization directions. These domains are visible as stripes in a single crystal BTO. If the polarization direction is perpendicular to the surface, the domain is called a *c*-domain and if it is parallel, it is an *a*-domain. There are two perpendicular *a*-domains on the surface. In each case, Ti can be shifted in positive or negative directions, which all together makes six different domains for BTO at room temperature. The border of positive and negative domains of the same type form so-called  $180^\circ$  domain walls. The other possibility is the boundary between *a*- and *c*-domains, which form  $90^\circ$  domain walls.

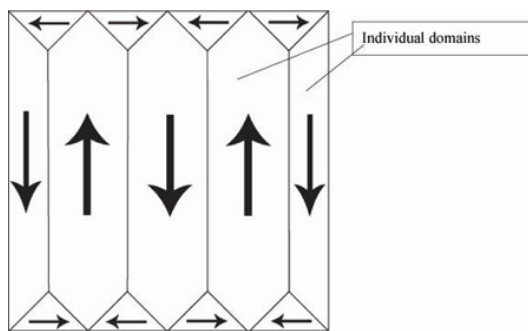


Figure 2.3: Domains and domain walls in BTO, taken from [14]

## 2.2 Strontium titanate

At room temperature strontium titanate (STO) has a cubic perovskite structure. Due to the smaller ionic radius of Sr compared to Ba, it has a smaller lattice constant than barium titanate,  $a = 390.5$  pm. The crystal is colorless to light yellow, similar to BTO [15, 16].

$\text{SrTiO}_3$  is cubic at room temperature and therefore, not ferroelectric due to the absence of polarization. It exhibits cubic-to-tetragonal phase transition at 105 K [17, 18] together with a small expansion of the unit cell with the new lattice constants  $a=391.0$  pm,  $c=391.2$  pm [19].

Both BTO and STO are insulating and for experimental usage they are doped to have sufficient conductivity by 0.05 wt% of C or Nb. The doping also changes the color of STO to black. STO is cheaper and easier to handle than BTO. In addition, the cubic phase has a large temperature range. Therefore, if the ferroelectric properties of BTO are not relevant, STO is used as a cheap replacement to grow and investigate properties of magnetic layers. The results can then be transferred to ferroelectric BTO.

## 2.3 Pt(111) single crystal substrate

Pt is a metal with fcc structure. It is quite inert with low reactivity towards oxygen. Therefore, it is a suitable substrate to grow oxides. The Pt(111) surface has unit cell of  $2.775$  Å [20]. This surface was used as substrate to grow barium titanate derived oxide quasicrystal, since, there is only 2% mismatch between the lattice constants of Pt(111)-(2 × 2) and  $\text{BaTiO}_3(111)$ . Therefore, epitaxial growth of BTO on Pt(111) is expected, as studied by Förster and Widdra [21]. Furthermore, Pt(111) surface does not show reconstruction at preparation temperatures in this work [22].

## 2.4 Barium titanate derived oxide quasicrystal

In most solid state text books solids are divided into two groups: crystalline and amorphous systems. Crystalline structures have local as well as long-range order and cover the whole space by repeating their primitive unit cell. On the contrary, amorphous systems have aperiodic structures. In addition to the periodic structure, tiling of space is also possible using another class of structures, which

## 2 Investigated materials

are quasicrystals. Contrary to crystals, quasicrystalline structures have no translational symmetry and no long-range real space order, but instead, self similarity. Self similarity means that one part of the structure has the same shape as the whole of it, but is just scaled down by a factor. This scaling factor depends on the tiling type.

One type of self similar structures starts from a dodecagon, which is tiled according to Niizeki-Gähler pattern with squares, rhombs and triangles as building blocks. The self similarity factor of this tiling is  $(2 + \sqrt{3})$ , as shown in Fig. 2.4 [23, 24].

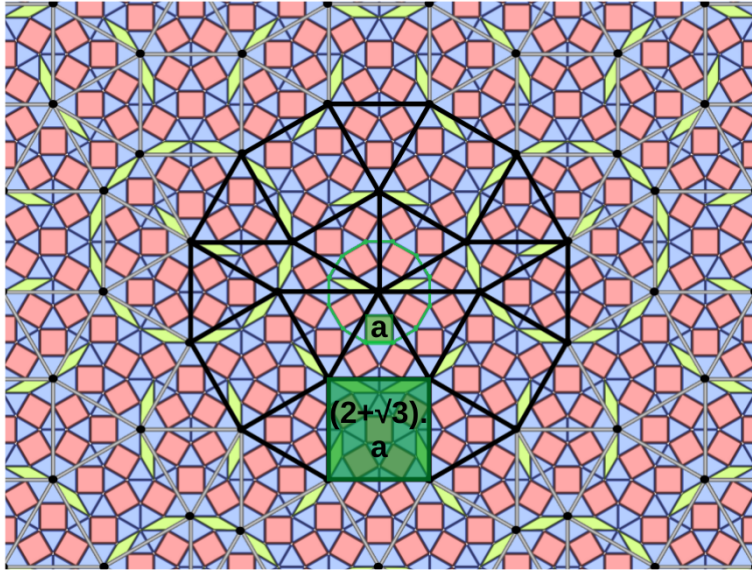


Figure 2.4: Niizeki-Gähler tiling [23, 24] consists of squares, triangles and rhombs, the image courtesy of S. Förster.

The building blocks of quasicrystals repeat with incommensurate frequencies, which means that the ratio of frequencies cannot be given by integer numbers [25, 26, 27]. Although quasicrystals do not show real space periodicity, they can be considered as projections from higher dimensional space on to real space, investigated by high dimensional crystallography [28].

Interestingly, architectures have used quasicrystals for Tilings in medieval Islamic architectures. For example, quasicrystals were used for the tiling of the Darb-I Imam shrine in Isfahan, Iran in 1453. This tiling is a remarkable piece of medieval architecture. The surface has been covered almost perfectly by a quasicrystal pattern with only 11 mismatched pieces out of 37000 [25, 26, 27]. The mathematical pattern of this tiling was developed by Penrose in 1979, which has opened up a new class of quasicrystals with pentaplexic pattern [29].

The first observed and crystallographically investigated quasicrystal was a metallic solid (Al-14-at.%-Mn) in 1984 by Dan Shechtman *et. al.* [30], for which Shechtman received the noble prize in chemistry in 2011. After Shechtman, other discovered quasicrystals were intermetallic systems [31, 32, 33, 34] and more recently some 2D soft materials [34, 35, 36, 37, 38, 39].

In 2013, Förster *et. al.* discovered the class of oxidic quasicrystals (OQC). The OQC has a 2D aperiodic overlayer, derived from BTO on Pt(111) with 3-fold rotational symmetry [40]. These oxide quasicrystals consist of dodecagonal Ti structures with 12-fold diffractive symmetry and



a fundamental length of 6.85 Å. The length has been derived from low-energy electron diffraction (LEED) and high resolution scanning tunneling microscopy (STM) images at 77 K (Fig. 2.5). The dodecaconal structure consists of squares, triangles and rhombs in a Niizeki-Gähler tiling.

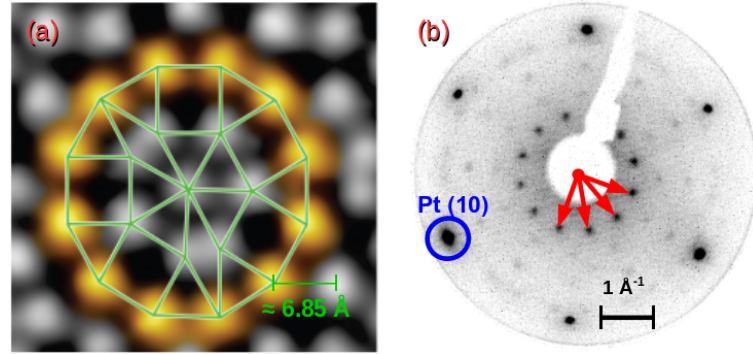


Figure 2.5: (a) STM image of the dodecaconal structure of the BTO-derived oxide quasicrystal, which is tiled according to Niizeki-Gähler tiling. The STM image was taken with a tunneling voltage of 0.1 V. The structure exhibits 12-fold diffractive symmetry, as given by the LEED image (b) taken at 66 eV electron energy. The (10) spot of the Pt substrate is illustrated in the image. Both measurements were performed at in 77 K [40].

OQCs are formed by the reduction of 3D BTO islands in UHV. Atoms of the 2D layer diffuse on the Pt surface through a wetting process by annealing in UHV on 1170 K. By heating in  $7 \times 10^{-7}$  mbar O<sub>2</sub> at 900 K 3D BTO islands are formed through a dewetting process. Wetting and dewetting of the Pt surface are reproducible processes and one can switch several times between 3D islands and 2D OQCs by heating in oxygen and UHV [40, 41].

In addition to BTO-derived oxide quasicrystals, 2D STO-derived OQCs on Pt(111) have also been discovered by Schenk *et. al.* [42]. This reveals the possibility of the formation of different 2D OQCs on Pt(111), which is independent of the lattice mismatch between the bulk structure of the overlayer and the fcc substrate. However, the STO-derived OQC has a 1.8% smaller fundamental length (6.72 Å) than the BTO-derived one (6.85 Å). Similarly, Ti-O distance in STO (1.95 Å) is 3% smaller than that of cubic BTO (2.01 Å). The ionic radii of Sr and Ba seem to have a similar effect on the fundamental lengths of OQCs as on the Ti-O distances in STO and BTO single crystals.

While discovering aperiodic OQC, a periodic structure was also observed on other parts of the sample. This periodic structure is called barium titanate derived Kepler-approximant. Kepler introduced such a periodic arrangement at 1619 [43]. Ti atoms in the Kepler-approximant arrange in squares and triangles with a side length of 6.7 Å, as shown by the STM image (Fig. 2.6 (a)). Since the Kepler-approximant is very similar to OQC, this structure can be considered as the periodic approximation of the aperiodic OQC. Squares and triangles have different arrangements in the Kepler-approximant and form different domains (Fig. 2.6 (b)). Figure 2.6 (c) shows the LEED pattern of the Kepler-approximant with its 6 different domains [44].

The lateral arrangement of Ba atoms in the Kepler-approximant has been determined by surface X-ray diffraction (surface XRD). It has been found that Ba atoms are at bridge sites between titanium atoms. Density functional theory (DFT) calculations indicate that every Ti is coordinated

## 2 Investigated materials

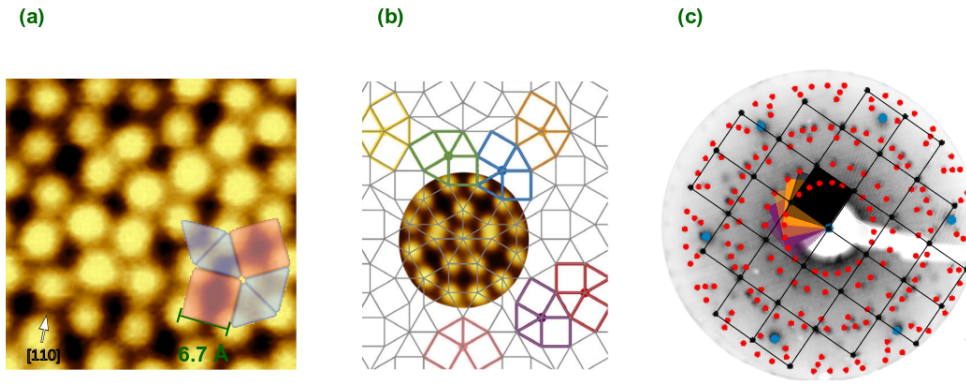


Figure 2.6: (a) STM image of the BaTiO<sub>3</sub>-derived Kepler-approximant, taken at a tunneling voltage of 1V. Different domains of the Kepler-approximant around BTO-derived OQC are shown in Fig. (b). (c) The LEED pattern of the Kepler-approximant on Pt(111) at an electron beam energy of 20 eV. The LEED pattern shows the 6 different domains of the BTO-derived Kepler-approximant [44].

by 3 O atoms. The vertical arrangements of Ti, Ba and Pt atoms were also optimized by a DFT calculation, as shown in Fig. 2.7 [44].

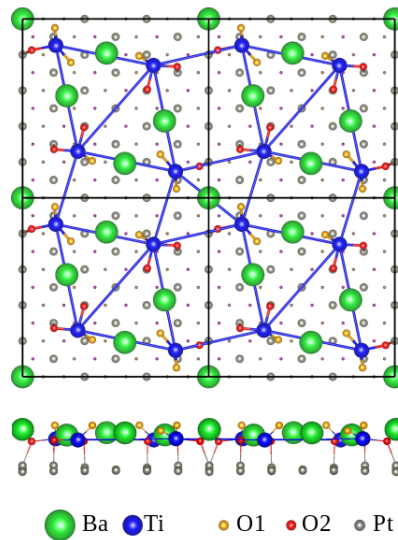


Figure 2.7: Top view and side view of structural model for the Kepler-approximant from a DFT calculation [44].

To understand the physical properties and possible applications of BTO-derived OQCs, their stoichiometry and structure need to be determined. The aperiodic nature of this system makes it impossible to apply conventional structural determination methods, like XRD. To investigate the structure of the BTO-derived OQC, local probing techniques like STM are suitable. However, STM only shows Ti atoms and their lateral arrangement and information about Ba and O and the arrangement of the atoms above the Pt(111) substrate need to be obtained by other methods. The main goal of the current work is to obtain this structural information by extended X-ray absorption fine structure (EXAFS), which does not require long range order.

# 3 Experimental Techniques

In this chapter the physical principles of the main experimental techniques are described, which have been used in this work. The employed techniques are: X-ray absorption spectroscopy (XAS), X-ray photoemission spectroscopy (XPS), extended X-ray absorption fine structure (EXAFS), scanning tunneling microscopy (STM) and atomic force microscopy (AFM).

## 3.1 The X-ray radiation source

Synchrotron radiation is the source of X-rays in this work. It has high intensity and the brilliance. Further more, the beam can widely be tuned in energy and has high degree of polarization as well as collimation.

The X-ray beam in the synchrotron is generated by accelerating relativistic electrons by using *undulators*. It consists of two parallel arrays of magnets, modules, which are oriented in alternating directions. By applying a corresponding phase-shift between the two modules, electrons move in sinusoidal or circular paths, which results in the generation of linearly or circularly polarized X-rays, as is illustrated in [45], according to [46].

The periodicity of the magnets in an undulator is quite small, which results in constructive and destructive interferences between generated photon cones. This lead to a very intense beam in a small energy range. The generated beam is monochromatized using a gratings in grazing incidence to the desired beam energy. To change the photon energy, the gap of the undulator and the tilt of the momochromator crystal are changed simultaneously.

Figure 8.2 (Ch.13 of [47]) presents a typical undulator spectrum. The flux of the generated X-rays is given as the number of photons per second per 0.1% BW, where BW is the bandwidth of the spectrum. The magnetic field inside an undulator is not a pure sinusoidal but has higher harmonics. Therefore, the undulator radiation also contains harmonics. As is derived in [48] and also shown in the figure, the odd harmonics have the highest intensities. For further information about the synchrotron facilities, interested readers are referred to [45, 48, 49, 50].

## 3.2 X-ray absorption spectroscopy (XAS)

While irradiating a thin film by X-rays, they will be absorbed and excite electrons from core levels of the atoms to the continuum or to higher unoccupied levels. In addition, the beam transmits

### 3 Experimental Techniques

through the film by an attenuated intensity, which is calculated according to Lambert-Beer's law ([45], Ch. 1 of [51], Ch. 9 of [52])

$$I_d = I_0 e^{-\mu d} \quad (3.1)$$

where  $I_0$  and  $I_d$  are the initial and the attenuated beam intensities,  $d$  the sample thickness and  $\mu$  the linear X-ray absorption coefficient of the material. In addition, the X-ray absorption cross-section,  $\sigma$ , which is the number of absorbed photons per atom divided by the number of incident photons per unit area, is related to  $\mu$  according to

$$\sigma = \mu/\rho \quad (3.2)$$

where  $\rho$  is the density of atoms.

The absorption process is determined by selection rules, which are described briefly in the following. A detailed description is given in Ch. 1 of [51].

The X-ray absorption cross-section ( $\sigma_a$ ) can also be interpreted as transition rate,  $W_{i \rightarrow f}$  [sec<sup>-1</sup>], divided by the incident photon flux ( $\Phi_0$  [number of photons/cm<sup>2</sup>s]). The transition rate is the probability of excitation of an electron from the initial (core) level  $|i\rangle$  to the final state  $|f\rangle$ . This leads to

$$\sigma_a = W_{i \rightarrow f} / \Phi_0 \quad (3.3)$$

The probability for this transition can be calculated by Fermi's Golden rule in first order time dependent perturbation theory, which leads to:

$$W_{i \rightarrow f} = \frac{2\pi}{\hbar} |\langle f | T_{i \rightarrow f} | i \rangle|^2 \delta(E_f - E_i - \hbar\omega) \quad (3.4)$$

Here,  $T_{i \rightarrow f}$  is the interaction operator, which in first order is approximated by the interaction Hamiltonian  $H_{int}$ ,  $\hbar\omega$  is the photon energy and  $\delta(E_f - E_i - \hbar\omega)$  takes care of energy conservation. In perturbation theory,  $H_{int}$  of the absorption process can be approximated as:

$$H_{int} = \sum_q [(\mathbf{e}_q \cdot \mathbf{p}) + i(\mathbf{e}_q \cdot \mathbf{p})(\mathbf{k} \cdot \mathbf{r})] \quad (3.5)$$

where  $\mathbf{e}_q$  is the unit vector for the polarization  $\mathbf{q}$  of the X-rays,  $\mathbf{k}$  and  $\mathbf{r}$  are the wave vector of the X-ray and the displacement vector and  $\mathbf{p}$  is the electron momentum. The first term in equation 3.5 is the electric dipole transition and the second term is the electric quadrupole transition, while the probability of the transition equals to the square of the matrix element.

The probability of the electric dipole transition is much larger than that of the quadrupole. For example for the *K*-edge of carbon, the electric dipole transition probability is three orders of magnitude larger than that of the quadrupole (Ch. 1 of [51]). So by keeping the dipole transition part and neglecting other terms, we obtain the Hamiltonian for the dipole transition approximation. Using the commutation law for  $\mathbf{p}$  ( $\mathbf{p} = m/i\hbar[\mathbf{r}, \mathbf{H}]$ ), one obtains for the transition matrix (interaction Hamiltonian) in the dipole approximation:

$$H_{int} = \sum_q (\mathbf{e}_q \cdot \mathbf{r}) \quad (3.6)$$

Finally, the substitution of  $H_{int}$  in Fermi's golden rule (equation 3.4) leads to the transition matrix element in the dipole approximation as the following:

$$W_{i \rightarrow f} = \frac{2\pi}{\hbar} |\langle f | (\mathbf{e}_q \cdot \mathbf{r}) | i \rangle|^2 \delta(E_f - E_i - \hbar\omega) \quad (3.7)$$

This is the polarization dependent X-ray transition probability of electrons per unit time in dipole approximation, from which the absorption cross-section can be derived. The schematic of the core hole creation process is shown in Fig. 3.1.

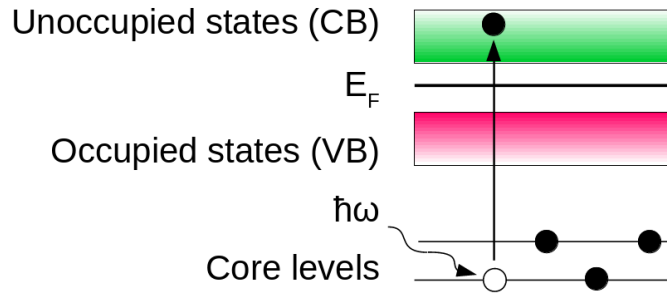


Figure 3.1: X-ray absorption process and excitation of the core electron to unoccupied states, derived from [53].

In this work,  $K$ ,  $L$  and  $M$ -edges have been investigated (Fig. 3.3). At the  $K$ -edge, an electron is excited from a  $s$  level. According to the dipole selection rule,  $\delta(l) = \pm 1$ . The outgoing photoelectron wave has  $p$  character and propagates in the direction of the electric field of the incoming X-ray. Applying the dipole selection rule to the transition at the  $L$ -edge, the outgoing wave is a mixture of  $s$  and  $d$  orbitals. Finally, at the  $M$ -edge, the outgoing wave is a mixture of  $p$  and  $f$  orbitals.

After the creation of the core hole, the system is highly excited and relaxes through radiant and non-radiant processes. In the radiant process, the hole is filled by an electron from higher subshells and a fluorescence photon is emitted with an energy equal to the energy difference between the subshell and the core state. The detection of fluorescence photons is the basis of fluorescence yield (FY) measurements of the X-ray absorption cross-section.

The non-radiant decay of the core hole is based on a two electron process, in which an electron from a higher subshell fills the hole and simultaneously a second electron is ejected. The kinetic energy of the second electron results from the overall conservation of energy. This electron is called *Auger* electron and can be detected by an electron analyzer, which is the basis of Auger electron spectroscopy. The name of the Auger process is derived from the states, which are involved in the process. For example, in the  $LMM$  transition, the excited core hole from  $L$  level is filled by an electron from an  $M$  level, together with the emission of an Auger electron also from an  $M$  level. The principles of the radiant and non-radiant decays of the core hole, as well as photoelectron excitation are shown in Fig. 3.2.

It is important to note that the kinetic energy of the Auger electron does not depend on the

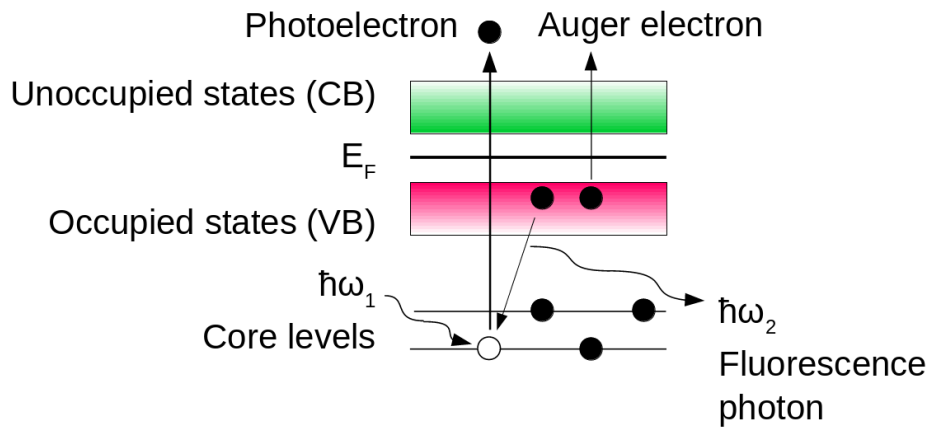


Figure 3.2: Fluorescence decay, Auger electron emission and X-ray photoelectron ejection processes, derived from [53].

energy of the X-ray beam and is characteristic for a specific element. The Auger process is used as the basis of Auger electron yield (AEY) to measure X-ray absorption (Sec. 3.2.3). Core levels are also investigated by X-ray photoelectron spectroscopy (XPS), which is described in detail in Sec. 3.3.

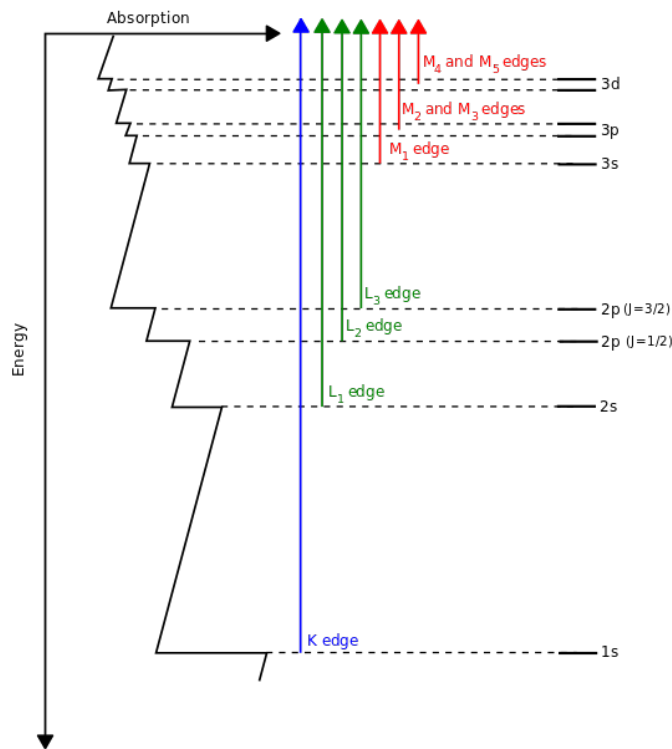


Figure 3.3: Different XAS transition processes [54].

### 3.2.1 The X-ray absorption spectrum

The X-ray absorption spectrum is a plot of the X-ray absorption cross-section versus the energy of the X-ray beam. An example of such a spectrum is shown in Fig. 3.4. The peak of the X-ray

absorption spectrum is called X-ray absorption resonance and appears in the similar energies as the binding energy of the excited core level. The resonance peak originates from excitations from the core level to an unoccupied state close to the vacuum level and reflects the increase in the density of states close to this level. After the resonance peak, a step-like background appears in the spectrum, which is called the edge jump. The edge jump originates from exciting a core electron to the continuum. The absorption edges in the spectrum are depicted as spikes in Fig. 3.3, while the spectrum is rotated by  $90^\circ$  [54].

The X-ray absorption spectrum consists of four regions. The first one is called pre-edge region and has an energy range of  $E < E_0$ , with  $I \ll I_0$ , where  $E_0$  and  $I_0$  are the energy of the absorption edge and the intensity of the spectrum at the edge position.  $I$  is intensity of the absorption spectrum at the energy  $E$ . The pre-edge features originate from transitions of electrons from core levels to half-filled or empty levels below the vacuum level. The second region is X-ray absorption near edge region (XANES) and corresponds to the energy range of 10 eV below the absorption edge to 10 eV above it. XANES features originate from transitions from core levels to empty states close to the vacuum level.

The next region is near edge X-ray absorption fine structure (NEXAFS) region, which corresponds to the energy range of 10 eV to 50 eV above the absorption edge. NEXAFS features result from multiple scattering of outgoing photoelectrons at atoms of the first and second coordination shells around the absorbing atom. NEXAFS features can also be viewed as transitions to unoccupied states close to the vacuum level. Finally, the extended X-ray absorption fine structure (EXAFS) has the energy range of  $+50 < E < +1000$  eV and is mainly due to single scattering of the ejected photoelectrons at neighbors. The last two regions contain valuable information about neighboring atoms and can be used to extract interatomic distances.

### 3.2.2 The X-ray absorption data analysis

The first step of analysis of an X-ray absorption spectrum is to subtract the background. The type of the background function depends on the origin of the full width at half maximum (FWHM) of the spectrum. In case FWHM originates from the *core hole lifetime*, a *Lorentzian* broadened step function needs to be subtracted. This step function is given by equation 3.8 (Appx. A of [52]):

$$I(E)_{Lorentzian} = H \left( \frac{1}{2} + \frac{1}{\pi} \arctan \left( \frac{E - P}{\Gamma/2} \right) \right) \quad (3.8)$$

where  $H$  is the step height in the spectrum,  $E$  the photon energy,  $P$  the edge position and  $\Gamma$  FWHM of the step.

Equation 3.8 can be used to subtract the background in  $K$ -edge absorptions. At higher order edges ( $L, M, \dots$ ), the absorption edge is split due to spin orbit splitting. In such cases, the total height of the background step is a combination of two contributions. For example, at the  $L_{2,3}$ -edges the step height of the  $L_2$  is half of that of the  $L_3$  and equation 3.8 is rewritten accordingly [55]:

$$I(E)_{Lorentzian} = H \left( \frac{2}{3} \left[ \frac{1}{2} + \frac{1}{\pi} \arctan \left( \frac{E - P_{L3}}{\Gamma_{L3}/2} \right) \right] + \frac{1}{3} \left[ \frac{1}{2} + \frac{1}{\pi} \arctan \left( \frac{E - P_{L2}}{\Gamma_{L2}/2} \right) \right] \right) \quad (3.9)$$

The background is shown in Fig. 3.4 for an arbitrary  $L$ -edge with the total step height of  $H$ . Further broadenings such as experimental or thermal broadenings can be included through a *Gaussian* broadened step function.

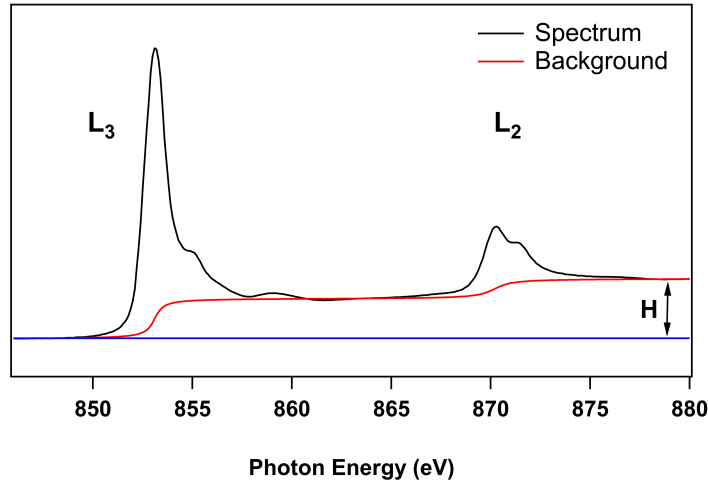


Figure 3.4: Background subtraction in an arbitrary  $L_{2,3}$  spectrum.

### 3.2.3 Detection methods

In the soft X-ray regime (photon energy below 2 keV), photoabsorption, which leads to electron emission, has a higher probability by orders of magnitude than coherent or incoherent scattering. To detect the absorption of X-rays, three methods are commonly used, transmission, fluorescence yield (FY) and electron yield (EY). They will briefly be discussed in this section. For more details please see Ch. 1 of [51], Ch. 5 of [56] and Ch. 6 of [57].

The first and the most direct method to detect X-ray absorption is transmission. The absorption of X-rays at the edge results in a drop in intensity of the transmitted beam. This method is a standard method to investigate thin films in the hard X-ray regime, because the intensity of the transmitted beam is high enough to be recorded. For energies less than 1 keV, the attenuation length of the X-ray is 1  $\mu\text{m}$ . Therefore, to perform transition measurements in the soft X-ray regime samples must be extremely thin. In addition, due to the high absorption of air in this regime, the measurement must be performed in vacuum.

The excited system with a core hole relaxes through two competing processes, fluorescence decay, a radiative decay and Auger electron decay, a non-radiative decay. In fluorescence yield (FY), the created fluorescence photons are recorded. The *mean free path* of the created fluorescence photons is of the same order of magnitude as the exciting X-rays. Therefore, this method is not really surface



sensitive, whereas Auger electron decay is more surface sensitive, due to shorter escape length of electrons.

The absorption of X-rays can be measured through both decay channels, if they are linearly proportional to the absorption cross-section, which is generally the case. However, in thick concentrated samples, measured in FY in grazing angle of incidence self-absorption needs to be taken into account. For details see Sec. 3.5.1.

The Auger decay dominates for energies below 1 keV. Fluorescence increases with energy and dominates for energies above 10 keV. For example, 3d metals have a strong fluorescence signal at the  $K$ -edge, whereas, the Auger process is stronger at other edges.

The Auger decay is the base of the electron yield (EY) detection method. EY consists of Auger yield (AY), partial electron yield (PEY) and total electron yield (TEY). To explain EY, we assume a system consisting of an over layer with core level A with the valance band overlapping with the valance band of the substrate (VB) core level B. The photoemission spectrum of this system is shown in Fig. 3.5. The vacuum energy level of the system ( $E_V$ ) is separated from the Fermi level ( $E_F$ ) by the work function ( $\phi$ ) and only electrons with energies higher than the work function can leave the sample.

Initially, when the photon energy is less than the binding energy of core levels A ( $h\nu < E_b(A)$ ), only the core level peak of the substrate is present in the spectrum (3.5 (a)). If the photon energy rises to ( $h\nu_2$ ), which is above the absorption energy level of core level A, the characteristic Auger peak of atom A develops at the kinetic energy ( $E_A$ ) (3.5 (b)). When the energy increases further to ( $h\nu_3$ ), the kinetic energy of the core level B shifts. In addition, the photoemission peak of the core level A shows up. Since the Auger peak position is independent of the initial photon energy, the Auger peak position remains constant (3.5 (c)), though its intensity is proportional to the transition probability of the core electrons A and therefore, the intensity of the Auger peak changes as a function of photon energy. The Auger yield is recorded by employing an electron energy analyzer and setting the window energy to  $E_A$ .

During the ejection of Auger electrons from the sample, a part of them receive the analyzer without any scattering. These are called *elastic Auger electrons* in contrary to the other part, which loose energy by exciting secondary electrons and are called *inelastic Auger electrons*. The hatched area in Fig. 3.5 includes contribution of the inelastic electrons, below which the contribution of the secondary electrons is. The figure also shows the different energy windows of AY, PEY and TEY.

In addition to the energy of the Auger peak, the energy distribution of inelastic Auger electrons does not depend on the initial photon energy. Taking into account this point, the transition probability of the core electrons in the atom can also be measured through partial electron yield (PEY), which records the elastic Auger electrons and a portion of inelastic Auger electrons, with a kinetic energy above the threshold  $E_p$ . Technically, this is set by applying a negative voltage  $-V_p$  to the entrance of an electron detector. Compared to AEY, PEY spectra have higher count-rates. However, the signal-to-noise ratio is worse in many cases.

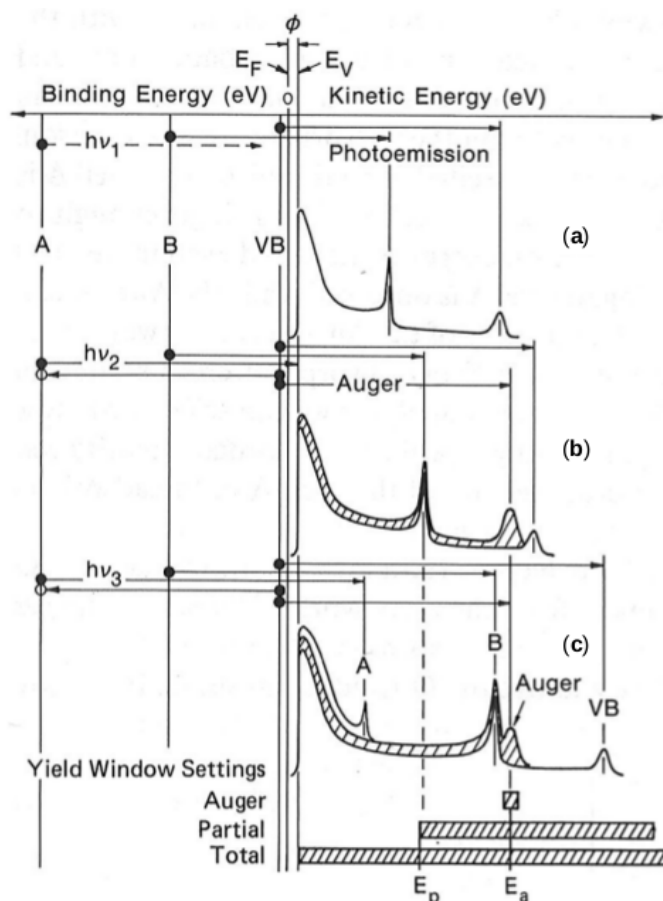


Figure 3.5: The energy level diagram and the schematic photoemission spectra at different energies [56].

The easiest method to record an electron yield spectrum is recording all ejected electrons, regardless of their kinetic energy, which is called total electron yield (TEY). This method includes secondary electrons with an energy less than 20 eV, which form the so called *inelastic tail* region of the spectrum. In spite of having the highest count-rate, the signal-to-noise ratio is lower than PEY. The electron emissions due to the X-ray absorption, charges the sample positively. This makes it possible to obtain a TEY spectrum by simply recording the neutralizing sample current by a pico-Amperemeter as a function of the photon energy.

Figure 3.6 is the universal curve of the inelastic mean free path of electrons in solids taken from [58]. As it shows, low kinetic energy secondary electrons have a large mean free paths and therefore, contain more bulk information.

It is very important to note that the inelastic Auger electrons as well as the secondary electrons originate from the primary elastic Auger electrons and their numbers are proportional to the number of elastic Auger electrons. Since the number of elastic Auger electrons is proportional to the absorption cross-section of the corresponding absorption edge, the numbers of inelastic and secondary electrons are also proportional to the absorption cross-section. Therefore, AEY, PEY and TEY lead to almost identical NEXAFS spectra, except for differences in signal-to-background and signal-to-noise ratios. Furthermore, PEY is more surface sensitive than TEY. Taking into account the inelastic mean free path of the electrons, AEY with an electron kinetic energy of 50 to 100 eV

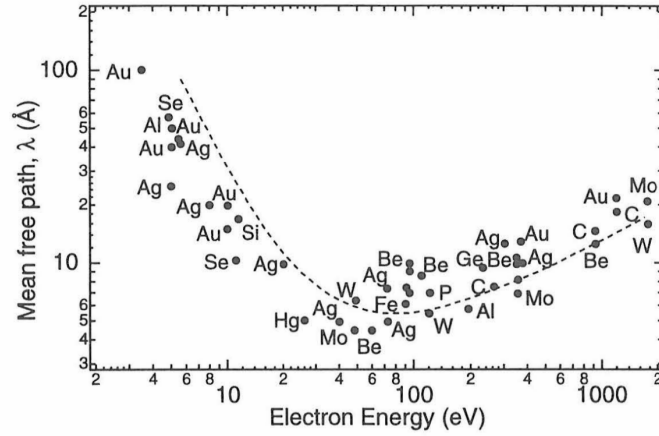


Figure 3.6: The universal curve of the inelastic mean free path of electrons (MFP) taken from [58] according to [59].

lead to maximum surface sensitivity and in addition, AEY is element specific. Finally, comparing EY methods to FY method, for Auger or fluorescence decays, different selection rules apply. In fortunate cases, the differences in spectra supply additional information about the system.

### 3.3 X-ray photoelectron spectroscopy (XPS)

XPS is based on the photoelectron excitation of a core levels of an atom in a specific chemical state. This method was first used to investigate NaCl by K. Siegbahn in 1956 [60] and due to its high potential in chemical analysis, it was initially named electron spectroscopy for chemical analysis (ESCA). In XPS, the core level emission lines of the elements are well separated and in addition, binding energies of different oxidation states of the element are distinguishable. These specifications make XPS a powerful element specific technique. Furthermore, by changing the emission direction from normal to grazing the measurements can be tuned from more bulk sensitive to more surface sensitive. Due to all of these nice advantages, XPS is one on the most common characterization methods in surface science.

As illustrated in Fig. 3.7 [61], the core electron with the binding energy of  $E_B^F$  relative to the Fermi level is ejected by the X-ray with the energy of  $h\nu$ . The kinetic energy of the ejected electrons is recorded using an electron energy analyzer. Initially, the photoelectron has a kinetic energy of  $E_k$ . Due to the electrical contact between the sample and analyzer, their Fermi levels are the same. However, because of the difference in work functions of analyzer  $\Phi_a$  and sample  $\Phi_0$ , the vacuum level of the analyzer increases by  $(\Phi_a - \Phi_0)$  and therefore, the recorded spectra in the analyzer has the kinetic energy of  $E_{k,a} = E_k - (\Phi_a - \Phi_0)$  and finally the binding energy of the core level relative to the Fermi level is given by:

$$E_B^F = h\nu - E_{k,a} - \Phi_a \quad (3.10)$$

where the work function of the analyzer,  $\Phi_a$ , is determined by measuring the reference emission lines.

### 3 Experimental Techniques

The mostly reliable core level binding energies are Au and Pt  $4f_{7/2}$  at 84 and 71.2 eV, respectively and Cu  $2p_{3/2}$  at 75 eV [62]. The reason is that the clean surfaces are easy and reliably to prepare and the emission lines are strong and have small line widths. The C  $1s$  emission line of adventitious carbon at 284.6 eV is also often used in the literature. However, a range from 284.6 to 285.2 eV has been reported as binding energy [63]. The reason is that the binding energy depends on the chemical state and thickness of the carbon layer on the surface and the physical and chemical nature of the substrate [64]. Therefore, one needs to be aware of this uncertainty, when referring to the C  $1s$  emission line. In addition to the emission lines of core levels, the Fermi level of the sample could be used to calibrate the binding energy.

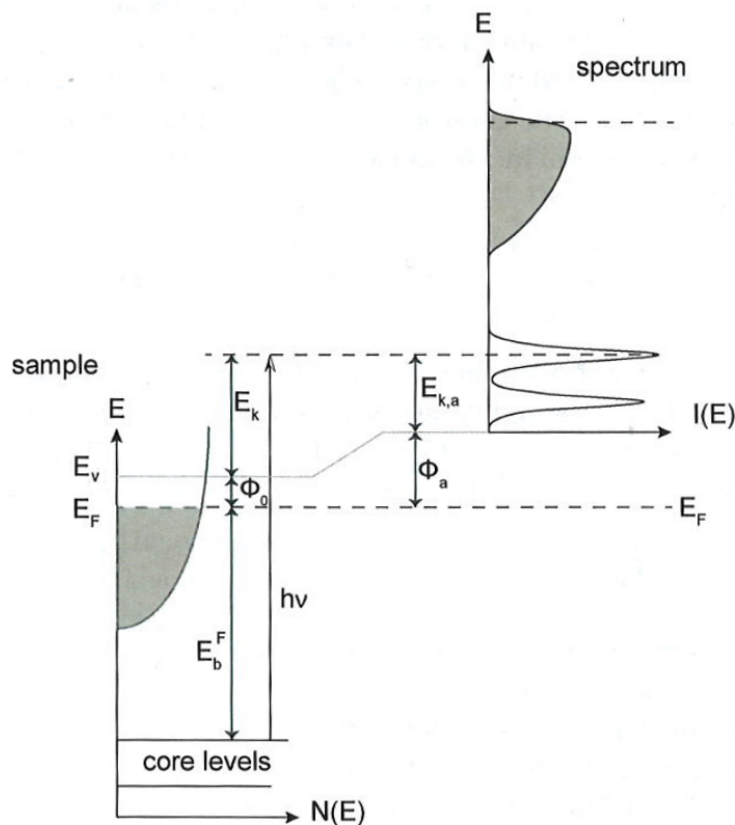


Figure 3.7: Energy diagram in the XPS process [61]

Excitations from  $s$  levels result in a singlet state and therefore, the XPS spectrum consists of one single peak. Excitations from other levels lead to doublets in the spectrum due to spin orbit splitting. The labeling of peaks in an XPS spectrum is derived from the excited core level and the total angular momentum, if spin orbit splitting is present.

The information depth in XPS is a few nanometers and related to the mean free path of electrons. After ejection, the excited electron system relaxes immediately. Two of the possibilities are the emission of *Auger electrons* or *fluorescence photons*, as described in details in Sec. 3.2.

The emitted Auger electron contributes also to the spectrum [65]. The Auger peaks are often broad and easily distinguished from the photoelectron emission lines. In addition, the Auger peaks do not depend on the photon energy and can be recognized by changing the photon energy, which

leads to a shift of the Auger peak in the XPS spectrum.

Photoelectrons and the Auger electrons may lose energy through inelastic scattering effects, which leads to the so called inelastic tail in the photoemission spectrum (the hatched area in Fig. 3.5). A reasonable quantification of the inelastic tail of XPS lines is derived by D. A. Shirley [66]:

$$U_S(E) = k_1 \cdot \int_E^{\infty} j(E') dE' + k_2 \quad (3.11)$$

where  $j(E')$  is the measured spectrum and  $k_1$  and  $k_2$  are constants and must be determined through fitting. Tougaard has also proposed a more complex solution, which is a bit better approximation [67]. However, Shirley's formula has been found to be sufficient for background subtraction in this work.

In addition to photoelectron peaks and Auger peaks, there may also be satellite contributions in the XPS spectrum. One type originates from many body effects while exciting photoelectrons. In addition to exciting a photoelectron, a part of the photon's energy is absorbed and excites electrons or plasmons. The process of exciting an electron to a bound state is called shake-up. Excitation to a continuum state is called shake-off (Ch. 4 of [56]). Satellite peaks are usually at several electron volts higher binding energies and therefore, are easily distinguishable from photoelectron peaks [68]. For the commonly used compounds, these peaks have been investigated and are well known.

## 3.4 Synchrotron beam lines

In this section the synchrotron beam lines, where the data of this work have been measured, are briefly introduced and the corresponding specifications are discussed.

### 3.4.1 The KMC-1 beamline at BESSYII

At the KMC-1 beamline, the X-ray beam is generated using a bending magnet with a radius of 3.45 m and a magnetic field of 1.31 T. The X-ray beam is then focused using a toroidal mirror. Three pairs of Si crystal pairs are used to monochromatize the beam in an energy range from 2005 eV to 12 000 eV. The energy resolution ( $E/\Delta E$ ) at 4 keV is 1000 [69, 70].

The endstation of the beam line consists of a UHV analysis chamber and a small UHV preparation chamber. The sample manipulator has four degrees of freedom in x, y and z directions and the polar angle to do measurements at normal and grazing incidence. The manipulator is also equipped with current heating as well as electron bombardment heating. The sample can be heated up to 1120 K and cooled down to 112 K with liquid nitrogen.

The analysis chamber is equipped with a hemispherical electron energy analyzer (SCIENTA R4000, SCIENTAOMICRON) with a 2D CCD detector. X-ray absorption measurements can be done simultaneously in TEY and FY modes. The fluorescence signal was recorded by a BRUKER XFLASH ®4010 detector, with a Be window.

### 3.4.2 The SuperESCA beamline at Elettra

The X-ray beam at SuperESCA is generated using an undulator with two modules. Each module has 98 periods with a period of 46 mm. They generate X-rays in the energy range from 90 eV to 1500 eV. The pre-focusing of the beam into the monochromator is done by a plane grating from ZEISS, which gives energy resolutions  $E/\Delta E$  of  $\sim 10^4$  @ 400 eV and  $\sim 5 \times 10^3$  @ 900 eV. Finally, an ellipsoidal mirror refocuses the monochromated beam onto the sample [71].

There are two chambers in the endstation. The top one is a preparation chamber with a base pressure of  $3 \times 10^{-9}$  mbar. The bottom one is an analysis chamber with  $\mu$ -metal magnetic shielding. The base pressure of the analysis chamber is  $3.5 \times 10^{-10}$  mbar. The manipulator has four degrees of freedom in x, y and z directions and polar angle  $\theta$ . The accessible temperature range is from 15 K to 1500 K, which is done by electron bombardment and current heating and liquid nitrogen or liquid helium cooling. Recording spectra is done by a hemispherical electron energy analyzer, PHOIBOS, SPECS GmbH with a mean radius of 150 mm. The detection of electrons is done by a homemade 1D detector, which enables fast recording of XPS spectra. X-ray absorption spectra can also be recorded by means of this electron energy analyzer in Auger yield.

## 3.5 Extended X-ray absorption fine structure (EXAFS)

In this section the physical principles of the extended X-ray absorption fine structure (EXAFS) will be discussed. In addition, the principles of the data analysis in EXAFS are given, which lead to the structure determination of systems.

### 3.5.1 Physical principles

The EXAFS range is between 50 to 1000 eV above the absorption edge and consists of oscillations, called as EXAFS modulations, with the size up to 10% of the step height. Prins [72] named these oscillations EXAFS and Kronig [73] specified that these modulations originate as a result of scattering of outgoing electrons at the potential of neighboring atoms. This affects the final state of the outgoing electrons and therefore, elements of the transition matrix. It is a short-range effect and provides structural information about the system with a typical precision better than 0.02 Å.

The physical basis of EXAFS is briefly discussed here. When the energy of the X-ray beam rises over the edge energy, photoelectrons are ejected, with a kinetic energy of  $E_k = E - E_0$  and a wave number  $k$  according to the following equation [74, 45]

$$k = \sqrt{\frac{2mE_k}{\hbar^2}} \quad (3.12)$$

where  $m$  is the non-relativistic mass of the electron,  $\hbar$  the *Planck* constant and  $E_k$  the kinetic energy of the photoelectron in the sample. The kinetic energy of a photoelectron with the binding energy  $E_0$  in a system is calculated according to

$$E_k = h\nu - E_0 \quad (3.13)$$

After the edge, the photoelectron propagates out of the absorbing atom (emitter) as a spherical wave, which will be then scattered at the potentials of neighboring (scattering) atoms. Thus, the final state of the system is the superposition of the outgoing and scattered electron waves, including constructive or destructive interference. The interference is determined primarily by the distance between the absorbing and scattering atoms. There, the atomic numbers play a secondary role in EXAFS modulation through the scattering factors in Eq. 3.16 [75, 76].

The EXAFS signal or *modulation function*  $\chi$  is expressed as a function of  $k$  in the following equation (for instance [45, 77, 75, 78]):

$$\chi(k) = \frac{\mu(k) - \mu_0(k)}{\Delta\mu} \quad (3.14)$$

where  $\mu(k)$  is the measured absorption coefficient,  $\mu_0(k)$  is the X-ray absorption of an isolated atom and  $\Delta\mu$  is the jump at the edge (Sec. 3.5.2). EXAFS oscillation decay quite fast as  $k$  increases and therefore, the modulation function is amplified for higher values of  $k$  by multiplying  $\chi$  by  $k$ ,  $k^2$  or  $k^3$ . Figure 3.8 (a) shows XANES and EXAFS regions at the Ti  $K$ -edge in a 0.5% Nb doped SrTiO<sub>3</sub>(001) crystal, measured in normal incidence, as described in Sec. 3.2.1. In addition, the modulation function  $\chi(k)$  and the  $k^2$  weighted modulation function  $\chi(k) \times k^2$  are illustrated in Fig. 3.8 (b). For a better comparison,  $\chi(k)$  has been multiplied by a factor of 5.

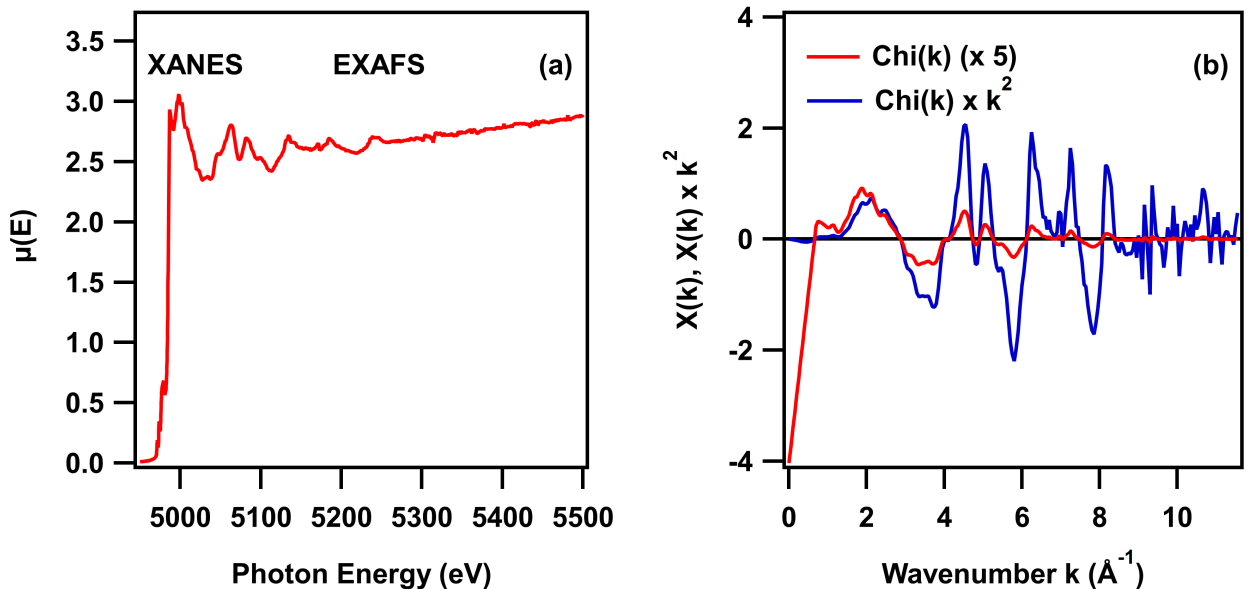


Figure 3.8: (a) XAS spectrum at the Ti  $K$ -edge in a STO(001) crystal and corresponding modulation functions (b).

Figure 3.8 shows that the modulation function is composed of different frequencies, which correspond to photoelectron scatterings at different atoms at corresponding distances from the emitter.

### 3 Experimental Techniques

These distances can be recognized in the radial distribution-like function  $\chi(R)$ , which results from the Fourier transformation of  $\chi(k)$  to  $R$ -space, as shown in Fig. 3.9. However, the peaks in this function are not located at actual distances. The reason is an energy dependent phase-shift  $\delta(k)$  during scattering, which is not taken into account in the Fourier transformation. This leads to the shift in the peak positions in  $\chi(R)$ .

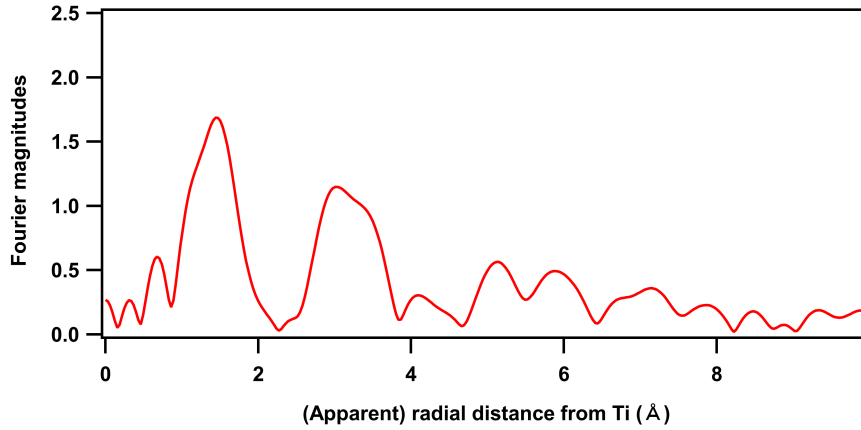


Figure 3.9: Fourier transformation of  $\chi(k) \times k^2$  of the Ti  $K$ -edge in STO(001) crystal

Disentanglement and identification of the contribution of different atoms to the modulation function has been discussed for example in the Appx. A in [56], [74] and Ch. 1 of [79]. In a simplified model, photoelectrons propagate with a spherical wave-function and are scattered elastically at the potentials of neighbors. The elastically scattered waves interfere and form EXAFS modulations, while the inelastically scattered waves cancel each other out due to the loss of coherence. Furthermore, the interference must occur only within the excitation time of the core hole. The limited lifetime of the core-hole and the inelastic scattering are introduced in the EXAFS equation as a damping factor:

$$\Psi(k, r) = \frac{e^{ikr} e^{-r/\lambda(k)}}{kr} \quad (3.15)$$

Here,  $\lambda(k)$  is the *mean free path* of the photoelectron, which is the average length that the photoelectron travels before it is inelastically scattered, or the core hole has been filled up. The *core hole lifetime* is of the order of fs. In combination with inelastic scattering processes, it results in a mean free path between 5 to 30 Å for the photoelectron [74].

Employing the equation 3.15 leads to the description of the modulation function (EXAFS equation) [45, 56, 74]:

$$\chi(k) = S_0^2 \sum_j \frac{N_j f_j(k) e^{-2R_j/\lambda(k)} e^{-2k^2\sigma_j^2}}{kR_j^2} \sin[2kR_j + \delta_j(k)] \quad (3.16)$$

The EXAFS signal integrates over all scattering atoms or *coordination shells*, with coordination number  $N_j$  and scattering amplitude  $f_j(k)$ , at a distance of  $R_j$  from the emitter and the phase-shift



of  $\delta_j(k)$ .  $S_0^2$  is an additional damping factor, representing intrinsic losses. The absorption of the X-rays by an atom is more complex and several electrons may be excited. In such multi-electron excitations, the photoemission peak is dominated by the signal from the *active* electrons. These active electrons are the ones, which are excited in the single electron excitation picture. However, in multi-electron excitations, *passive* electrons are also excited, which in XAS, lead to features at higher energies than the resonance (Ch. 4 of [56]).

Typically,  $S_0^2$  is  $0.7 < S_0^2 < 1$  and assumed to be constant.  $S_0^2$  is also a simple means to treat the difference between plane and spherical waves, although this difference clearly depends on  $k$  [80]. Due to the inelastic mean free path and the  $\frac{1}{R^2}$  terms in Eq. 3.16, EXAFS is a local probe to investigate the structure up to a distance of 5 Å from the emitting atom.

$\sigma_j$  is the mean square relative positional fluctuation of the emitting and backscattering atoms and is part of the Debye-Waller factor  $e^{-2k^2\sigma_j^2}$ .  $\sigma_j$  makes the damping of the corresponding oscillation for higher values of  $k$  stronger. This damping is due to the static (structural) and dynamic (thermal) disorders in the positions of atoms [77]. Oscillations of atomic positions of coordination shells are described by the Einstein model and the Debye model. The Einstein model assumes uncorrelated fluctuations of the emitter and the scatterer, which leads to the following expression for  $\sigma_{ij}$  in a single scattering process:

$$\sigma_{ij}^2 = \frac{\hbar^2}{M_r \omega} \left( \frac{1}{\exp(\hbar\omega/k_B T) - 1} + \frac{1}{2} \right) \quad (3.17)$$

where  $k_B$  is the Boltzmann constant and  $M_r$  is the reduced mass, which is  $M_r = M_i M_j / (M_i + M_j)$ . The frequency  $\omega$  is a parameter and determined by fitting the calculated spectrum to the experiment, which is taken at temperature  $T$  K.

The next proposed model is the Debye model, which is given as:

$$\sigma^2 = \frac{\hbar}{2M_r} \int \rho_j(\omega) \coth\left(\frac{\hbar\omega}{2k_B T}\right) \frac{d\omega}{\omega} \quad (3.18)$$

where

$$\rho_j(\omega) = \frac{3\omega^2}{\omega_D^2} \left[ 1 - \frac{\sin(\omega R_j/v)}{\omega R_j - v} \right] \quad \omega_D = \frac{k_B \theta_D}{\hbar}$$

Here,  $\theta_D$  is the Debye temperature,  $v = \omega_D/k_d$  and  $k_D = (6\pi^2 N/V)^{1/3}$ , with  $N$  the number of allowed wavevectors (or ions) in the total crystal volume  $V$ . The Debye model is a more accurate approximation for systems with a primitive lattice and also for scattering processes from the second and higher shells in systems with non-primitive lattices. In the scattering processes of the first shell in systems with a non-primitive lattice and maybe also other complicated systems like molecules and amorphous systems, the Einstein model results in more accurate results. However, due to simplicity and sufficient accuracy the Einstein model is used more often. For a more detailed discussion, interested readers are referred to [80], Ch. 1 of [81] and [82].

As already mentioned, the core hole lifetime is of the order of a few fs, while thermal vibrations are of ps. Therefore, during every excitation process, the photoelectron encounters a new configuration

### 3 Experimental Techniques

of the structure around the emitter and the EXAFS signal is an average over all possible atomic arrangements. One of the solutions for dealing with a system, which consists of a distribution of disordered atoms, is using the *cummulant expansion*. In this solution,  $\chi(k)$  is expressed by a simplified form of the EXAFS equation, where  $k$  is a complex number, which also accounts for the mean free path  $\lambda(k)$ . Averaging over all of possible configurations leads to:

$$\chi(k) = \left\langle \sum_j \frac{f_j(k) e^{i2kR_j + i\delta_j(k)}}{kR_j^2} \right\rangle \quad (3.19)$$

One may also average over the most sensitive term of equation 3.19,  $e^{i2kR_j}$ , which leads to:

$$\chi(k) = \sum_j \frac{f_j(k) e^{i\delta_j(k)}}{kR_j^2} \langle e^{i2kR_j} \rangle \quad (3.20)$$

The average of the exponential term can be described by the *cummulants* of the distribution function, which is the probability of finding an atom at a distance  $R$  from another atom of the selected type:

$$\langle e^{i2kR_j} \rangle = \exp \left[ \sum_{n=1}^{\infty} \frac{(2ik)^n}{n!} C_n \right] \quad (3.21)$$

where the coefficients  $C_n$  are the cummulants of the distribution (Ch. 6 of [81]). The first cummulant is the average distance between the emitter and the scatterer and the second is the mean square relative positional fluctuation  $\sigma^2$ .  $C_{3,4}$  measure the skewness and kurtosis of the distribution, representing the asymmetry in the distribution of the distance between emitter and scatterer. It is obvious that for a Gaussian distribution  $C_3$  and  $C_4$  are zero.

In addition to single scattering, the EXAFS signal also consists of multiple scatterings, which are important, specially beyond the first coordination shell. The detailed theoretical calculation can be found in [83]. Multiple scattering can simply be represented by a single scattering process with effective scattering amplitude and phase-shift. Half the path length is taken as effective nearest neighbor distance. The number of paths increases exponentially by including multiple scattering processes. Considering the decrease of the wave amplitude with increasing path length, a limit in the path length can be set to terminate the number of paths. The limit is the sensitivity range of EXAFS ( $\approx 5 \text{ \AA}$ ), which leads the longest path length to be 10 to 11  $\text{\AA}$ .

To include the multiple scatterings paths,  $\sigma^2$  for the path needs to be calculated. The important scatterings are shown in Fig. 3.10, where  $\sigma^2$  for single scattering at atoms 1 and 2 is  $\sigma_1^2$  and  $\sigma_2^2$ , respectively. As shown in [84], for collinear multiple scatterings,  $\sigma^2$  can be given as a linear combination of  $\sigma_1^2$  and  $\sigma_2^2$ . In case of collinear double and triple scatterings,  $\sigma^2 = \sigma_2^2$ , for collinear double and triple scatterings through the emitter,  $\sigma^2 = 2 \times \sigma_1^2$  and for a rattle scattering between the emitter and scatterer 1,  $\sigma^2 = 4 \times \sigma_1^2$ . Finally, as given by Ravel in the documentation of the analysis package Artemis, for triangular paths,  $\sigma^2$  can be approximated as  $\sigma^2 \approx \sigma_1^2 + 0.5 \times \sigma_2^2$  [85,

86].

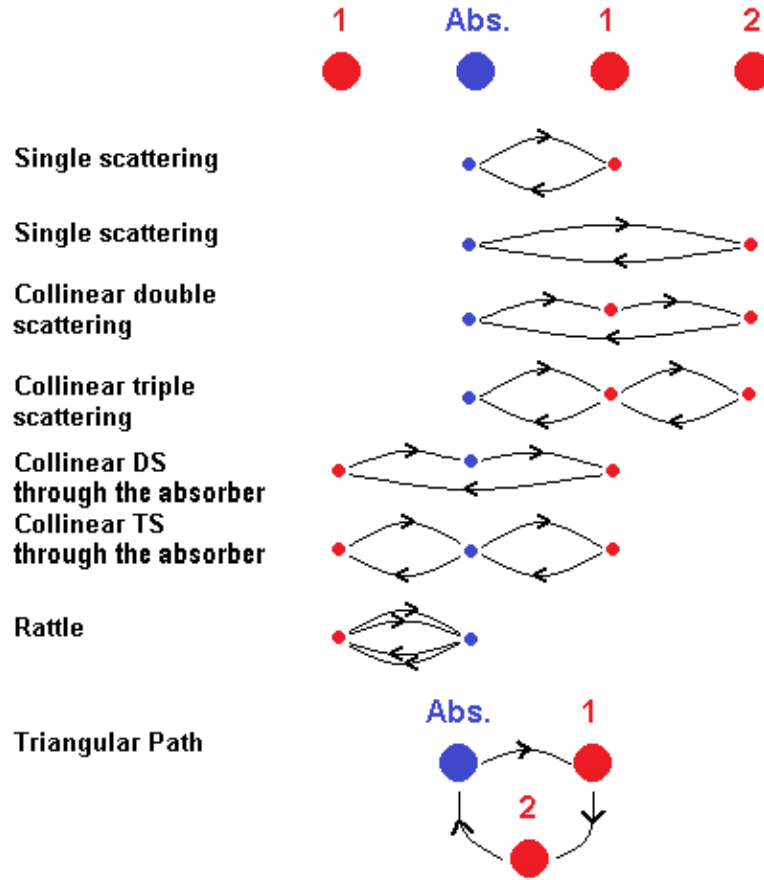


Figure 3.10: The schematic of the single scattering and important collinear and triangular multiple scatterings taken from [85] according to [84]

To extract distances and coordinations of neighboring atoms, exact values of the scattering amplitude  $f(k)$  and the phase-shift  $\delta(k)$  for every individual path must be calculated. Previously, these parameters were determined experimentally only for single scattering processes from the first coordination shell of the system with a known structure [74]. However, calculated scattering factors are accurate enough for the data analysis and also can be extended to further shells, as well as multiple scattering. In this work, scattering factors were calculated using FEFF version 6 (1995 [87]) and FEFF8-lite (1998 [88]), initially developed by Rehr et al. in 1991 [89]. Parameter adjustment was done using IFEFFIT, within the software package *DEMETER* [86]. In IFEFFIT the misfit between the model and the experiment is calculated by an R-factor [74, 90, 91, 92]

$$R = \frac{\sum_i^{N_{data}} [y_i^{data} - y_i^{model}(x)]^2}{\sum_i^{N_{data}} [y_i^{data}]^2} \quad (3.22)$$

where  $N_{data}$  is the number of fitted points,  $y_i^{data}$  the experimental data,  $y_i^{model(x)}$  the model, which depends on the variable fitting parameter  $x$  according to fitting in  $k$  or  $R$ -space. Obviously, in every fitting process, the number of fitting parameters must be smaller than the number of independent

### 3 Experimental Techniques

data points ( $N_{ind}$ ), which in IFEFFIT is given by:

$$N_{ind} \approx \frac{2\Delta k \Delta R}{\pi} + 1 \quad (3.23)$$

where  $\Delta R$  and  $\Delta k$  are employed ranges in  $k$  and  $R$  [74].

There is an important effect, which affects measurements in FY, namely *self-absorption* (or *over-absorption*). It occurs in thick ( $\approx 1$  micron) and concentrated sample, if the relative percentage in composition of an element is more than 10% and the measurement is done in any off-normal angle of incidence. In such a case, the absorption of the incoming photons is nearly complete and therefore, the absorption is not proportional to the absorption coefficient any more. This leads to a damped or even structureless EXAFS signal. This effect is more pronounced in grazing incidence, since the penetration depth of the X-rays is smaller, which means the absorption of all photons is higher ([74], Ch. 3 of [79], [93, 94]).

#### 3.5.2 The EXAFS data analysis

As the first step of the EXAFS data analysis, the measured signal is converted to  $\mu(E)$ , which is the total linear absorption coefficient and the modulation function  $\chi(k)$  is extracted from it. To convert the measured signal to  $\mu(E)$ , the spectrum is normalized to the incoming X-ray flux, which depends on the absorption detection method (Ch. 6 of [77]). In EY and FY measurements,  $\mu(E)$  is calculated by

$$\mu(E)x = \frac{F}{I_0} \quad (3.24)$$

where  $x$  is the sample thickness and  $I_0$ ,  $I$  and  $F$  are the incident and the fluorescence (or the electron yield) intensities [77].

After converting the signal to  $\mu(E)$ , the edge position  $E_0^{exp}$  must be determined. The edge energy is commonly assigned to the point of inflection of  $\mu(E)$  and later taken as starting value when fitting the modulation function. In the next step, the pre-edge background in  $\mu(E)$  is subtracted. It originates from instrumental background or absorption at earlier edges. In EY mode, the slope is negative, because the state density of the vacuum decreases with increasing the energy. On the contrary, in FY mode, the slope is positive, because higher energy X-rays penetrate deeper into the sample and excite more photoelectrons [77].

Instrumental drifts from the detector as well as the absorption tail from earlier edges are treated by fitting a line in the pre-edge region of  $\mu(E)$ . Elastic and Compton-scattered X-rays may also enter the energy window of the fluorescence detector. To correct for this, the so called *Victoreen* pre-edge function ( $E^n \mu(E)$  for  $n = 1, 2, 3$ ) is subtracted (Ch. 2 of [95]).

The next step after pre-edge subtraction is to normalize  $\mu(E)$  such that it starts at 0 in the pre-edge region and increases to 1 above the edge. This is done by normalizing the spectrum to the edge-jump height  $\Delta\mu$ . The edge-jump height is determined by fitting a low order polynomial in the spectrum region, which is far from the edge, where no features are present. The polynomial is then

extrapolated to the edge to calculate the height of the edge-jump. Since the height is employed to scale  $\mu(E)$ , which is proportional to the coordination number of scattering atoms, errors in its determination lead to errors in the coordination numbers.

As the proceeding step to extract modulations, a background is subtracted. This background ( $\mu_0(E)$ ) is the absorption coefficient of an isolated emitter without any neighboring atoms. The absorption is determined empirically by fitting a slowly varying spline through the spectrum,  $\mu(E)$ . By subtracting this spline, low frequency oscillations are removed from the modulation function, while higher frequency oscillations are kept. Low frequency oscillations lead to features at low  $R$  values in the radial distribution function, which do not correspond to scattering of any neighbors. Details about the frequency of the spline will be discussed later.

The background subtraction results in the modulation function  $\chi$ , according to:

$$\chi(E) = \frac{\mu(E) - \mu_0(E)}{\Delta\mu} \quad (3.25)$$

As mentioned before, it is more appropriate to describe modulations as a function of the electron wavenumber  $k$ . In the EXAFS community it is more common to report  $k$  ( $R$ ) in  $\text{\AA}^{-1}$  ( $\text{\AA}$ ), which leads to:

$$k = \sqrt{\frac{2m(E - E_0^{exp})}{\hbar^2}} \quad (3.26)$$

in which  $m$  is the non-relativistic mass of the electron,  $E$  the photon energy and  $E_0^{exp}$  the energy of the absorption edge and with  $E$  in eV and  $k$  in  $\text{\AA}^{-1}$ , the equation leads to [77]:

$$k = \sqrt{0.2625 \left[ \frac{\text{\AA}^{-2}}{\text{eV}} \right] (E - E_0^{exp})} \quad (3.27)$$

Finally, the substitution of  $E$  with  $k$  leads to Eq. 3.14 in Sec. 3.5.1. The measured and the normalized XAS spectra at the Ti  $K$ -edge from a 0.5% Nb doped SrTiO<sub>3</sub>(001) crystal in normal incidence are presented in Fig. 3.11. The subtracted background is also shown.

$\chi(k)$  is determined by the final state of the absorption transition and results from the interference of outgoing waves with waves, (back-)scattered at neighboring atoms. Fourier transformation is a mathematical tool to separate modulations, which correspond to distances of atoms. The result of the Fourier transformation,  $\chi(R)$ , corresponds to a radial distribution function with peaks, indicating the distances of neighbors from the emitter.

The subtracted spline as the background from  $\mu(E)$  varies slowly. The spline is adjust such that the Fourier coefficients at low  $R$  values, which have no physical meaning, become small. To determine how low the frequency of the spline should be,  $R_{bkg}$  factor is used.  $R_{bkg}$  is the threshold radius, below which no peak in  $\chi(R)$  should be present after the transformation. Since bond lengths below 1.5  $\text{\AA}$  do rarely exist [74] and also there is up to 0.7  $\text{\AA}$  change in peak positions due to phase-shifts, setting  $R_{bkg}$  to 0.8 – 1  $\text{\AA}$  is reasonable [96].  $\chi(R)$  is a complex function and usually the magnitude of  $\chi(R)$  is displayed.  $\chi(R)$  contains valuable information about distances of neighbors and phase-shifts in the scattering processes, as well as the probability of finding a specific atom at

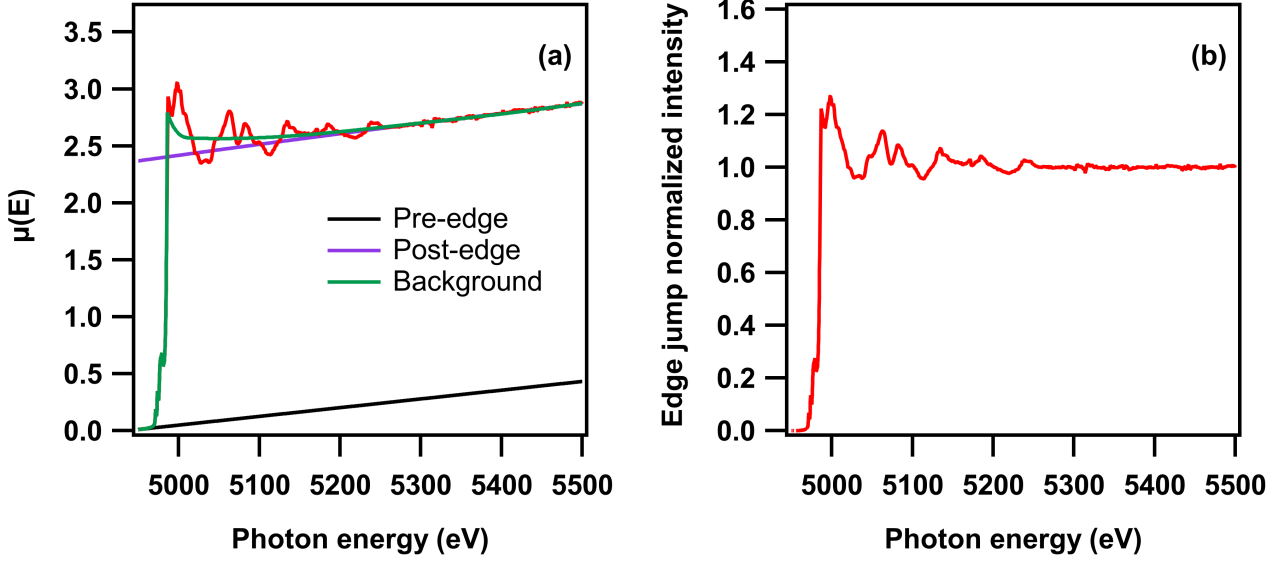


Figure 3.11: (a) Subtracted background of the experimental Ti  $K$ -edge spectrum from a STO single crystal, in normal incidence, together with fitted lines in the pre-edge and the post-edge regions. The resulted normalized spectrum is shown in Fig. (b).

a distance  $R$  from the emitter,  $g(R)$ .

Due to discrete nature of the data, fast Fourier transformation (FFT) with conjugate  $k$  and  $2R$  (equations 3.28 and 3.29) can be used. The point number of  $\chi(k)$  for FFT ( $N_{fft}$ ) is a power of 2 (typically  $N_{fft} = 2048$ ) with a  $\delta k$  spacing of  $0.05 \text{ \AA}^{-1}$ , which needs the range of the experimental  $\chi(k)$  to be  $102.4 \text{ \AA}^{-1}$ . Obviously, no experimental data has such a long range, however, the experimental data will be zero-padded until the end of this range to increase the density of points in  $\chi(R)$ , which results in  $\delta R = \pi / (N_{fft} \delta k) \approx 0.0307 \text{ \AA}$ .

$$\tilde{\chi}(R_m) = \frac{i\delta k}{\sqrt{\pi N_{fft}}} \sum_{n=1}^{N_{fft}} \chi(k_n) \Omega(k_n) k_n^w e^{(2i\pi n m / N_{fft})} \quad (3.28)$$

$$\tilde{\chi}(k_n) = \frac{2i\delta R}{\sqrt{\pi N_{fft}}} \sum_{m=1}^{N_{fft}} \chi(R_m) \Omega(R_m) e^{(-2i\pi n m / N_{fft})} \quad (3.29)$$

Here  $R_m = m\delta R$ ,  $k_n = n\delta k$  and  $k_n^w$  is the  $k$  weighting parameter. The truncations at the end of the data range may create small waves in the Fourier transformed functions. To overcome this problem, window functions  $\Omega(k_n)$  and  $\Omega(R_m)$  are used in equations 3.28 and 3.29. The window function is 0 at low values of  $k$  or  $R$  and increases gradually to 1 and then reduces to 0 at high values (Ch. 13 of [97]).

# 4 Projection Analysis of EXAFS Modulations of STO

A projection method for the analysis of EXAFS modulations has been developed. In this method the experimental modulations are projected onto calculated ones from singular neighboring atoms. Compared to the usual analysis with a Fourier transform, systematic errors in initial values for nearest neighbor distances are significantly reduced from 40 to 80 pm to below 10 pm. Tests of the method are presented with experimental and calculated EXAFS modulations for SrTiO<sub>3</sub>.

## 4.1 The projection method

In the EXAFS analysis reasonable initial guesses for the distances of neighboring atoms must be made. Fourier transformation gives the atomic distances with offsets up to 0.7 Å, but no hint about the element of the neighbor. In this section a projection method is introduced, which can make quite reasonable and also element specific initial guesses for the fitting process.

Hofmann et al. developed an element specific method to determine the structure of the adsorbate by scanned-energy-mode photoelectron diffraction [98]. Including the phase-shift decreases the uncertainty to 0.2 Å. It is applicable to the first shell, as well as further coordination shells. This method is similar to Fourier transformation of the modulation function  $\chi_{expt.}(k)$  (equation 4.1) and replaces  $\exp(ikr)$  by  $\chi_{calc.}$ , the modulation function due to a single scattering process from an scattering atom at a distance  $r_i$ .

$$u(r) = \int_k \chi(k) e^{ikr} dk \quad (4.1)$$

$$c(r_i) = \int_0^\infty \chi_{expt.}(k) \cdot \chi_{calc.}(k, r_i) dk \quad (4.2)$$

Mathematically,  $c(r_i)$  is the projection of the experimental modulation function on to  $\chi_{calc.}$ . The nice thing is that by taking into account of the phase-shifts, the maximum of  $c(r_i)$  is much closer to the actual distance of the scattering atom. In the projection method, a set of calculated modulation functions is created for a single neighboring scattering atom at a range of distances. All phase shifts along the scattering paths of outgoing electrons are properly taken into account by means of multiple scattering calculations with spherical wave fronts (FEFF8-lite [88]). The resulting set of modulation functions serves as basis for the projection of the experimental modulation function. For small distances the triple scattering path (the so-called rattle mode) made a significant contribution to

the calculated modulation function and has been included. Other multiple scattering paths, which include other neighboring atoms have been neglected. The accuracy of this method is typically 0.1 Å and decreases to 0.2 Å only in unfortunate cases [99].

A typical experiment is based on measurement at discrete values in  $k_j$ . With equidistant steps, i.e. a constant width  $\Delta k$  in experiment and calculation, the integral in equation (4.2) can be approximated by a sum:

$$c(r_i) = \sum_j \chi_{expt.}(k_j) \cdot \chi_{calc.}(k_j, r_i) \cdot \Delta k \quad (4.3)$$

In the original version for photoelectron diffraction the coefficients have been multiplied with  $r_i$  to prevent unreasonable high coefficients for low values of  $r_i$  [98]. This is not required, if the method is applied to actual experimental EXAFS modulation functions, in particular since a suitable lower limit in  $r_i$  can be set.

To get closer to a direct correspondence of the coefficient and the number of scatterers, a normalization is included, derived from the following idea. Let us assume that the experimental modulation consists of modulations resulting from a number of the same atoms all at the same distance. Then, the coefficient  $c(r_i)$  need simply be divided by the projection of the calculated modulation function onto itself, in other words, the normalization factor  $n(r_i)$  results from:

$$n(r_i) = \sum_j \chi_{calc.}(k_j, r_i) \cdot \chi_{calc.}(k_j, r_i) \cdot \Delta k \quad (4.4)$$

and a normalized coefficient  $c_{norm}$  can be defined as:

$$c_{norm}(r_i) = \frac{c(r_i)}{n(r_i)} = \frac{\sum_j \chi_{expt.}(k_j) \cdot \chi_{calc.}(k_j, r_i)}{\sum_j \chi_{calc.}(k_j, r_i) \cdot \chi_{calc.}(k_j, r_i)} \quad (4.5)$$

Note, that the calculation can be simplified by reducing the step width  $\Delta k$ , as long as it is constant and the same in experiment and calculation. Raw and normalized projection coefficients  $c(r_i)$  and  $c_{norm}(r_i)$  are real numbers and represent the agreement between experimental and calculated modulation functions. The position of large positive values indicate the distance to neighboring scatterers. Due to the oscillatory character of modulation functions, there can be an anti-phase relation between the experimental and calculated modulation functions. In such a case, the projection coefficients  $c(r_i)$  and  $c_{norm}(r_i)$  become negative. Since the coefficients are thought to indicate the presence of a scatterer, negative values do not make sense and should be replaced by zero or at least relatively small values. In the original version for photoelectron diffraction negative values are suppressed by exponentiation of the projection coefficients  $c(r_i)$  [98]:

$$C(r_i) = e^{c(r_i)} \quad (4.6)$$

This emphasizes the maximum of positive values. However, together with the previously mentioned multiplication with  $r_i$ , the scaling of the coefficients  $C(r_i)$  becomes arbitrary and there is no



direct correspondence to the number of scattering atoms. A simple transformation, which keeps the correspondence, would set negative values to zero and keep positive values unchanged. A smoother variant of this transformation, i.e. a transformation with a continuously differentiable as well as bijective transfer function, is the positive branch ( $y > 0$ ) of a hyperbola with the straight line  $y = x$  as asymptote for positive  $x$  and the x-axis as asymptote for negative  $x$ . The corresponding equation for this type of hyperbola is:

$$y^2 - xy = a^2 \quad (4.7)$$

with  $a$  as shape parameter controlling the y-intercept of the hyperbola.

For the transformation of  $c_{norm}(r_i)$  we need a rearranged form of equation 4.7. The branch for  $y > 0$  is simply obtained from the positive part of the general solution of the quadratic equation:

$$y = \frac{x}{2} + \sqrt{\frac{x^2}{4} + a^2} \quad (4.8)$$

Tests with our data revealed that a value of 0.05 for the y-intercept  $a$  yields reasonable curves. For curves from other systems, other values might be more appropriate. With a value of 0.05 for the y-intercept  $a$  the transformed coefficient  $c_{trans}(r_i)$  becomes:

$$c_{trans}(r_i) = \frac{c_{norm}(r_i)}{2} + \sqrt{\frac{c_{norm}^2(r_i)}{4} + 0.05^2} \quad (4.9)$$

Nearest neighbor distances can directly be derived from the maxima of the coefficient  $c_{trans}(r_i)$ . Applying this method to actual experimental data will show the limits of this approach, as has been discussed for photoelectron diffraction [100]. An interesting question is whether the correspondence of the coefficient and the number of scattering atoms is actually improved compared to the original method for photoelectron diffraction. One can expect good correspondence for strong next neighbor scatterers, because this results in simple dominating modulations. Overestimating the numbers of scatterers can be expected for weak scatterers at far distances, since noise might be enough to give high coefficients.

## 4.2 Experimental procedures

Commercial single crystal SrTiO<sub>3</sub> (CrysTec GmbH) with a polished (100) surface with 0.5 wt% Nb-doped has been cleaned by rinsing with deionized water in air. Elemental composition and cleanliness were checked with photoelectron spectroscopy (XPS) at a photon energy of 2003 and 2503 eV. Overview spectra showed all photoemission and Auger emission lines of the respective elements. Surface contaminants with carbon could be detected, but were low enough to be safely neglected in the rather bulk-sensitive x-ray absorption spectra taken at the Ti  $K_\alpha$  x-ray emission line in normal incidence. No further assessment of the photoelectron spectra was required.

### 4.3 XAS measurements

XAS measurements have been performed at the Ti  $K$ -edge in normal incidence at RT. The monochromatization of the X-ray beam was done using Si(311) crystal pairs. The FY spectrum at the Ti  $K$ -edge has been recorded by selecting a region of 200 eV around the Ti- $K_{\alpha_{1,2}}$  emission lines. The integration time was 10 s. The Ti- $K_{\alpha_{1,2}}$  emission lines correspond to the fluorescence processes originated from the electron transition from  $2p_{3/2,1/2}$  levels to fill the core hole in  $1s$  level. The involved excitation processes are within the core levels and are far away from the valence band.

The recorded spectra have been normalized to the absorption spectrum of a metal mesh (with 80% transparency) [69]. In addition, the data points due to the glitches of the monochromator crystals have been deleted. The spectra have been then normalized to the step edges, as described in Sec. 3.5.2. Full energy range TEY and FY spectra are given in Fig. 4.1 (a) and zoomed in XANES regions are presented in Fig. 4.1 (b). Both are in agreement with literature data and the resolution of features is at least as good [101, 102, 103, 104, 105, 106, 107]. In the Auger decay and fluorescence decay of the core hole different transitions of electrons are involved and therefore, the corresponding X-ray absorption features may not be in principle similar (Sec. 3.2.3). However, for the Ti  $K$ -edge spectrum in STO, the measurements in TEY and FY modes lead to almost identical XANES and EXAFS features, while only some small intensity differences have been detected. The pre-edge feature A originates from 6-fold coordination of the Ti by O atoms in the bulk STO [101].

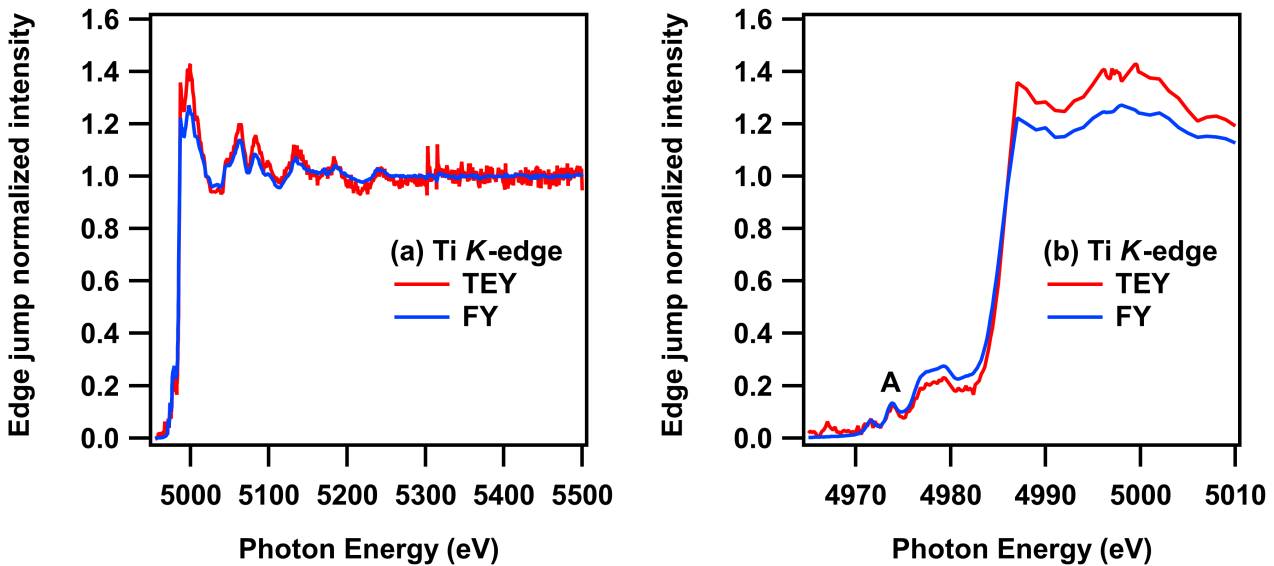


Figure 4.1: (a) X-ray absorption spectra of the Ti  $K$ -edge of STO(001) crystal in normal incidence in TEY and FY detection mode and (b) the corresponding XANES regions. The pre-edge transition A is in agreement with reported data [101, 108, 109, 110].

## 4.4 Data analysis

To analyze X-ray absorption spectrum of the Ti  $K$ -edge of STO, FY spectrum was selected, since it has the better signal to noise ratio. The  $k^2$ -weighted modulation function,  $\chi(k) \times k^2$  and the corresponding radial distribution function,  $\chi(R)$  were obtained employing the DEMETER package [86] and are shown in Fig. 4.2. The energy position of the absorption edge has been determined as point of inflection at 4985.3 eV. Since the absolute value of the edge is not relevant for the subsequent data analysis, no further care has been employed regarding the calibration of the monochromator.

Employing DEMETER package [86], scattering paths in the bulk STO were calculated. Peaks of three of the neighboring atoms around of Ti are shown in Fig. 4.2 and their apparent distances in  $\chi(R)$  are in agreement with reported data [102, 111]. The energy dependence of phase-shifts cause shifts on peak positions in the Fourier transformation of different scattering atoms. The shift of the peak of the first O shell (with the bond length of 195 pm [16]) in the Fourier transformation is 45 pm, while shifts of closest Sr and Ti atoms (with the distances of 338, 390.5 pm [16]) are 28, 50 pm, respectively. Contrary to our results published analyses could clearly resolve two contributions in the range of 248 to 385 pm [111, 112, 113, 114]. Most likely the longer energy range of their measurements leads to the better resolution. All publications agree on the assignment of the two peaks to Ti-Sr and Ti-Ti scattering paths. However, it needs to be mentioned that the shortest double scattering paths with O and Ti also give contributions in this range. The apparent path lengths of the paths Ti-O-O-Ti and Ti-O-Ti-Ti are 333.5 pm and 405 pm.

As is obvious from the figure, the intensities of the scattering paths longer than 650 pm are very small, in agreement with the general statement in the introduction about EXAFS.

### 4.4.1 Projection method: Oxygen

Figure 4.3 shows the projection coefficients of the Ti  $K$ -edge EXAFS modulations according to equation (4.9) as function of Ti-O distance. It shows a pronounced maximum at 195.5 pm, in excellent agreement with the actual Ti-O distance. The method is clearly superior to the Fourier transform in Fig. 4.2. The difference of the initial guess of the Ti-O distance from its actual value ( $<1$  pm) is much better than the original expectation of  $<10$  pm.

The full width at half maximum (FWHM) of the peak is 20 pm. This is 3.5 times smaller than the width of the peak in the Fourier transform and is mainly due to the fact that only the magnitude of the Fourier transform can be discussed, whereas the phase has to be neglected. At least its discussion is so hard, that it is not done regularly. The relevance of the phase actually depends on the range in  $k$  of the modulation function. The shorter the range, the more important becomes the phase of the frequency. This means that the advantage of projection method is even more pronounced in cases, where the range is limited for example because of other absorption edges. So far, we have no indications that the modulation function of SrTiO<sub>3</sub> is a particularly fortunate case for the projection method, but this question should be addressed with further cases. The discussion shows that the main goal has been achieved and a valid initial value for the next neighboring atom

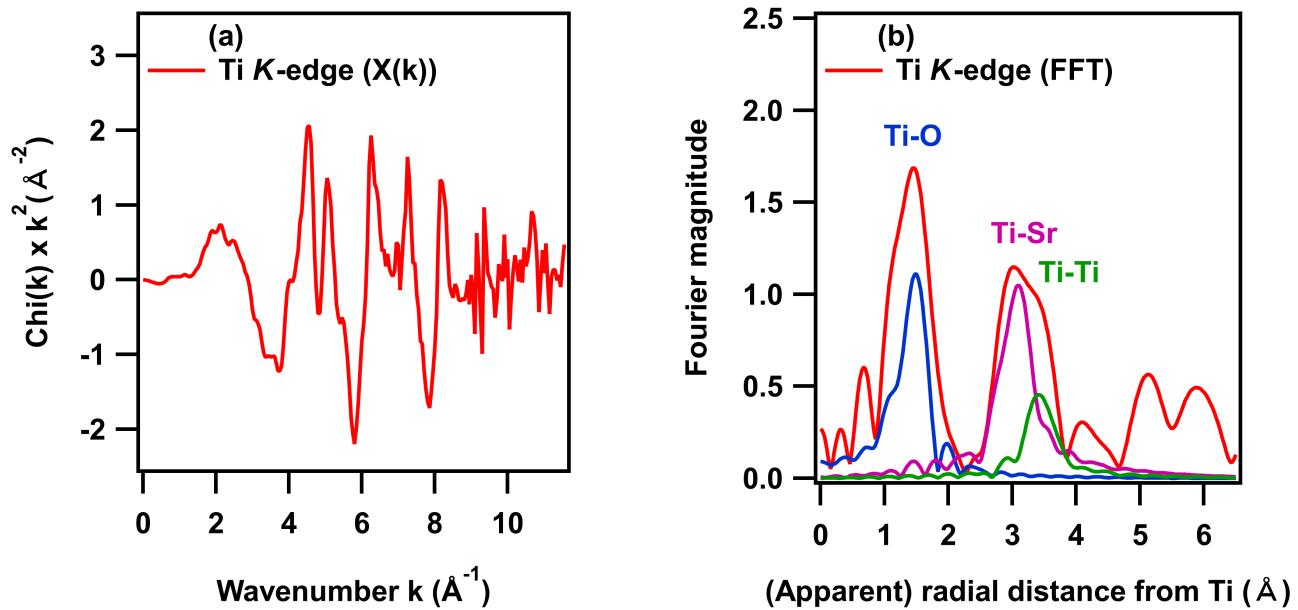


Figure 4.2: (a) Modulation function and (b) Fourier transformations of single scattering processes from first shells of neighboring atoms of Ti in STO bulk [16], as is calculated by FEFF6 using DEMETER software package [86].

has been obtained from which a full-scale calculation will converge to the best value without any difficulties.

Besides discussing the position of the maximum, the question is, how well its value relates to the number of neighboring atoms, the effective coordination number. In  $\text{SrTiO}_3$ , the Ti is coordinated by an octahedron of six O atoms. The linear polarization of the x-rays gives an effective coordination number of 2. As the projection coefficient at 195 pm has a value of 0.7, there is a deviation by a factor of 3. Obviously, the correspondence is good enough to postulate the presence of neighboring O atoms at this distance, but the actual coordination number cannot be derived from the projection coefficient, which is actually similar to the interpretation of the magnitude in the Fourier transform.

Further maxima of the projection coefficient show up at longer distances for 311 pm, 356 pm, 404 pm, and 477 pm. They closely resemble peaks and shoulders of the Fourier transform in Fig. 4.2, although with improved resolution. Having in mind the actual structure of  $\text{SrTiO}_3$ , it is clear that they do not result from scattering at O, but from other atoms (Sr and Ti). The values of the projection coefficients at the peaks at 356 pm and 404 pm are about a factor 2 higher than that at 195 pm. Assuming the same correspondence factor, this would indicate an effective coordination number of 4. The reason for such high values is, that Sr and Ti are stronger scatterers than O. In order to mimic the large modulations from Sr and Ti, a high projection coefficient scales up the small modulations from O. This means that the high coefficients can actually be taken as a hint that there is no O at that distance but stronger scatterers. However, one set of projection coefficients is too few, to decide whether this argument is generally valid or has a high risk of over-interpretation.

Surprisingly, no peak is present for the 2<sup>nd</sup>-nearest oxygen at a distance of 436.5 pm. Presumably,

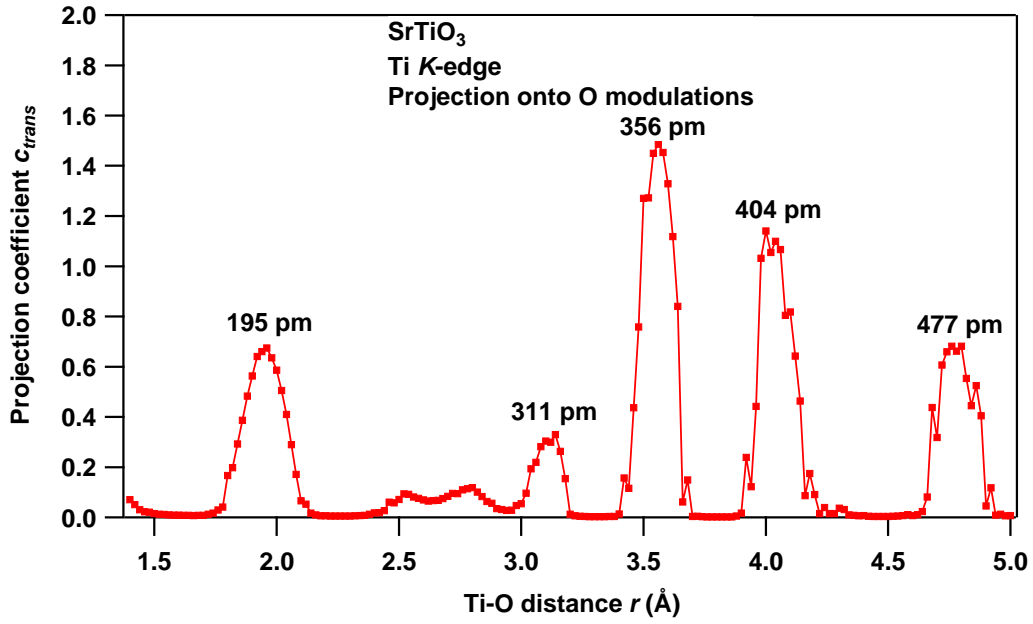


Figure 4.3: SrTiO<sub>3</sub>: Projection coefficient  $c_{trans}$  of the Ti *K*-edge EXAFS modulations as function of Ti-O distance  $r$ .

scattering at O is too weak and the decay for long paths too strong to give any contribution. The Fourier transform also points to this, since it has a low magnitude in the range from 375 to 400 pm with a pronounced minimum at 387 nm, exactly where the shifted peak is to be expected.

Finally, the peak at 477 pm does not correspond to any direct single scattering path, but the effective path length of 471 pm of the shortest triple scattering paths fits well.

In summary, applying the projection method for an oxygen scatterer to the same data set and using the same prior information as in the analysis of the Fourier transform, the distance of the next neighboring O atoms can be deduced with much improved accuracy and precision. Different coordination numbers cannot be distinguished so far and peaks from other atoms further away may be misinterpreted as O atoms, but can be ruled out taking into account prior knowledge of the structure as in the interpretation of the Fourier transform. Compared to the original version of the projection method for photoelectron diffraction, the arbitrary scaling of the coefficients has been replaced and a correspondence to the effective coordination number within a factor of 3 has been achieved.

#### 4.4.2 Projection method: Strontium

Figure 4.4 shows the projection coefficients of the Ti *K*-edge EXAFS modulations according to Eq. 4.9 as a function of Ti-Sr distance  $r$ . It shows numerous maxima, which can be grouped into a set of three at low distances (184 pm, 228 pm, and 271 pm) and a set of four at high distances (303 pm, 342 pm, 386 pm, and 423 pm). Taking into account the structure of SrTiO<sub>3</sub> it is obvious that the first set does not correspond to scattering at Sr atoms, but mimics the scattering at the O atom at 195 pm, which is the most prominent component of the modulation function. The peaks of

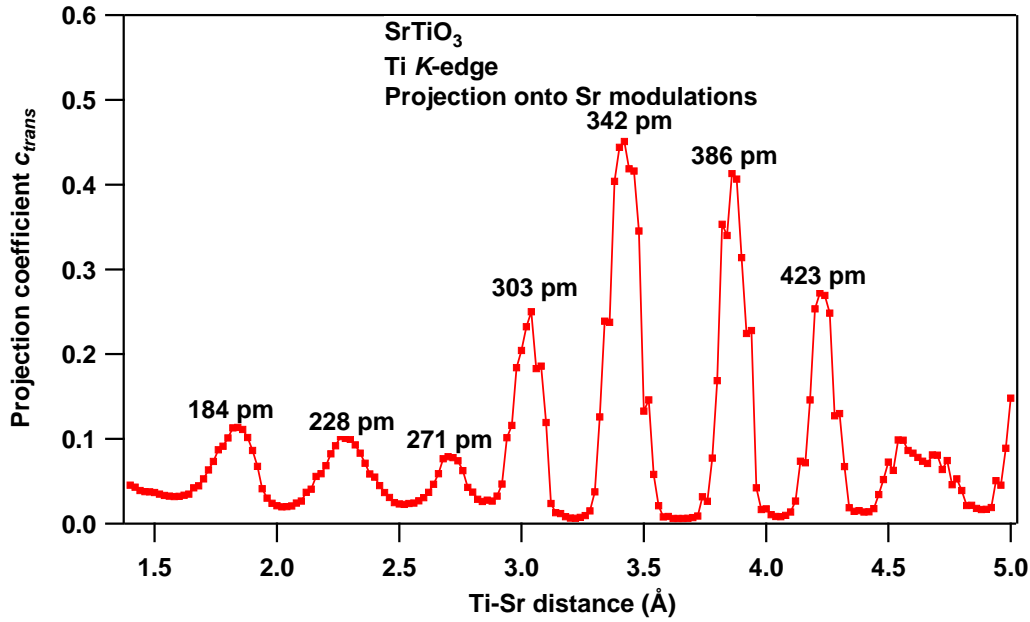


Figure 4.4: SrTiO<sub>3</sub>: Projection coefficient  $c_{trans}(r)$  of the Ti *K*-edge EXAFS modulations as function of Ti-Sr distance  $r$ .

this set may also result from accidental coincidence of the calculated curves with the experimental one. Until now, no theoretical considerations are at hand about how to estimate the significance of a peak in the curve of projection coefficients. Therefore, we aim to obtain an estimate on the basis of numerous test cases.

The strongest peak in the second set of peaks is at 342 pm and corresponds well to the actual Ti-Sr distance of 338 pm, resulting in a difference of  $<5$  pm, again an excellent agreement. The projection coefficient is 0.45, whereas the effective coordination number for Sr is 2.67, a factor of 5.9 larger. The FWHM of the peak is 15 pm, smaller than the 20 pm of the oxygen related peak. Presumably, the smaller FWHM results from the longer distance, because the longer distance results in a higher frequency in the modulation function and this in turn leads to a larger number of oscillations in the given range of  $k$ , so that the sensitivity for changes in distance increases.

The origin of the next peak at 386 pm is obvious from the known structure. It originates from the scattering of Ti atoms in neighboring unit cells at 390.5 pm. Since it belongs to a different scatterer, it will not be discussed further.

Although the peaks at 303 pm and 423 pm have smaller values than the two peak that can be attributed to actual neighboring atoms, they are still too large to be simply neglected. Since there are no atoms, they presumably result from an effect called "multiple site coincidence", which has been described for modulation functions in photoelectron diffraction [115]. An experimental modulation function may fit quite well to more than one modulation function and high coefficients are also obtained for distances not actually present in the system, but nearby the actual value. Actually, this can also happen with the Fourier transformation if the energy range of the experimental modulation is too short and the orthogonality of trigonometric functions breaks down. One way to resolve such an ambiguity is to extend the experimental data set. For an unknown system

this ambiguity means that not only the largest peak can be taken as initial value for the distance, but that the distances from the other peaks also need to be tested. Regarding the subsequent full multiple scattering calculations, three outcomes are possible. First, the calculations with the two distinct initial distance converge to the same model. Second, the two runs yield different models, but one has a much better agreement with the experimental curve and can be presented as final result. Third, the two runs yield two models with comparable agreement with the experiment and no preferred model can be specified. The important point of this is the chance, that the projection model explicitly indicates the possibility of more than one solution and corresponding initial values, whereas the Fourier transform only shows a broadening of the peak.

As with the projection with oxygen, we assign the peaks above 450 pm to the shortest triple scattering paths.

In summary, the reference example  $\text{SrTiO}_3$  shows that the projection method is quite well suited to yield initial guesses for next neighbor scattering atoms. The deviations from actual values are well below 10 pm. This is quite an improvement over the values from a Fourier transform even if they are corrected for their systematic offset. In addition to the starting values for distances, hints regarding to the elemental character of a scatterer is obtained. However, the preference for the correct element is weak.

#### 4.4.3 Projection method: Titanium

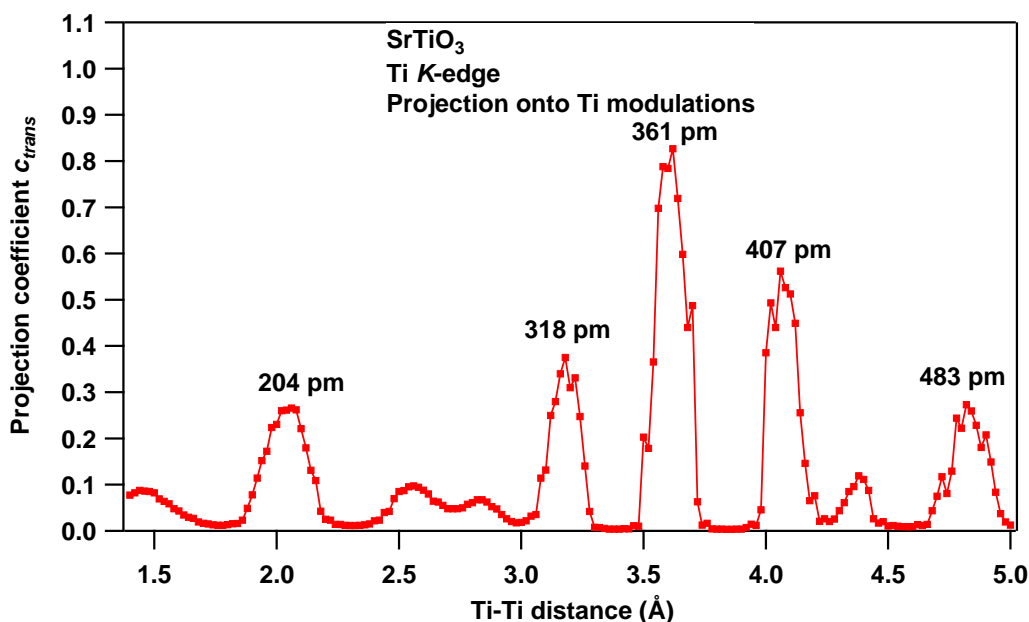


Figure 4.5:  $\text{SrTiO}_3$ : Projection coefficient  $c_{trans}(r)$  of the Ti  $K$ -edge EXAFS modulations as function of Ti-Ti distance  $r$ .

Finally, the projection coefficients with neighboring Ti atoms are displayed in figure 4.5. As with the coefficients with Sr, there is a peak originating from the neighboring O, which shows up at 204 pm here. Next comes a set of three peaks at 318, 361, and 407 pm. The peak at 318 pm results

from the same multiple site coincidence effect as in the projection coefficients for O and Sr. The peak at 361 pm mimics the scattering at Sr. Only the peak at 407 pm corresponds to an actual Ti atom, which is 390.5 pm away. The difference is 16.5 pm, noticeably larger than for the projection coefficients for O and Sr. Since the FWHM of the peak is 14 pm, the difference is a significant deviation. The Ti-O-Ti-Ti double scattering path (405 pm) might contribute to the peak. The last peak in the curve corresponds to the shortest triple scattering paths.

Summarizing the results for SrTiO<sub>3</sub>, the following can be stated. The next nearest O atom can clearly be resolved with very little deviation from its actual position. Sr and Ti can also be assigned. The deviation for Sr is also very small. Whereas the magnitudes of the coefficients clearly favor the assignment of the first peak to O, the additional prior knowledge of the structure is required for the assignments of the Sr and Ti related peaks at higher distances, in particular in the case of the peaks resulting from multiple site coincidences and multiple scattering paths.



# 5 Structural determination of BTO-derived OQC on Pt(111)

In this chapter the structure of BTO-derived OQCs on Pt(111) is investigated by EXAFS. To be sure about the experimental results and the analysis procedure, reference investigation of a BTO single crystal is performed and its structure is investigated by EXAFS.

## 5.1 Barium titanate single crystal

To investigate the structure of BTO-derived OQC by EXAFS, a number of reference measurements and the data analysis on a bulk BTO(001) single crystal have been performed. The experimental conditions were the same as for STO measurements. Fluorescence measurements were done by selecting a region of 200 eV around the Ti- $K_{\alpha_{1,2}}$  emission lines for the Ti  $K$ -edge and the Ba  $L_3$ -edge. Ti- $K_{\alpha_{1,2}}$  emission lines correspond to the electron transition from  $2p_{3/2,1/2}$  levels to fill the core hole in the  $1s$  level. The integration time was 5 s. Ba- $L_{\alpha_{1,2}}$  fluorescence emission lines are due to transitions from Ba  $3d_{5/2,3/2}$  levels to  $2p_{3/2}$  level. The involved excitation processes are within the core levels and are far away from the valence band.

X-ray absorption spectra of the Ti  $K$ -edge and the Ba  $L_3$ -edge in normal incidence ( $2^\circ$  from normal to the surface of the crystal) are presented in Fig. 5.1 (a,c), which are recorded in TEY and FY modes. The spectra are in agreement with the published data for the Ti  $K$ -edge ([106, 107, 108, 116, 117, 118]) and the Ba  $L_3$ -edge ([107, 108]). Corresponding XANES regions are presented in Fig. 5.1 (b,d). The pre-edge transition A represents the six-fold coordination of Ti by oxygen, in agreement with reported data [101, 108, 109, 110]. As with STO (Sec. 4.3), TEY and FY lead to similar features in the X-ray absorption spectra. They are also similar at the Ba  $L_3$ -edge (Fig. 5.1 (b,d)). The intensity difference of the resonance peaks and the pre-edge features reflect the differences in the transition probabilities involved in the fluorescence and Auger decay of the core-hole.

To investigate the directional anisotropy of the system, X-ray absorption spectra at the Ti  $K$ - and the Ba  $L_3$ -edges have also been recorded in grazing incidence ( $72^\circ$ ). The comparison is shown in Fig. 5.2 (a,b). As is obvious from the spectra in the whole region (Fig. 5.2 (a,c)), as well as those in XANES region (Fig. 5.2 (b,d)), the directional anisotropy is very small.

As discussed in Sec. 3.5.1, self-absorption effect attenuates EXAFS modulations in FY in grazing incidence for thick and concentrated samples. To investigate this effect, Ti and Ba spectra in TEY

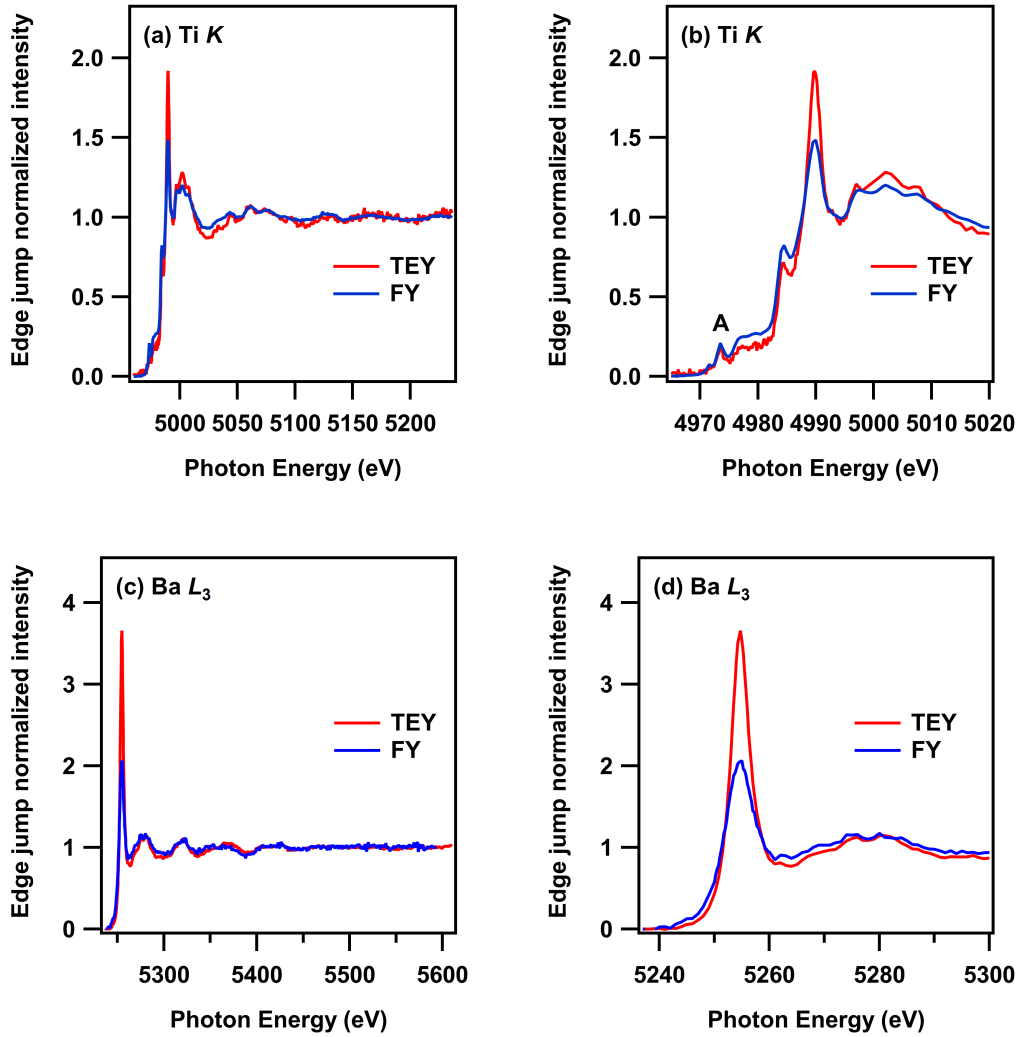


Figure 5.1: X-ray absorption spectra of BTO(001) crystal at the Ti  $K$ -edge (a) and the Ba  $L_3$ -edge (c) in normal incidence in TEY and FY detection mode. (b,d) The zoomed XANES regions.

normal and grazing incidences have been compared (not shown here). The level of the directional anisotropy in TEY is quite similar as that in FY, which indicates that the present differences originate mainly from the structural anisotropy and not from self-absorption effects. This reflects that the fractions of  $c$ -domains and the two perpendicular  $a$ -domains are similar.

Due to similar features in the absorption spectra, only spectra in normal incidence in FY are shown as bulk spectra in the next sections.

### 5.1.1 Structure determination of the BTO single crystal

As reference analysis, the structure of bulk BTO has been determined by using DEMETER software package [86]. The analysis has been performed on the Ti  $K$ -edge spectrum. Since the BTO single crystal consists of different domains (Sec. 2.1), two perpendicular  $a$ -domains and one  $c$ -domain have been considered in the calculations. This has been done by adequately selecting the polarization directions of the incident X-ray beam. The modulations are not sensitive whether the  $a$  and  $c$ -

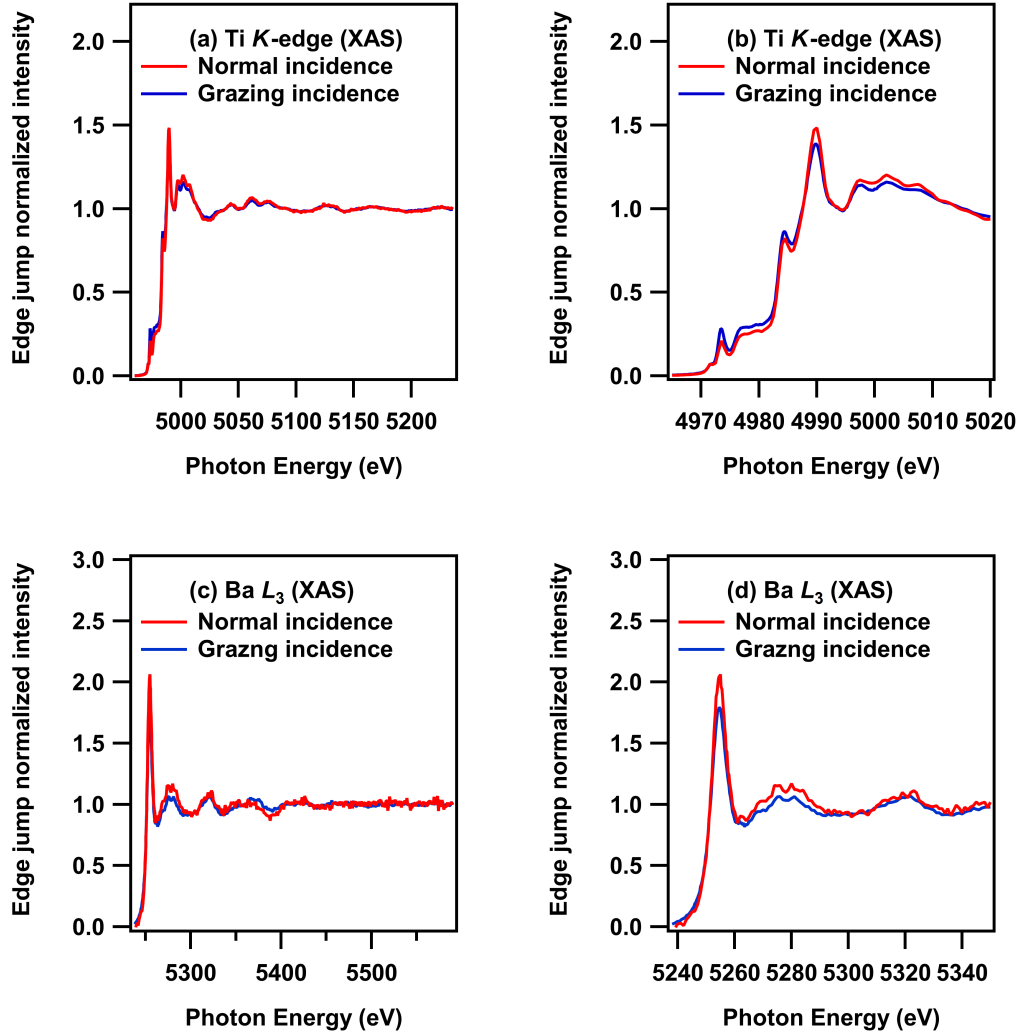


Figure 5.2: Directional anisotropy of FY measurements of a BTO(001) crystal at the Ti *K*-edge (a) and the Ba *L*<sub>3</sub>-edge (c) in 2° and 72° from the surface normal, together with the XANES regions (b,d).

domains are in the positive or negative directions. Therefore, plus or minus direction of the domains was not considered in the calculation. Since the directional anisotropy in the experiment was small, equal percentages were assumed for all domains. All single and multiple scattering paths with paths length below 6.5 Å have been used to perform the calculations.

The energy of the edge has been determined as 4983.5 eV using the first and the second derivatives of the spectrum. In addition, adjusting this value has been allowed through out the fit within limits  $\pm 10$  eV, as proposed in the documentations of DEMETER [85].

The analysis with FEFF calculations have been performed in the *R*-space and the structural results are compared with the reference data [7] in Tab. 5.1. In the table Ti-O Tet S (Ti-O Tet L) means the shorter (the longer) oxygen atom along the tetragonal distortion of the unit cell, Ti-O Equ means the distance of four equatorial oxygen atoms and Ti-Ba S (Ti-Ba L) is the shorter (longer) bond length of Ti and Ba. The labels are illustrated in Fig. 5.3.

Due to the weak dependence of the modulation function, the errors of the resulting  $\sigma^2$  were larger

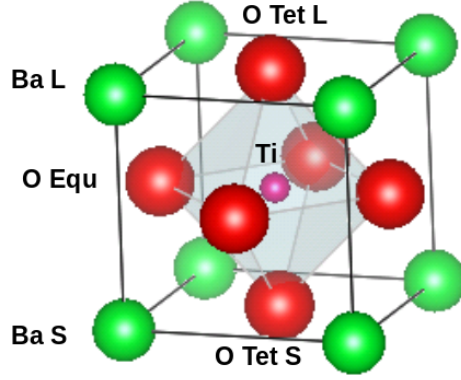


Figure 5.3: Illustration of labels of the atoms in a BTO unit cell, used in Tab. 5.1.

Table 5.1: The results of the structure determination of bulk BTO, using FEFF6 calculations. Values are given in Å.

| $R$ -factor | a               | c               | Ti-O Tet S    | Ti-O Tet L    | Ti-O Equ | Ti-Ba S | Ti-Ba L |
|-------------|-----------------|-----------------|---------------|---------------|----------|---------|---------|
| 0.14        | $3.95 \pm 0.03$ | $4.01 \pm 0.04$ | $1.8 \pm 0.1$ | $2.2 \pm 0.1$ | 1.98     | 3.39    | 3.48    |
| Ref.        | 3.9905          | 4.0412          | 1.75          | 2.29          | 2.009    | 3.415   | 3.528   |

than the  $\sigma^2$  values. Therefore, the  $\sigma^2$  values for O and Ba were set to 0.007, 0.0075 Å<sup>-2</sup> [108, 119] and  $\sigma^2$  of Ti was set to 0.007 Å<sup>-2</sup> for all coordination shells. As discussed in Sec. 3.5.1,  $\sigma^2$  is the 2nd cummulant. Considering the difficulties in determination of  $\sigma^2$ , it is obvious that interpreting the 3rd or 4th cummulants in terms of vibrational distributions is pure speculation. Hence, no analysis to determine them has been performed.

The mismatch factor ( $R$ -factor) of the fit is 0.14 and the energy adjustment in the edge position ( $\Delta E$ ) was calculated to  $-3.7 \pm 0.4$  eV.

$S_0^2$  in Eq. 3.16 is a damping factor, originating from intrinsic losses of the signal due to shake-up and shake-off processes. The reasonable range for  $S_0^2$  is between 0.7 to 1, if one data set is used in the calculations [80]. Here,  $S_0^2$  has been calculated as  $0.2 \pm 0.03$ . Since data sets of three BTO domains have been used, the calculated value of  $S_0^2$  lies close to the reasonable range. The fitting results are given in Fig. 5.4 (a,b). The number of independent points in the fit was calculated according to the specified fitting range in  $R$ -space ( $0.9 \leq R \leq 5.7$  Å) and the Fourier transformation range in  $k$ -space ( $0.3 \leq k \leq 7.8$  Å<sup>-1</sup>) by using a *Hanning* windows (Sec. 3.5.2). A Hanning function has been selected, since it did not lead to any obvious artifacts. The number of independent points for the fit was 22.55 points, while there were 7 fitting variables.

As presented in Tab. 5.1, the deviation of the calculated bond length of Ti O Tet L from the reference is less than 0.1 Å and for all other bond lengths are less than 0.05 Å. Although the available energy range for the modulations of the Ti  $K$ -edge in BTO is short, there is good agreement between experiment and calculations within reasonable error limits.

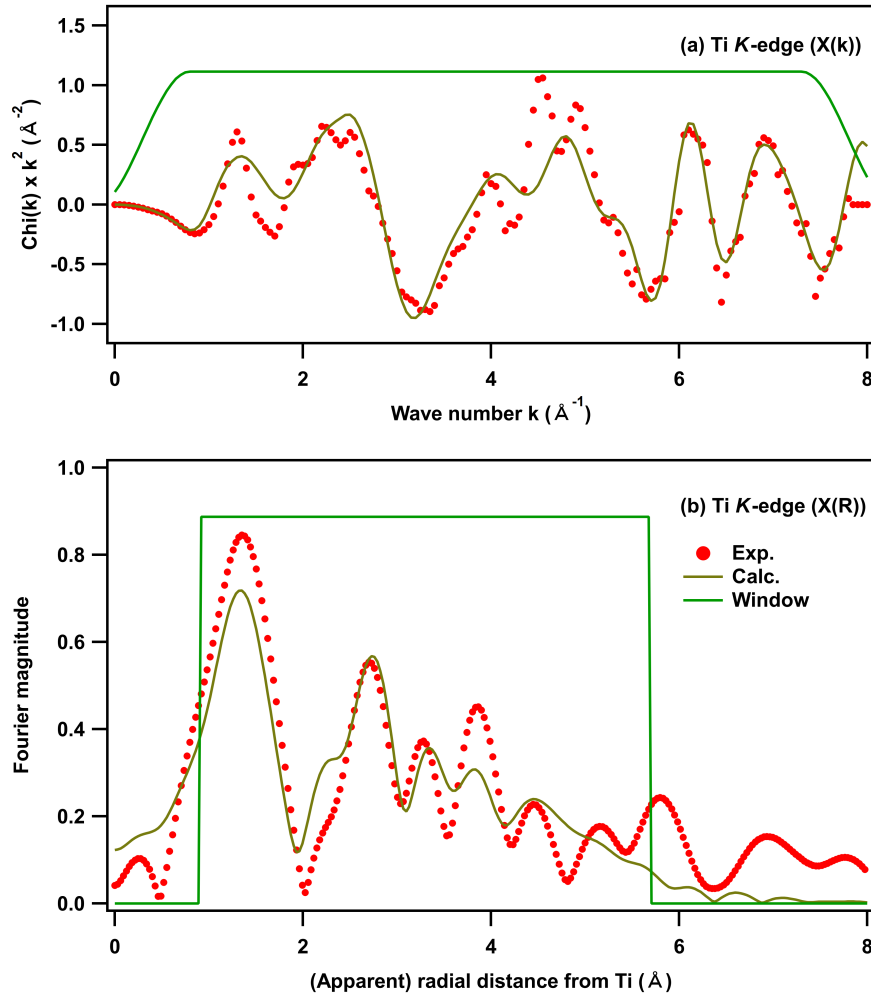


Figure 5.4: The FEFF analysis results of bulk BTO(001) crystal ( $R$ -factor= 0.14) in  $k$ -space (a) and  $R$ -space (b). The window in  $k$ -space corresponds to the selected region for Fourier transformation, while the fitting has been done in  $R$ -space in the specified region.

## 5.2 Structural determination of BTO-derived OQC on Pt(111)

2D barium titanate derived oxide quasicrystal (OQC), discovered by Förster et al. at 2013, opens a new field of physical properties and applications [40]. As the initial step of understanding this system, its structure must be determined. Due to the aperiodic nature of the quasicrystalline system, the structural determination needs local probe techniques. The arrangement of Ti atoms has been determined based on STM and LEED images (Fig. 2.5). LEED is sensitive to Ti, Ba and O atoms. Therefore, the building blocks of the OQC system, squares, triangles and rhombs apply to all atoms. But the arrangement of the atoms in the building blocks remains unclear. Furthermore, STM cannot give any information about the Ti-Pt distance, since Pt is below the OQC layer. Therefore, another local probe technique needs to be employed, which also gives the information about Pt. Consequently, EXAFS has been used to investigate this quasicrystalline system.

### 5.2.1 Sample preparation of OQC on Pt(111)

The sample preparation is described in details in Sec. 4.2 of the master thesis of C. Dresler [120]. A brief outline is given here. A Pt(111) crystal was used as the substrate to grow the OQC layer. The cylindrical Pt(111) crystal (Surtau Preparation Laboratory NL) has a diameter of 9 mm and a height of 1 mm. It was fixed to the sample holder by spot welded Ta wires. Initially, there was BTO on the crystal, which was removed by cycles of argon-ion-sputtering, heating in UHV and O<sub>2</sub>. The sputtering was done by an ion energy of 600 eV and a background pressure of  $5 \times 10^{-6}$  mbar of Ar. The ion current on the sample was 3 to 6  $\mu$ A. After sputtering, the crystal was heated in vacuum of  $5 \times 10^{-9}$  mbar and at a temperature of 1100 to 1200 K. As soon as the crystal cooled down to 900 K, it was heated at this temperature in  $1 \times 10^{-6}$  mbar oxygen. After several cycles less than 10% of a monolayer BTO remained on the surface of the Pt sample, as derived from the Auger electron spectroscopy (AES). The long range order of the sample was checked with LEED. The well known (111)-(1  $\times$  1) pattern with sharp spots has been obtained.

Once the clean Pt(111) substrate was prepared, 1 ML of BTO was deposited via simultaneous evaporations of BaO and Ti. The deposition was done in an oxygen pressure of  $1.2 \times 10^{-6}$  mbar, while the Pt crystal was kept at room temperature. The sample was then heated at 875 K for 10 min in  $1.2 \times 10^{-6}$  mbar oxygen and then cooled down to 383 K at the same O<sub>2</sub> pressure. The thickness of the sample was determined by the AES to be 3 Å with a stoichiometry of 1:0.3:1.36 (Ti:Ba:O). This thickness is assigned here to 1 ML BTO. The sample was again heated to 1123 K for 10 min in  $1.2 \times 10^{-6}$  mbar oxygen and then UHV-flashed at 1243 K for 2 min. After cooling down, the sample was heated a second time in UHV at 1263 K for 5 min. The high resolution low energy electron diffraction (SPALEED) pattern of the sample (Fig. 5.5) reveals the formation of the BTO-derived Kepler-approximant [44].

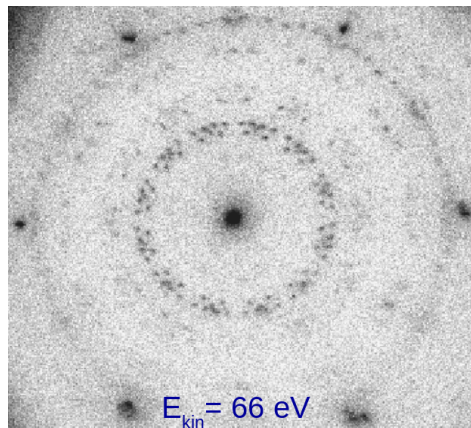


Figure 5.5: SPALEED pattern of 3 Å BTO on Pt(111), taken at an electron kinetic energy,  $E_{kin}$  of 66 eV.

After preparation, the sample was transferred through air to the KMC-1 beamline at BESSYII. The UHV chamber of that beamline had a pressure  $5 \times 10^{-8}$  mbar. Initially, the sample was annealed at 1020 K, first for 240 s in  $5.9 \times 10^{-7}$  mbar O<sub>2</sub> and then for 600 s in  $1 \times 10^{-6}$  mbar O<sub>2</sub>. The sample was then cooled down in  $1 \times 10^{-6}$  mbar oxygen to 500 K, when the oxygen dosing valve was closed. After taking the XPS and XAS spectra, the sample was then heated up at a

pressure of  $5 \times 10^{-8}$  mbar to 1120 K and kept for 210 s and was then cooled down. After cooling down and taking XPS spectra, XAS spectra were recorded in two angles of incidence and with two monochromator crystals.

The UHV chamber in KMC-1 beamline has not been equipped with LEED, therefore, the preparation of barium titanate derived OQCs on Pt(111) has been checked at home after repeating the preparation, i.e. reducing (oxidizing) the sample with the same procedure in an UHV chamber with a pressure of  $5.6 \times 10^{-8}$  ( $1 \times 10^{-6}$  mbar  $O_2$ ). LEED images have been taken, which confirms the formation of OQC. It was taken at 66 eV and is shown in Fig. 5.6 (a). The 12-fold ring and the Y-like group with 12-fold symmetry show the formation of dodecagonal quasicrystals in the reduced sample, as discussed in [40].

XAS spectra were taken in different angles of incidence and with different monochromator crystals. While performing the XAS measurements, no change of the spectrum has been observed.

14 hours after the sample preparation at home, the LEED image at 66 eV was taken again (Fig. 5.6 (b)). However, the OQC LEED pattern was not present anymore and only Pt substrate spots remained. This shows the lack of QC order of Ti atoms and instability of the sample in that pressure. As mentioned, after the sample preparation in KMC-1 beamline by annealing the sample to 1120 K at pressure of  $5 \times 10^{-8}$  mbar, XPS spectra have been taken, which took about 6 hours. Then XAS spectra were recorded, which took about 24 hours. No change has been observed between the first and the last XAS spectrum at the Ti *K*-edge, while there was a time difference of about 23 hours in between.

The oxidized sample did not show any LEED pattern of an overlayer, although the formation of BTO(111) islands is expected via oxidation [41]. This indicates an amorphous structure of the overlayer.

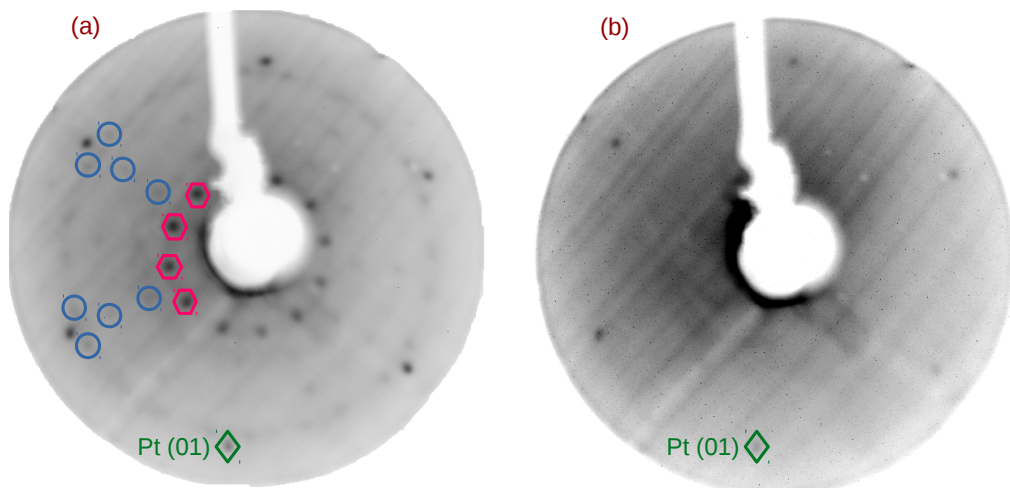


Figure 5.6: (a) The LEED image of the reduced 1 ML BTO sample was taken at 66 eV electron kinetic energy, was prepared as at KMC-1 beamline. (b) The same sample after 14 hours in an UHV chamber with a base pressure of  $5.6 \times 10^{-8}$  mbar.

To investigate the morphology of the sample, AFM images under ambient air conditions have been taken and are shown in Fig. 5.7. Three regions can be distinguished in the phase image. The dark high spots are assigned to BTO islands. The line profile of the zoomed region of Fig. 5.7 (c) shows that the height of the dark spots is 10 Å.

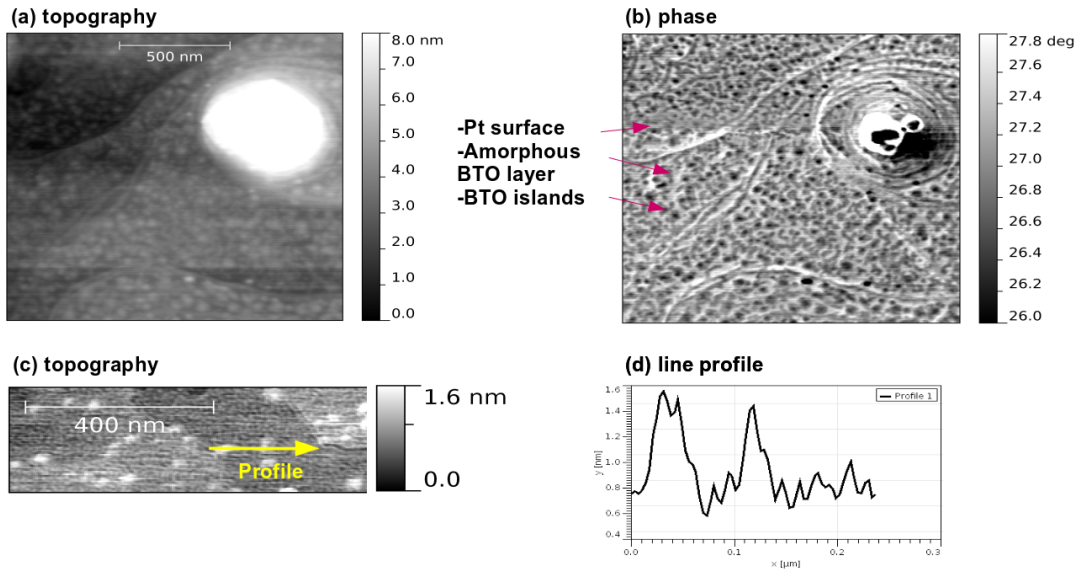


Figure 5.7: AFM image of the oxidized sample of 1 ML BTO on Pt(111), measured in tapping mode with a cantilever with a spring constant of 43 N/m. (a,b) The topography and the phase images, measured with a drive amplitude of 0.3 V and a drive frequency of 300 kHz. Scan size and scan speed are  $1.5 \times 1.5 \mu\text{m}^2$  and  $1.5 \mu\text{m/s}$ . (c) The topography of a zoomed region, measured with a drive amplitude of 0.6376 V and a drive frequency of 288 840 Hz and a scan speed of  $1 \mu\text{m/s}$ . (d) Corresponding line profile analysis.

Around the dark spots, there is a dark gray area with a height of  $3 \text{ \AA}$ , which can be assigned to an amorphous BTO layer. The height of these regions has been calculated from the shoulder of the main peaks in the line profile. The light gray region can be assigned to the Pt surface, which has been freed due to the dewetting process [41]. The shining spot in Fig. 5.7 (a) corresponds to a large Pt island on the surface. The BTO islands as well as the layer cover a considerable fraction of the surface, however, they do not show any LEED pattern. As a result of that, the structure of BTO in the oxidized sample is amorphous.

## 5.2.2 X-ray absorption measurements

X-ray absorption spectra at the Ti *K*-edge and the Ba *L*<sub>2,3</sub>-edges of the sample in the reduced and the oxidized states were taken in normal and  $70^\circ$  off normal incidences. The XAS spectra were taken in TEY and FY detection modes. The monochromation of the X-ray beam was done using both Si(111) and Si(311) crystal pairs. The signal from the Si(111) crystal pair was shifted by  $8.5 \pm 0.8 \text{ eV}$  to higher energies from the Si(311), indicating a calibration problem of the monochromator. The Si(111) crystal pair has a higher flux of X-rays. There was no signal visible in the TEY measurement using either of two crystals. Employing FY, XAS spectra have been obtained. FY spectra at the Ti



$K$ -edge and the Ba  $L_3$ -edge were measured by selecting a wide range (99%) of the signal peak area (200 eV) around the Ti- $K_{\alpha_{1,2}}$  and Ba- $L_{\alpha_{1,2}}$  emission lines as the energy window of the fluorescence detector, with an integration time of 10 s. Ti- $K_{\alpha_{1,2}}$  emission lines correspond to the fluorescence processes originating from the electron transition from  $2p_{3/2,1/2}$  levels to fill the core hole of the  $1s$  level. Ba- $L_{\alpha_{1,2}}$  fluorescence emission lines are also due to transitions from  $3d_{5/2,3/2}$  levels to  $2p_{3/2}$  level.

As mentioned in Sec. 4.3 and 5.1 for STO and BTO single crystals, XAS spectra at the Ti- $K$  and Ba- $L_3$ -edges have been taken in TEY and FY measurements modes and no difference has been observed between the XAS spectra recorded in two measurement modes. The involved excitation processes in FY of STO and BTO single crystals and BTO-derived OQC are within the core levels and are far away from the valence band. Therefore, it is expected to have similar EXAFS modulations in XAS spectra taken in FY and TEY detection modes at the Ti  $K$ - and the Ba  $L_3$ -edge in BTO-derived OQC.

The X-ray absorption spectra has been normalized to a mesh current and then to the edge jump. The resulting spectra of the reduced sample are shown in Fig. 5.8 (a,b). For comparison, the FY spectrum of bulk BTO in near normal incidence ( $2^\circ$ ) is also presented.

According to Ref. [101, 108, 109, 110] peak A represents the 6-fold coordination of the Ti atom by oxygen in the bulk. Considering stoichiometry and the thickness ( $3 \text{ \AA}$ ) of the deposited BTO layer on Pt, a 6-fold coordination of Ti by oxygen can be ruled out. In addition, fourfold and fivefold coordination lead to strong pre-edge features at 2 and 1 eV lower than peak A [105, 109, 110]. The absence of such features excludes four and fivefold coordinated Ti. Hence, 3-fold or lower coordination of Ti atoms by oxygen is a reasonable assumption. It confirms the choice of threefold coordination of Ti for the calculation of the Kepler-approximant [44], which has been assumed for further structural determination analysis.

Due to the 2D nature of OQC, a strong anisotropy of the absorption spectra in normal and grazing incidences is expected. Surprisingly, the directional anisotropy is very weak. As shown in Sec. 5.1, the directional anisotropy for bulk BTO is also weak. Therefore, there may be the possibility of presence of bulk BTO islands in the sample. However, the absorption spectrum of bulk BTO is quite different from that of OQC sample in XANES, as well as EXAFS regions. This shows that the OQC system has a completely different structure and bulk islands are below the detection limit.

The normalized absorption spectra at the Ba  $L_3$ -edge of the reduced sample in normal and grazing incidence in FY are displayed in Fig. 5.9. For comparison, the spectrum of bulk BTO in normal incidence ( $2^\circ$ ) in FY is also presented. The directional anisotropy at the Ba  $L_3$ -edge is also negligible, similar to that at the Ti  $K$ -edge.

Heating BTO-derived OQC in oxygen leads to the formation of islands with a height of several monolayers [40, 41]. Therefore, the absorption spectrum of the oxidized sample is expected to be quite different from the reduced one. The normalized absorption spectra at the Ti  $K$ -edge of the reduced and the oxidized sample in grazing incidence are shown in Fig. 5.10. Surprisingly,

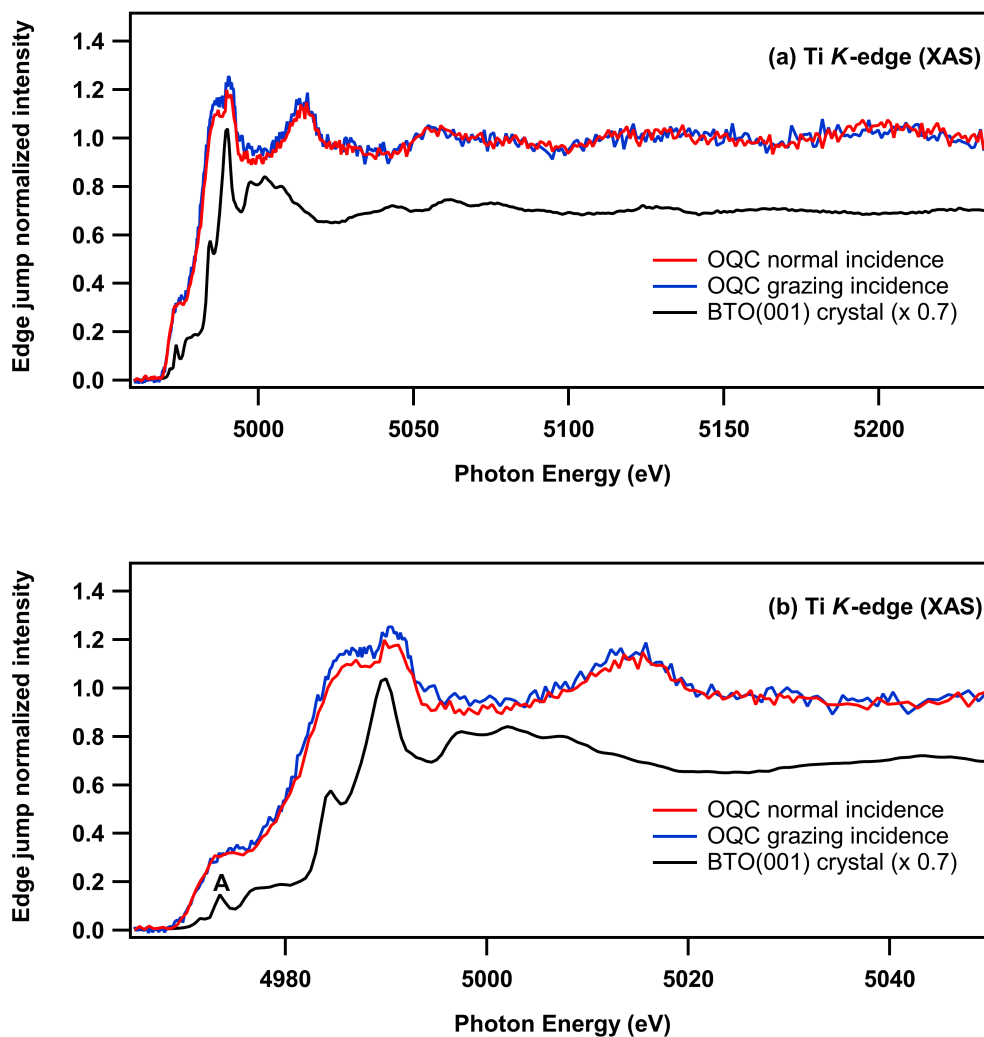


Figure 5.8: (a) The Ti *K*-edge absorption spectrum of the OQC (the reduced 1 ML BTO) in normal and grazing incidence in FY and the absorption spectrum of BTO single crystal in normal incidence in FY. (b) Zoomed XANES region.

the spectra at the Ti *K*-edge look quite similar. This implies that due to reducing residual gases resulting from the high base pressure of the chamber, the process of dewetting of the Pt surface and formation of islands has not succeed.

The absorption spectra at the Ba  $L_3$ -edge in grazing incidence in the reduced and the oxidized sample in FY are presented in Fig. 5.11 and compared with the bulk spectrum in FY in grazing incidence ( $72^\circ$ ). The spectrum in the oxidized sample has a shift of  $0.3 \pm 0.1$  eV to lower energies. In addition, the oxidized sample shows higher resonance intensity comparing to the reduced sample, which is also higher than the bulk. This increase reflects changes in the bonds of the Ba  $5d$  and the O  $2p$  states, compared to bulk BTO.

After recording all spectra, the sample has shortly been exposed to air at room atmosphere. Then, the absorption spectrum in the XANES region at the Ti *K*-edge has been taken in normal incidence (not been shown here). Interestingly, the absorption spectra are quite similar in both

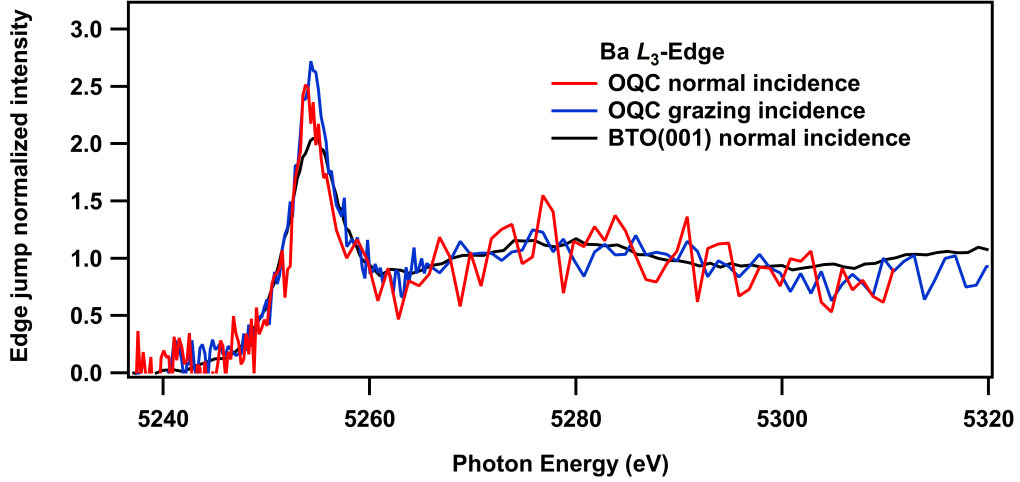


Figure 5.9: X-ray absorption spectrum of the Ba  $L_3$ -edge of the OQC (the reduced 1 ML BTO) in normal and grazing incidence and bulk BTO in normal incidence. All the spectra have been recorded in FY.

reduced and air-exposed samples. This observation suggests that the local structure in the reduced sample is quite stable, even when exposed to air.

### 5.2.3 X-ray photoemission measurements

To determine the chemical states of the reduced and oxidized samples, XPS measurements have been performed by using the synchrotron radiation source in KMC-1 beamline. The monochromatized beam of 2003 eV has been obtained using Si(111) crystal pairs, while the measurements have been performed in normal emission (incidence as close as possible to  $90^\circ$  from normal of the sample). The XPS measurements of the reduced sample have been carried out immediately after sample preparation and they have been followed by the XAS measurements.

The binding energies of the spectra have been referred to the Pt  $4f_{7/2}$  emission line at 71.2 eV [62]. The spectra have been normalized to the integration time of the analyzer. The inelastic fraction of the spectrum has been approximated by a Shirley background for the Ti, the Ba and the Pt emission lines [66] and has been subtracted (Sec. 3.3). However, for O and C emission lines, subtraction of a Shirley background was not possible, due to the curvature of the foot points of the spectra. In those cases, a polynomial has been subtracted. This of course, changes the stoichiometric number of oxygen, determined by XPS by 20%.

Deconvolutions of the spectra have been done using pure *Gaussian* or *Lorentzian* functions and a Gaussian-Lorentzian product function [121]:

$$I(E) = I_0 \left[ \left( 1 + \frac{4M(E - E_B)^2}{\Gamma^2} \right) \exp \left( \frac{4(1 - M) \ln(2)(E - E_B)^2}{\Gamma^2} \right) \right]^{-1} \quad (5.1)$$

Here,  $I_0$  is the intensity of the function at the peak position,  $E_B$  the binding energy and  $\Gamma$  is the FWHM of the peak.  $M$  is the mixing ratio, which is 0 for a pure Gaussian and 1 for a pure

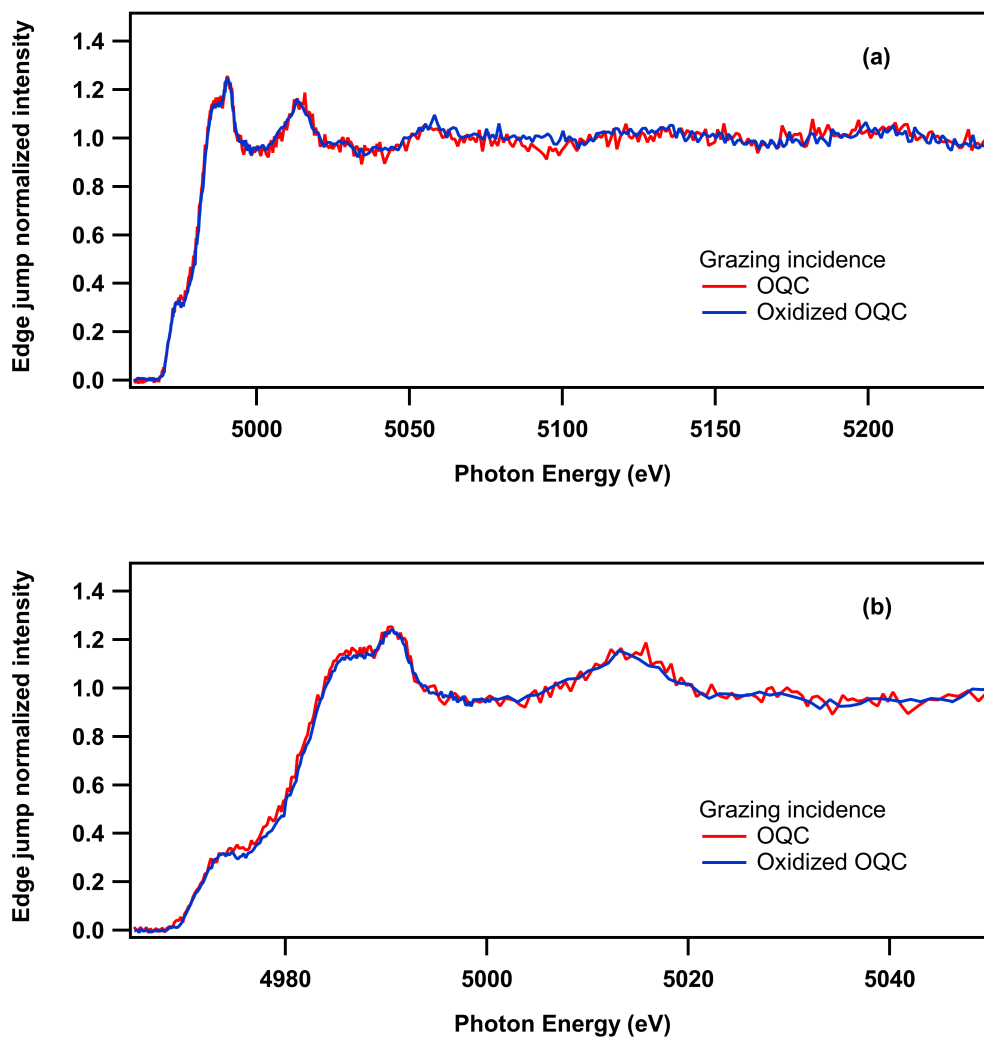


Figure 5.10: X-ray absorption spectra at the Ti  $K$ -edge (a) and the zoomed region (b) of 1 ML BTO in the reduced (OQC) and the oxidized (oxidized OQC) state, recorded in FY mode in grazing incidence.

Lorentzian line shape.

C  $1s$  and Pt  $4f$  X-ray photoemission spectra for the reduced and the oxidized cases are shown in Fig. 5.12. Due to the high excitation energy, no surface component is visible in the Pt spectrum. In the oxidized case the intensity of Pt  $4f$  lines has decreased to less than half. Considering the incidence angle of  $90^\circ$ , this change may be due to some tiny changes in the measurement position. Therefore, the spectrum areas cannot be compared individually and all the areas have been normalized to the Ti area for stoichiometry determinations in Sec. 5.2.3.

Due to the high base pressure in the measurement chamber, there are carbon species on the surface. The C spectra have been fitted by a Lorentzian peak, which is broader in the oxidized case by 0.17 eV. The binding energy of the C peaks in both cases fits to elemental carbon or similar aliphatic compounds ([122]: cyclohexane  $C_6H_{12}$  285.2 eV). The general assumption is that carbon in such compounds has weak interactions with oxides and are not expected to change the structure of OQC easily. The stoichiometry determination shows that for every Ti atom there are 6 carbons

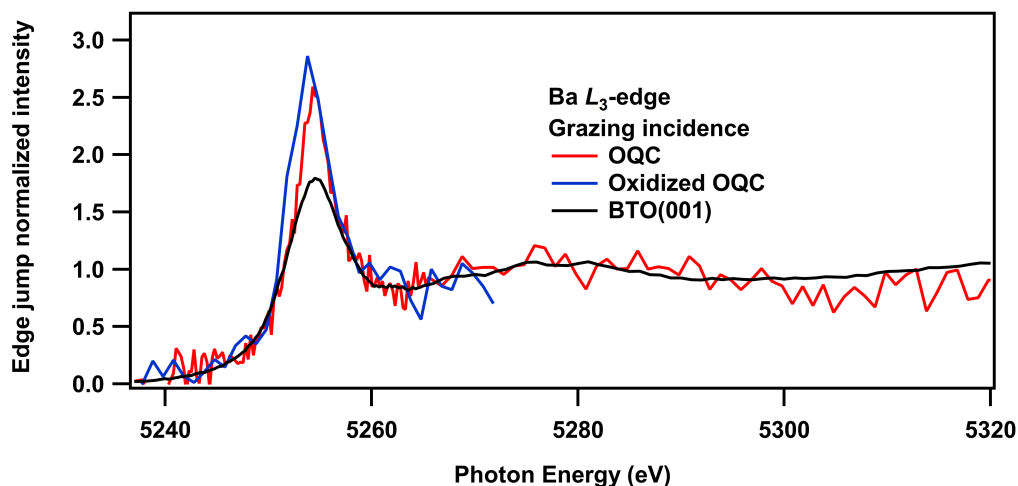


Figure 5.11: X-ray absorption spectra at the Ba  $L_3$ -edge of 1 ML BTO in the reduced (OQC) and the oxidized (oxidized OQC) states, recorded in FY mode in grazing incidence. The absorption spectrum of BTO(001) crystal in FY in normal incidence is presented.

(5.2.3). Considering the C-C bond length and the Ti-Ti bond length in the OQC (1.54 and 6.85 Å), it is clear that at most there are 2 ML carbon contamination on the surface.

Considering the excitation photon energy for the XPS measurement (2003 eV), the inelastic mean free path of photoelectrons in  $C_6H_{12}$  at the Ba  $3d_{5/2}$  emission lines is larger than 33 Å, calculated according to [123, 124]. Therefore, the coverage of the OQCs with 2 ML of the inert carbon compounds does not disturb the experiment and the stoichiometry determination.

Ti  $2p$  emission line of the reduced and the oxidized sample are presented in Fig. 5.13. In general, the number of the  $2p_{3/2}$  orbitals and therefore, the area of this part of the spectrum is two times as those in the  $2p_{1/2}$  part [55] (the reference is for XAS but the origin of the effect is the same). Practically, the area ratio of the two regions depends also on the details of the background subtraction. In the cases of the oxidized and the reduced samples, this ratio has been determined to be 0.62. Furthermore, the  $2p_{1/2}$  part of the spectrum is known to be wider. The broadening originates from multiplet transitions, which depend on the hybridization of the Ti  $3d$  and the O  $2p$  levels [125]. The spin-orbit splittings of the fitting components have been set to 5.8 eV.

The first Ti component in Fig. 5.13 at 456.6 eV fits to  $Ti^{3+}$  in  $Ti_2O_3$  [126]. For the first component, the FWHM ratio of  $2p_{1/2}$  to  $2p_{3/2}$  is 1.55. This component does not shift during oxidation, however, it changes its line shape from a pure Lorentzian with a FWHM of 1.2 eV to a pure Gaussian with a FWHM of 1.13 eV (Fig. 5.13 (a,b)). The contribution of this component in the spectrum also decreases from 77% in the reduced spectrum to 37% in the oxidized one.

The second component of spectrum in the reduced case is at 457.9 eV and fits to the binding energy of  $Ti^{4+}$  in  $BaTi_2O_5$ , which indicates the presence of a Ti-rich phase. The reported binding energy for Ti  $2p_{3/2}$  line is 457.8 eV [127], while no other binding energies of other elements in  $BaTi_2O_5$  has been reported in the reference.

The formation of a Ti-rich phase is in agreement with the stoichiometry determination (Sec.

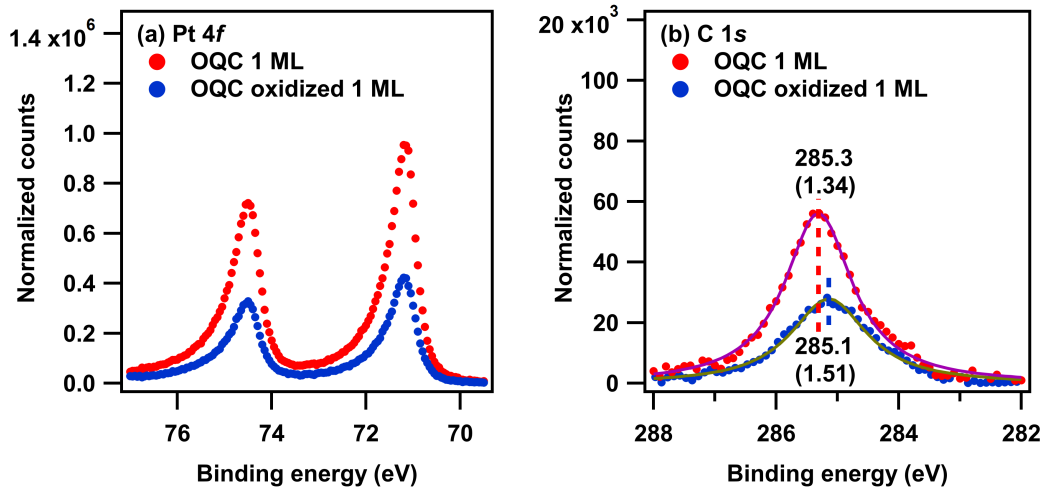


Figure 5.12: XPS spectra of the Pt 4*f* (a) and the C 1*s* emission lines of 1 ML BTO in the reduced (OQC) and the oxidized (oxidized OQC) states, recorded in normal emission. FWHMs of the C spectra are given in the parenthesis.

5.2.3). Where, the amount of Ti is larger than the amount of Ba. This may result in a phase change from  $\text{BaTi}_2\text{O}_5$  to  $\text{BaTi}_2\text{O}_4$  (Fig. 8.1 (a,b)) [128, 129, 130]. However, this phase change is unlikely, since it occurs above 1573 K [128], while the sample preparation temperatures were 1020 and 1120 K (Sec. 5.2.1). The formation of a Ba-rich phase will be discussed, in the next paragraphs.

The third component in Fig. 5.13 (a) at 459.5 eV fits to the 4+ oxidation state of 6-fold coordinated Ti in  $\text{TiO}_2$ -rutile [131]. As is presented in Fig. 5.13 (b), there is a  $\text{Ti}^{4+}$  component at 458.6 eV, which fits to the 5-folded coordinated Ti in a fresnoite glass ( $\text{Ba}_2\text{TiSi}_2\text{O}_8$ ) at 458.4 eV. The corresponding O 1*s* and the Ba  $3d_{5/2}$  at 530.3 and 780.0 eV also fit to the experimental data at 530.1 and 780.3 eV in Fig. 5.14 (b) and 5.15 (b) [132]. It needs to be noted that the binding energies in the reference [132] have been referred to adventitious C 1*s* at 284.8 eV, which may lead to uncertainty up to 0.6 eV, as discussed in Sec. 3.3.

The formation of 3D BTO islands in a dewetting process from the OQC layer has been reported [41]. The X-ray absorption spectra and the Fourier transform of the reduced and the oxidized samples are quite similar (5.16). The Fourier transform clearly shows that the radial distances of neighbors have not changed during the oxidation. However, 3D islands have different arrangement of neighbors, in particular Ti-Pt distances should be different. Furthermore, via oxidation and formation of 3D islands in the 4 ML BTO on Pt(111) (Sec. 6.3), an O 1*s* component arises at 529.6 eV binding energy, which is not present in the oxidized case of 1 ML sample. The presuming explanation is that the dewetting process of the Pt surface and formation of 3D BTO islands have not occurred. The deconvolution of the O 1*s* spectra of the reduced and the oxidized sample (1 ML) is presented in Fig. 5.14 (a,b) and the comparisons with the 4 ML sample in both oxidation states are given in Fig. 5.14 (c,d).

The deconvolution of the O 1*s* spectra of the 1 ML BTO has been performed using a set of three Gaussian peaks with different widths. The widths have been kept the same for the analysis of the

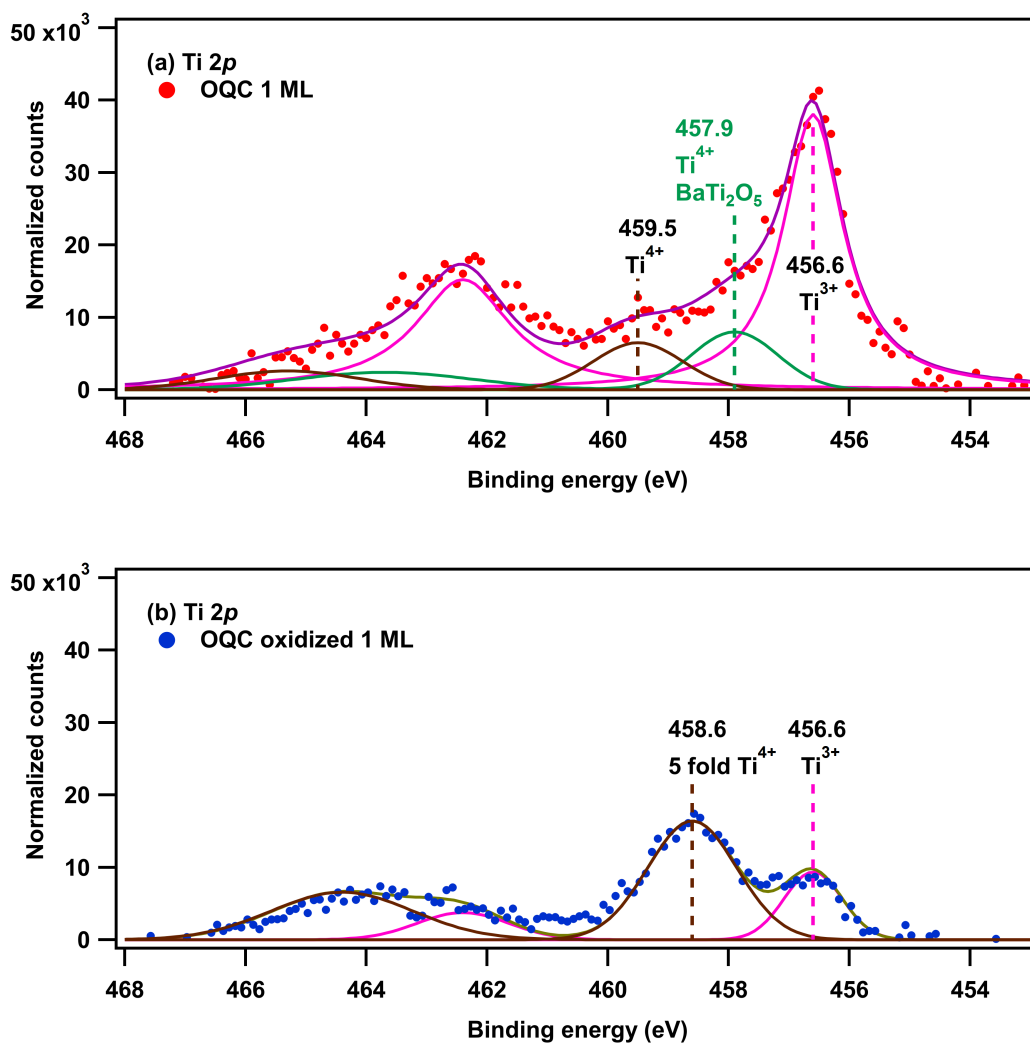


Figure 5.13: XPS spectra of the Ti 2p emission line of 1 ML BTO in (a) the reduced (OQC) and (b) the oxidized (oxidized OQC) states, recorded in normal emission.

reduced and the oxidized spectra (5.14 (a,b)). In the reduced (the oxidized) case, the main peak at 530.1 eV (530.05 eV) can be assigned to O bonded to  $\text{Ti}^{3+}$  in  $\text{Ti}_2\text{O}_3$  ( $\text{Ti}^{4+}$  in BTO). That is because the difference between the Ti  $2p_{3/2}$  and the O 1s binding energies is  $73.3 \pm 0.2$  eV [133] ( $73.15 \pm 0.25$  eV [64]) in  $\text{Ti}_2\text{O}_3$  and  $71.35 \pm 0.05$  eV in BTO [64, 134]. The binding energies of the main peaks agree also with the adsorbed atomic oxygen on Pt(111) at 530.2 eV. Atomic oxygen desorbs from the Pt surface above 800 K [135, 136]. Readsorption cannot be ruled out, because of the high base pressure. Such a component would be quite broad with a FWHM of 2.6 eV, 2.5 times wider than that in Fig. 5.14. Adsorbed oxygen on the Pt surface can therefore, be excluded [137].

The second component of the O 1s spectra is at 531.2 eV, the same position in the reduced and in the oxidized state. This feature can be assigned to OH adsorbed on the Pt surface at  $531.5 \pm 0.5$  eV. The binding energy fits and the large widths is characteristic for OH-groups [137]. Although it desorbs from the surface above 1070 K [137], due to the high pressure of the chamber, readsorption while cooling down may occur.

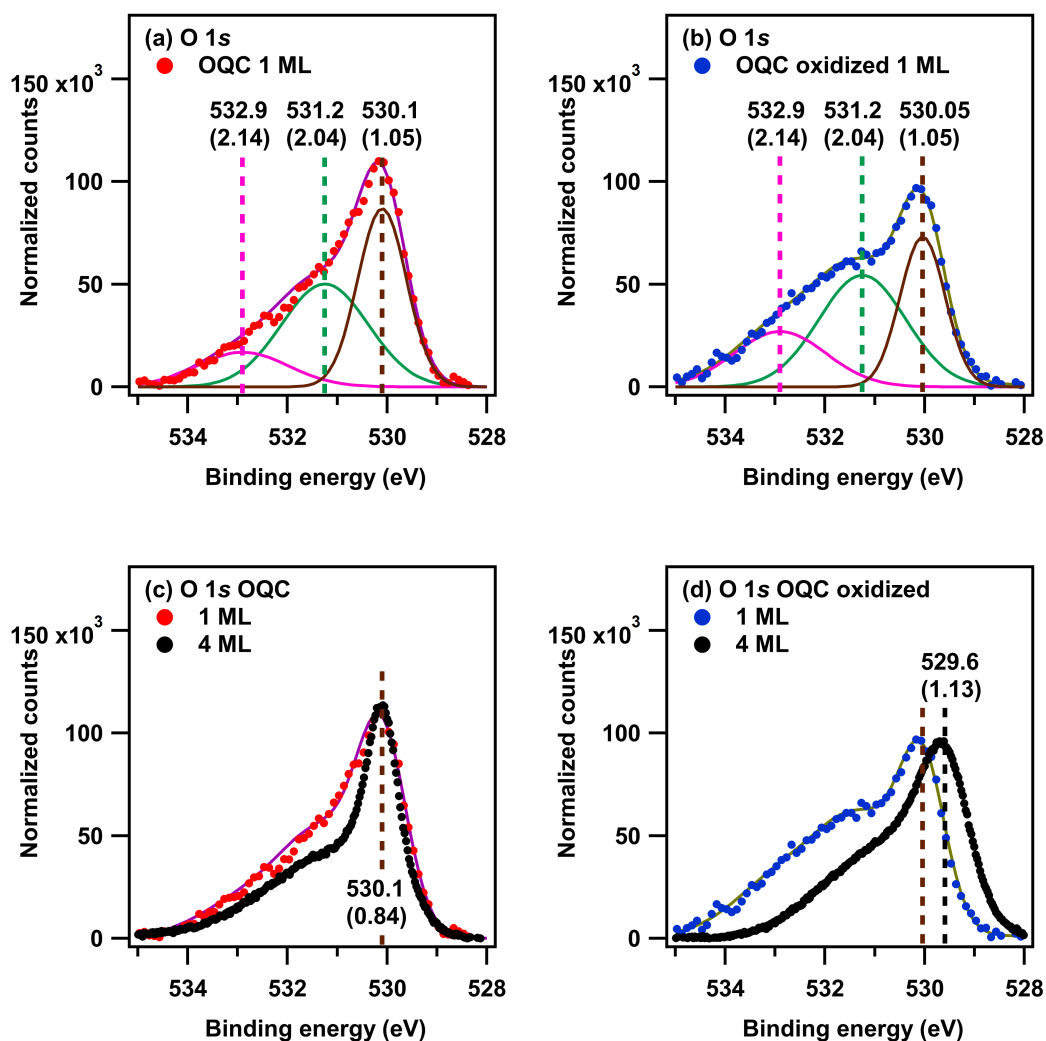


Figure 5.14: O 1s emission line of 1 ML BTO in the reduced (OQC) and the oxidized (oxidized OQC) states (a,b) and comparison with the 4 ML BTO (c,d) in the reduced (OQC) and the oxidized (oxidized OQC) states. FWHM of every component has been given in parenthesis below the peak position.

The OH groups could also be bonded to Ba. The experimental values of the O 1s and the Ba  $3d_{5/2}$  emission lines at 531.2 and 780.3 eV in Fig. 5.14, 5.15 agree with the literature, 531.2 and 780.4 eV [138, 139]. Although the decomposition of Ba(OD)<sub>2</sub> on a thick BaO film is complete at 550 K [140], uptake of OH by Ba could result from high pressure of the chamber. The binding energy of this component also fits to that in BaCO<sub>3</sub> (531.7 eV), whereas the binding energy of the C 1s in BaCO<sub>3</sub> (289.9 eV) does not fit to the experiment and rules out carbonate [141]. Similar broad components in cobalt oxide compounds have been assigned to O at defects [142]. This broad peak may also be assigned to unknown structures.

The third component of the O 1s at 532.9 eV fits to adsorbed water on the Pt surface, as reported previously, (533.8 eV [137], 532 ± 0.3 eV [143]). However, water desorbs from Pt at 210 K [144]. This component has a similar binding energy, as O in CO at bridge sites on Pt(111) surface (532.6 eV), however, the corresponding C 1s emission line (285.8 eV) is not present in the experiment [145].



The comparison with the O 1s of the reduced 4 ML sample, taken at 999 K in UHV (Fig. 6.6 (b)) reveals that the third component corresponds to some adsorbate from the residual gases. Since, the broad component with FWHM of 1.86 eV at 532.7 eV is not present at this temperature, while it is at RT.

Ba  $3d_{5/2}$  spectra of the 1 ML of the reduced and the oxidized samples are presented in Fig. 5.15. The spectra are deconvoluted with 3 Gaussian functions. The main component of the spectra at 780.3 eV may be assigned to a Ti-O-Ba configuration for both cases. In addition, the binding energy of the Ba  $3d_{5/2}$  in bulk BTO has been reported as 779.5 eV, while the energy difference of the Ti  $2p_{3/2}$  and Ba  $3d_{5/2}$  is 320.5 eV [134, 146]. So, the main component of the reduced case at 780.3 eV fits to bulk BTO with the corresponding Ti emission line at 459.5 eV. The corresponding O 1s line then should have a shift of 71.3 eV [64], which means the peak to be at 530.8 eV. Although in the deconvolution, no peak at this energy is present, the peak at 531.2 eV is so wide that it may have such a component.

The second component of the spectrum at 781.96 eV may be due to an asymmetric line-shape. The third component of the oxidized sample at 778.97 eV fits to Ba in BaO (778.9 eV). However, the corresponding O 1s energy at 528.4 eV is not present. The corresponding emission lines in BaO<sub>2</sub> at 530.8 and 780.8 eV do not fit to the experiment [147], which excludes oxygen as peroxide.

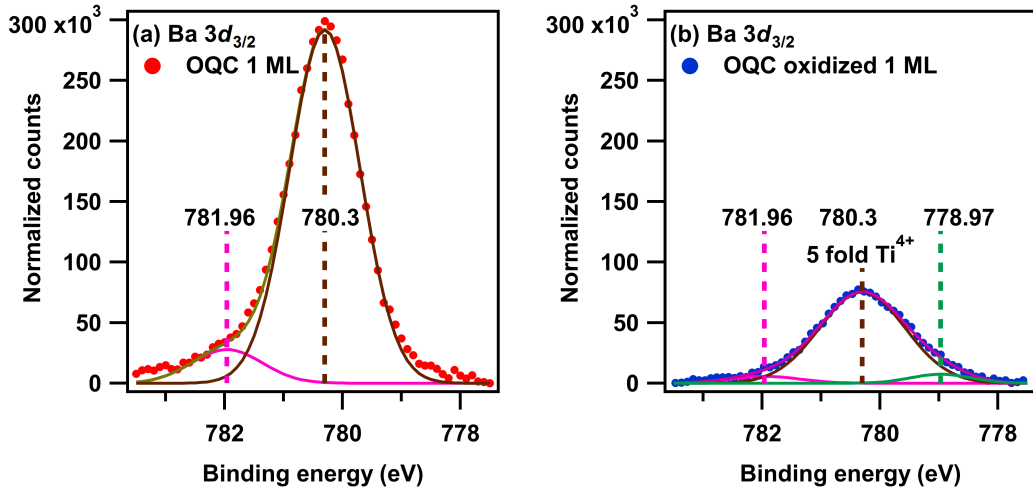


Figure 5.15: (a,b) The Ba  $3d_{5/2}$  emission line of 1 ML BTO in (a) the reduced (OQC) and (b) the oxidized (oxidized OQC) states, recorded in normal emission.

Barium orthotitanate, Ba<sub>2</sub>TiO<sub>4</sub>, is another Ba-rich compound, with fully oxidized Ti<sup>4+</sup>. In this compound, Ti atoms are 4-fold coordinated by oxygen, which is similar to 4-fold coordinated Ti<sup>4+</sup> in fresnoite glass. Hence, their core level emission lines are also expected to be similar. The binding energy of 4-fold coordinated Ti<sup>4+</sup> in fresnoite glass is 457.4 eV [132], which is not a major component in Ti spectra in Fig. 5.13. This agrees with the absence of the characteristic pre-edge feature of 4-fold coordinated Ti in XAS spectra at the Ti *K*-edge, as discussed in Sec. 5.2.2. Therefore, Ba-rich regions as a major contribution can be excluded.

Table 5.2: The stoichiometry of 1 ML BTO in the reduced and the oxidized states, calculated from relative step heights in the absorption spectra at the Ti *K*-edge and the Ba *L*<sub>3</sub>-edge.

| System                              | Ba/Ti step height | Ti | Ba  |
|-------------------------------------|-------------------|----|-----|
| BTO single crystal normal incidence | 0.260             | 1  | 1   |
| Reduced state normal incidence      | 0.188             | 1  | 0.7 |
| Reduced state grazing incidence     | 0.089             | 1  | 0.7 |
| Oxidized state grazing incidence    | 0.152             | 1  | 1.2 |

In summary, in the reduced spectra following components are present: 6-fold Ti<sup>3+</sup> like in Ti<sub>2</sub>O<sub>3</sub> with emission lines at 456.6 and 530.1 eV, Ti<sup>4+</sup> like in BaTi<sub>2</sub>O<sub>5</sub> with an emission line at 457.9 eV, 6-fold Ti<sup>4+</sup> like in TiO<sub>2</sub>-rutile with an emission line at 459.5 eV, 6-fold coordinated Ti<sup>4+</sup> like in BTO with emission lines at 459.5, 530.8 and 780.3 eV and OH groups on Pt and Ba with emission lines at 531.2 and 780.3 eV. In the oxidized case, the components are: 6-fold Ti<sup>3+</sup> like in Ti<sub>2</sub>O<sub>3</sub> with emission lines at 456.6 and 530.05 eV, 5-fold coordinated Ti<sup>4+</sup> like in Ba<sub>2</sub>TiSi<sub>2</sub>O<sub>8</sub> with an emission line at 458.6, 6-fold Ti<sup>4+</sup> like in BTO with emission lines at 458.6, 530.05 and 778.97 eV and OH groups on Pt and Ba with emission lines at 531.2 and 780.3 eV. However, the evidence for OH groups in the system is weak and does not rule out other explanations.

### OQC stoichiometry determination

The step height of the absorption spectrum is characteristic for an element and does not depend on the structure of the system. Furthermore, the involved levels in the fluorescence transitions are far enough in energy relative to the valence band. Therefore, the step heights of the spectra depend directly on the number of the element in the system and is not affected by the structure. As a result, the stoichiometry of the systems have been determined using the relative step heights of Ba to Ti in FY spectra. The bulk measurements have been performed in normal incidence and the ratio of the step heights in bulk have been used as the reference for Ti:Ba ratio of 1:1.

Considering the extreme thickness of the sample, no difference is expected between the stoichiometry in normal and grazing. That is because FY has been employed as the recording method, which has a penetration depth in the same order as that of the X-rays and the signal does not decay due to the change of the penetration depth of the fluorescence photons in grazing versus normal incidence. Hence, the stoichiometry of the oxidized sample in grazing incidence is calculated by referring to the step height of the reduced sample in grazing, which has been assumed to have the same stoichiometry as in normal incidence. Although it is not really clear why the ratio in the step height decreases to 50%, when changing from normal to grazing incidence. The results are presented in Tab. 5.2.

The stoichiometry has also been determined using XPS. First, the spectrum is normalized to the integration time per measured point. Second, the inelastic fraction of the spectrum is subtracted and the area of the resulting spectrum is divided by the sensitivity factor  $S_A$ . The sensitivity factor

Table 5.3: The values of  $\sigma_A$  and the calculated values of  $\lambda_{m,E}$  and  $S'$  according to Eq. 5.2 calculated for different elements at a photon energy of 2003 eV.

| Element | $\sigma_A$ | $\lambda_{m,E}$ | $S'$    |
|---------|------------|-----------------|---------|
| Ti      | 0.05429    | 26.6 Å          | 0.00093 |
| Ba      | 0.31467    | 22.2 Å          | 0.00571 |
| O       | 0.02137    | 25.6 Å          | 0.00037 |
| C       | 0.00735    | 28.9 Å          | 0.00012 |

has been derived according to (Ch. 4 of [148] and Ch. 5 of [149]):

$$S_A \propto \sigma_A G(E) \lambda_{m,E} \quad (5.2)$$

For simplification, the result of the multiplication is called here  $S'$ . Here,  $\lambda_{m,E}$  is the mean free pass of the photoelectron with the kinetic energy  $E$  in the matrix  $m$ . It has been determined employing the specifications of bulk BTO according to [123, 124].  $G(E)$  is the analyzer efficiency and for most analyzers is approximated by the inverse of the kinetic energy of the photoelectron (Ch. 4 of [148], [150]). Finally,  $\sigma_A$  is the photoionization cross section of the core level of the corresponding element at the excitation energy, which depends on the element, the excited core level and the photon energy.

The photoionization cross sections have been taken from the website of Elettra synchrotron [151] (according to [152, 153]). However, they have been calculated up to a photon energy of 1500 eV. The investigated core levels are  $1s, 2p, 3d, 4f$  levels, which do not have any nodal points. Therefore, it was possible to extrapolate the reported cross sections to 2003 and 2005 eV, in which the measurements of the 1 ML sample and the BTO single crystal (as a reference) have been performed. The sensitivity factor also depends on the geometry of the experimental setup. The measurements have been performed at  $0^\circ$  emission angle for the reduced and the oxidized samples and at  $2^\circ$  emission angle for the BTO single crystal. Since the geometry has not been changed for the measurements of each sample, no geometry dependent factor needs to be included in Eq. 5.2.

The values of  $\sigma_A$ ,  $\lambda_{m,E}$  and the  $S'$  corresponding to the photon energy of 2003 eV are given in Tab. 5.3, while those values of 2005 eV are very close, hence, they are not presented here. To determine the stoichiometry, the areas have been divided by  $S'$  and the results have been normalized to those of Ti. For the O  $1s$  spectra, the contributions of the adsorbates at 532.9 eV have been subtracted. The reported  $\sigma_A$  of the Ba  $3d$  corresponds to both  $3d_{3/2}$  and  $3d_{5/2}$  emission lines. Since the measurements have only been performed in the  $3d_{5/2}$  region, the corresponding areas have been multiplied by  $5/3$  to approximate the total Ba  $3d$  area. The results of the calculated stoichiometries by different experimental methods for the 1 ML sample and the BTO single crystal are given in Tab. 5.4.

The initial stoichiometry determination of the sample by AES leads to Ti:Ba:O:C ratio of 1:0.3:1.36:0 (Sec. 5.2.1). This is in qualitative agreement with the ratio of 1:0.7, determined by XAS in the reduced sample in normal incidence (Tab. 5.2 and 5.4). However, this ratio does

Table 5.4: The stoichiometry of 1 ML BTO in the reduced and the oxidized states, as well as bulk BTO, determined by different experimental techniques. The presented measurement angles are the incidence angles in XAS and the emission angles in XPS from the normal of the sample surface.

| System                    | Exp. Tech.        | Measur. angle | Ti | Ba  | O    | C   |
|---------------------------|-------------------|---------------|----|-----|------|-----|
| BTO/Pt initial deposition | Auger Elec. Spec. | -             | 1  | 0.3 | 1.36 | 0   |
| Reduced sample            | XAS               | 0°            | 1  | 0.7 | -    | -   |
| Reduced sample            | XAS               | 70°           | 1  | 0.7 | -    | -   |
| Reduced sample            | XPS               | 0°            | 1  | 1   | 3.6  | 5.8 |
| Oxidized sample           | XAS               | 70°           | 1  | 1.2 | -    | -   |
| Oxidized sample           | XPS               | 0°            | 1  | 0.6 | 7.6  | 6.4 |
| Bulk BTO                  | XPS               | 2°            | 1  | 1.1 | 3.5  | 7.2 |

not fit to the results of XPS, which give the ratio of 1:1:3.6:5.8. Furthermore, there is a drastic increase in the amount of Ba in the oxidized sample by XAS (1:1.2), which does not agree with its decrease, determined by XPS (1:0.6:7.6:6.4). The reason of this inconsistency remains unclear.

The next source of the systematic errors in the analysis is due to the details of the background subtraction. In the cases of O and C spectra, it was not possible to determine a Shirley background and only polynomials have been subtracted. This increases the uncertainty in the calculations up to 20%. In addition, there may still be some contributions of the adsorbates in O on the Pt surface in the spectrum, which have not been subtracted. It also needs to be mentioned that a Shirley background is only an approximation and the actual portion of the inelastic electrons may be much higher, as discussed in Ch. 4 of [68]. Even for the bulk sample, which has a much better signal to noise ratio, the stoichiometry (1:1.1:3.5:7.2) is not as expected. Maybe the surface termination also plays a role. As discussed in Sec. 5.2.3, the amount of carbon on the 1 ML sample is maximum 2 ML. Considering the inelastic mean free path of the excited photoelectrons of the Ba  $3d_{5/2}$  emission lines in  $C_6H_{12}$  is larger than  $33 \text{ \AA}$  (Sec. 5.2.3), XPS measurements are not disturbed by the adsorbed carbon layer. Despite performing the experiments with utmost care, the reasons of inconsistency in the stoichiometry from XAS and XPS remain unclear.

## 5.2.4 OQC EXAFS data analysis

The modulation functions and the corresponding Fourier transformed functions have been derived from the Ti  $K$ -edge absorption spectra of the reduced and the oxidized sample in normal and grazing incidence. The Fourier transformation has been done in the range of  $0.4$  to  $8 \text{ \AA}^{-1}$  of the modulation function. The derived spectra are presented in Fig. 5.16 (a,b) using DEMETER software package [86]. As is obvious from the figures, the absorption spectra and their Fourier transformations show little differences. In addition, the most prominent feature at  $2 \text{ \AA}$  is present in all the Fourier transforms. Therefore, a structural model for OQC should exhibit only minimal directional anisotropy.

Due to the low thickness of the sample, the noise level in the experimental data is considerably

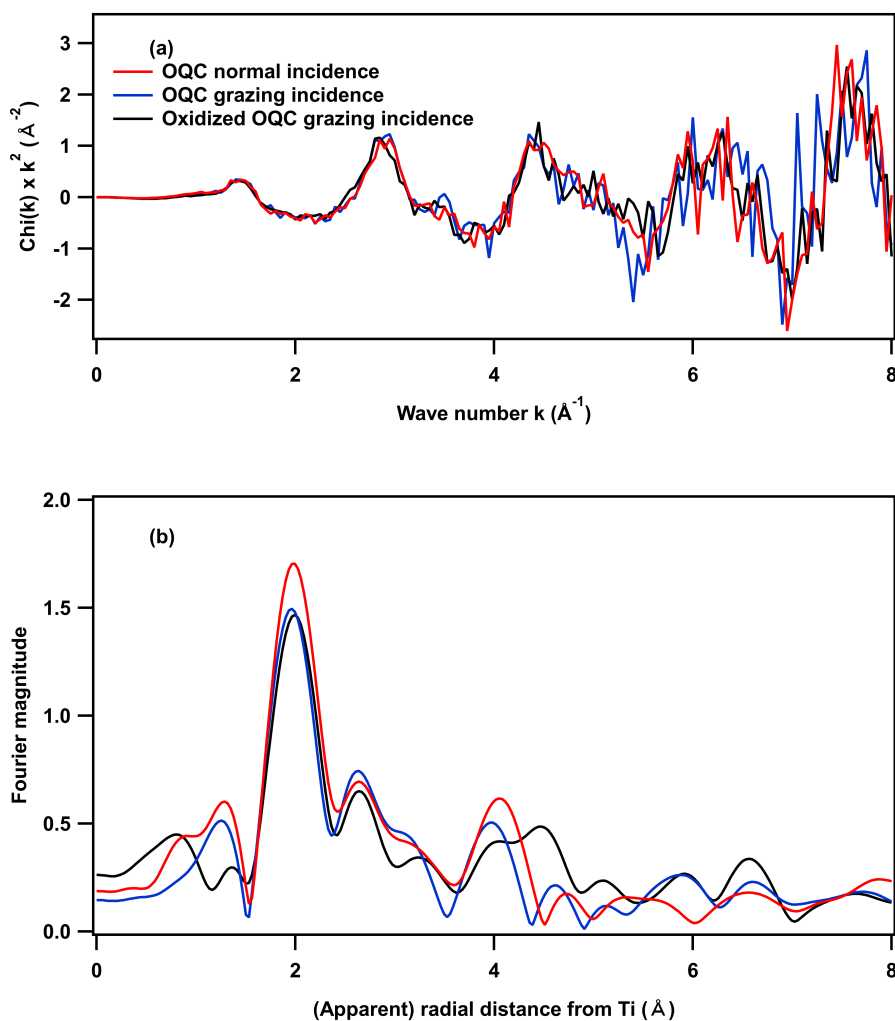


Figure 5.16:  $k^2$  weighted modulation function of 1 ML BTO at the Ti  $K$ -edge in the reduced (OQC) and the oxidized (oxidized OQC) state, at the Ti  $K$ -edge in normal and grazing incidence (a) and the corresponding Fourier transformations (b).

high. The influence of experimental noise on the Fourier transformed functions has been checked by fitting a smoothing spline to the modulation function in each angle of incidence and Fourier transform them. This shows that the intensity of the peaks at distances higher than  $\approx 5.4 \text{\AA}$  are strongly influenced by the noise. However, this distance is beyond the sensitivity range of EXAFS.

### The single scattering Fourier transformed functions

The Fourier transformation presents the apparent distance of neighbors around the absorbing atom regardless of the element type of the neighbor (Sec. 3.5.1). Figure 5.17 (a) displays the comparison between the  $k^2$  weighted modulation function of the reduced sample at the Ti  $K$ -edge in normal incidence and an O at a distance of  $2.6 \text{\AA}$  from Ti in a single scattering process. Obviously, the main modulation in the experiment can be explained by this oxygen. The corresponding Fourier transformation functions are depicted in Fig. 5.17 (b). The Fourier transformation of the oxygen is a single peak with some small shoulders and fits to the position of the main feature. There is a

shift of  $0.57 \text{ \AA}$  in its peak position, which originates from the energy dependence of the phase-shift of the scattering process (Sec. 3.5.1).

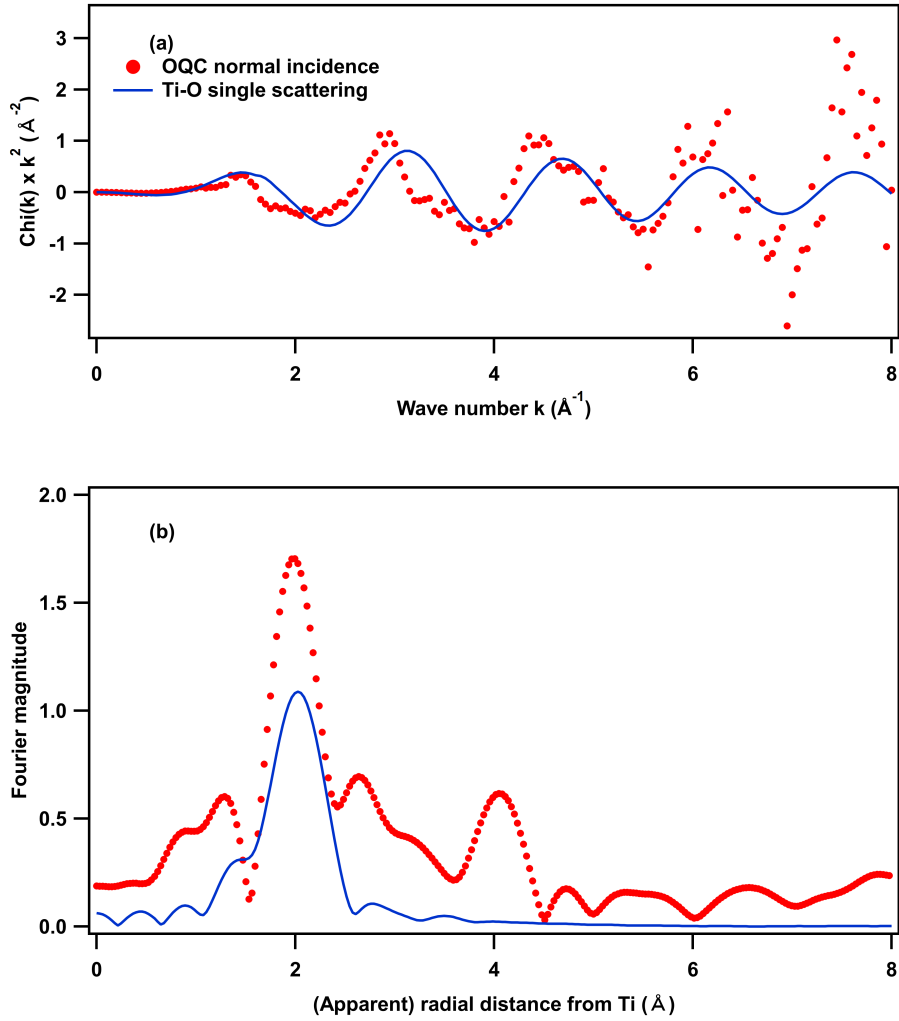


Figure 5.17: (a)  $k^2$  weighted modulation function of 1 ML BTO in the reduced (OQC) state at the Ti  $K$ -edge in normal incidence and the modulation function of a single scattering process from an O atom at a distance of  $2.6 \text{ \AA}$  and (b) the Fourier transformations.

The modulation function due to the single scattering process of a Pt atom in normal incidence at a distance of  $2.7 \text{ \AA}$  from Ti is presented in Fig. 5.18 (a) and the Fourier transformation function is given in Fig. 5.18 (b). The selection of this distance is due to the results of FEFF calculations, presented in Tab. 5.6. At high energies the modulation function of Pt fits well to the experiment. The backscattering phase-shift of Pt changes considerably at wavenumber between 5 to  $6 \text{ \AA}^{-1}$ , which is reflected in the shape of the modulation function in this range [154]. This leads to the presence of at least two main frequencies in the modulation function and two peaks in the Fourier transform with an intensity ratio of 3 to 2. There is a shift of  $0.54 \text{ \AA}$  between the actual distance of Pt from Ti and the position of the larger peak in the Fourier transformation function.

Considering the shapes of O and Pt Fourier transformed functions, the peak in the experimental data at  $2 \text{ \AA}$  can be assigned to O and the first feature of Pt atoms. The peaks at  $2.6 \text{ \AA}$  can be

assigned to the second feature of Pt.

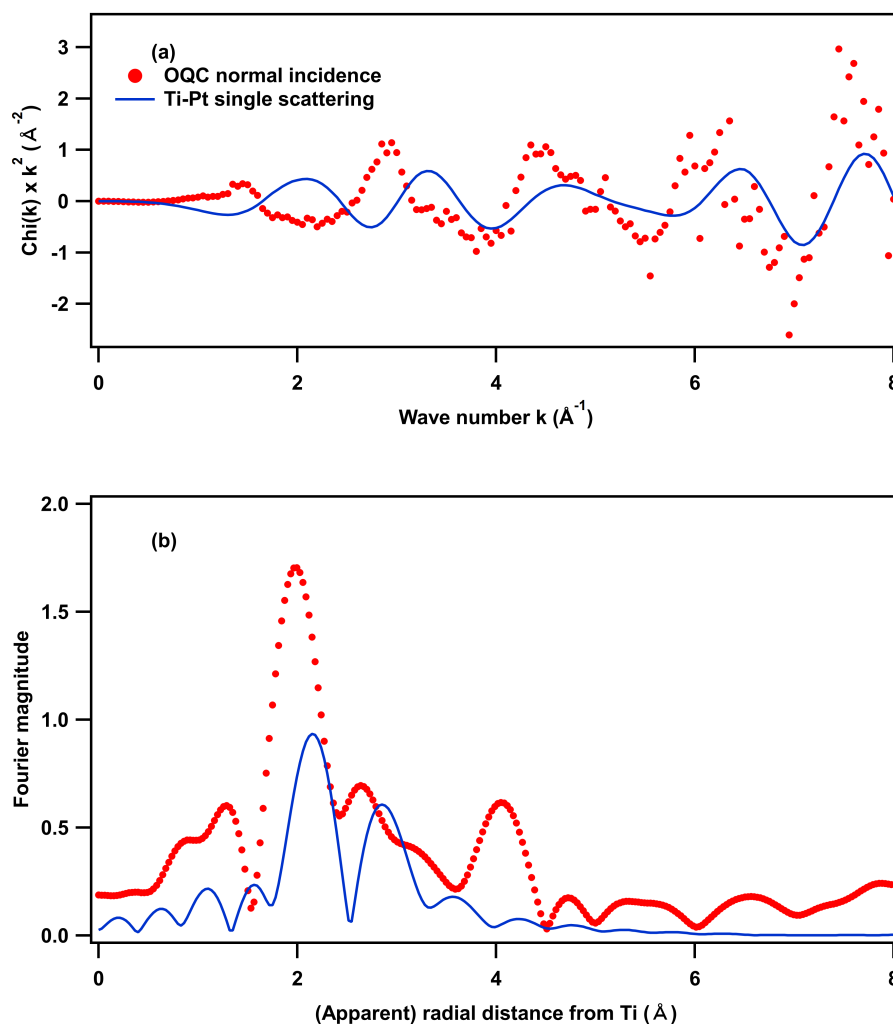


Figure 5.18: (a)  $k^2$  weighted modulation function of 1 ML BTO in the reduced (OQC) state at the Ti  $K$ -edge in normal incidence and the modulation function of a single scattering process from a Pt atom at a distance of 2.7  $\text{\AA}$  (a) and (b) the corresponding Fourier transformations.

### Single scattering model with two neighbors

The experimental spectra of the reduced sample in normal and grazing incidences contain two strong features at 2 and 2.6 eV, which fit to an O at 2.6  $\text{\AA}$  and Pt at 2.7  $\text{\AA}$ . As the first step of the structure analysis, the region of 1.54 to 2.94  $\text{\AA}$  in  $R$ -space has been analyzed, by employing the range of 0.4 to 8  $\text{\AA}^{-1}$  in  $k$ -space for the Fourier transformation by using DEMETER for fitting. For windowing in this work, a Hanning function has been selected, since it did not lead to any artifacts. The analysis has only been done in normal incidence and by using a model composed of an O and a Pt in the same line as Ti. In addition, only single scattering processes have been considered. As discussed in Sec. 3.5.2, the edge position is quite important for an EXAFS analysis and needs to be included as fit parameter, whereby shifts should be less than  $\pm 10$  eV. Initially, the edge position

was set at 4983.85 eV and initial distances of O and Pt at 2.6 and 2.7 Å. The edge energy shift was varied from  $-10$  to  $+10$  eV and the resulting final distances and the  $R$ -factors have been reported in Fig. 5.19. This analysis yielded a second reasonable distance for Pt at 2.3 Å. Therefore, the analysis has been repeated with the same initial distance of O but with a Ti-Pt distance of 2.3 Å. The results of the analysis are presented in Fig. 5.19.

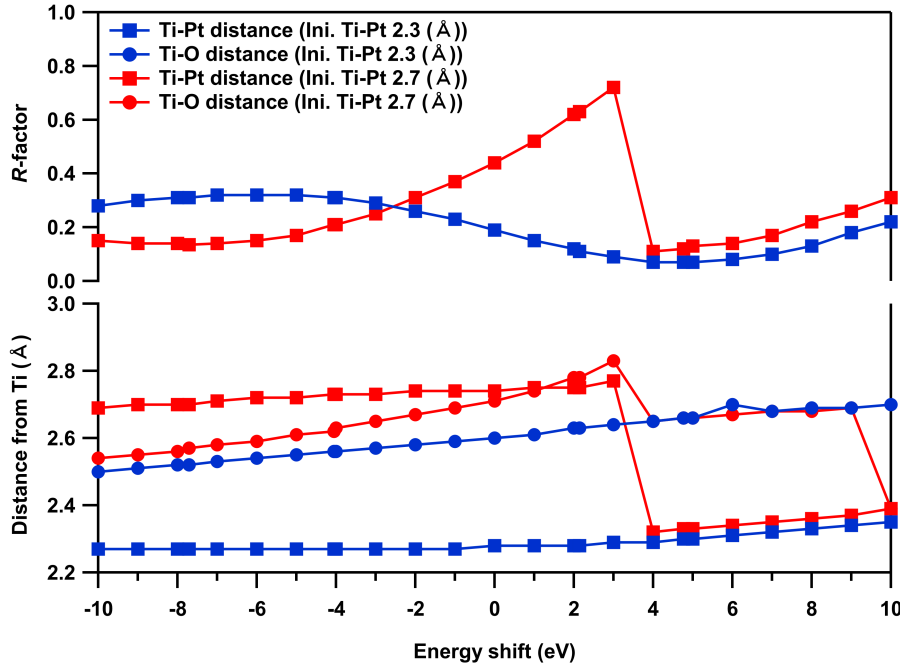


Figure 5.19: Results of fitting in a system composed of a Ti atom as the emitter and an O atom and a Pt atom as scatterers with the initial distances from Ti as 2.6 and 2.3 Å (colored as blue) and 2.6 and 2.7 Å (colored as red). Only single scattering processes have been considered. The Top:  $R$ -factor as a function of the shifts in the edge energy. Bottom: Calculated distances of O and Pt from Ti with the above mentioned initial values.

For the model with the initial value of 2.3 Å as the Ti-Pt distance, the best fit has an  $R$ -factor of 0.07, an energy shift of  $+4$  eV, a Ti-O distance of 2.65 Å and a Ti-Pt distance of 2.29 Å. For the model with an initial value of 2.7 Å as Ti-Pt distance, two energy shifts lead to the best fittings:  $+4$  eV leads to an  $R$ -factor of 0.11 and distances of 2.32 and 2.65 Å for Pt and O. A comparable  $R$ -factor (0.135) is gained by an energy shift of  $-7.71$  eV. This energy shift leads to distances of 2.7 and 2.57 Å for Pt and O. On the basis of these results, the main component in the radial distribution function in the radius range of 1.54 to 2.94 Å can be explained by O and Pt atoms at distances of 2.57 and 2.65 Å and at distances of 2.3 and 2.7 Å.

### Single scattering model with four and six neighbors

After determining the distances of the nearest neighbors, the experimental data need to be analyzed simultaneously in the longer range of the radial distribution function, for normal and grazing angles of incidence. The directional anisotropy in the experimental data was negligible. Therefore, a



simple model is to position scattering atoms in such a way that no directional anisotropy results. The analysis of Sec. 5.2.4 has shown that the experimental data indicate Pt at two distances (2.3 and 2.7 Å) and O at 2.57 Å. The small peak at 1.3 Å in the radial distribution function in normal incidence also implies the presence of an atom at a short distance. A reasonable solution is an O at 1.7 Å. However, the Fourier magnitude of this component is quite small, which implies a small coordination number for it. Based on these constraints, a model with two Pt atoms and two O atoms is developed, as presented in Fig. 5.20 (a).

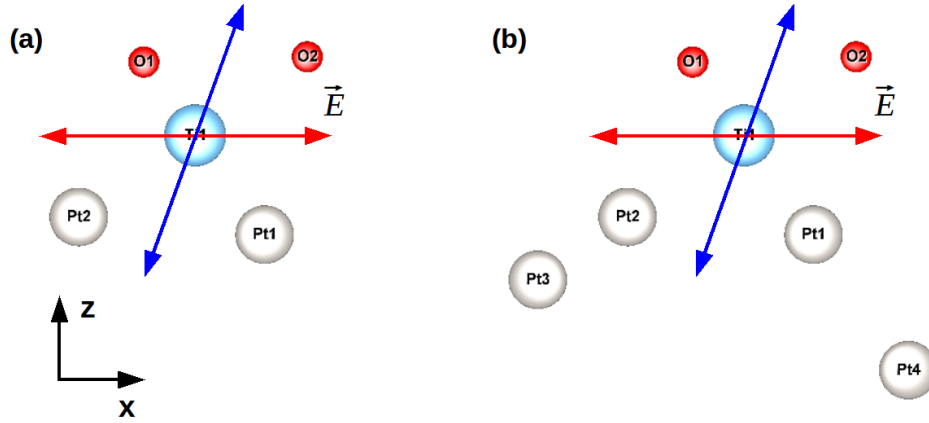


Figure 5.20: The side view of the models with four (a) and six (b) scattering atoms around a Ti atom as the emitter. The electric fields of the incoming beams are shown in red for normal incidence (along  $x$  axis) and blue for grazing incidence ( $70^\circ$  from  $x$  axis).

Optimizing the distances of this model yields an  $R$ -factor of 0.05 together with a shift of the edge energy of  $-6.2$  eV. For the analysis only single scatterings have been considered. The same atoms have been set to have the same mean square relative displacement,  $\sigma^2$ , regardless of their coordination shell:  $\sigma_{Ti-O}^2 = 0.0007 \text{ \AA}^{-2}$  and  $\sigma_{Ti-Pt}^2 = 0.00066 \text{ \AA}^{-2}$ . The resulting Ti-Pt distances are  $2.26 \pm 0.03 \text{ \AA}$  and  $2.72 \pm 0.02 \text{ \AA}$ . The first Ti-O distance is  $2.54 \pm 0.02 \text{ \AA}$  and there is another oxygen at  $1.76 \pm 0.04 \text{ \AA}$ . The fit was performed in a region of 1.1 to 3.6 Å in  $R$ -space. The sensitivity range of EXAFS is 5 Å and therefore, the fitting range can be extended.

To increase the fitting range in  $R$ -space, different atoms have been added to the model in a trial and error method. Best results have been gained by adding two Pt atoms at 4.8, 5.4 Å, still within the sensitivity range of EXAFS and leads to the fitting range of 1.18 to 4.8 Å in the radial distribution function. The results of the fitting are given in Tab. 5.5. For the analysis only single scatterings have been considered. Like in the previous case, the same atoms have been set to have the same mean square relative displacement,  $\sigma^2$ , regardless of their coordination shell:  $\sigma_{Ti-O}^2 = 0.0007 \text{ \AA}^{-2}$  and  $\sigma_{Ti-Pt}^2 = 0.00066 \text{ \AA}^{-2}$ . There are small peaks above 4.8 Å in the radial distribution function. However, explaining them is beyond the sensitivity of EXAFS. Figure 5.20 (b) shows the model with six scattering atoms. The calculated modulation functions and radial distribution functions in normal and grazing incidences are presented in Fig. 5.21 and 5.22, where distances of the atoms are shown by bars. It needs to be mentioned that the corresponding bar to the O at 1.75 Å is not exactly at the peak position. That is due to the superposition of the peak of O

Table 5.5: The results of FEFF6 calculations of the model presented in Fig. 5.20 (b). The distances are given in Å and the shift in the edge position,  $\Delta E$  in eV.  $cn$  stands for the coordination number of each atom.

|      | O <sub>1</sub>     | O <sub>2</sub>     | Pt <sub>1</sub>    | Pt <sub>2</sub>    | Pt <sub>3</sub>    | Pt <sub>4</sub>    | $\Delta E$        | $R$ -factor |
|------|--------------------|--------------------|--------------------|--------------------|--------------------|--------------------|-------------------|-------------|
| OQC  | 1.75<br>$\pm 0.04$ | 2.55<br>$\pm 0.02$ | 2.24<br>$\pm 0.02$ | 2.73<br>$\pm 0.01$ | 4.80<br>$\pm 0.02$ | 5.41<br>$\pm 0.03$ | -5.5<br>$\pm 0.6$ | 0.07        |
| $cn$ | 0.5                | 1.35               | 0.91               | 1.43               | 4.8                | 16.82              | -                 | -           |

at 1.75 Å and the tails of other peaks at higher distances, which slightly shifts the apparent peak position.

For the analysis, each atom has been set to have the same coordination number ( $cn$ ) in calculations for normal and grazing incidences, with the exception of O<sub>1</sub> in normal (set as 0.5) and grazing (set as 0.28) incidences. This is due to slightly higher intensity of this component in the radial distribution function in normal incidence. The coordinations numbers of the atoms in calculations in the model with four single scattering atoms have been set to the same values as in six single scattering case, presented in Tab. 5.5.

$S_0^2$  in Eq. 3.16 depends on the angle of incidence of the photons. Since the directional anisotropy of the experimental data is negligible, the losses of EXAFS signal due to shake-up and shake-off processes and therefore, the  $S_0^2$  factor has been considered the same for both measurements. The reasonable range for  $S_0^2$  is between 0.7 to 1 [80]. In the model with four and six single scattering atoms,  $S_0^2$  factors have been calculated as  $1.06 \pm 0.06$ .

The calculations take into account only single scatterings, which indicates the present neighboring atoms in the experiment with their corresponding distance. It needs to be mentioned that the presented coordination numbers have been used to do the fit and should not taken as the absolute final values. The comparison between the number of two O atoms indicate that the majority of O atoms within the sample have a long distance of 2.55 Å. In addition, the further away Pt atoms have larger coordination numbers (4.8 and 16.82). This is expected, since increasing the distance from Ti atom makes more Pt atoms from the substrate available for backscattering processes.

According to the stoichiometry determination in 5.2.3, the amount of Ba atoms is smaller than the that of Ti atoms. Furthermore, in the Kepler-approximant, Ti-Ba distance is 3.37 Å [44]. Therefore, in the OQC system, Ba is also expected to be found at a distance of 3 to 4 Å from Ti. However, there are many more Pt atoms in this radial range. They are strong scatterers and due to their large number, make strong contributions. Therefore, the contribution of one Ba is difficult to be extracted. As a result, the model can explain the experimental data without Ba.

## The cluster model

The model of six scattering atoms presents the radial distribution of neighboring atoms. However, the actual situation is more complicated. Multiple scattering processes are important, specially in high frequency range. Furthermore, a realistic model needs to be proposed, in which the Ti atom is on top of a Pt(111) surface.

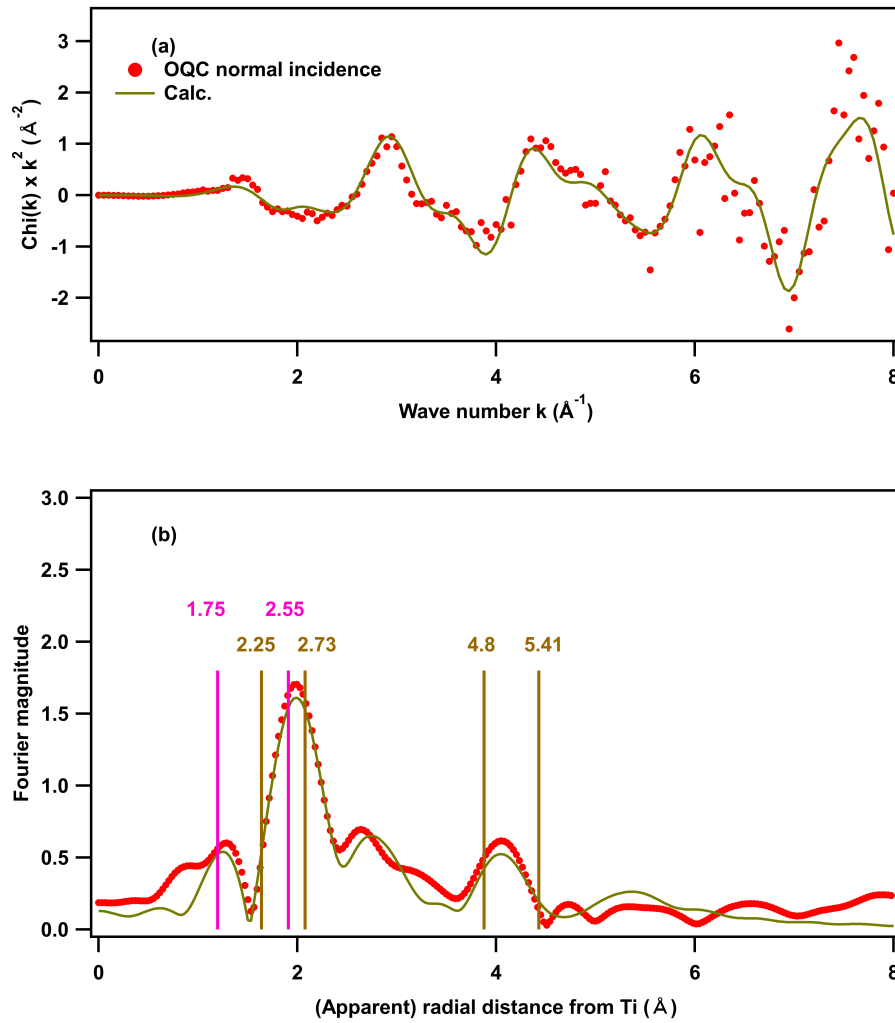


Figure 5.21: (a)  $k^2$  weighted modulation function of 1 ML BTO at the Ti  $K$ -edge in the reduced state (OQC) and results of FEFF structural analysis of the model in Fig. 5.20 (b) in normal incidence and (b) the Fourier transforms. The pink bars correspond to O atoms, the light brown bars to Pt atoms.

To construct a realistic model, modulation functions have been calculated for Ti in a grid of sites on a Pt(111) surface and compared to the experimental modulation function in grazing incidence, since it is more sensitive to scattering at Pt atoms. The grid of sites was selected with step size of  $0.4 \text{\AA}$ . The height of Ti above the Pt surface was chosen in such a way that Ti be always at a distance of  $2.7 \text{\AA}$  from the closest Pt atom. It has been found that two cases lead to the best agreement with the grazing incidence signal: close to fcc and close to hcp three-fold hollow (3-FH) sites. The close to 3FH hcp site leads to forward focusing of the electron wave backscattered from Pt atoms in the second layer by the ones in the first layer. This forward focusing effect made the fitting a bit worse in the final steps of the analysis. Therefore, only the close to fcc 3-FH site has been considered for further analysis.

Due to the aperiodic nature of the OQC system, Ti atoms occupy different sites above the Pt surface. However, the detailed discussions and analysis of all possible sites of Ti above the Pt surface, which are given later, show that averaging the BTO layer in the presented cluster here

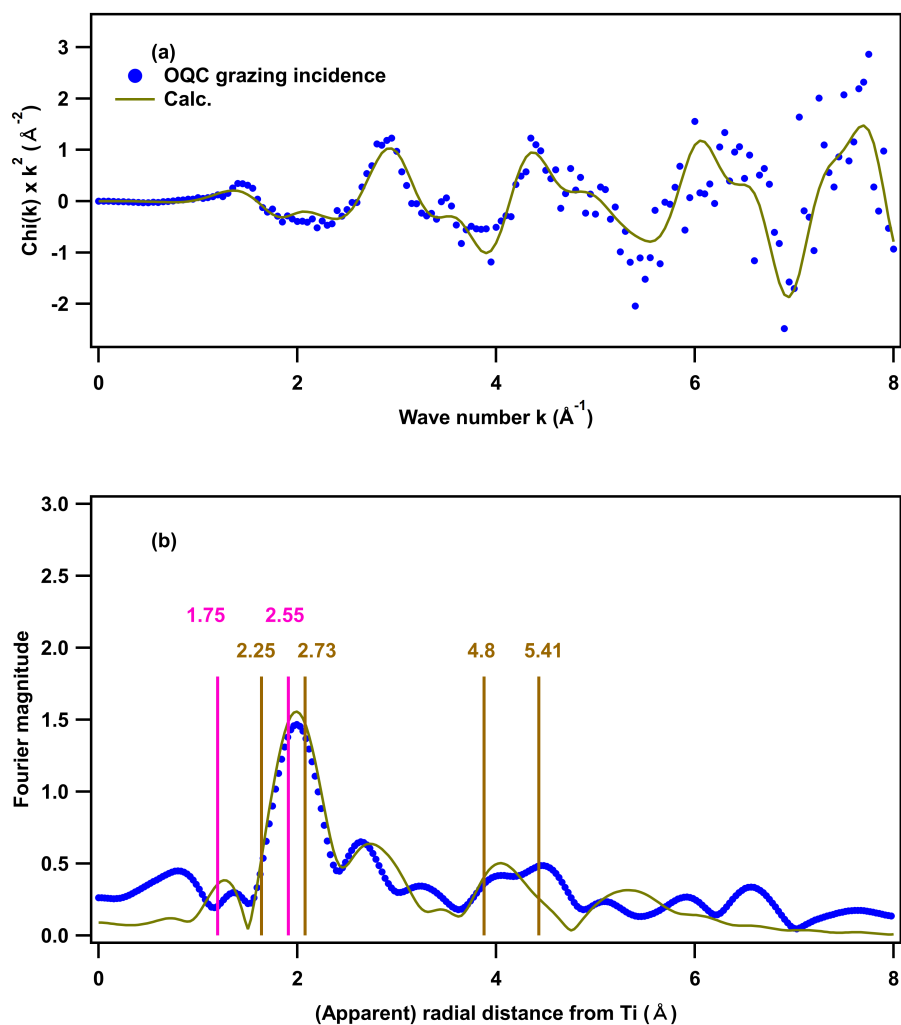


Figure 5.22: (a)  $k^2$  weighted modulation function of 1 ML BTO at the Ti  $K$ -edge in the reduced state (OQC) and results of FEFF structural analysis of the model in Fig. 5.20 (b) in grazing incidence and (b) the Fourier transforms. The pink bars correspond to O atoms, the light brown bars to Pt atoms.

over all sites explains the experimental data in grazing incidence quite well. In addition, it is shown that the selected site in the cluster can describe the experiment for both angles of incidence, unexpectedly well.

Figures 5.23 and 5.24 present the experimental and calculated modulation functions at the Ti  $K$ -edge in grazing and normal incidence. In this model, a Ti atom was put at 2.28  $\text{\AA}$  above the Pt surface at close to a fcc 3-FH site with a distance of 2.69  $\text{\AA}$  to the closest Pt. In the calculations, all single and multiple scattering paths have been included. The maximum path length has been set to  $2 \times 5.8 \text{\AA}$ . As is obvious from the figures, the results of the FEFF calculations describe the experiment extremely well in grazing incidence. The region between 1.5 to 2.4  $\text{\AA}$  can be described by oxygen atoms at 2.55  $\text{\AA}$ , which is not at the same height as the Ti atom. The peak at 4.41  $\text{\AA}$  corresponds to Pt at 5.41  $\text{\AA}$ , which is at the sensitivity limit of EXAFS. This peak cannot completely be described by Pt. Since it is present only in grazing incidence, no assignment of the peaks except to Pt at 5.41  $\text{\AA}$  is reasonable and cannot be described by this model. The peak also cannot be

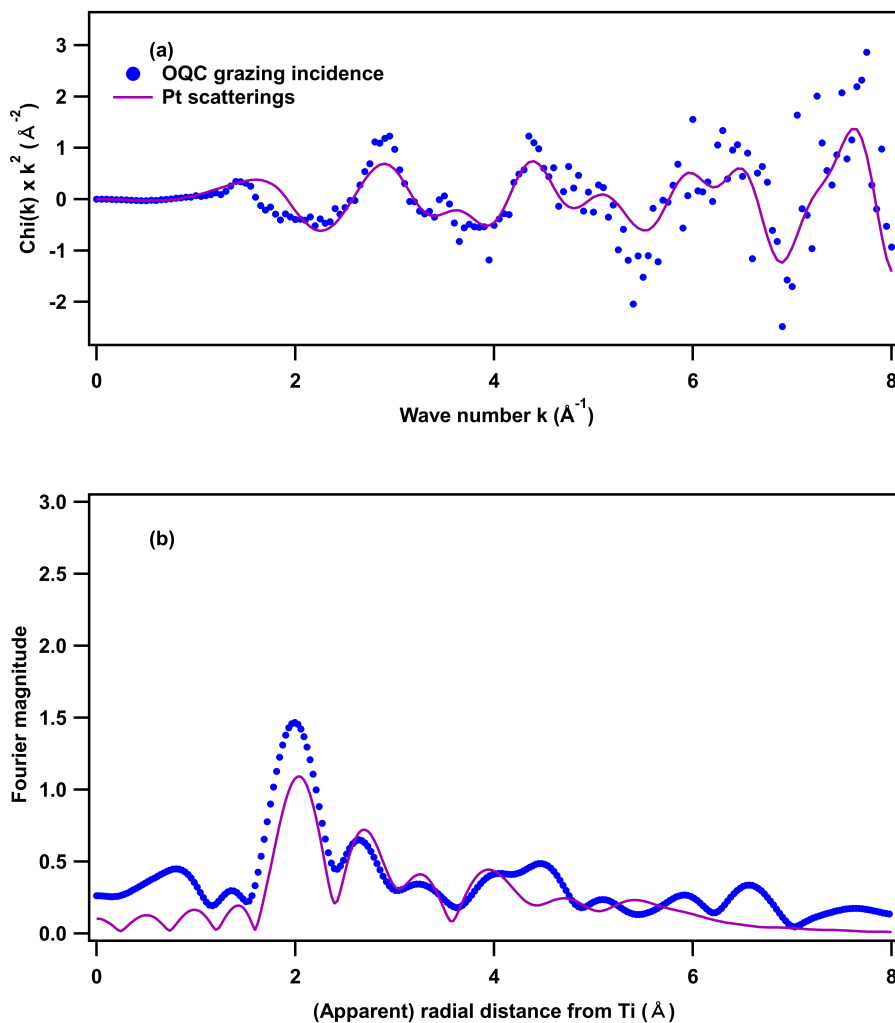


Figure 5.23: The modulation function (a) and the Fourier transform (b) of 1ML BTO in the reduced state (OQC) at the Ti  $K$ -edge and the calculations resulting from all single and multiple scattering processes in a model composed of one Ti atom  $2.28 \text{\AA}$  above the Pt surface at close to fcc 3-FH site, in  $70^\circ$  incidence angle.

described better by a model with Ti at close to hcp 3-FH site. It probably originates from the occupation of other sites of the Pt surface by Ti atoms.

Figure 5.24 presents the calculated results for the same system as in Fig. 5.23, but in normal incidence. As expected, the contribution of Pt is not as large in normal incidence. However, the main peak at  $4.05 \text{\AA}$  is described by Pt atoms. As discussed, the peaks at  $1.3$  and  $2 \text{\AA}$  can be assigned to O atoms at  $1.75$  and  $2.55 \text{\AA}$  at the same height as Ti above the Pt surface. Therefore, there are in-plane and out-of-plane O atoms at  $2.55 \text{\AA}$ , while the O atoms at  $1.75 \text{\AA}$  are only in-plane. Furthermore, the peak at  $2.65 \text{\AA}$  cannot completely be explained by Pt in normal incidence. It can be assigned to an in-plane Ba at  $3.15 \text{\AA}$ .

Based on these findings, a new model is constructed, which is presented in Fig. 5.25 (a). Similar to the Kepler-approximant, Ti has three neighboring O atoms: two in-plane at  $1.7$  and  $2.5 \text{\AA}$  and one out-of-plane at  $2.5 \text{\AA}$ . In addition, there is an in-plane Ba at  $3.15 \text{\AA}$ , which is slightly shorter than

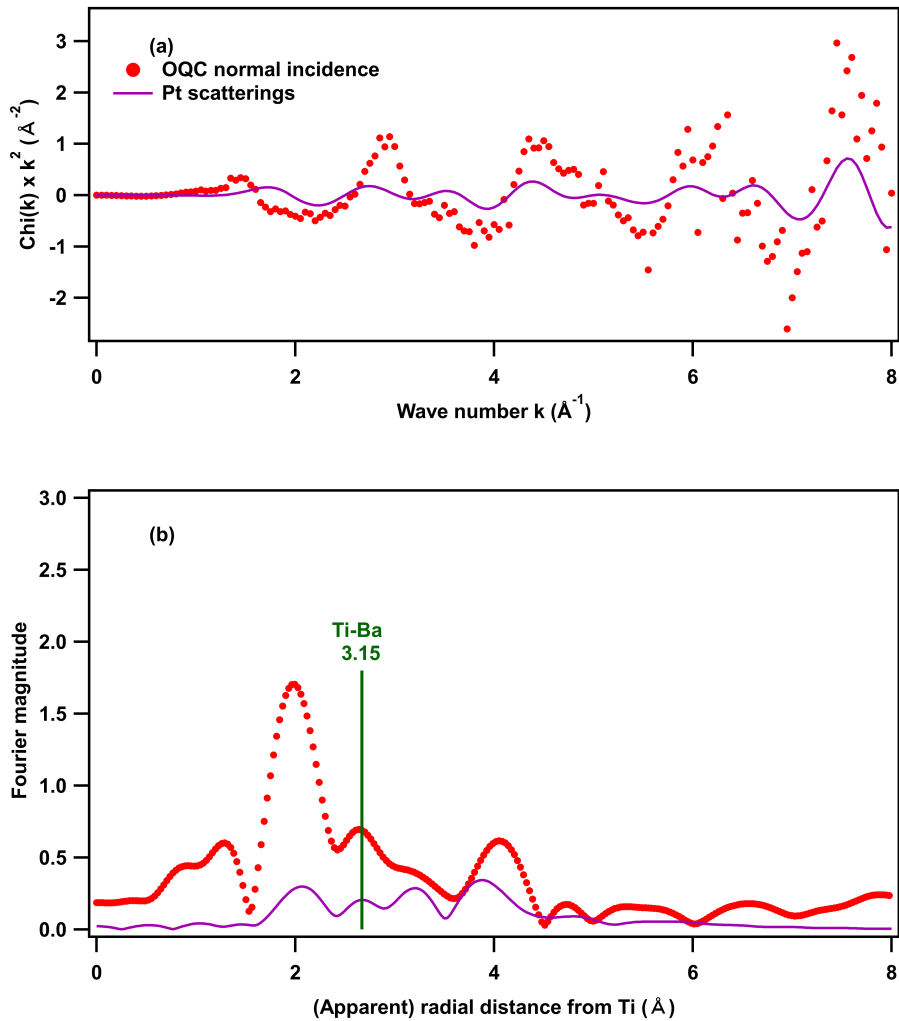


Figure 5.24: The modulation function (a) and the Fourier transform (b) of 1ML BTO in the reduced state (OQC) at the Ti  $K$ -edge and the calculations resulting from all single and multiple scattering processes in a model composed of Ti atom  $2.28 \text{\AA}$  above the Pt surface at close to fcc 3-FH site, in normal incidence angle. A presumable distance of a Ba atom at  $3.15 \text{\AA}$  is illustrated as a green bar.

the Ti-Ba distance in the Kepler-approximant ( $3.37 \text{\AA}$ ). As shown in Fig. 2.5, BTO-derived OQC has a 12-fold diffractional symmetry, indicating 12 orientations of the BTO layer. In quasicrystals with the Niizeki-Gähler tiling pattern (Fig. 2.4), the combinations of building blocks can be found in 12 orientations and the probability of all orientations are assumed here to be equal. Although the deviations from this assumption and whether that leads to any noticeable effects in EXAFS needs to be investigated.

The orientation of the BTO layer in each of the 12 domains may be different. As discussed in Sec. 9.4 of [56], the azimuthal angular dependence vanishes for systems with 3-fold and higher rotational symmetries. The 12 orientations of squares, triangles and rhombs in STM implies that any structural element needs to be present in 12 orientations. For EXAFS this means that no azimuthal anisotropy can be observed. To reduce the effort in calculations only two orientations

rotated by  $90^\circ$  need to be taken into account. Therefore, performing FEFF analysis on the two presented clusters in Fig. 5.25 (a,b) is enough to include all possible orientations of the BTO layer in OQCs. Indeed, making the assumption of equal probability of all 12 orientations, makes it technically easy to solve the structure. Using the LEED pattern of Fig. 5.6, the azimuthal orientation of the Pt surface has been selected as in Fig. 5.25 (a), with the polarization of the X-rays horizontally aligned.

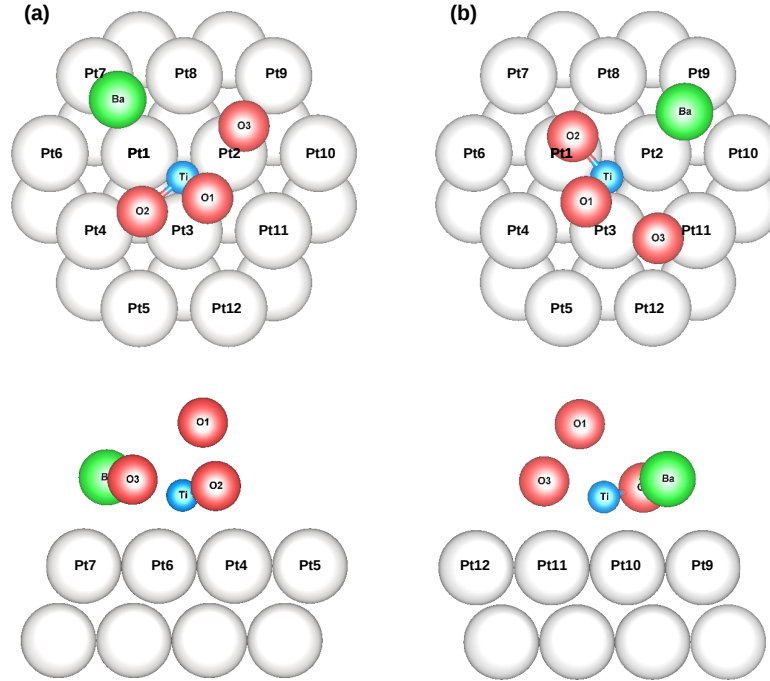


Figure 5.25: Top and side view of the cluster model for BTO-derived OQC. Due to the possibility of presence of different orientations of Ba and O atoms around Ti, two orientations have been considered (a,b), rotated by  $90^\circ$ .

FEFF6 calculations [87] have been performed on the presented models in Fig. 5.25 in normal and grazing angles of incidence to calculate modulation functions for the scattering paths. The parameter optimization has been done using DEMETER [86], simultaneously on normal and grazing experimental data. The maximum path length has been set to  $2 \times 5.8 \text{ \AA}$ , covering a radius of  $5.8 \text{ \AA}$  from Ti. The  $k$  range of the Fourier transformation has been selected as  $0.4 \leq k \leq 8 \text{ \AA}^{-1}$  and the fitting has been performed in  $R$ -space with a range of  $1.1 \leq k \leq 5 \text{ \AA}$ . The selected range in  $R$  covers all pronounced features in the radial distribution function within the sensitivity range of EXAFS. The numbers of independent points and variables in the fit were 37.16 and 8, respectively. The fit results are presented in Fig. 5.26 and 5.27 and Tab. 5.6.

$S_0^2$  in Eq. 3.16 is a damping factor, originating from intrinsic losses of the signal, due to shake-up and shake-off processes, which in principle depend on the angle of incidence of the photons. Since the directional anisotropy of the experimental data is negligible, the losses of EXAFS signal due to shake-up and shake-off processes and therefore,  $S_0^2$  factor have been considered the same for both measurements. The reasonable range for  $S_0^2$  is between 0.7 to 1 [80]. For the presented model, two orientations of BTO layer have been taken into account, which leads to the reasonable range of 0.35

Table 5.6: The results of FEFF6 calculations on the cluster for BTO-derived OQC (Fig. 5.25), with distances of atoms from Ti in Å and the shift in the edge position,  $\Delta E$  in eV.  $x$  and  $y$  positions of Ti are referred to Pt<sub>1</sub>, while  $z$  (in Å) is referred to Pt<sub>4</sub>, since Pt<sub>1,2,3</sub> can have a relaxation of  $\Delta z_{Pt}$ .  $n_{O_3}$  refers to the number of O<sub>3</sub> atoms. The corresponding distance of the Kepler-approximant, derived from surface X-ray diffraction and density functional theory calculations are included for comparison [44].

|             | $d_{O_{1,3}}$      | $n_{O_3}$      | $d_{O_2}$         | $d_{Ba}$           | $d_{Pt_1}$         | $z_{Ti}$ | $\Delta z_{Pt}$    | $\Delta E$        | R-factor |
|-------------|--------------------|----------------|-------------------|--------------------|--------------------|----------|--------------------|-------------------|----------|
| OQC         | 2.56<br>$\pm 0.02$ | 3<br>$\pm 0.8$ | 1.71<br>$\pm 0.1$ | 3.15<br>$\pm 0.08$ | 2.69<br>$\pm 0.02$ | 2.28     | 0.08<br>$\pm 0.05$ | -5.6<br>$\pm 0.8$ | 0.14     |
| Kepler-app. | -                  | -              | 1.72              | 3.37               | 2.62               | 2.54     | 0.1                | -                 | -        |

to 0.5 for  $S_0^2$ , while through the fit, it has been determined as  $0.41 \pm 0.06$ .

The optimized distances of 8 atoms have been specified by bars in Fig. 5.26. In case of Pt atoms, there are too many distances corresponding to all Pt atoms in the cluster. Hence, the cluster have been divided into different groups of atoms according to their distances from Ti. Only one Pt distance in each of these groups has been specified in the figure, which has the most pronounced contribution to the calculations. Since the arrangement of the atoms in the cluster has been done also according to the results of the model with six scatterers (Fig. 5.20), the optimized distances are quite similar in both cases (Fig. 5.21). The largest difference with the six single scatterings model is a Pt atom at  $5.63 \text{ \AA}$  ( $+0.22 \text{ \AA}$ ).

The same type of atoms have been set to have the same values of the mean square relative displacement ( $\sigma^2$ ). Optimizing them leads to negative values for  $\sigma^2$  of Ti-O and Ti-Pt paths and an order of magnitude larger value for  $\sigma_{Ti-Ba}^2$ . Setting them to reported values ( $\sigma_{Ti-O}^2 = 0.007 \text{ \AA}^{-2}$ ,  $\sigma_{Ti-Ba}^2 = 0.0075 \text{ \AA}^{-2}$  [108, 119],  $\sigma_{Pt-Pt}^2 = 0.0053 \text{ \AA}^{-2}$  [155]) leads to a high  $R$ -factor. Hence, they have been set to small values but within reasonable limits:  $\sigma_{Ti-O}^2 = 0.0007 \text{ \AA}^{-2}$ ,  $\sigma_{Ti-Ba}^2 = 0.0098 \text{ \AA}^{-2}$ ,  $\sigma_{Ti-Pt}^2 = 0.00066 \text{ \AA}^{-2}$ . Therefore, these values do not represent actual mean square relative displacements of the atoms but compensate so far unknown deficiencies of the model.

The coordination numbers of O<sub>2</sub> and O<sub>1</sub> have been set to 0.23 and 0.38, else their errors are as large as their values. The coordination numbers of O<sub>3</sub> has been determined through the fit. The distances of O<sub>1</sub> and O<sub>3</sub> have been coupled to be the same, due to the negligible directional anisotropy in the data. The coordination numbers of all other atoms have been set to 1. Pt atoms have the bulk structure in (111) direction, with the exception of Pt<sub>1,2,3</sub>, which are allowed to relax in  $z$  direction.  $x$  and  $y$  positions of Ti are set at  $1.35 \text{ \AA}$  and at  $-0.75 \text{ \AA}$ , referred to Pt<sub>1</sub>. The Ti-Pt<sub>1</sub> distance is a fit parameter, from which the  $z$  position of Ti above the Pt surface derives. Because of the relaxations of Pt<sub>1,2,3</sub>, Pt<sub>4</sub> serves as a reference for the Pt surface. Distances of Ti to all other Pt atoms are then determined assuming a bulk structure for Pt(111) surface with a unit cell of  $2.775 \text{ \AA}$  [20].

The results indicate that the assumption of the bulk structure for Pt(111) surface is reasonable and gives two additional Pt groups (at  $3.93$  and  $4.77 \text{ \AA}$ ), which are not present in the six single scatterings model of Fig. 5.20 (b). In addition, the agreement between the cluster model and the



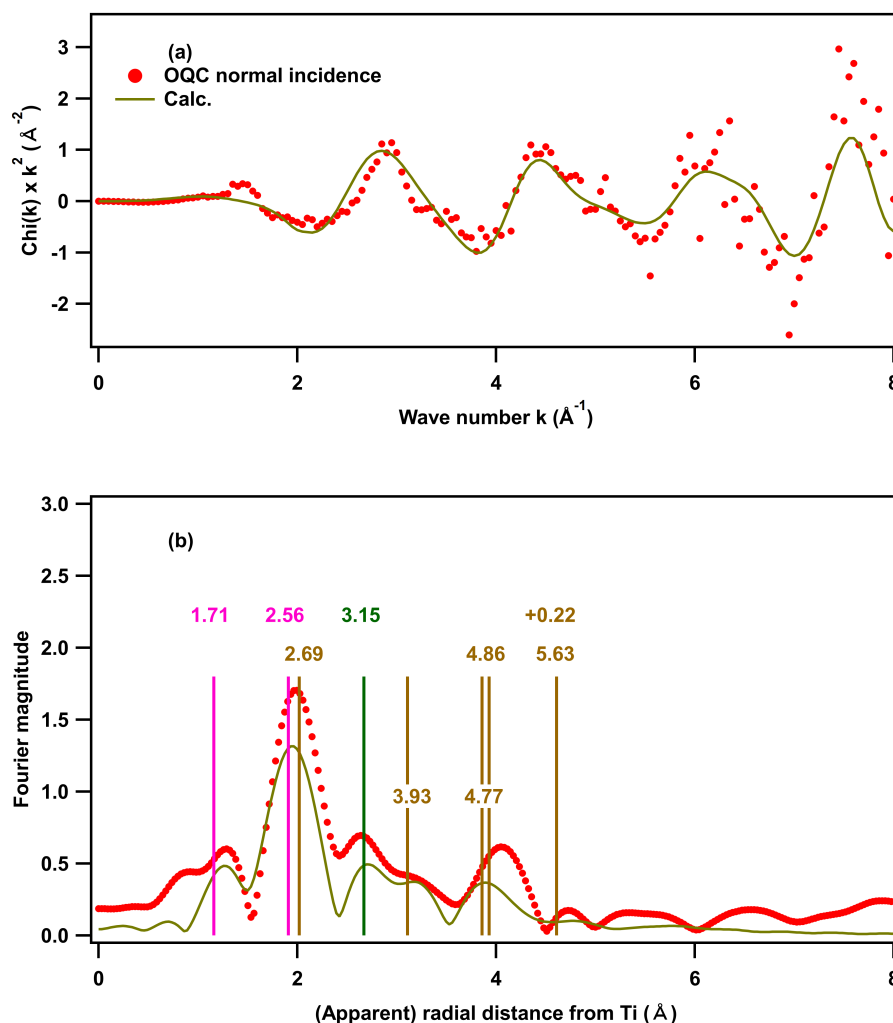


Figure 5.26: The modulation function (a) and the Fourier transform (b) of 1 ML BTO in the reduced state (OQC) at the Ti  $K$ -edge and FEFF calculations on the cluster model (Fig. 5.25) after optimization of distances of a model with six scatterers (Fig. 5.22) in normal incidence. The bars correspond to distances of atoms from Ti: pink (O), light brown (Pt) and green (Ba).

experiment is excellent. The distances of the first O and Pt neighbors agree to the distances of the Kepler-approximant, whereas the agreement in Ti-Ba distance is not as good [44].

The coordination number of  $\text{O}_3$  is  $3.0 \pm 0.80$ . Taking into account that the two domains and the effect of the polarization give an effective coordination number of 1.5 in each domain, this is exactly the value, when three O atoms are arranged in a symmetric triangle, with linear polarization.

In the presented model,  $\text{O}_1$  is found at a distance of  $2.56 \text{\AA}$  in  $70^\circ$  grazing angle above the Ti, which is not chemically realistic. However, the occupation number is small and with a large error ( $0.4 \pm 0.4$ ). This suggests that the origin of this O is adsorbed water or some contamination. Another model suggests embedding of  $\text{O}_1$  into the defects of the Pt substrate, as shown in Fig. 5.28, which will be discussed later.

The significance of the out-of-plane  $\text{O}_1$  was checked by performing a fit without it. The fit resulted in the same agreement with an  $R$ -factor of 0.14 and the same structural parameters. The

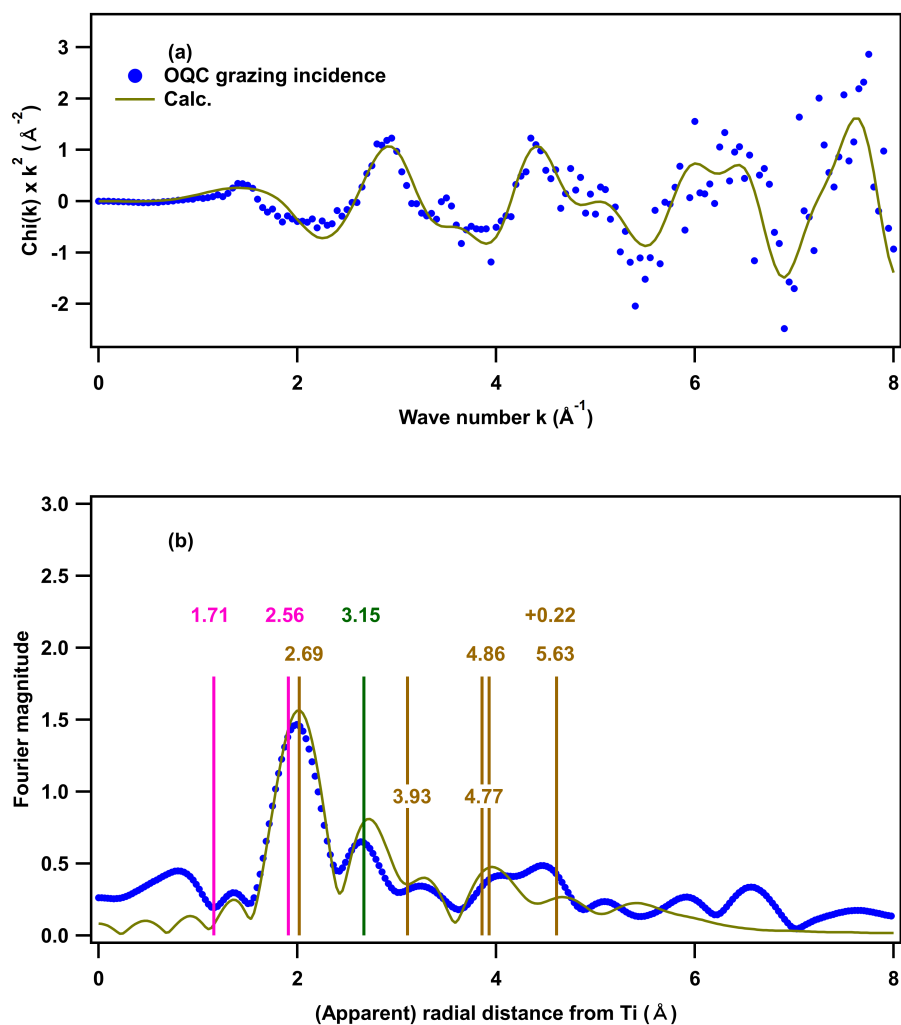


Figure 5.27: The modulation function (a) and the Fourier transform (b) of 1 ML BTO in the reduced state (OQC) at the Ti  $K$ -edge and FEFF calculations on the cluster model (Fig. 5.25) after optimization of distances of a model with six scatterers (Fig. 5.22) in grazing incidence. The bars correspond to distances of atoms from Ti: pink (O), light brown (Pt) and green (Ba).

coordination number of the short distance  $O_2$  was found as  $0.2 \pm 0.2$ . This indicates that small part (less than 10%) of the three O atoms around the Ti is at the short distance with  $1.71 \text{\AA}$ .

The six single scattering model (Sec. 5.2.4) predicts the presence of a Pt atom at a distance of  $2.24 \text{\AA}$ , which has not been found by the cluster model. The short bond length of this Pt atom suggests that there is an ambiguity in the results of the six single scatterings model. This ambiguity originates from the available energy range of the measurement and is an inherent problem of the analysis of BTO-derived OQC by EXAFS. In the light of this, the finding of a STO derived OQC is very promising [42], where a long energy range is available at the Ti  $K$ -edge.

Except squares and triangles, rhombs are also present in the building blocks of BTO-derived OQC with a Ti-Ti bond length of  $3.55 \text{\AA}$ . The number of this bond is 2 out of a total of 40 (Fig. 2.5 (a)). This suggests presence of the short bond length O at  $1.71 \text{\AA}$  at the connecting line of Ti atoms at the rhombs only. This idea was investigated by FEFF6 analysis on clusters derived from

those in Fig. 5.25. A Ti atom was added so that O<sub>2</sub> is between two Ti atoms, with Ti-Ti and Ti-O<sub>2</sub> bond lengths of 3.55 and 1.78 Å. The occupation numbers of this additional Ti and O<sub>2</sub> have been set to 0.05. For the analysis,  $\sigma_{Ti}^2$  was set to 0.0008 Å<sup>-2</sup> and the calculations were performed in the same way as for the cluster model of Fig. 5.25.

The result of the calculations is that the experimental data are not sensitive to the presence of Ti atoms in the rhombs. This result is in line with the large number of Pt atoms at similar distances, which completely hide the presence of the rare Ti atoms from rhombs. Furthermore, the short distance O may also originate from bulk-like BTO in islands, which may rarely be present in the sample.

Finally, it needs to be mentioned that later versions of the FEFF codes are available, with improvements for the systems with the *f*-shell electrons [156]. Hence, calculations were performed with the Pt atoms of Fig. 5.25 with FEFF6 and FEFF8-lite. As expected, there were no relevant differences between their results. Therefore, FEFF6 which is included in DEMETER software package is accurate enough for the calculations of this work.

### Cluster model with defects

The cluster model in Fig. 5.25 shows reasonable agreement with the experiment. This model indicates the presence of O atoms at a distance of 2.56 Å at an angle of 70° from the surface plane of Ti. O atoms in the presented model were above the Ti atom. Alternatively, the oxygen is embedded in a defect of the Pt substrate. Bonds between O and Pt atoms gives a valid explanation for the long Ti-O distance. Such a model is presented in Fig. 5.28.

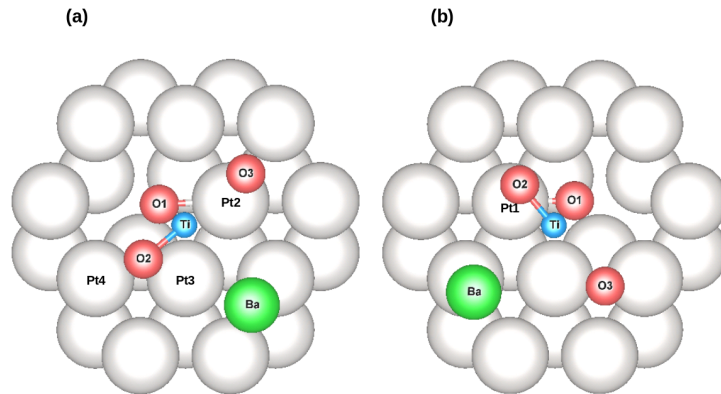


Figure 5.28: Top view of the cluster model for BTO-derived OQC with defects. Due to the possible presence of different orientations of Ba and O atoms around Ti, two orientations have been considered (a,b), rotated by 90°.

Similar to the cluster model in Fig. 5.25, the model with defect is also composed of two orientations of O and Ba atoms, rotated by 90°. The analysis is done with both orientations, simultaneously in normal and grazing incidences. All of the analysis details are the same as in the cluster model, including the Fourier transformation range in *k*-space and the fitting range in *R*-space. There were 9 variables in the fit and the number of the independent points was 37.16. The error of the coordination number of O<sub>2</sub> was not reasonable. Therefore, *no<sub>2</sub>* was set to 0.18. The resulting curves of

Table 5.7: The results of FEFF6 calculations on the cluster model in Fig. 5.28 ( $R$ -factor: 0.18). The distances are given in Å, the shift in the edge position,  $\Delta E$ , in eV.  $x$  and  $y$  positions of Ti are referred to Pt<sub>1</sub> and have been set to 1.35 and  $-0.75$  Å, while  $z$  of Ti and  $\Delta z_{Pt}$  of Pt<sub>1,2,3</sub> are referred to Pt<sub>4</sub>. The coordination number of O<sub>1,3</sub> are determined through the fit.

|     | $d_{O_{1,3}}$ | $d_{O_2}$  | $n_{O_1}$ | $n_{O_3}$ | $d_{Ba}$   | $d_{Pt_1}$ | $z_{Ti}$ | $\Delta z_{Pt}$ | $\Delta E$ | $S_0^2$   |
|-----|---------------|------------|-----------|-----------|------------|------------|----------|-----------------|------------|-----------|
| OQC | 2.57          | 1.73       | 0.5       | 2.7       | 3.18       | 2.69       | 2.31     | 0.1             | -3.7       | 0.5       |
|     | $\pm 0.02$    | $\pm 0.13$ | $\pm 0.4$ | $\pm 0.7$ | $\pm 0.08$ | $\pm 0.03$ |          | $\pm 0.06$      | $\pm 0.9$  | $\pm 0.1$ |

the calculations in normal and grazing incidence are given in Fig. 5.29, 5.30, respectively and the resulting values in Tab. 5.7.

The agreement of the cluster model with defects with the experiment is not as good as in the cluster model case. The  $R$ -factor increases from 0.14 to 0.18, although all distances and coordination numbers remained. Hence, this model is clearly a second choice.

### Mapping of the Pt surface

The calculated curves from cluster model presented in Fig. 5.25 show reasonable agreement with experimental data. The key result is the presence of a Pt atom at distance of 2.69 Å. In the cluster model, Ti atoms occupies only one site above the Pt surface. Due to the aperiodic nature of the QC system, Ti occupies several sites, as shown in Fig. 5.31 (a). An interesting question arises: how is it possible that only one site explains the structure so well?

To answer this question, one should consider that EXAFS is a local probe technique within 5 Å from the emitter. This method only indicates the distance of the atoms, while it does not depend so much on the angular distributions. Therefore, the actual situation may be that Ti atoms occupy different lateral sites on the Pt surface, whereby the distance to the first Pt neighbor remains constant at 2.69 Å in all cases. This can easily be achieved by small height variations above the Pt surface, as illustrated in Fig. 5.31 (b).

The Pt surface has been mapped by a uniformly distributed lateral mesh of Ti atoms in the illustrated region in Fig. 5.32 (a) by steps of 0.1 Å, such that Ti-Pt distance to be kept at 2.69 Å. This hexagonal mesh occupies more than 100 sites and is fine enough for the analysis. The reason for that will be discussed in more details shortly. Such a mesh leads to a height distribution of Ti atoms up to 55 pm (0.55 Å), as presented in Fig. 5.32 (b). The asymmetry of the distribution becomes obvious by considering two extreme cases: starting from an on top position and moving one step leads to a smaller height change than starting from a 3-FH, as illustrated in Fig. 5.32 (c), while in both cases the Ti-Pt distance is kept constant.

Experimentally, the height distribution of Ti atoms can be assessed in an STM image of a BTO-derived OQC (Fig. 5.33 (a)). The analysis, done by S. Schenck, is compared to our approach, in Fig. 5.33 (b).

In addition to the QC arrangement, Ti atoms in Fig. 5.33 (a) make the Kepler-approximant arrangement. However, the exclusion of atoms in the Kepler-approximant is not a must for the validation of the results, as explained in the following. The building blocks of the Kepler-approximant

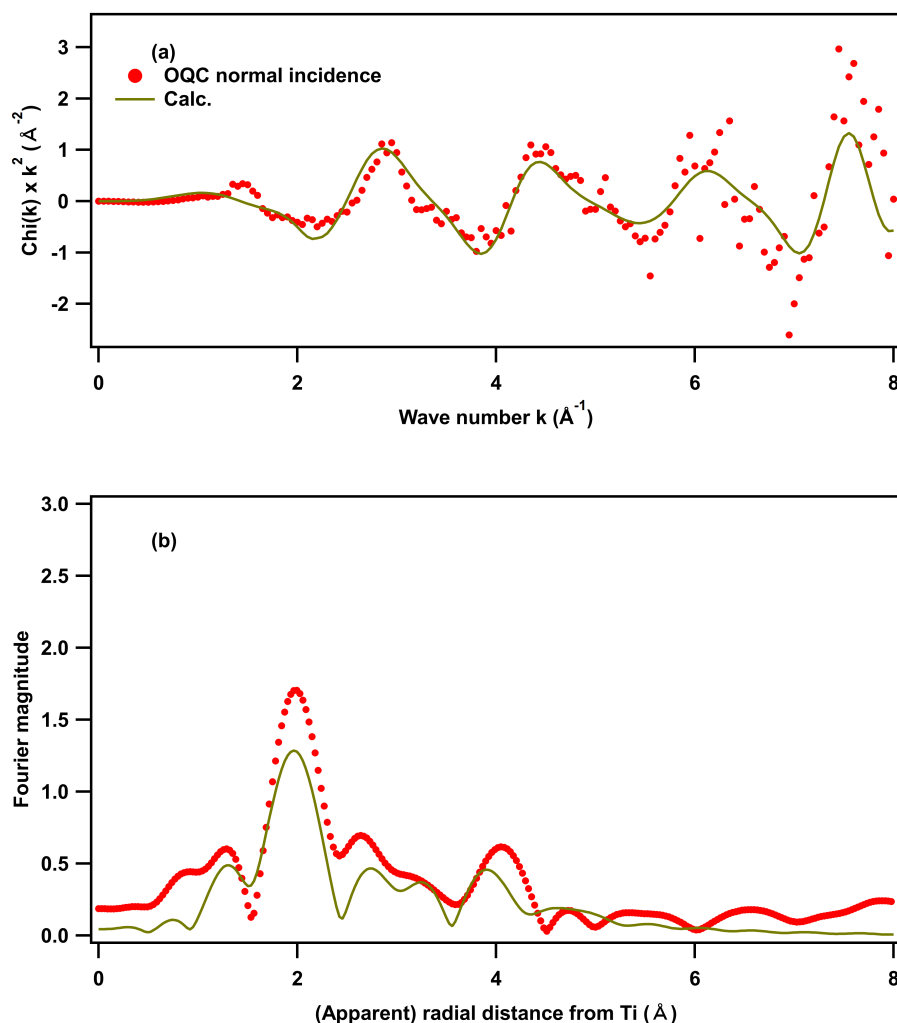


Figure 5.29: Experimental and calculated modulation functions and FFT of EXAFS at the Ti  $K$ -edge in normal incidence, calculated with model of Fig. 5.28.

are quite similar as those of QC. Therefore, even excluding the atoms of the Kepler-approximants is not expected to change the height variation distribution, considerably. Furthermore, when performing the EXAFS analysis, one can decrease the height variation by adjusting the Ti-Pt bond lengths of Ti atoms in the on top and fcc 3-FH sites. After adjusting the thermal broadening by  $\sigma_{Pt}^2$  there will be only minor changes in the calculated modulation function. In addition, the Pt(111) surface has been assumed to be flat, while it may also have corrugations at atoms close to Ti. This effect has also not been taken into account. Finally, there are stripes in the STM image, which correspond to height variations up to 12 pm. Considering these points, the height variation in the STM image (FWHM: 24 pm) and in the model derived from Fig. 5.32 are in good agreement. This shows that the assumption of a constant Ti-Pt distance is not in contradiction to a quasicrystalline structure with a large number of adsorption sites.

The modulation functions have been calculated for the lateral mesh with Ti above the Pt surface. Since the signal from Pt is mostly visible in grazing incidence, the calculations have been done for an angle of incidence of  $70^\circ$ . The modulation function for each point of the mesh is the sum over all

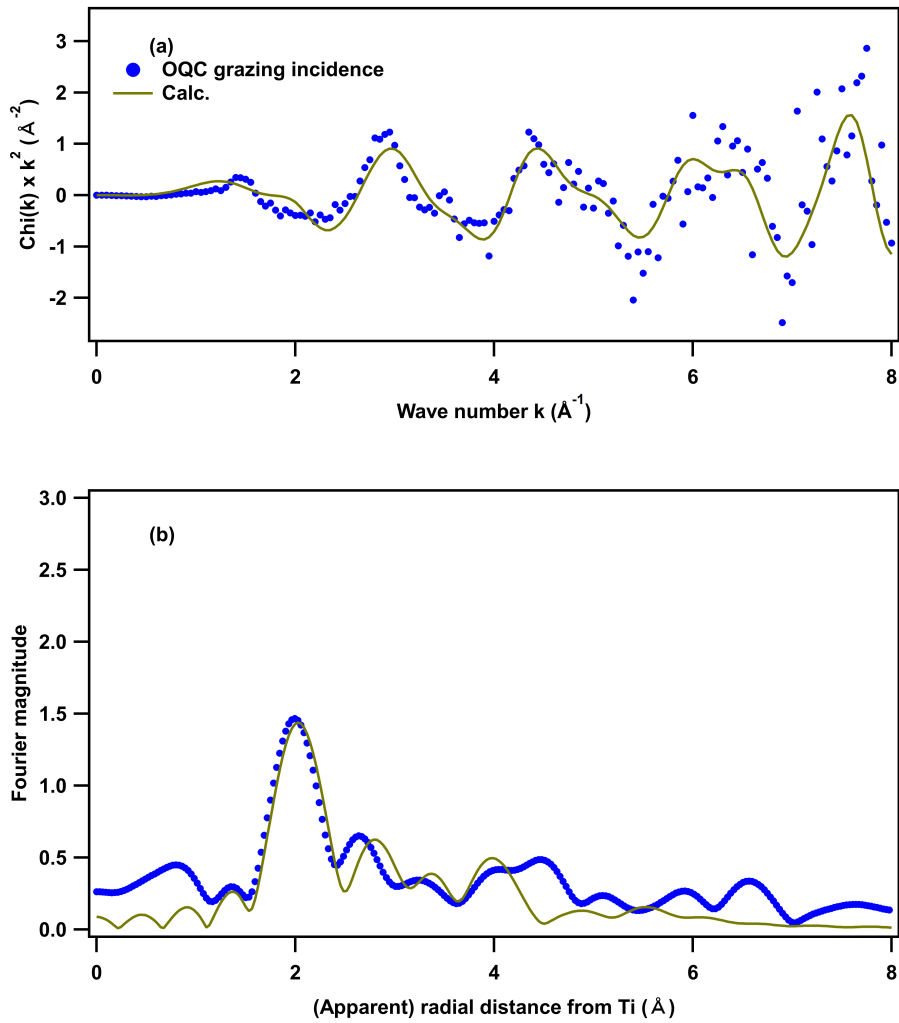


Figure 5.30: Experimental and calculated modulation functions and FFT of EXAFS at the Ti  $K$ -edge in grazing incidence, calculated with model of Fig. 5.28.

single and multiple scattering paths from Ti and the atoms of the first two layers of bulk Pt. The maximum path length was set to  $2 \times 5.8 \text{\AA}$ , which covers a radius of  $5.8 \text{\AA}$  from Ti. The calculations have been done using FEFF8-lite [88, 157, 158]. Figure 5.34 (a) shows the modulation functions for a series of positions along a line from the top to the 3FH site. The gradual change from one curve to the next shows that the step size of  $0.1 \text{\AA}$  is fine enough.

The average of the modulation functions from all of points of the mesh have been taken. To obtain the average of a uniform distribution, every point of the corners of the mesh has been weighted by  $1/3$ , the points on the edges by  $1/2$  and the points inside the mesh by 1. Finally, the average modulation function was summed with the modulation function, due to all single and multiple scatterings of the BTO layers in Fig. 5.25 (a,b). This calculation has been performed by DEMETER (using FEFF6) to include the values of the calculated coordination numbers of the O atoms. For the calculations of the BTO layer and averaging the mesh,  $S_0^2$  was set to 1. The result of this superposition is compared with the modulation function of the cluster model and the experiment in Fig. 5.34 (b). For comparison, the edge shift of  $5.6 \text{eV}$  has also been

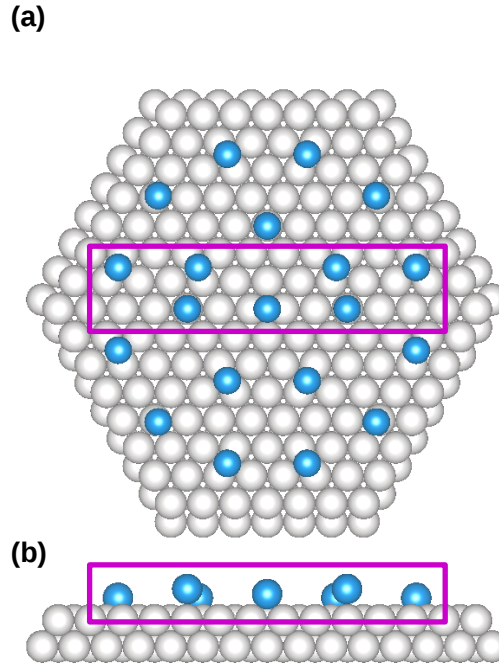


Figure 5.31: (a) An extreme example of lateral site distribution of Ti atoms in BTO-derived OQC on Pt(111) surface, leads to the height variation of atoms, shown in (b), due to the constant Ti-Pt distance.

applied to the experiment to be consistent with the calculated results (Tab. 5.6). For the purposes of consistency, multiple scatterings between BTO layers and Pt has not been included in both calculated modulation functions, which lead to negligible differences in the modulation function of the cluster.

It needs to be noted that to test the sensitivity of the calculations of the clusters in Fig. 5.25 to  $\sigma_{Ti-Pt}^2$ , this parameter was set to zero, which results to marginal differences. The resulting modulation function is shown in Fig. 5.34 (b). For the purpose of consistency, the calculations with all sites of the mesh have also been performed by setting  $\sigma_{Ti-Pt}^2$  to zero.

Figure 5.34 (b) shows that the results of the clusters in Fig. 5.25 and the mesh are similar and agree to the experiment within the noise level. Obviously, the off-3FH site is a good representative of the mix of sites present in the OQC. Furthermore, the results of the off-3FH site fit slightly better to the experiment, which indicate the existence of preferred sites above the Pt substrate.

For performing the analysis, all of the points of the mesh has been assumed to have the same occupation probability. However, the reasonableness of this assumption should be investigated. To investigate the distribution of Ti atoms on the Pt surface, the structure of the first till the fifth generations of QC have been calculated by S. Schenck. The meaning of different generations of the QC structure is given in the following: considering the edge of the building blocks in QC with Niizeki-Gähler tiling as  $a$ , the edge in the second generation is  $(2 + \sqrt{3})^1 \times a$ , in the third generation  $(2 + \sqrt{3})^2 \times a$  and so on (see Fig. 2.4).

To investigate the occupation probability of sites on a Pt surface, all atoms of five generations of QC were back-folded on a Pt unit cell, as shown in Fig. 5.35. For the purpose of simplicity of

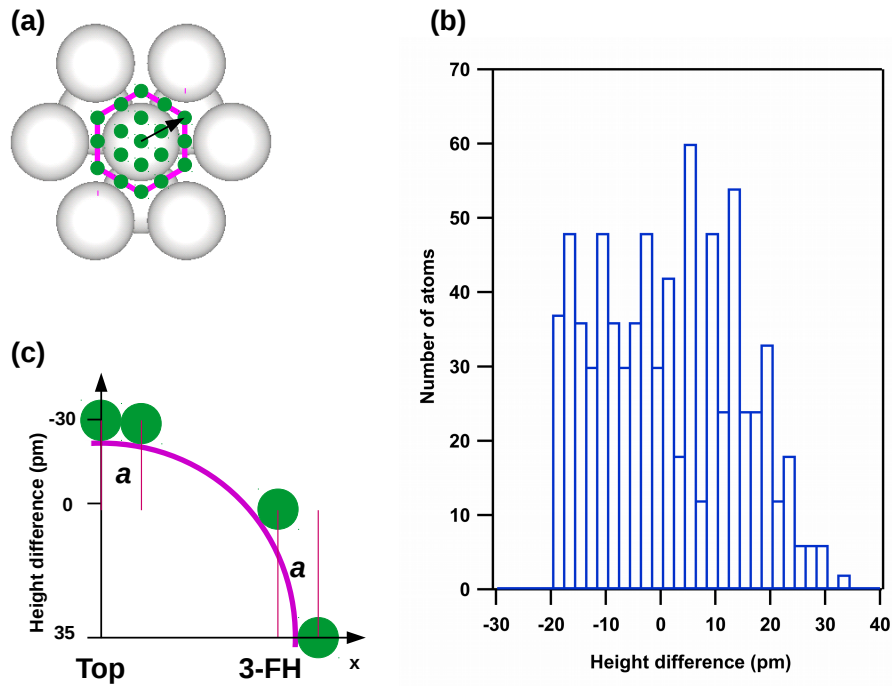


Figure 5.32: (a) The region of the lateral mesh of Ti atoms with steps of  $0.1 \text{ \AA}$  and the corresponding height difference distribution (b). (c) The illustration of the asymmetry in the height distribution.

calculations, the origin of the unit cell was selected so that all Ti positions have positive values. In addition, the difference between fcc and hcp 3-FH sites due to the presence of the second Pt layer has not been taken into account. This is valid, due to the weak effect of the second layer in the formation of QC layer. Experimentally, the edge of the building blocks in OQC has been determined as  $6.85 \text{ \AA}$  [40] and the lattice constant of Pt(111) surface  $2.775 \text{ \AA}$  [20]. The results of the back-folding of Ti atoms are presented in Fig. 5.36. The figure shows uniform coverage of the Pt surface by the back-folded Ti atoms of five generations. To a large extent, it approves the equal probability of occupation of each point at the Pt surface by Ti atoms.

While back-folding the atoms, it has been found that the resulting pattern is extremely sensitive to the ratio of the Ti-Ti to Pt-Pt distances. To look for other possible patterns, the Pt-Pt bond distance was kept at  $2.775 \text{ \AA}$  and the Ti-Ti bond distance was varied carefully in the range of  $6.8$  to  $6.9 \text{ \AA}$ . It has been seen that a slightly higher value of  $6.873309 \text{ \AA}$  results in the pattern of Fig. 5.37 (a). In this most extreme case, the centers of blobs have a distance of about  $0.4 \text{ \AA}$ , which is the largest distance found by a systematic scan of all values. Even in such a case, one would still obtain a reasonable sampling of the underlying the Pt substrate. Furthermore, this pattern is only one possibility out of hundred thousands and its occurrence probability is extremely small.

Further investigations lead to finding an interesting pattern, presented in Fig. 5.37 (b). The figure shows a completely nonuniform distribution of the back-folded points in only three regions. For the calculations of this pattern, the Pt-Pt bond distance has been kept at  $2.775 \text{ \AA}$ , whereas the Ti-Ti bond distance has been set at  $22.31502375 \text{ \AA}$ , which is unreasonable and does not affect the presented results here.



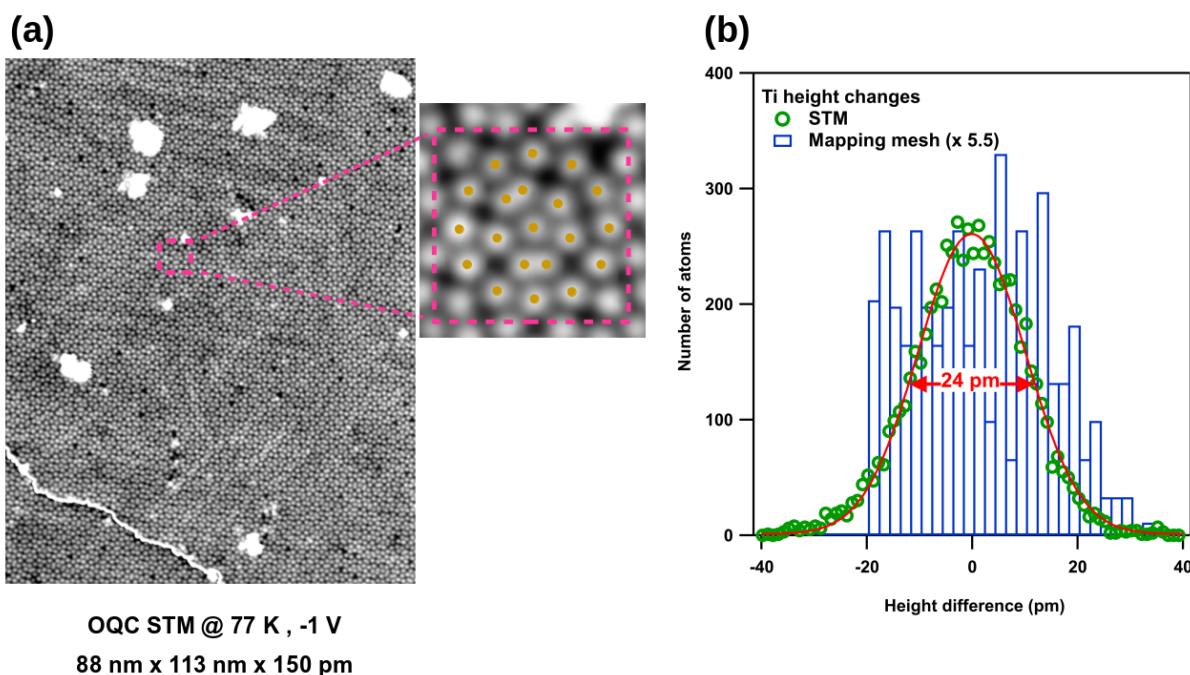


Figure 5.33: (a) An STM image of a large area of BTO-derived OQC sample taken with  $-1$  V tunneling voltage at 77 K. (b) The comparison of the corresponding height variation of the atoms in the image (a) and the calculated one, shown in Fig. 5.32.

### 5.2.5 Summary

The geometrical structure of BTO-derived OQC has been investigated in this chapter using XAS spectra in normal and grazing incidences, which unexpectedly, did not show any pronounced directional anisotropy. The analysis of the EXAFS data resulted in two values for Ti-O bond-lengths: an in-plane O at  $1.71 \text{ \AA}$  and an in- and an out-of-plane O at  $2.56 \text{ \AA}$ . The shorter in-plane and the out-of-plane O atoms have small coordination numbers (0.23 and 0.38) with large errors, whereas the longer in-plane O is more prominent with a coordination number of 3. The shortest Ti-Pt distance has been found as  $2.69 \text{ \AA}$ . Although Ba is a strong scatterer, only small hints have been found about an in-plane Ba at  $3.15 \text{ \AA}$ . The low coordination number of the out-of-plane O indicates that the spectrum in grazing can be described almost completely by scatterings from the Pt substrate. The values obtained for the short in-plane Ti-O and the short Ti-Pt distance agree quite well with the distances, achieved by density functional theory (DFT) calculations in the Kepler-approximant, whereas in case of Ti-Ba distance, the agreement is not as good.

The quasicrystalline nature of the structure imposes occupation of different sites above Pt by Ti atoms. Surprisingly, the presented cluster with only one site, off-3FH fcc, explains the experiment as good as averaging over all possible sites, or even slightly better. This indicates the presence of preferred sites of Pt for Ti. In addition, a pattern of occupation sites of Pt has been found by back-folding Ti atoms in the QC structure in a Pt unit cell, which hints to the same direction. Due to the interaction between the OQC layer and the crystalline Pt substrate, the Ti-Pt bond-length has been found to be kept constant regardless of the site of Ti. This predicts height differences in Ti atoms in the OQC layer, as approved by STM.

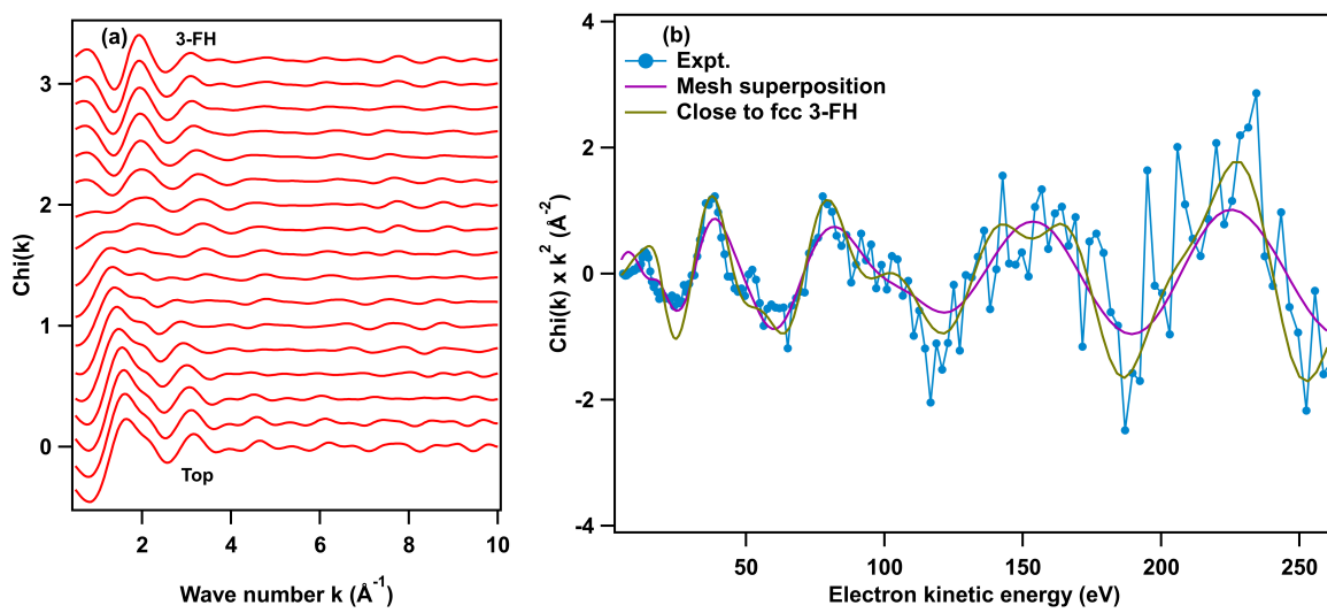


Figure 5.34: (a) The individual modulation functions of the lateral mesh, discussed in the text, at the Ti  $K$ -edge in grazing incidence starting from on top position to fcc 3-FH site. (b) The comparison of  $k^2$ -weighted modulation functions of the superposition of the sites in the lateral mesh (Fig. 5.32), the cluster model with Ti at close to fcc 3-FH site (5.25) and the experiment (OQC) at the Ti  $K$ -edge in grazing incidence.

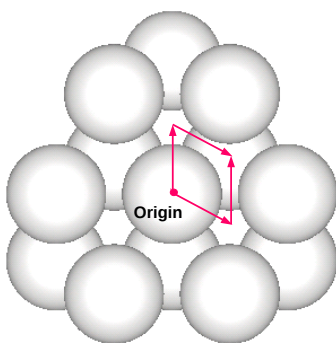


Figure 5.35: The selected area of the Pt surface to back-fold Ti atoms in the QC structure, as discussed in the text.

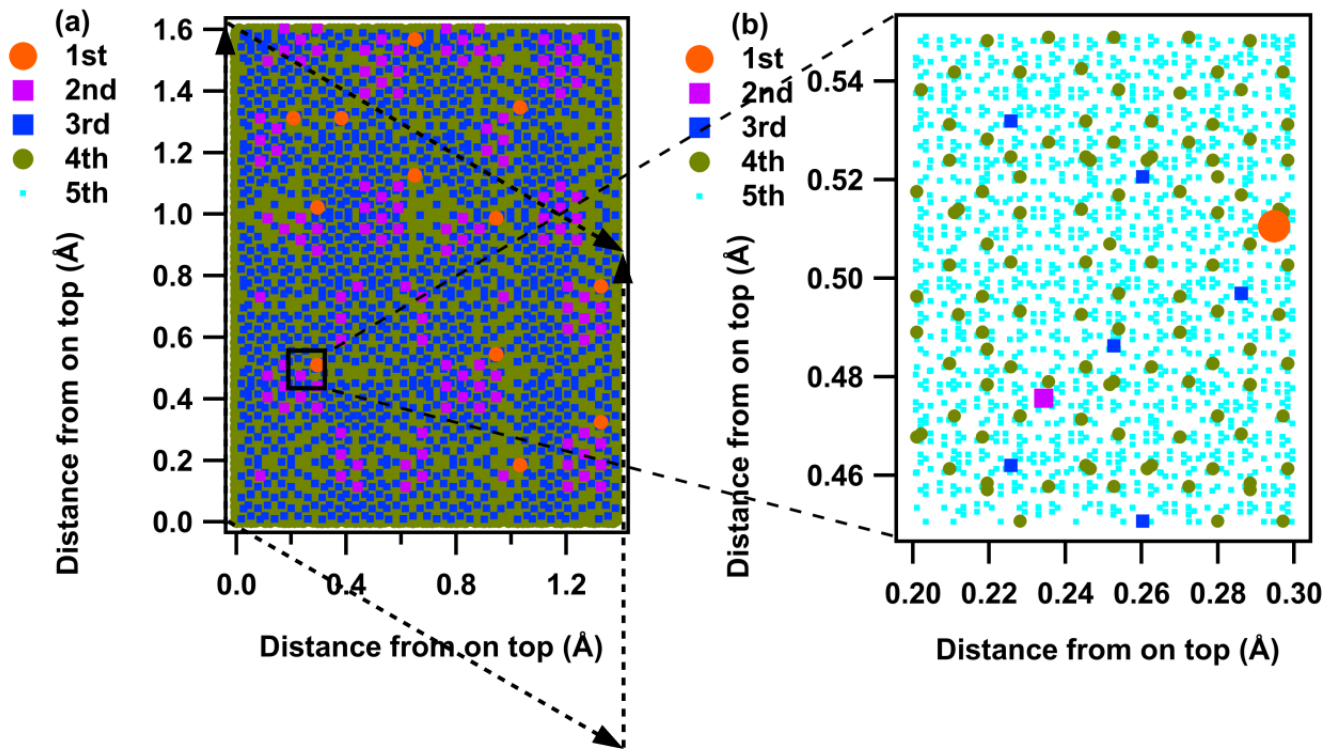


Figure 5.36: (a) The result of back-folding Ti atoms in different generations of the QC structure on the selected Pt area, shown in Fig. 5.35. The Pt-Pt and Ti-Ti bond distances are set to 2.775 Å [20] and 6.85 Å [40]. The arrows show the selected Pt area, as shown in Fig. 5.35. (b) The zoomed region.

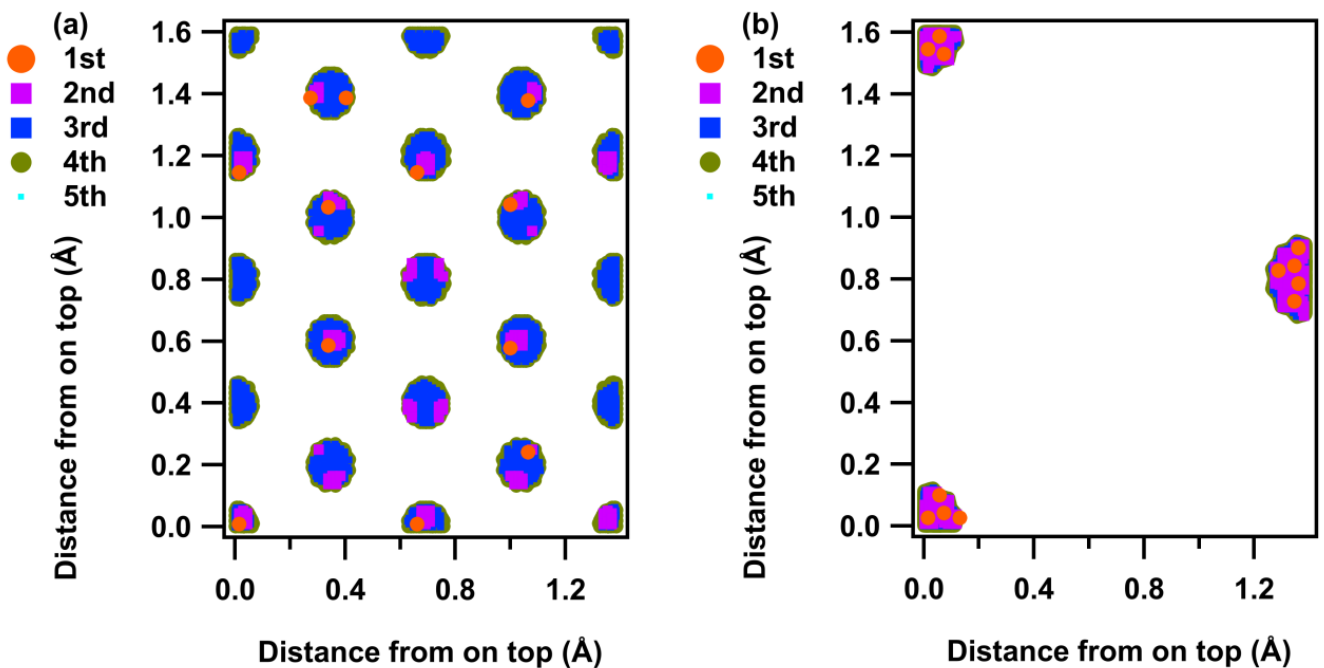


Figure 5.37: The result of back-folding Ti atoms in different generations of the QC structure on the selected area of Pt(111) surface, shown in Fig. 5.35. The Pt-Pt bond distance is set to 2.775 Å [20] and the Ti-Ti bond distance is assumed to be 6.873309 Å (a) and 22.3150237 Å (b).



# 6 Growth and decay of BTO-derived OQC on Pt(111)

In this chapter the growth and decay of OQCs and BTO islands have been monitored using fast and high resolution photoelectron spectroscopy. Changes in the Ti  $2p$ , O  $1s$ , Ba  $3d$  and Pt  $4f$  photoemission lines reflect changes of the oxidation states and coordinations during wetting and dewetting of the Pt surface. Wetting and dewetting are induced by heating in ultra high vacuum or an oxygen atmosphere.

## 6.1 Experimental procedures

The chemical states of the elements in ultrathin films of BTO on Pt(111) are investigated by high resolution X-ray photoemission spectroscopy at the SuperESCA beamline (Sec. 3.4.2). The Pt(111) crystal has been bought from Surtau Preparation Laboratory NL (Rene Koper) and ultrathin films of BTO have been deposited, as described in [40].

The Pt(111) single crystal has been cleaned by several cycles of Ar ion sputtering, O<sub>2</sub> annealing at 870 K and UHV heating up to 1270 K. BTO was deposited by radiofrequency-assisted magnetron sputtering at room temperature from a stoichiometric BaTiO<sub>3</sub> disk target with a diameter of 5.08 cm (Thin Film Consulting, Grafenberg, 99% purity), with a distance of 10 cm from the Pt crystal. The sputtering has been performed with a mix of 80% Ar and 20% O<sub>2</sub> with a total pressure of  $4.5 \times 10^{-3}$  mbar and with a power of 30 W and at a rate of  $0.7 \text{ nm min}^{-1}$ . The sputtering was followed by heating in UHV, after which the formation of BaTiO<sub>3</sub>(111) islands has been verified by LEED. By increasing the temperature to 1250 K, BTO-derived OQCs were formed. The initial thickness determination by XPS indicates an average thickness of 3 to 4 ML, as is used for the naming of the sample through out this chapter. However, as shown by AFM measurements, the actual average coverage is 2 to 3 times higher.

The sample has then been transported through air to the beamline and introduced into a UHV chamber with a base pressure of  $3.5 \times 10^{-10}$  mbar. After a UHV flash at 1100 K, the 12-fold LEED pattern of BTO-derived OQC appeared. After performing high resolution XAS and XPS measurements at room temperature, the sample was annealed at 825 K under an oxygen partial pressure of  $5 \times 10^{-7}$  mbar for 1100s and cooled down in oxygen. The oxygen valve was closed at 375 K. While carrying out experiments, XPS spectra have been recorded. After oxidizing the sample, a barely visible  $2 \times 2$  LEED pattern of BTO islands appeared at an electron kinetic energy

of 66 eV. The LEED image shows the coalescence of BTO-derived OQC into BTO(111) islands, through dewetting of Pt(111) surface. The islands are 2 to 3 ML thick, as estimated from the portion of the freed Pt surface, as observed in low-energy electron microscopy (LEEM) images [41].

After recording the spectra, the sample has been further annealed in  $1 \times 10^{-5}$  mbar  $O_2$  at 925 K for 1200 s. The sample was then cooled down in oxygen and the oxygen valve was closed at 420 K. The sharpness of the LEED pattern of this further annealed state, taken at an electron kinetic energy of 66 eV has decreased even further. This implies either formation of new amorphous structures and/or losing the long range order in the previously formed islands.

After recording XPS and XAS spectra, the sample was annealed in UHV, while XPS spectra on the Ti 2*p* and the Pt 4*f* emission lines have been recorded. 1780 s after starting to heat, the experiment has been stopped due to a beam loss in the synchrotron. The experiment has been continued after 90 min and the sample has been heated up to 1025 K and finally cooled down in UHV to RT. The total duration of the second part of the experiment was 6000 s. LEED images have approved the formation of the OQC on the Pt surface, again. XAS and XPS measurements have also shown that after the oxidation reduction cycle, the system is in its initial state.

After performing synchrotron measurements, the sample was transferred home in reduced state, through air for AFM and PFM (piezoresponse force microscopy) experiments under ambient air conditions and EELS measurement under UHV. The AFM images taken at different positions in tapping mode show 35% to 47% coverage of the surface by BTO islands with a height of 10 to 17 nm and a width of 30 to 50 nm. It implies that only a small portion of the signal in the synchrotron measurements originated from the OQCs and the main part is due to islands. However, the high resolution of the data makes it possible to investigate the chemical states of the elements during the growth and the decay of OQCs.

The ferroelectric properties of the islands have been investigated by piezoresponse force microscopy (PFM) in direct contact mode in remanence, using a MFP-3d from Asylum research. To measure the ferroelectric behavior of the sample in contact mode, a small alternating voltage of 0.25 V is applied to the piezo, which oscillates the AFM tip. This results in oscillations of the islands in *z* direction at the contact position, due to the inverse piezoelectric effect. The amplitude of these oscillations is plotted as a function of the polarization voltage of the islands in Fig. 6.1 (b). The phase difference of the applied alternating voltage to the piezo for polarization of the islands and the tip response (in degree) is also plotted, which shows the hysteresis curve of the polarization. The plotted curves imply a ferroelectric nature of the islands. The coercive voltages, shown by the arrows, direct to voltages of -1 and 1.7 V, at which the polarization directions in the hysteresis loop change. However, this preliminary PFM measurement does not completely agree with the butterfly amplitude curve and further investigations are required to study the ferroelectricity of the islands, which is beyond the scope of this work.

Figure 6.1 (a) shows the topography of 4 ML BTO on Pt(111), as measured by AFM (MFP-3d) under ambient air in tapping mode with a cantilever spring constant of 0.6 N/m. The image was measured with a drive amplitude of 0.05 V, a drive frequency of 68 kHz, a scan size of  $1.5 \times 1.5$

$\mu\text{m}^2$  and a scan speed of  $1.5\ \mu\text{m}/\text{s}$ . Figure (b) shows PFM measurements on the islands in contact mode in remanence with a cantilever spring constant of  $1.03\ \text{N}/\text{m}$ . Top: the phase difference of the applied alternating voltage to the piezo and the tip responses (in degree), which shows the islands polarization hysteresis. Bottom: island oscillation amplitude (in pm), which shows the corresponding butterfly curve. The arrows direct to the voltages, where the polarization directions change (coercive voltage). The PFM measurements were performed with a drive frequency of  $324\ \text{kHz}$ , a drive amplitude of  $0.25\ \text{V}$  and an applied force of  $39.6\ \text{nN}$  to the islands.

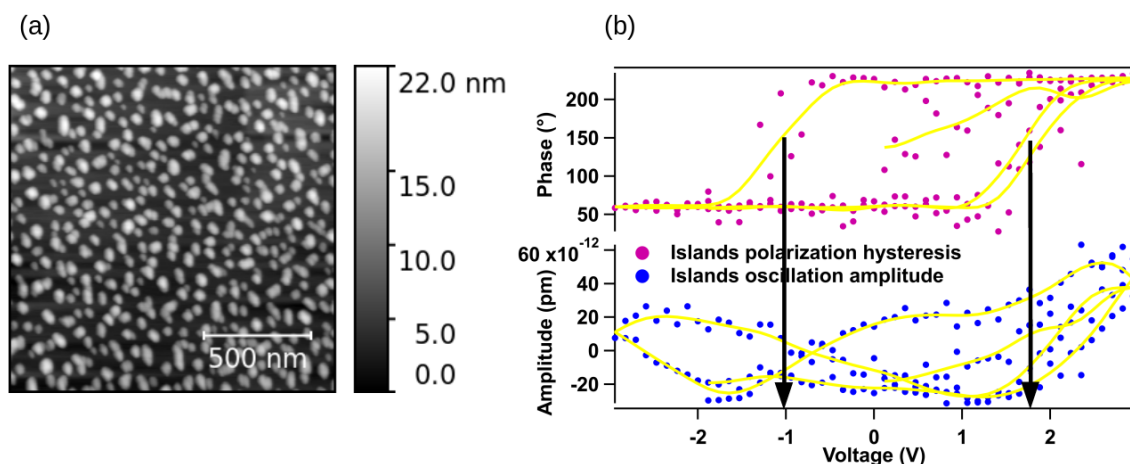


Figure 6.1: (a) Topography of 4 ML BTO on Pt(111) measured by AFM (MFP-3d) under ambient air in tapping mode. (b) PFM measurements on the islands in contact mode in remanence. Top: The phase difference of the applied alternating voltage to the piezo and the tip responses (in degree). Bottom: Island oscillation amplitude (in pm). See text for the measurements parameters.

## 6.2 Binding energy calibration

High resolution X-ray photoemission spectra of the Ti  $2p$ , the O  $1s$ , the Ba  $3d_{5/2}$  and the Pt  $4f$  emission lines have been recorded. The measurements have been done with an integration time ( $\Delta t$ ) of  $0.1\ \text{s}$ . The pass energy ( $E_p$ ) of the analyzer has been set to  $4\ \text{eV}$  to record Pt spectra and  $10\ \text{eV}$  for other measurements. The experiments have been performed at photon energies of  $140$  and  $200\ \text{eV}$  for Pt lines, at  $670\ \text{eV}$  for Ti and O lines and at  $1000\ \text{eV}$  for the Ba line. In addition, in every preparation, overview spectra with an integration time of  $0.05\ \text{s}$  and a pass energy of  $10\ \text{eV}$  were recorded at a photon energy of  $1000\ \text{eV}$ . No surface contamination has been observed in the overview spectra. During the oxidation/reduction experiments, here called ramps, Ti  $2p$  ( $E_p = 10\ \text{eV}$ ,  $\Delta t = 0.05\ \text{S}$ ) and Pt  $4f$  ( $E_p = 7\ \text{eV}$ ,  $\Delta t = 0.03\ \text{S}$ ) lines have been measured at a photon energy of  $670\ \text{eV}$ . The measurements have been performed at normal and  $70^\circ$  off normal emission angles. The XPS spectra in normal emission are shown in this chapter and the spectra in grazing emission are presented in appendix (Fig. 8.3 and 8.4). The fittings of the spectra in grazing emission were performed with the same parameters as in normal emission. The observed directional anisotropy is discussed in Sec. 6.3.

The spectra have been normalized to the current from the last focusing mirror of the beamline. Alternatively, spectra have been normalized to the high kinetic energy part of a spectrum, typically 3 to 5 points were sufficient. This normalization will be called normalization to the footpoints in this work. The inelastic fraction of each spectrum has been approximated by a Shirley background and subtracted. The calibration of the binding energy can be done using the positions of the Fermi edge or the Pt  $4f_{7/2}$  emission line. According to the NIST database, there is a range of 70.6 to 71.3 eV for the binding energy of latter. For easier comparison with literature, we choose 71.2 eV, the most commonly value [62]. Figure 6.2 shows the valance band region of Pt after such a calibration. Obviously, the point of inflection has a shift of 0.15 eV from 0 eV. This ambiguity illustrates the importance of the calibration, when comparing absolute binding energies.

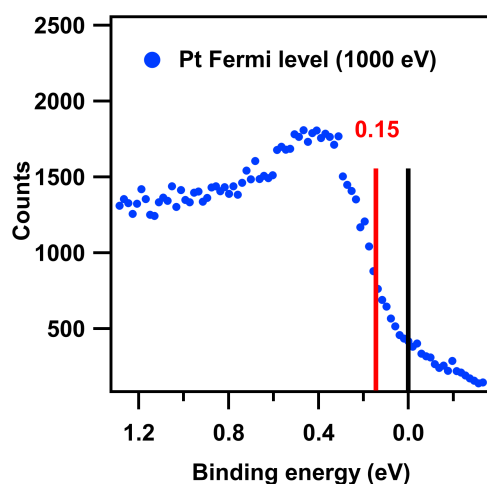


Figure 6.2: Fermi level of Pt, corrected in the binding energy by referring to the Pt  $4f_{7/2}$  line in the overview spectrum, taken at 1000 eV. The black bar shows the zero binding energy, while the point of inflection of the spectrum is at 0.15 eV.

### 6.3 X-ray photoemission spectroscopy

High resolution XPS spectra of the Ti, the O and the Ba emission lines of the sample in the reduced, the oxidized and the further annealed states are presented in Fig. 6.3, 6.4 and 6.5. All spectra are taken at room temperature and are normalized to the mirror current. They are quite complex and manifest different oxidation states and coordinations.

The deconvolution of the Ti spectra has been done using 5 doublets. From collection of spectra four Ti species have been derived. O and Ba spectra have been deconvoluted by 5 and 4 peaks. The line shape of every peak in the reduced state and the ones, which have been modified in the oxidized and the further annealed state are given in Tab. 8.1.

In this section, the components will be discussed and compared with values of known compounds. Considering the binding energies in the Ti spectra, the first two components at lower energies are assigned to  $Ti^{3+}$  and the ones at higher energies are assigned to  $Ti^{4+}$ . The O 1s line in the further



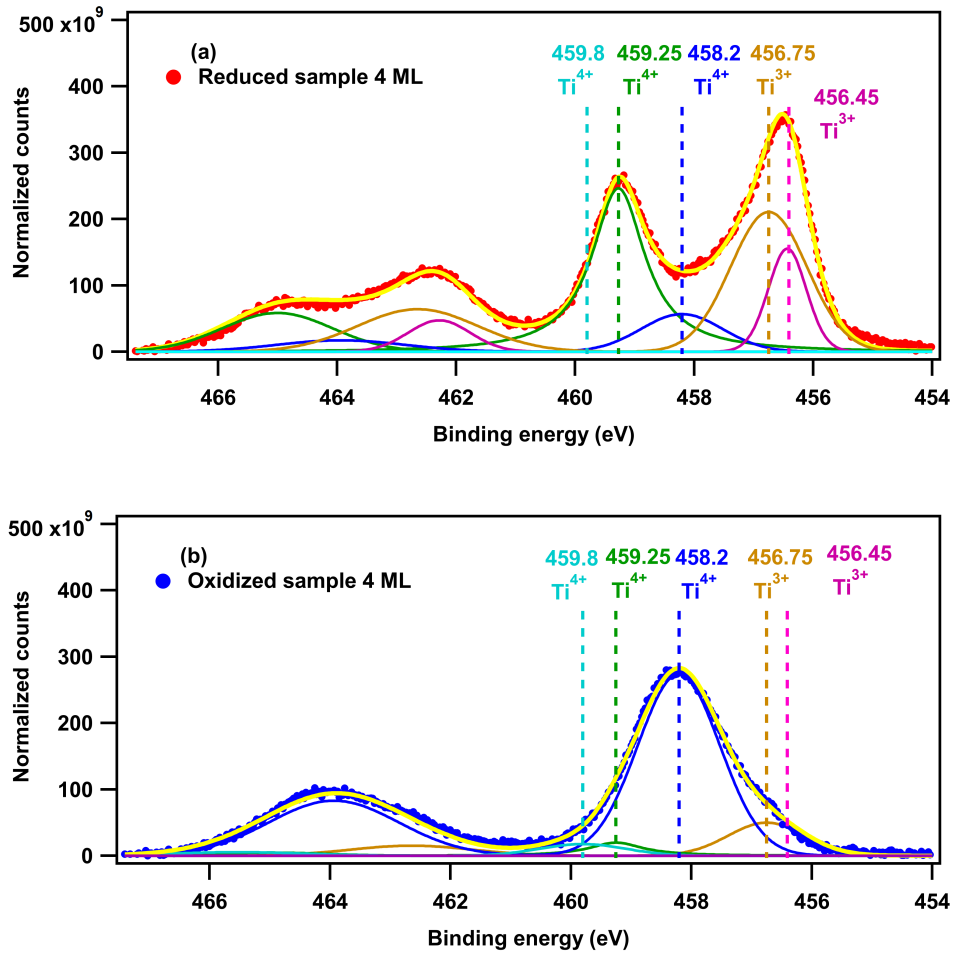


Figure 6.3: High resolution XPS spectrum of the Ti  $2p$  emission lines, taken in normal emission at room temperature, at a photon energy of 670 eV for 4 ML BTO sample (a) in the reduced state, annealed in UHV and (b) oxidized state, annealed in  $5 \times 10^{-7}$  mbar  $O_2$ .

annealed state is broad. Its fit has been performed using components with similar line shapes as in the reduced and oxidized states. However, due to its quite wide width, the resulting deconvolution is not unique and may not be reliable.

The Ti component at 456.75 eV fits to the binding energy of  $Ti^{3+}$  in  $Ti_2O_3$  with the O line at 530.1 eV in the reduced, at 529.6 eV in the oxidized and at 529.5 and 529.8 eV in the further annealed states [64, 126, 133]. The peak at 529.8 eV in the further annealed state has been observed only in grazing emission and therefore, is a surface feature.

The Ti component at 458.2 eV fits to 5-fold coordinated  $Ti^{4+}$  in  $BaTiSi_2O_8$  [132]. As discussed in Sec. 6.7, the O line at 529.6 eV arises during oxidation, which makes it plausible to be considered as the connected oxygen to the 5-fold coordinated Ti with the emission line at 458.2 eV.

The Ti peak at 459.25 eV in the reduced state is less intense in the XPS spectrum of the sample with 1 ML BTO on Pt(111) in Sec. 5.2.3 (Fig. 5.13 (a)). The 1 ML sample contains small islands with a height of 1.6 nm in the oxidized state (Fig. 5.7), whereas the heights of the islands in the 4 ML sample are 10 to 17 nm (Sec. 6.1). Therefore, the Ti peak at 459.25 eV in the reduced state

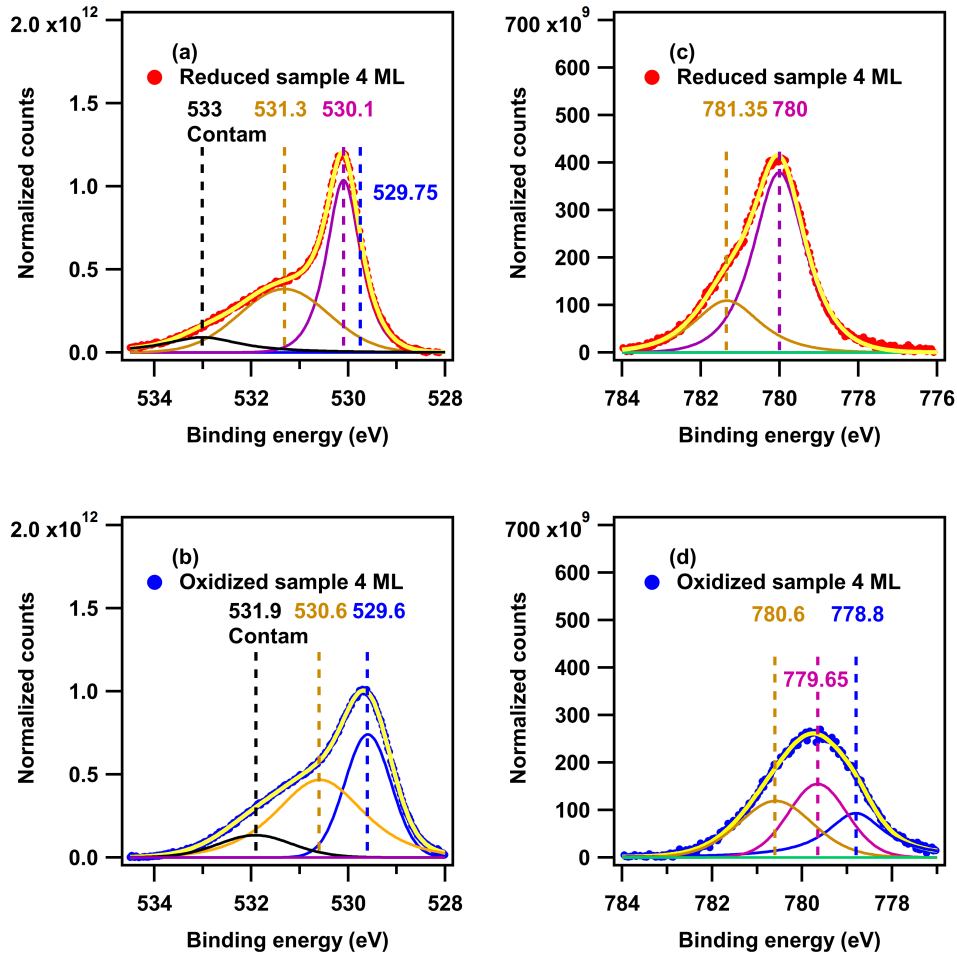


Figure 6.4: High resolution XPS spectrum of the O  $1s$  and Ba  $3d_{5/2}$  emission lines, taken in normal emission at RT, at a photon energy of 670 (O  $1s$ ) and 1000 eV (Ba  $3d_{5/2}$ ) for 4 ML BTO sample (a,b) in the reduced state, annealed in UHV and (c,d) in the oxidized state, annealed in  $5 \times 10^{-7}$  mbar O<sub>2</sub>.

can be assigned to a Ti<sup>4+</sup> component in large islands. This component is shifted to 459.05 eV in grazing emission Fig. 8.3 (a). Without further experimental evidence, one cannot say much about reasons.

The Ti peak at 459.25 eV in the reduced state can be assigned to Ti in BTO with the corresponding O and Ba lines at 530.1 and 780 eV [134]. The same Ti component at 459.25 eV in the oxidized state also fits to Ti in UHV fractured BTO with the O line at 530.6 eV [146] and bulk and surface Ba components at 779.65 and 780.6 eV [159]. Ti peak at 459.05 eV in further annealed state also fits to Ti in UHV fractured BTO with the O line at 530.45 eV [146] and bulk and surface Ba components at 779.65 and 780.6 eV [159]. However, no directional dependence has been observed for the two Ba components, which indicates undercoordinated Ba in the bulk.

The Ti peak at 459.25 eV in the reduced and the oxidized states at 459.25 eV and in the further annealed state at 459.05 eV can also be assigned to 6-fold coordinated Ti<sup>4+</sup> in Ba<sub>2</sub>TiSi<sub>2</sub>O<sub>8</sub> by O atoms. This Ti component can also be assigned to Ti<sup>4+</sup> in rutile with the O line at 530.1 eV in the reduced, at 530.6 eV in the oxidized and at 530.45 and 530.7 eV in the further annealed state.

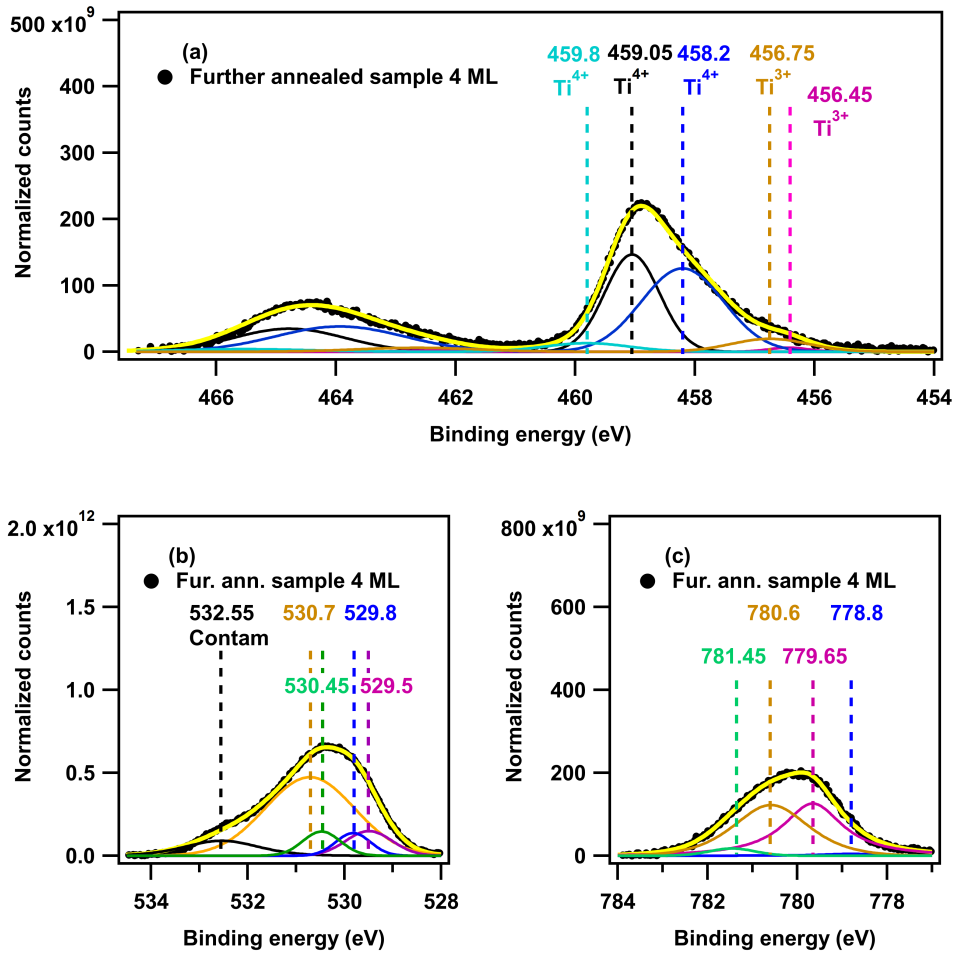


Figure 6.5: High resolution XPS spectrum of (a) the Ti 2*p* and (b) the O 1*s* (taken at 670 eV) and (c) the Ba 3*d*<sub>5/2</sub> (taken at 1000 eV) emission lines of 4 ML BTO sample in the further annealed state, annealed in  $1 \times 10^{-5}$  mbar O<sub>2</sub>, taken at normal emission at room temperature.

Comparing normal and grazing spectra in the further annealed state reveals that the component at 530.45 eV is a bulk feature, whereas the one at 530.7 eV is a surface feature [131, 132].

The O peak at 530.1 eV in the reduced state is not present in the oxidized state, while the surface feature at 529.75 eV shifts by 0.15 to 0.2 eV to lower binding energies, as discussed in Sec. 6.7. Probably, the origin of this shift is the change in the structure and coordination number and not band bending, because the direction of the shift does not agree: via oxidation, the sample turns more *p*-doped, which would cause a shift to higher binding energies.

The broad O features with binding energies at 531.3 eV in the reduced, at 530.6 eV in the oxidized and at 530.7 eV (as a surface component) in the further annealed state fit to OH groups in Ba(OH)<sub>2</sub> with the Ba lines at 780, 780.6 and 780.6 eV, respectively [138, 139]. In addition, the peak at 531.3 eV in the reduced state agrees with the binding energy of OH groups on the Pt surfaces [137, 143].

The existence of OH groups bonded to Ba in the sample is questionable. The broad peak at 531.3 eV still exists at 999 K, as shown in Fig. 6.6 (b), while the decomposition of Ba(OD)<sub>2</sub> in

a thick BaO film is complete at 550 K [140]. Even the dehydration of bulk  $\text{Ba}(\text{OH})_2$  is complete at 1025 K [160]. Although the peak area at 531.3 eV has reduced from 47% to 35% of the total spectrum area during annealing in UHV, it still has a large portion, which implies that this feature may be a real characteristic of OQCs. In addition, no OH groups have been detected in EELS measurements (private communication, F. O. Schumann).

Most likely, the peak at 531.3 eV is not a satellite, since no satellite peaks have been observed for BTO in this energy range [146]. Furthermore, according to the NIST database, all O 1s satellites are above 533.3 eV and the energy shift of the only exception at 531.9 eV from the main peak is 1.9 eV [161]. Similar broad features in cobalt oxide compounds have been assigned to surface O species, O at defects and also OH groups [142, 162, 163, 164].

The O peak at 530.1 eV in the reduced and the surface feature at 529.8 eV in the further annealed states fit to adsorbed  $\text{O}_2$  on the Pt surface [137, 165]. Although no oxygen molecules remain on the Pt surface at a temperatures above 825 K [136], they may have re-adsorbed, while cooling down the sample in  $\text{O}_2$  pressure, as well as by adsorption from the residual gas in UHV.

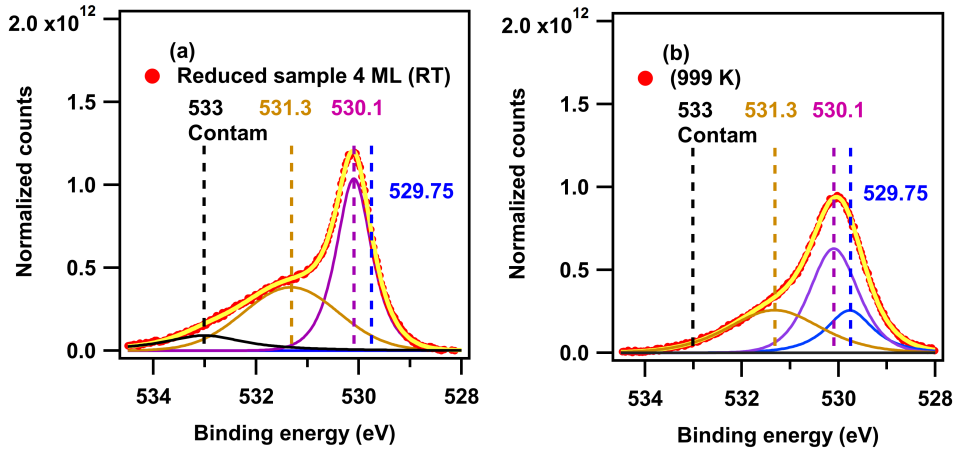


Figure 6.6: High resolution XPS spectrum of the O 1s emission line of 4 ML BTO sample in the reduced state, taken at (a) room temperature and (b) annealed at 999 K in UHV at a photon energy of 670 eV in normal emission.

The last O peak at 533 eV in the reduced and at 531.9 eV in the oxidized states at room temperature is not present at 999 K in UHV (Fig. 6.6 (b)) and 826 K in  $5 \times 10^{-7}$  mbar  $\text{O}_2$  (Fig. 6.15 (a)). This reveals that this component can be assigned to contamination due to residual gas in the chamber. This peak is much more pronounced in the further annealed state and appears as a surface feature at 532.55 eV with the intensity as high as the main O peak and forms a double peak feature in grazing emission (Fig. 8.4 (c)). Although this peak also fits to  $\text{H}_2\text{O}$  on the Pt surface [166, 167], no water can remain on the surface above 210 K [144], as discussed in Sec. 5.2.3.

There are some other peaks in the spectra, which cannot be assigned to any compound and therefore, can be originated from defects or characteristics of the investigated system. These features in the Ti spectra are at 456.45 and 459.8 eV in all states, where the peak at 459.8 eV in the reduced state is a surface feature. The features assigned to defects in the Ba spectra are at 781.35 eV in

the reduced and at 778.8 eV in the oxidized state. In the further annealed state, the surface feature at 778.8 eV and the bulk feature at 781.45 eV may also be assigned to defects. The surface O 1s component in the reduced state at 529.75 eV is also unknown.

The reported  $\text{Ti}^{4+}$  binding energies in fresnoite glasses ( $\text{Ba}_2\text{TiSi}_2\text{O}_8$ ), reported in [132] show a decrease with lowering the coordination number of Ti atoms. The intensity change of  $\text{Ti}^{4+}$  at 459.25 and 458.2 eV in the investigated sample in this work is also interpreted as changes in the amount of Ti atoms with 6 and lower coordination numbers, as discussed in Sec. 6.7 and 6.8.

The presented spectra in this chapter have been taken always at the same position of the sample, labeled as  $z = 197$  mm. To investigate sample inhomogeneities, the Ti 2p spectrum has been taken at a different position, labeled as  $z = 191$  mm in normal emission at RT. The spectra at the two positions are presented in Fig. 6.7. The intensity of 6-fold coordinated  $\text{Ti}^{4+}$  component in the spectrum at  $z = 191$  mm is almost two times as the one at  $z = 197$  mm, while intensity changes of the other components are not significant. This indicates that the spectrum at  $z = 191$  mm contains more information about the large islands. Figure 6.7 also illustrates the inhomogeneity of the sample.

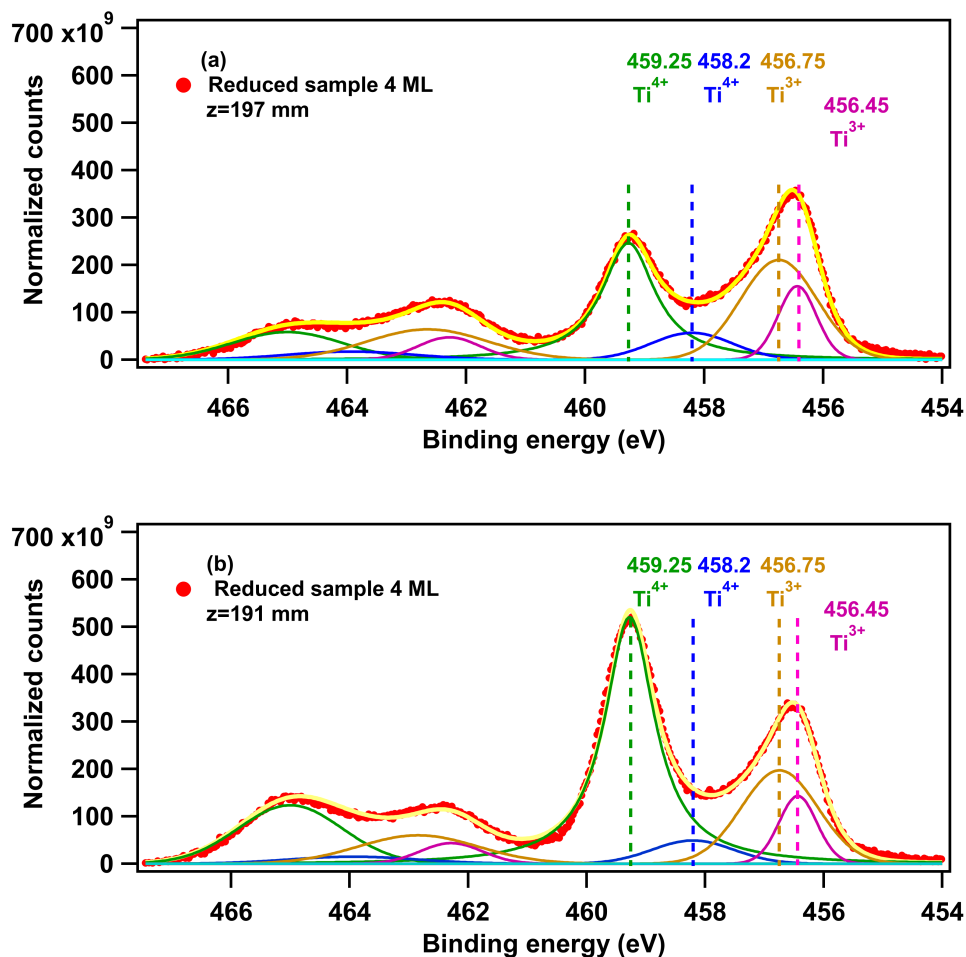


Figure 6.7: High resolution XPS spectrum of the Ti 2p emission lines, taken in normal emission at room temperature, at a photon energy of 670 eV for 4 ML BTO sample in the reduced state, annealed in UHV, recorded at a position labeled as (a)  $z = 197$  mm and (b)  $z = 191$  mm.

In summary, the Ti component at 456.75 eV can be assigned to 6-fold coordinated  $\text{Ti}^{3+}$ , like in  $\text{Ti}_2\text{O}_3$ , with the O emission line at 530.1 eV in the reduced, 529.6 eV in the oxidized and 528.5 and 529.8 eV in the further annealed state. There is no literature reference for the  $\text{Ti}^{3+}$  component at 456.45 eV. Tentatively, we assign it to 5-fold coordinated  $\text{Ti}^{3+}$ . The  $\text{Ti}^{3+}$  component of OQC, which is presumably 3-fold coordinated is also in the range of these two  $\text{Ti}^{3+}$  components. The Ti component at 459.25 eV in the reduced state can be assigned to 6-fold coordinated  $\text{Ti}^{4+}$  in  $\text{BaTiO}_3$  with the O and the Ba emission lines at 530.1 and 780 eV. In the further annealed state, the Ti component at 459.05 eV can also be assigned to Ti in BTO with the O component at 529.5 and 530.7 eV and the bulk and surface Ba components at 779.65 and 780.6 eV, respectively.

The Ti component at 458.2 eV can be assigned to 5-fold coordinated  $\text{Ti}^{4+}$ , as in  $\text{BaTiSi}_2\text{O}_8$ . The two strong O components at 530.6 and 531.3 eV are preferably assigned to O at defects and not to OH groups, due to some negating evidences. The small O component at the highest binding energy in all spectra can be assigned to surface contaminations.

### 6.3.1 Investigation of satellites in the Ti 2*p* emission lines

Satellite peaks in photoelectron spectra can yield valuable information about a system. To investigate this, high resolution XPS spectra with a wider energy range have been recorded for the Ti 2*p* emission lines of 4 ML BTO sample in the reduced, the oxidized and the further annealed state in normal emission at RT and are presented Fig. 6.8. To be consistent with literature, only linear backgrounds have been subtracted from the spectra. The small peaks centered at 471.40 and 477.35 eV with an energy difference of 13.15 and 13.30 eV from the Ti 2*p*<sub>1/2,3/2</sub> peaks in the oxidized state are close to the reported shake-up satellites, separated by 13.2 eV in bulk BTO [146]. Analogous shake-up satellites with a separation of 13.6 eV are observed in STO. In STO, these satellites are assigned to transitions from 2*p* *e<sub>g</sub>* states (mainly O character) to 3*d* *e<sub>g</sub>* states (mainly Ti character) [168]. These satellites are assigned similarly in BTO [169].

Ti 2*p* emission lines of 4 ML BTO sample in the further annealed state shows similar satellites as in the oxidized state, with an energy separation of 13.2 from the Ti 2*p*<sub>3/2</sub> peak, in agreement with literature for bulk BTO. The noise level of the second satellite peak in the oxidized and the further annealed state is too high to reliably determine the energy separation from the Ti 2*p*<sub>1/2</sub> peak.

Shake-up satellites have also been observed with  $\text{Ti}^{3+}$  in  $\text{Ti}_2\text{O}_3$  at 471 and 477 eV [170]. The satellite at 471 eV is separated by 12 eV from the main Ti 2*p*<sub>3/2</sub> peak. Considering the position of  $\text{Ti}^{3+}$  component in the 4 ML BTO sample in the reduced state, Fig. 6.8 (a) (at 456.55 eV) the corresponding satellite is expected to be observed at 468.55 eV. The superposition of such a satellite feature with the satellites of the  $\text{Ti}^{4+}$  component results in the broad feature observed at 467.3 to 479.3 eV in the reduced state.

It needs to be mentioned that the discussed satellites of the  $\text{Ti}^{4+}$  components correspond to BTO and STO single crystals, in which Ti atoms are 6-fold coordinated by O atoms. Since no difference in the satellites was found and no data for compounds with 4- and 5-fold Ti is known, no additional information about the system can be gained.

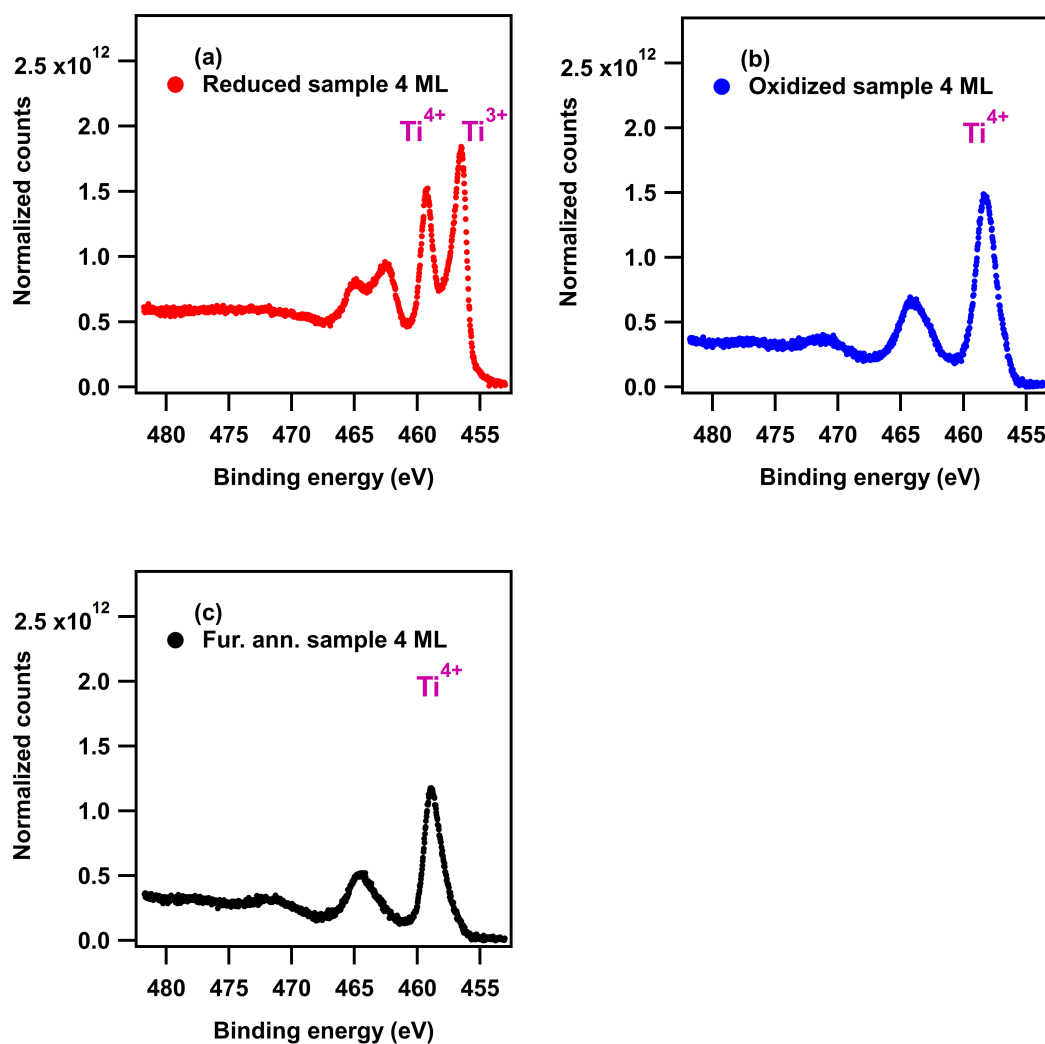


Figure 6.8: High resolution XPS spectrum of the Ti  $2p$  emission lines, taken in normal emission at room temperature at a photon energy of 670 eV for the 4 ML BTO sample in (a) the reduced, (b) the oxidized and (c) the further annealed state.

## 6.4 Stoichiometry

The stoichiometry of 4 ML BTO on Pt(111) has been determined using XPS. First, the spectra have been normalized to the mirror current and then to the number of scans and the integration time per measured point. In addition, a Shirley background has been subtracted. The total Ba  $3d$  area has been approximated by multiplying the Ba  $3d_{5/2}$  line by a factor of 5/3. Then the spectrum area of each emission line has been divided by  $S'$ , according to Eq. 5.2. The results have been normalized to those of Ti and are reported in Tab. 6.2.

As discussed in Sec. 6.3, the O  $1s$  components with binding energies of 531.9 to 533 eV are assigned to contaminations and have been excluded from the spectrum area. Their resulting O stoichiometric ratios are labeled O1 in Tab. 6.2. In a similar calculation, the broad O peaks at 530.6, 530.7 and 531.3 eV have also been subtracted. The resulting values are labeled O2.

The values of photoionization cross section,  $\sigma_A$ , have been taken from [151] (according to [152,

Table 6.1: The values of  $\sigma_A$  and the calculated values of  $\lambda_{m,E}$  and  $S'$  according to Eq. 5.2 calculated for the Ti  $2p$  and the O  $1s$  emission lines at 670 eV and for the Ba  $3d$  at 1000 eV photon energies.

| Element | $\sigma_A$ | $\lambda_{m,E}$ | $S'$    |
|---------|------------|-----------------|---------|
| Ti      | 0.92467    | 6.8 Å           | 0.02953 |
| Ba      | 1.63133    | 6.9 Å           | 0.05102 |
| O       | 0.31353    | 5.6 Å           | 0.01245 |

Table 6.2: The stoichiometry of 4 ML BTO on Pt(111) in the reduced, the oxidized and the further annealed state, determined by XPS, taken in normal and grazing emission angles. O1 stands for O values resulting from subtracting only the contamination peaks from the total O area, while O2 values result from subtracting the broad feature, assigned to O in OH or surface defects, in addition.

| State            | Measur. Tempe. | Emission angle | Ti | Ba   | O1   | O2   |
|------------------|----------------|----------------|----|------|------|------|
| Reduced          | RT             | 0°             | 1  | 0.65 | 3.25 | 1.7  |
| Reduced          | RT             | 70°            | 1  | 0.95 | 4.6  | 2.35 |
| Reduced          | 999 K          | 0°             | 1  | -    | 4.3  | 2.8  |
| Oxidized         | RT             | 0°             | 1  | 0.75 | 5.25 | 2.35 |
| Oxidized         | RT             | 70°            | 1  | 0.95 | 6.15 | 2.75 |
| Further annealed | RT             | 0°             | 1  | 0.8  | 5.5  | 1.55 |
| Further annealed | RT             | 70°            | 1  | 1.1  | 9    | 1.3  |

153].  $\lambda_{m,E}$  is the mean free path of photoelectrons with a kinetic energy of  $E$  in the matrix  $m$ . The values of  $\lambda_{m,E}$  have been determined employing the specifications of bulk BTO, according to [123, 124]. The values of  $\sigma_A$ ,  $\lambda_{m,E}$  and  $S'$  are reported in Tab. 6.1 for photon energies of 670 eV for Ti  $2p$  and O  $1s$  and 1000 eV for Ba  $3d_{5/2}$  emission lines.

The photon energies have been selected to be quite surface sensitive. Except in the further annealed state in grazing emission, the sample in each oxidation state is Ti rich, which is more pronounced in the reduced state with a Ba:Ti ratio of 0.65 in normal emission. This ratio increases to 0.75 and 0.8 in the oxidized and the further annealed states, which indicates increase of Ba in the surface via oxidation. This also agrees with the generally higher Ba:Ti ratio in grazing emission. The rise in this ratio is in agreement with the results for 1 ML BTO, presented in Tab. 5.4, calculated from XAS data.

By excluding the O  $1s$  component with a binding energy of 531.9 to 533 eV (assigned to contaminations), the calculated O:Ti ratios (labeled as O1) show unreasonably large values, particularly in grazing emission. This indicates the presence of oxygen containing adsorbates. The subtraction of the broad O component (at 530.6, 530.7 and 531.3 eV) yields O2, which under estimates the amount of oxygen, in particular for the further annealed state. Although a satisfying separation of the components cannot be achieved, the uptake of oxygen during the oxidation and the accumulation of oxygen at the surface are obvious.

The increase in O:Ti ratio in the oxidized and further annealed states, as well as the larger values in grazing emissions are in agreement with falls in the  $Ti^{3+}$  and rises in  $Ti^{4+}$  components



in the oxidized and further annealed states. Unexpectedly, the amount of O value increases in the reduced state at 999 K, which may be due to an elongation of the sample holder and a change in the investigated spot and inhomogeneities of the sample. The unreasonable values of O:Ti ratios show that the subtraction of contamination components cannot be done properly, particularly in the further annealed state, where the O spectra are quite broad.

## 6.5 X-ray absorption spectroscopy

X-ray absorption spectroscopy has been performed on the sample at the Ti *L*-edge, the O *K*-edge and the Ba *M*-edge in Auger electron yield mode in normal and grazing ( $70^\circ$  from normal) incidences. The corresponding Auger transitions are Ti L<sub>23</sub>M<sub>23</sub>V, O KVV and Ba M<sub>4</sub>N<sub>45</sub>N<sub>45</sub>. The kinetic energy of the Auger electrons are 420, 506 and 598 eV with inelastic mean free paths of 10.23, 11.61 and 13.05 Å in bulk BTO, calculated according to [123, 124]. The values of inelastic mean free path of the Auger electrons mean mixed surface and bulk sensitive XAS measurements.

The X-ray absorption spectra of the sample at two angles of incidence in different oxidation states at the Ti *L*-edge, the O *K*-edge and the Ba *M*-edge are presented in Fig. 6.9, 6.10 and 6.11, respectively. Different transitions in the spectra are labeled according to [171]. For comparison, XAS measurements of a BTO(001) crystal recorded in TEY mode is also given [171].

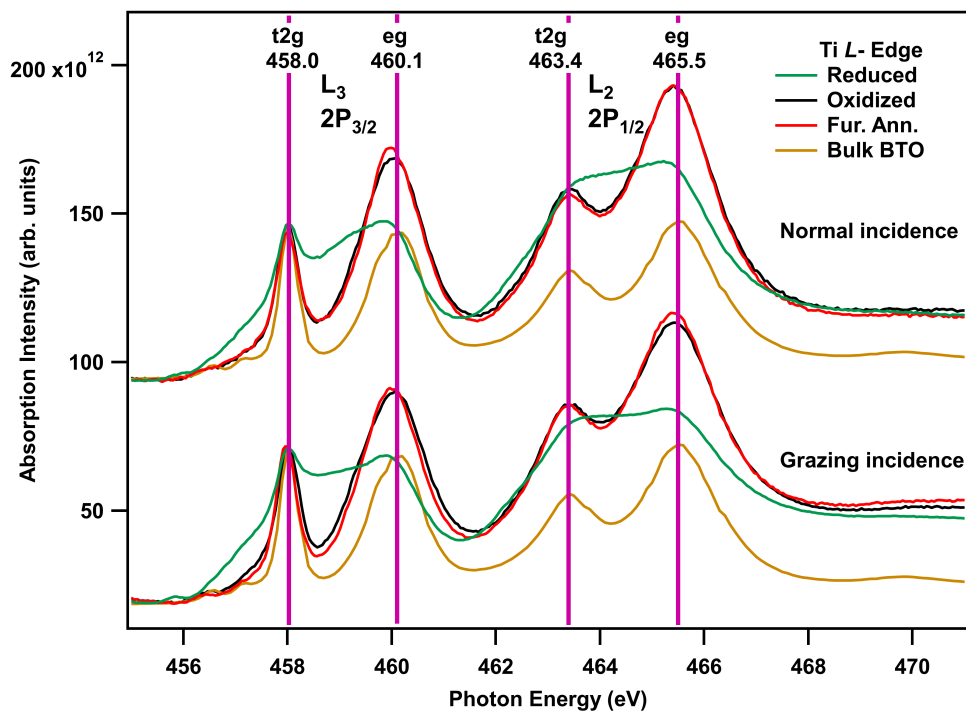


Figure 6.9: X-ray absorption spectrum at the Ti *L*-edge of the reduced, the oxidized and the further annealed state of 4 ML BTO on Pt(111) in normal and  $70^\circ$  off normal incidences and the BTO(001) in normal incidence. The spectra of the 4 ML (bulk) BTO sample were recorded in AEY (TEY) measurement mode. The peaks are labeled according to [171].

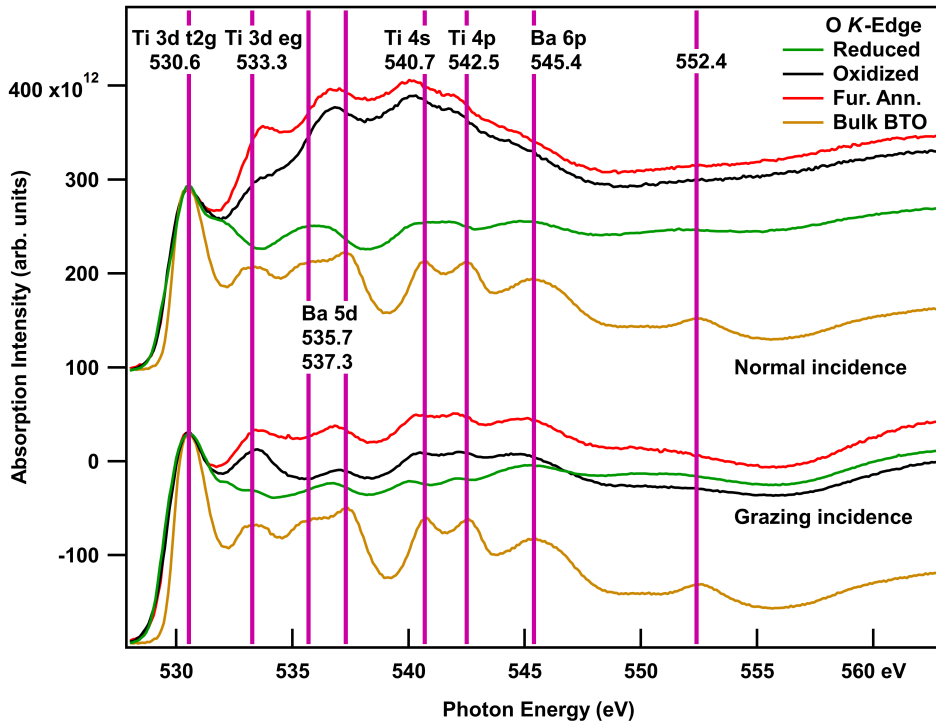


Figure 6.10: X-ray absorption spectrum at the O  $K$ -edge of the reduced, the oxidized and the further annealed state of 4 ML BTO on Pt(111) in normal and  $70^\circ$  off normal incidences and bulk BTO(001) in normal incidence. The spectra of the 4 ML (bulk) BTO sample were recorded in AEY (TEY) measurement mode. The peaks are labeled according to [171].

Figure 6.9 shows a small directional anisotropy in all oxidation states at the Ti  $L$ -edge, similar to the Ti  $K$ -edge (Sec. 5.2). All presented spectra are normalized to have the same height in the  $t_{2g}$  peak at the  $L_3$ -edge. Considering the pre-edge and the post-edge features of the spectra in the reduced state, the spectra in normal and grazing incidences can be viewed as a superposition of the spectra of 6-fold coordinated Ti in bulk BTO and 6-fold coordinated  $\text{Ti}^{3+}$  in  $\text{Ti}_2\text{O}_3$  [172, 173]. This is in agreement to the formation of the OQC layer and the presence of large islands, as also found by AFM (Fig. 6.1 (a)) and XPS measurements in Sec. 6.1 and 6.3.

In the  $\text{Ti}^{3+}$  spectra, the states between the  $t_{2g}$  and  $e_g$  ones are due to lifting the degeneracy of the  $e_g$  levels, where the  $b_{1g}$  level remain at its position and the  $a_{1g}$  level shifts to lower energies. The  $t_{2g}$  levels at 458 eV remain unchanged.

The main XPS line of  $\text{Ti}^{4+}$  in the oxidized state in Fig. 6.3 (b) has the same binding energy as 5-fold coordinated  $\text{Ti}^{4+}$  in a fresnoite glass (458.4 eV [132]). In the further annealed state in Fig. 6.5 (a), the component, which fits to 5-fold coordinated  $\text{Ti}^{4+}$ , is present, while that, which fits to the 6-fold coordinated, is shifted to 459.05 eV. Considering the surface sensitivity of XPS, the presence of an XPS line at 458.2 eV in the oxidized state implies that Ti in small islands and at the surfaces of the large islands has a lower coordination than in the bulk, like a 5-fold coordination. By further annealing the sample in oxygen, the coordination of some  $\text{Ti}^{4+}$  change to 6-fold.

This scenario is in agreement with the XAS measurements. The Ti  $L$ -edge spectra in the oxidized and the further annealed states are quite similar and also similar to bulk. However, the  $t_{2g} - e_g$

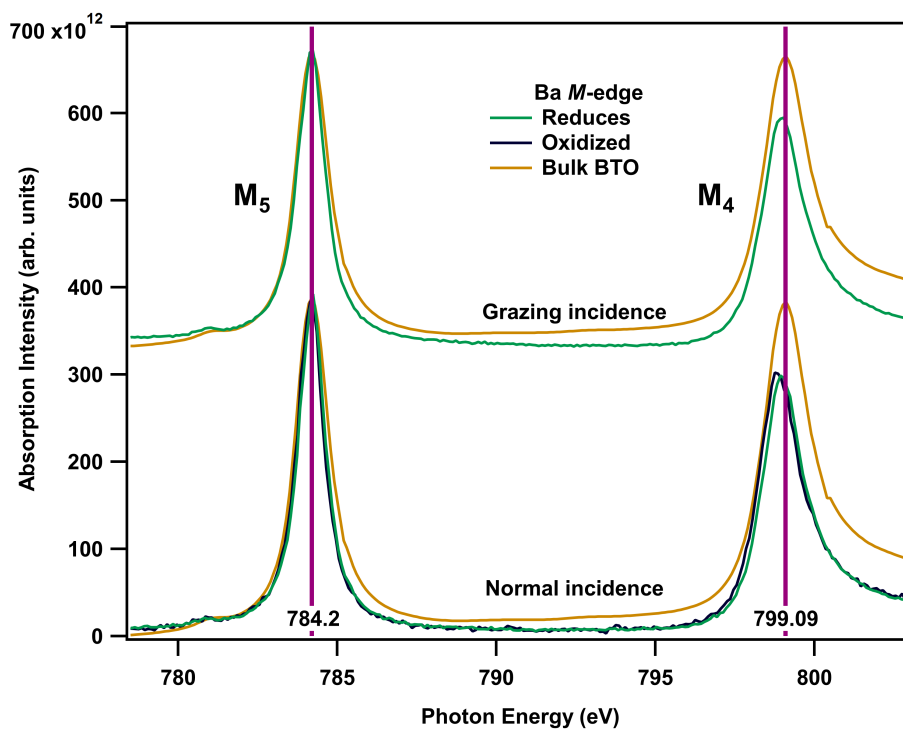


Figure 6.11: X-ray absorption spectrum at the Ba  $M$ -edge of 4 ML BTO sample in the reduced and the oxidized state in normal and  $70^\circ$  off normal incidences and bulk BTO(001) in normal incidence. The spectra of the 4 ML (bulk) sample were recorded in AEY (TEY) measurement mode.

splitting at the  $L$ -edge is 0.1 eV smaller than that of bulk. The 5-fold coordinated  $\text{Ti}^{4+}$  in fresnoite also shows a small decrease in the  $t_{2g} - e_g$  splitting [174]. This point implies that the spectra of the oxidized and the further annealed are composed of 5- and 6-fold coordinated Ti. In addition, the FWHM of the  $e_g$  level at the  $L_3$ -edge in the oxidized state is 1.25 eV, which is broader than that of bulk (1.1 eV), while that of the further annealed one is slightly narrower. This point hints to the presence of at least two structures in the oxidized state, while the amount of the 5-fold coordinated structure in the further annealed state has decreased, which results in the narrowing of the spectra. However, this is a small effect.

The O  $K$ -edge spectra of different oxidation states in two angles of incidence are presented in Fig. 6.10, which are normalized to the first peak at 530.6 eV. The spectra show some differences from bulk. O states are strongly affected by neighbors. This leads to a more complex situation at the O edge than at the Ti edge. Some features in the spectra at the O  $K$ -edge are similar to those in the bulk, but other contributions are clearly present.

In the reduced state, the dip at 532 eV is filled, as expected. This is due to lifting the degeneracy of the  $e_g$  levels, as described above. In all oxidation states, the two Ba  $5d$  resonances are combined to one, while Ba  $6d$  remains overruled by something else. Filling the dips at 539 and 544 eV in the bulk spectra agrees with the presence of the peaks in  $\text{Ti}_2\text{O}_3$ , which are due to a transition from O  $1s$  to O  $2p$ , hybridized with Ti  $4s$  and  $4p$  states [175].

The filling of the dip of the bulk spectrum at 532 eV in the oxidized and the further annealed states may be assigned to the transition of the O  $1s$  to O  $2p$  orbitals hybridized with Ti  $3d$  orbitals

in 5-fold coordinated  $\text{Ti}^{4+}$  similar to fresnoite [176]. Even though the Ti  $L$ -edge and the Ba  $M$ -edge (Fig. 6.9 and 6.11) of the oxidized and the further annealed states are very bulk-like, the spectra of the O  $K$ -edge do not show pure 6-fold coordination of Ti atoms. The features indicate a change in coordination like 5-fold coordination or at least distorted octahedral coordination.

The Ba  $M_{4,5}$ -edge spectra of different oxidation states in two angles of incidence are presented in Fig. 6.11, which are normalized to the first peak at 784.2 eV. The spectra are similar to that of bulk, with well-resolved pre-edge features. However, they are dominated by extremely pronounced resonances, which even hide the step at the  $M_5$ -edge. There is a decrease in the spin-orbit splitting of all spectra, compared to bulk, which can be due to the background in the bulk spectrum. As the spectra show, the oxidation state of Ba in the reduced and oxidized cases remains  $\text{Ba}^{2+}$  and due to the small differences, no more specific conclusion about changes in coordination, which affect hybridization of the Ba  $4f$  and the O  $2p$  levels can be drawn.

In summary, XAS spectra confirm the interpretation of the results from XPS spectra given in Sec. 6.7 and 6.8. The spectra at the Ti  $L$ - and the O  $K$ -edge in the reduced state can be viewed as the superpositions of the spectra of bulk BTO with 6-fold coordinated  $\text{Ti}^{4+}$  and  $\text{Ti}_2\text{O}_3$  with 6-fold coordinated  $\text{Ti}^{3+}$ . The spectra at the Ti  $L$ -edge in the oxidized and further annealed states are composed of 5- and 6-fold coordinated Ti, while the amount of the 5-fold coordinated structure in the further annealed state has decreased. The spectra at the O  $K$ -edge in the oxidized and further annealed states do not show pure 6-fold coordination of Ti atoms and hint to the direction of lowering the coordination, like in a 5-fold coordination or at least a distorted octahedral coordination.

## 6.6 UHV annealing of the reduced 4 ML BTO on Pt(111)

A 4 ML BTO overlayer on Pt(111) in the reduced state was heated in UHV from room temperature up to 999 K. Figure 6.14 (a) shows the Ti  $2p$  spectra taken at RT and at 999 K. All  $\text{Ti}^{4+}$  components show a shift to 0.5 eV to lower binding energies, whereas almost no shift (only 0.05 eV shift) has been observed in the  $\text{Ti}^{3+}$  components. Figure 6.13 shows the corresponding O  $1s$  spectra at RT and at 999 K. The changes in the spectra are compatible with shifts of two components by 0.35 and 0.5 eV, similar to the shifts in the Ti  $2p$  spectra. However, the broadness of the spectra and the overlapping of the components do not exclude other fits.

To investigate these shifts in more details fast XPS measurements have been performed while ramping the temperature from RT up to 950 K and down to RT, as shown in Fig. 8.5. Ti  $2p$  and O  $1s$  emission line have been recorded and analyzed according to the components in Figs. 6.14 and 6.13. The shift of green  $\text{Ti}^{4+}$  component, which is the combined shift of all  $\text{Ti}^{4+}$  components and the shift of the blue O  $1s$  component are shown in Fig. 6.12. In this experiment the overall shift in the O and Ti emission lines are 0.25 and 0.4 eV and occur simultaneously. The shift of the O  $1s$  line is completely reversible, whereas the backward shift is smaller than the forward shift in the Ti  $2p$ , as illustrated in Fig. 8.6. The simultaneous shift of both components and the pre-dominant reversible process indicate that the reason for this shift is not a change in chemical state but a field

effect across an insulator, for example band bending.

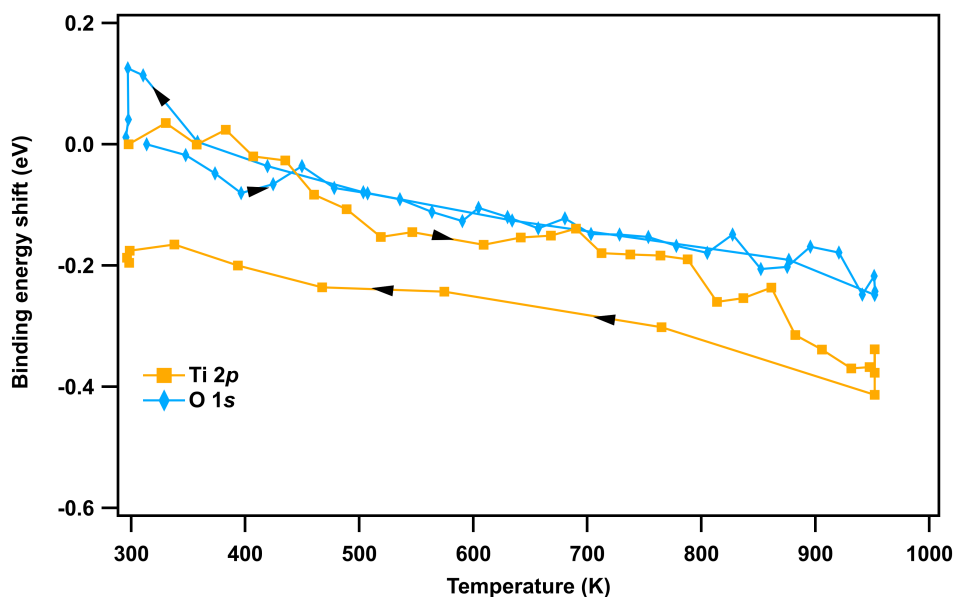


Figure 6.12: The binding energy shifts of the green  $\text{Ti}^{4+}$  (in Fig. 6.3) and the blue O 1s components (in Fig. 6.13) during heating the 4 ML BTO sample in UHV up to 950 K and cooling down to RT, taken at a photon energy of 670 eV, in normal emission (Fig. 8.5).

The presence of  $\text{Ti}^{3+}$  means doping and an increase in conductivity, which in turn suppresses such field effects and leads to  $\text{Ti}^{3+}$  and O components, which do not shift. Therefore, we expect an inhomogeneous distribution of  $\text{Ti}^{3+}$  in across the surface.

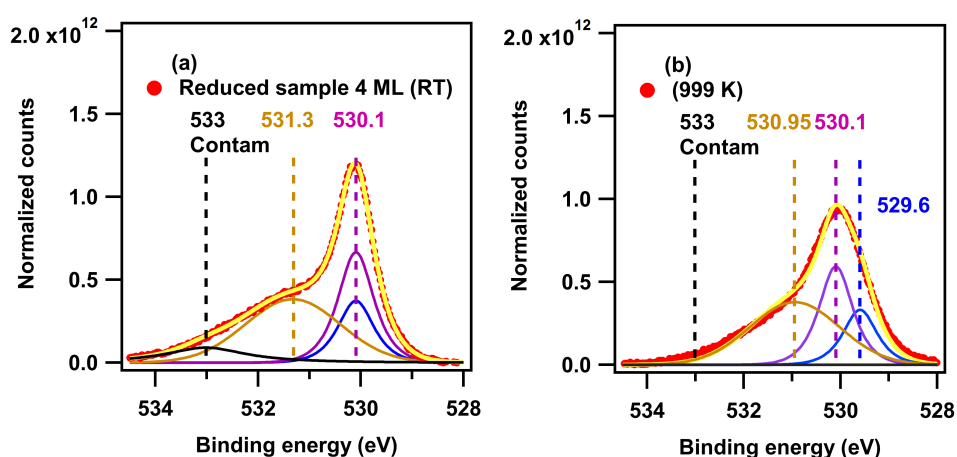


Figure 6.13: High resolution XPS spectrum of the O 1s emission lines, taken in normal emission at (a) RT and (b) 999 K for 4 ML BTO sample in the reduced state at a photon energy of 670 eV.

## 6.7 Oxidation of 4 ML BTO on Pt(111)

Monitoring the dewetting of the Pt surface via the coalescence of the wetting layer into islands is extremely interesting. It enables to investigate the coordination changes in the islands and the layer. As the sample in the reduced state was at 387 K, oxygen was injected into the chamber up to a pressure of  $5 \times 10^{-7}$  mbar and the sample was heated first to 774 K and then to 825 K. At this state, high resolution spectra of the Ti 2*p*, the O 1*s* and the Ba 3*d* emission lines were recorded (Fig. 6.14 (b) and Fig. 6.15). The sample was then cooled down in O<sub>2</sub>. The oxygen valve was closed at 373 K and the measurement stopped at 363 K. After taking a LEED image at 66 eV, XAS and XPS spectra of Fig. 6.3 (b) and Fig. 6.4 (b,d) were recorded. The  $1 \times 1$  pattern confirms the formation of BTO islands.

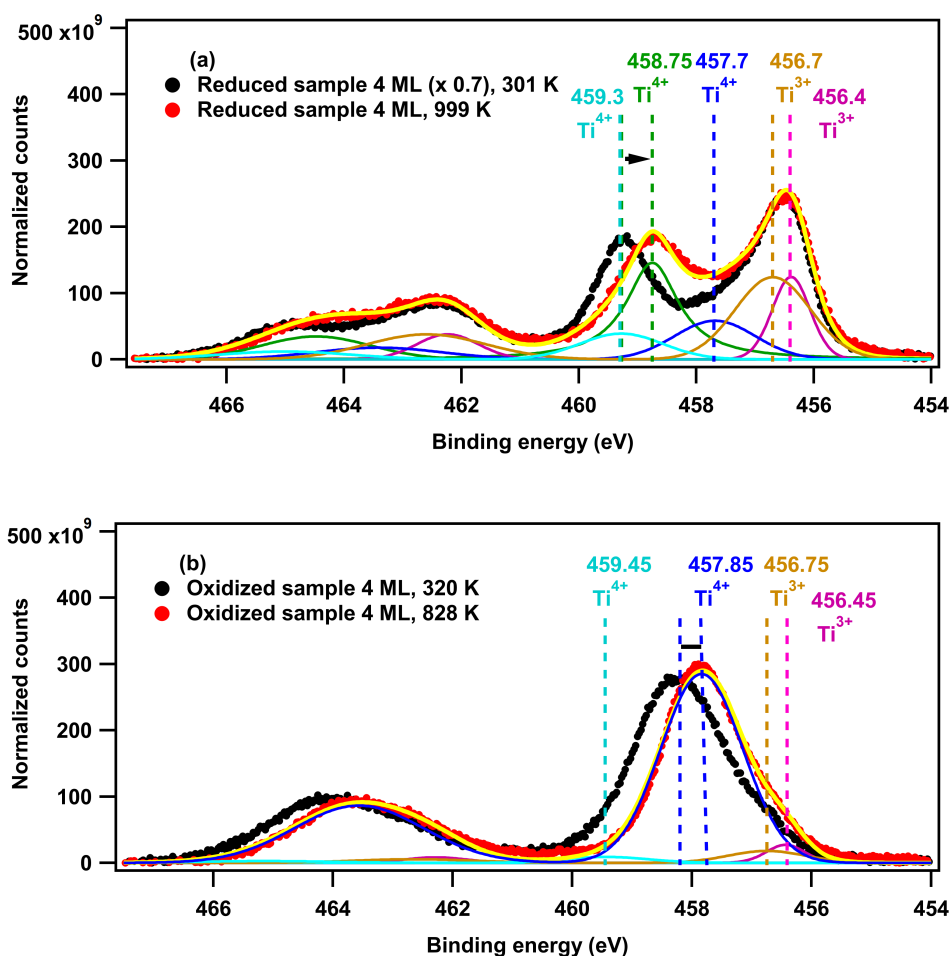


Figure 6.14: High resolution XPS spectrum of the Ti 2*p* emission lines of the 4 ML BTO sample in normal emission, (a) taken in the reduced state at 301 and 999 K (UHV annealed) and (b) taken in the oxidized state at 320 and 828 K (oxygen annealed at  $5 \times 10^{-7}$  mbar O<sub>2</sub>), at a photon energy of 670 eV.

While heating and cooling the sample, XPS spectra of the Ti 2*p* and the Pt 4*f* emission lines have been recorded at a photon energy of 670 eV. The binding energies of the Ti 2*p* spectra have been determined by referring to Pt 4*f* lines with a precision of  $\pm 0.05$  eV.

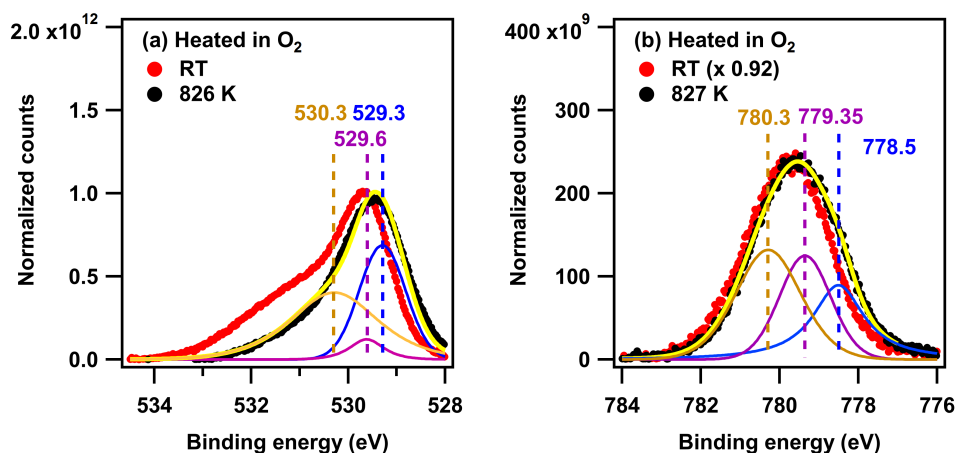


Figure 6.15: High resolution XPS spectrum of the 4 ML BTO sample of (a) the O  $1s$  and (b) the Ba  $3d_{5/2}$  emission lines, taken at RT (sample in the oxidized state) and at 826 K (oxidizing at  $5 \times 10^{-7}$  mbar  $O_2$ ) with a photon energy of 670 eV for the O  $1s$  line and 1000 eV for the Ba  $3d_{5/2}$  line in normal emission.

Similar to the shifts in binding energy observed during the UHV annealing of the reduced sample, shifts in binding energy have also been observed with the oxidized sample. For example, during oxidation,  $Ti^{4+}$  components shifted by 0.35 eV to lower binding energies at 828 K compared to those at RT in the reduced or oxidized states (Fig. 6.3 (a,b)), whereas  $Ti^{3+}$  components remained constant. During cooling, the O  $1s$  and the Ba  $3d_{5/2}$  components shift up by 0.3 eV, which is close to the 0.35 eV shift of  $Ti^{4+}$  components.

Figure 6.16 presents the relative binding energy shifts of the two  $Ti^{4+}$  components in the reduced (the green peak) and in the oxidized (the blue peak) states. As a guide for the eye, a straight line has been fitted to the points of the reduced sample. Since the points of the oxidized sample show the same behavior, it indicates that the same field effect is the reason for the shift. Since in the oxidized sample all islands are supposed to be rather insulating, it confirms the idea that on the reduced sample, insulating and conducting regions are present. Figures 6.12 and 6.16 are combined in Fig. 8.7.

The spectra of the Ti  $2p$  lines while heating and cooling ramps are presented in Fig. 6.17. The spectra have been normalized to the footpoints of the corresponding Pt spectra. The spectra have been fitted by the same components as the high resolution spectra in Fig. 6.3. The changes in binding energies and relative areas of the individual components during the experiment are presented in Fig. 6.18. With a photon energy of 670 eV, the inelastic mean free path of the photoelectrons from Ti atoms is 6.8 Å (Tab. 6.1). This leads to a high surface sensitivity, so that the main portion of the spectrum originates from small islands, which are about 3 ML and are formed by the coalescence of the OQC layer via oxidation [41], as well as from a surface layer of 4 to 5 ML of large islands (Fig. 6.1). Although the high resolution spectrum before the ramp at 402 K shows a binding energy of 459.05 eV for the green  $Ti^{4+}$  component (Fig. 8.8), injecting oxygen leads to a shift of this component to its lowest value at 458.9 eV in the first spectrum of the ramp at 387 K

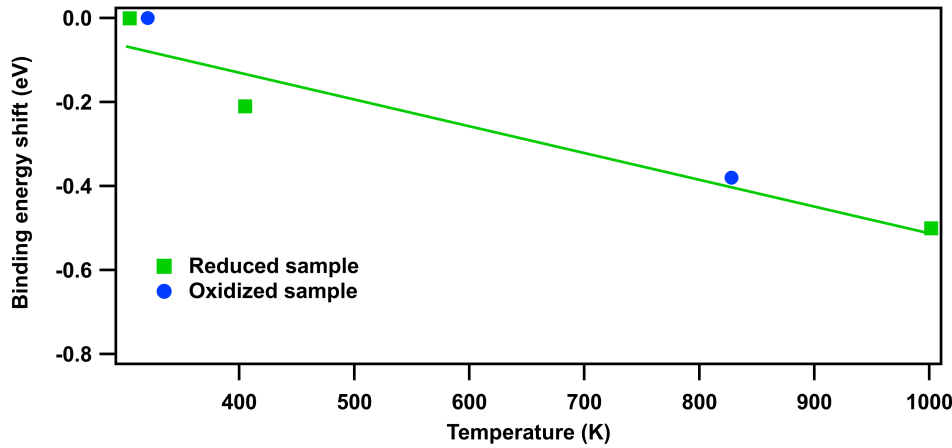


Figure 6.16: Binding energy shifts of the  $\text{Ti}^{4+}$  components in Fig. 6.14 via heating in UHV, referenced to the green  $\text{Ti}^{4+}$  component at 549.25 eV at 301 K in the reduced state, shown as green squares and are fitted with a line. The blue circles indicate the shifts in the blue  $\text{Ti}^{4+}$  component, referenced to its binding energy at 548.2 eV (at 320 K) in the oxidized state, while oxidizing of the 4 ML BTO sample at  $5 \times 10^{-7}$  mbar  $\text{O}_2$ .

and further heating does not affect the binding energies any longer. This shows the role of oxygen uptake in the binding energy of the  $\text{Ti}^{4+}$  components. The back shifting of the binding energies during cooling from 458.9 eV at 825 K to 459.05 eV at 363 K has been resolved by the experiment and shown by the analysis in Fig. 6.18.

During the oxidation, the relative area of the blue  $\text{Ti}^{4+}$  component (at 458.2 eV at RT) grows dramatically and the relative area of the orange  $\text{Ti}^{3+}$  component at 456.75 eV decreases to one half at the end of the ramp. The relative area of the magenta  $\text{Ti}^{3+}$  component at 456.45 eV and the green  $\text{Ti}^{4+}$  component (at 459.25 eV at RT) vanish almost completely. The light blue  $\text{Ti}^{4+}$  component (at 459.8 eV at RT) is too small for the detection of any change.

As shown in Fig. 6.18, from room temperature to 725 K, there is a simultaneous decrease in the green  $\text{Ti}^{4+}$  and both  $\text{Ti}^{3+}$  components and an increase in the blue  $\text{Ti}^{4+}$  one. The conversion of the green  $\text{Ti}^{4+}$  to the blue  $\text{Ti}^{4+}$  is complete, whereas the conversion of  $\text{Ti}^{3+}$  to  $\text{Ti}^{4+}$  is partial (25%), presumably  $\text{Ti}^{3+}$  at the surface and not in the bulk. 50% conversion of  $\text{Ti}^{3+}$  is achieved at the temperature of 775 K and 75% at 825 K.

The observed growth and decay of components suggest the following scenario. During the initial heating of the reduced sample in oxygen (below 725 K) oxygen vacancies at the surface are filled and  $\text{Ti}^{3+}$  at the surface are converted to  $\text{Ti}^{4+}$ , but  $\text{Ti}^{3+}$  in the bulk of islands remains unaffected. The complete conversion of the 6-fold to the 5-fold  $\text{Ti}^{4+}$  at such low temperatures casts some doubt on the assignment of the 5-fold  $\text{Ti}^{4+}$ . Maybe the blue line originates from a different and so far unknown  $\text{Ti}^{4+}$  species. The temperature increase to 825 K results in a further decrease of  $\text{Ti}^{3+}$  and dewetting of the Pt surface and the formation of small islands, in which  $\text{Ti}^{4+}$  is also 5-fold coordinated by oxygen.

Further annealing the sample in oxygen results in the growth of a new  $\text{Ti}^{4+}$  component at



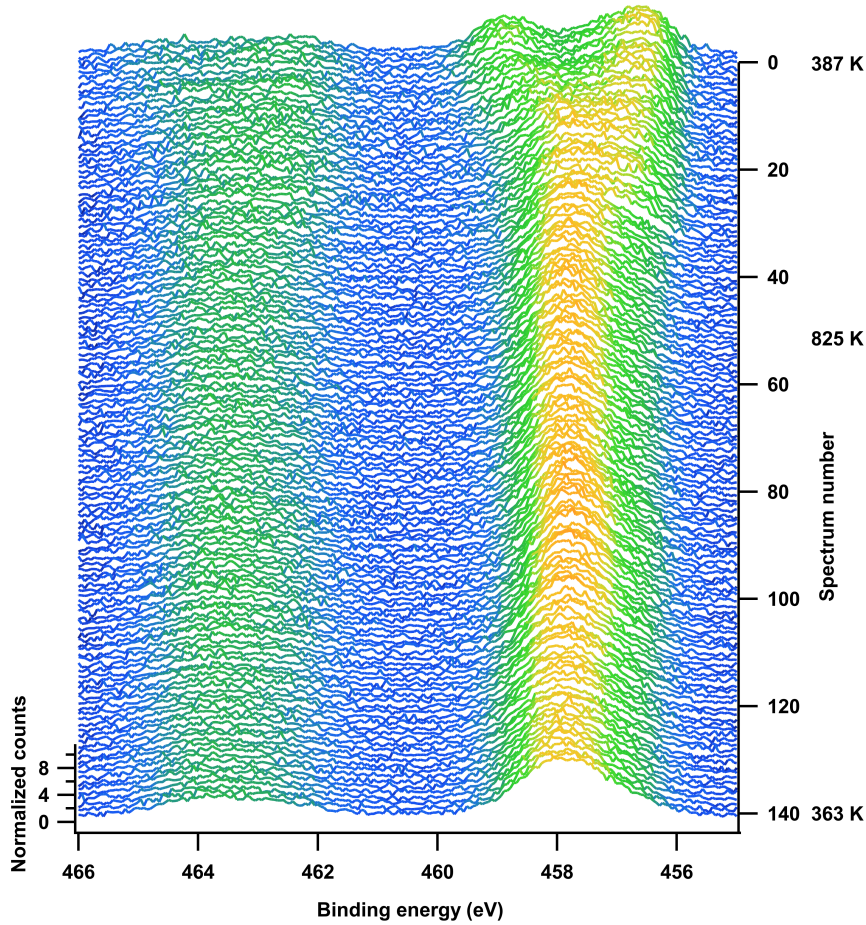


Figure 6.17: The Ti  $2p$  emission lines of 4 ML BTO on Pt(111), taken in normal emission during oxidation in  $5 \times 10^{-7}$  mbar  $O_2$ . The binding energy of every individual spectrum has been corrected by referring to the Pt  $4f$  spectrum.

459.05 eV (Fig. 6.5 (a)), which is shifted by 0.2 eV compared to the green  $Ti^{4+}$  component at 459.25 eV (Fig. 6.3 (a)). Due to similar binding energies, this new component is also assigned to 6-fold coordinated  $Ti^{4+}$ . Annealing the sample in UHV below 675 K (Sec. 6.8), results in two processes: 1) Reduction of 5-fold coordinated  $Ti^{4+}$  to  $Ti^{3+}$ . 2) Transformation of 5-fold coordinated  $Ti^{4+}$  to 6-fold coordinated  $Ti^{4+}$  (Fig. 6.22). In the temperature range between 870 to 1020 K rewetting of the Pt surface and the formation of OQCs occur. While rewetting, the small islands with 6-fold coordinated  $Ti^{4+}$  collapse. The collapse of the 6-fold coordinated  $Ti^{4+}$  results in a sudden increase in the orange component of  $Ti^{3+}$  with the binding energy of 456.75 eV (at RT). This concurrently results in a sudden decrease in the surface component of the Pt  $4f$  signal, which proves the simultaneousness of these two processes. During the formation of OQCs, no pronounced intensity change has been observed in 5-fold coordinated  $Ti^{4+}$  or the magenta component of  $Ti^{3+}$ .

The jump in the relative area ratio of the orange  $Ti^{3+}$  and the blue  $Ti^{4+}$  components at 774 K originates from a short pause in the experiment, while the temperature and  $O_2$  pressure have been kept constant. It needs to be mentioned that the presented experiment durations in this chapter are the sum of all of measurement times, while the time of pauses have been skipped. Since the

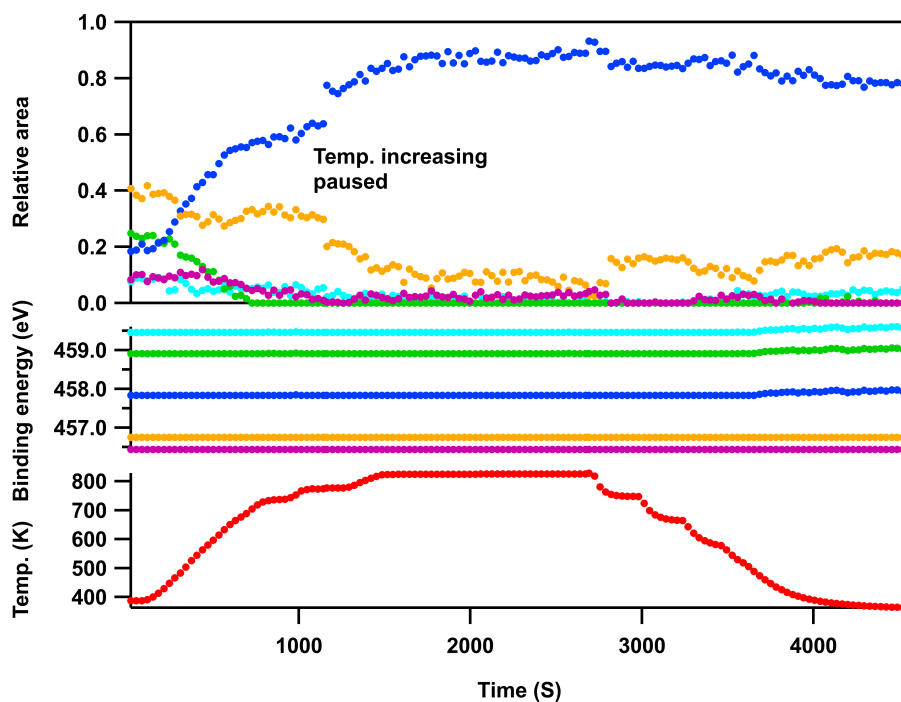


Figure 6.18: Temperature, relative areas and binding energies of individual components of the Ti 2*p* emission lines of 4 ML BTO on Pt(111) versus time, taken in normal emission during oxidation in  $5 \times 10^{-7}$  mbar O<sub>2</sub>, shown in Fig. 6.17. The color codings of the components are the same as Fig. 6.3.

temperature has been kept at 774 K, the processes continued, which resulted in the increase of the blue Ti<sup>4+</sup> and the decrease of the orange Ti<sup>3+</sup> component.

The relative area changes of the total Ti<sup>3+</sup> and the total Ti<sup>4+</sup> components are presented in Fig. 6.19. The relative total Ti<sup>3+</sup> area decreases from 0.5 in the reduced state to 0.2 in the oxidized state, while the relative total area of Ti<sup>4+</sup> increases from 0.5 to 0.8.

As discussed previously, OQCs coalesce into BTO(111) islands via oxidation. This leads to a decrease in the total area of the XPS spectra of the BTO elements. The coalescence of OQC into islands also leads to an increase in total area in the XPS of Pt 4*f* spectra. To investigate the variation of the total spectrum areas, they need to be properly normalized. Two methods of normalization have been tried in this work. The first approach is normalizing to the mirror currents, before background subtraction. The results are appended to the right axis as blue curves in Fig. 6.19.

The second approach is normalizing to the footpoint of the Pt spectra. The results are appended to the left axis as the curves in Fig. 6.19. Comparing the two approaches, the normalization to Pt footpoints leads to smaller temperature dependent fluctuations in the total area of Pt, while no pronounced difference is present in case of Ti.

The XPS measurements have been performed at 670 eV, which is quite surface sensitive for Ti and more bulk sensitive for Pt. However, no distinct change in the total areas of Ti and Pt have been observed by either of the two normalization methods. The expectations are not met, specially regarding the Ti total area, considering the surface sensitivity of measurements. This may be due

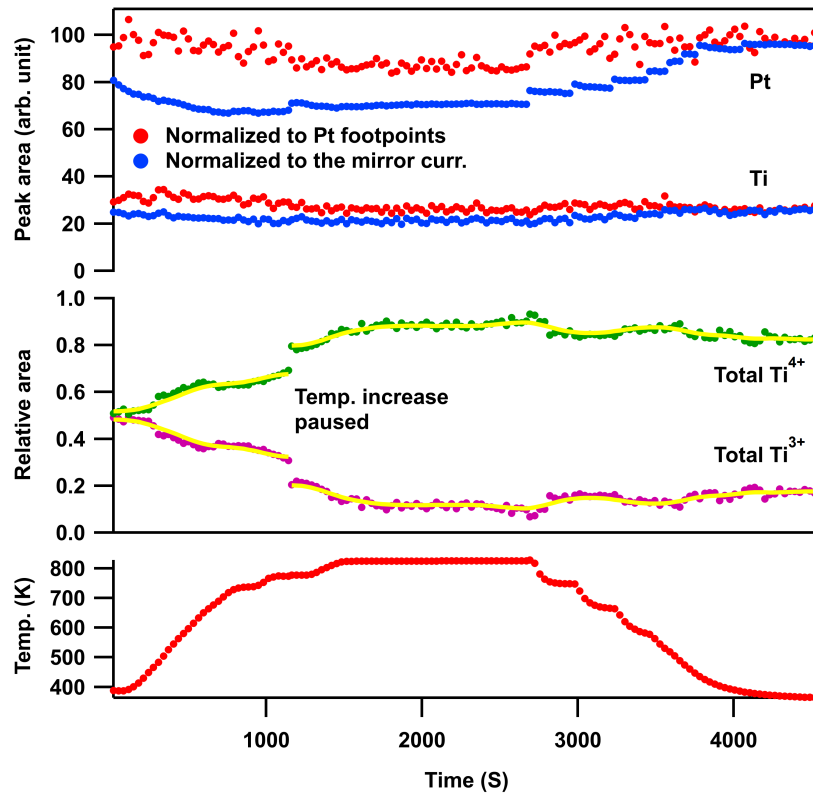


Figure 6.19: Relative areas of the total Ti<sup>3+</sup> and the total Ti<sup>4+</sup> contributions of the Ti 2*p* emission lines of 4 ML BTO on Pt(111) versus time, during oxidation in  $5 \times 10^{-7}$  mbar O<sub>2</sub>, shown in Fig. 6.17, taken in normal emission. The total Ti and Pt areas normalized to the mirror current (Pt footprints) are appended to the right (left) axis.

to an elongation of the sample holder and a change in the investigated spot and inhomogeneities of the sample.

A second oxidation ramp has been performed on the sample once it had been brought back to the reduced state. The sample has been annealed in  $5 \times 10^{-7}$  mbar O<sub>2</sub>, starting at room temperature and up to 825 K and then cooled down in O<sub>2</sub> to room temperature. While performing this experiment, Ti 2*p* and O 1*s* emission lines have been recorded. The O spectra are presented in Fig. 6.20. For the presentation, the O spectra have been normalized to their footprints.

The fits of the O spectra have been performed using the peaks with the same line shapes as those in Fig. 6.4 (a,b). Results of the fits are presented in Fig. 6.20. The color codings of the components are the same as Fig. 6.4. For performing the fits, the energy difference between the peaks at 529.75 and 530.1 eV was set to 0.35 eV and the energy difference of the next two peaks was set to 1.35 eV. All peaks were allowed to shift their energies via the ramp. These conditions were set because the peak at 533 eV at RT is assigned to contaminations and the peak at 531.3 eV at RT is probably due to OH groups or defects. Hence, they are allowed behave differently as the first two peaks at 529.75 and 530.1 eV at RT. After fitting, the difference between the fit and the experimental spectrum is smaller than 1% of the overall peak area.

During the ramp, the O 1*s* component at 529.75 eV undergoes a shift of 0.65 eV towards lower

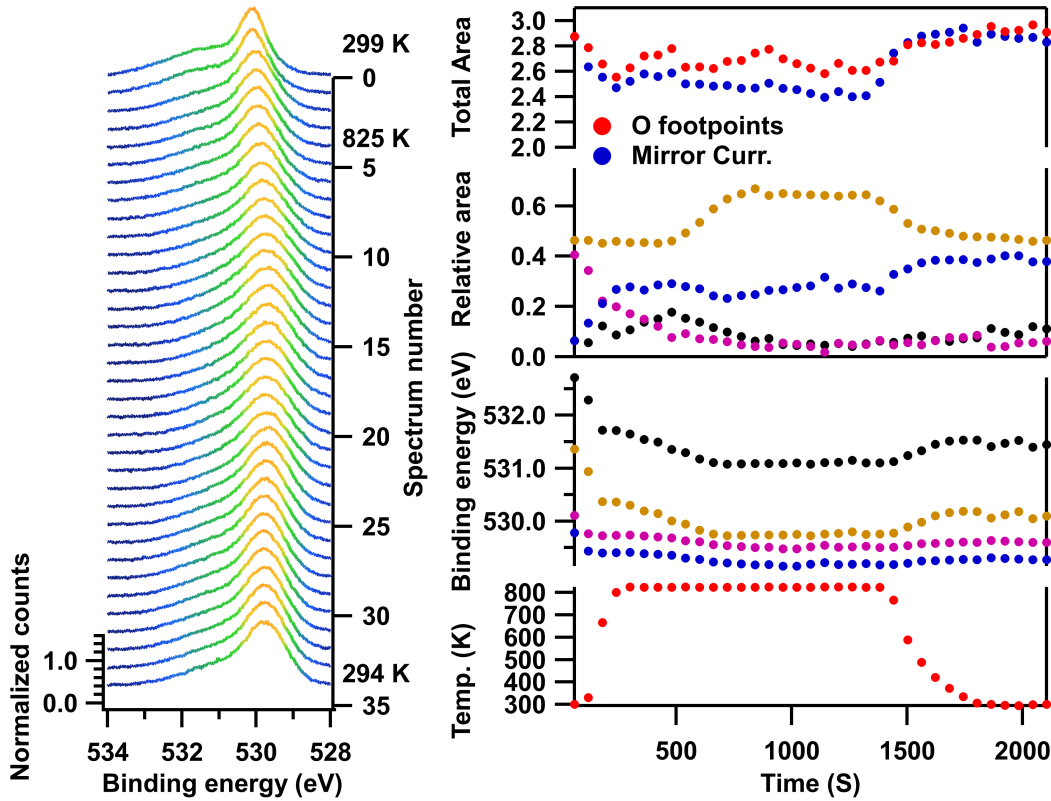


Figure 6.20: The O  $1s$  emission line of 4 ML BTO sample during oxidation in  $5 \times 10^{-7}$  mbar  $O_2$ , taken at a photon energy of 670 eV in normal emission. Temperature, relative areas and binding energies of individual components are plotted versus time. The color codings of the components are the same as in Fig. 6.4 (a,b). The total spectrum areas normalized to the mirror current (O footpoints) are appended to the right (left) axis.

binding energies while heating and shifts back by 0.15 eV while cooling. This leads to a total shift of 0.5 eV via oxidation. However, the comparison to the high resolution spectra in Sec. 6.3, which their binding energies have been corrected properly, reveals that the total shift via oxidation is 0.15 to 0.2 eV. The validity of this has been checked by comparing the shifts of the tops of the main components in the high resolution O  $1s$  peaks in the reduced and oxidized states (Fig. 6.4 (a,b)) and the initial and final spectra of the ramp. The top of O peak in the reduced state at 530.1 eV shows a shift by 0.4 eV to lower energies in the oxidized state (529.7 eV), while the comparison of the first and last spectrum of the ramp shows 0.7 eV, an additional shift of 0.3 eV. This additional shift arises from not adequately referencing the O spectra. Subtracting this additional 0.3 eV shift from the 0.5 eV shift of the spectra of the ramp leads to the expected 0.2 eV shift of the O  $1s$  components during the oxidation process. Besides changes, which originate from the chemical changes, there are clear indications for shifts from field effects, like band bending.

Variations of relative areas of components are shown in Fig. 6.20. The figure clearly presents the decay and the growth of the magenta and blue components via oxidation, which can be assigned to the O attached to  $Ti^{4+}$  in a 6-fold and 5-fold arrangements. The broad component at 531.3 eV at

room temperature (assigned to OH or O in defects), increases considerably at higher temperatures and decreases while cooling. This component was set to have higher binding energy than the magenta one, as a fit constraint. As a result, this component got quite close to the magenta peak and took a high portion of spectrum area at high temperatures. The black component in Fig. 6.20, assigned to the contaminations (Sec. 6.3), approaches zero at high temperatures, while it grows again while cooling. This may be due to readsorbing residual gases.

To avoid the high intensities for the broad peak, the fit was repeated by keeping differences between all peaks the same as in Fig. 6.4 (a,b) and the results are presented in Fig. 8.9. Although the new fit is not completely satisfying, two main results agree with the initial approach: The 0.5 eV shift in the binding energy of the major peak, which partially results from the decay of the magenta component (in the reduced state) and the growth of the blue component (in the oxidized state). The large area of the orange component, even at high temperatures, which makes the assignments to OH or oxygen at defects questionable. We suggest further XPS investigations to resolve the nature of this component.

Through the oxidation, the total area of the O 1s spectrum is expected to increase. To investigate this, the O spectra have been normalized to their footpoints and to the mirror current. The results are appended to the left and the right axis in Fig. 6.20. By increasing temperature from RT to 825 K, the total area decreases in both approaches and almost keeps its level, as the temperature is kept at 825 K. The initial decrease may be due to desorption of oxygen by increasing the temperature. During cooling, the total area increases in both approaches indicating adsorption of oxygen by the system. However, the expected change is about 10%, whereas the observed changes are higher. At the end of the ramp, the amount approaches the initial value.

In summary, the rewetting of Pt(111) surface during oxidation of BTO-derived OQCs has successfully been monitored by XPS at the Ti 2*p* and O 1s emission lines. It has been found that during the initial heating in oxygen (below 725 K), Ti<sup>4+</sup> in the top layers of large islands changes coordination from 6- to 5-fold. The reason is attributed to the penetration of O atoms to deeper layers of the large islands to react with Ti<sup>3+</sup>. The temperature increase to 825 K results in the sudden decrease in Ti<sup>3+</sup> at 457.75 eV due to dewetting of the Pt surface and formation of small islands, in which Ti<sup>4+</sup> is also 5-fold coordinated by oxygen. The fall of the magenta and the raise of the blue component of the O 1s via oxidation may be assigned to the decay and growth in the O species attached to Ti<sup>4+</sup> in a 6-fold and 5-fold arrangements. The binding energy shifts in Ti<sup>4+</sup> components are due to band bending and affect emission lines of other components while annealing in oxygen, with almost the same amount.

## 6.8 Reduction of 4 ML BTO on Pt(111)

The sample in the further annealed, oxidized state (Fig. 6.5) was heated in UHV up to 676 K, where the recording was stopped due to a beam loss. The experiment could be continued after 90 min by heating the sample up to 872 K, where the temperature was kept constant and high resolution

XPS spectra have been taken. The experiment was then continued by increasing the temperature to 1029 K and then cooling down to 419 K. Via the reduction ramp in UHV, the Ti 2*p* and the Pt 4*f* emission lines were recorded at a photon energy of 670 eV in normal emission. The binding energies of the Ti 2*p* lines were referenced to the Pt 4*f* lines. The fluctuations in the Pt spectra were between  $-0.15$  to  $+0.2$  eV. The resulting Ti 2*p* and the Pt 4*f* spectra are presented in Fig. 6.21 and 6.25.

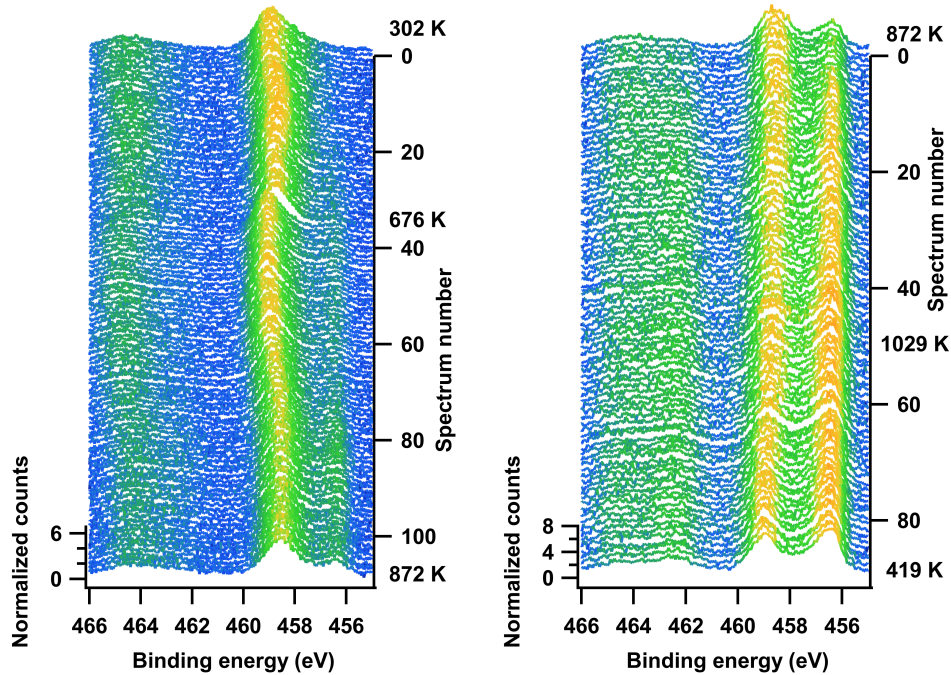


Figure 6.21: The Ti 2*p* spectra while reducing the 4 ML sample in UHV by heating up to 1029 K, taken in normal emission. The binding energies of the spectra were corrected by referencing to the Pt 4*f* lines.

The fitting of Ti spectra has been performed employing the peaks with the same line shapes as those in Fig. 6.5 (a) with minor changes, which will be explained later.  $\text{Ti}^{4+}$  components were allowed to move, while their binding energy differences were kept constant. Similarly, the  $\text{Ti}^{3+}$  components were allowed to shift, independently from the  $\text{Ti}^{4+}$  components, but with a fixed difference to each other. The shifts in binding energies, as well as variations of relative areas are presented in Fig. 6.22.

As mentioned in Sec. 6.7, via further annealing the sample at 925 K in  $1 \times 10^{-5}$  mbar  $\text{O}_2$ , a similar  $\text{Ti}^{4+}$  component as the green one in Fig. 6.3 (a) grows with a binding energy of 459.05 eV. It is colored black in Fig. 6.5 (a). During reduction in UHV, this component vanishes completely, while the green component grows. The fit of the whole ramp was performed by doublets as in Fig. 6.3 by adding the black doublet in Fig. 6.5 to resolve the intensity transfer between the green and the black  $\text{Ti}^{4+}$  components, as depicted in Fig. 6.23. It needs to be mentioned that the light blue Ti component at 459.8 eV at RT in Fig. 6.3 is small and could not reliably be determined. Therefore, it was not included in the fit.

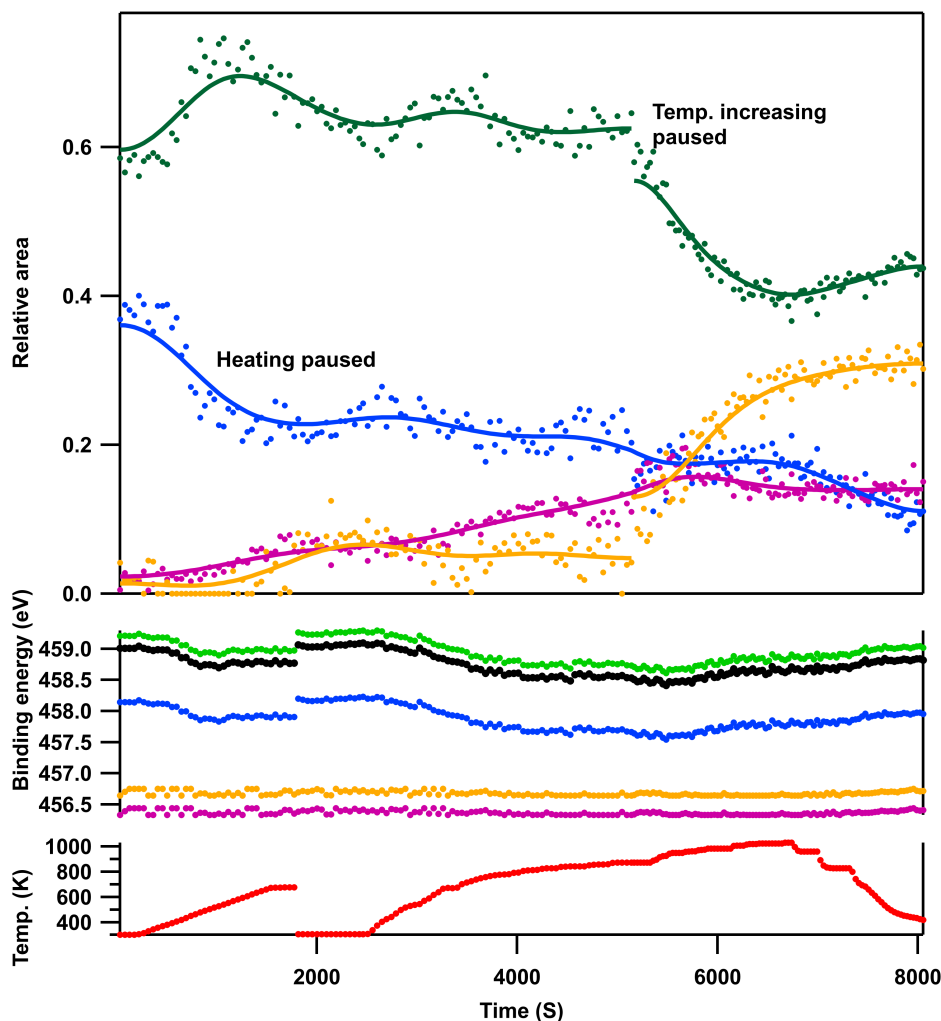


Figure 6.22: Temperature, relative areas and binding energies of individual components of the Ti 2*p* emission lines of 4 ML BTO on Pt(111) versus time, taken in normal emission during reduction in UHV, shown in Fig. 6.21. The color codings of the components are the same as Fig. 6.3 (a,b) and 6.5 (a).

The attempt to resolve the intensity changes between the black and the green Ti<sup>4+</sup> components was not successful, since the energy difference between the two was too small (0.2 eV). Hence, the sum of their relative intensities is depicted in dark green in Fig. 6.22. During the pause in the experiment at  $t = 5140$  s (871 K), a high resolution Ti 2*p* spectrum in normal emission was recorded, as shown in Fig. 6.23. The black Ti<sup>4+</sup> component has dramatically decreased. Therefore, the intensity of this component was set to zero for fitting the rest of the ramp. Since the binding energies of the black and the green Ti<sup>4+</sup> components are so similar, here both are assigned to 6-fold coordinated Ti<sup>4+</sup>.

The binding energies of Ti<sup>4+</sup> components shift with temperature. The maximum observed shift is 0.55 eV, while it shifts back as the sample was cooled down to 419 K. At this temperature, the green Ti<sup>4+</sup> component has a binding energy of 459.05 eV, which agrees quite well with the binding energy of that in a high resolution spectrum at 402 K (459.05 eV, Fig. 8.8). Ti<sup>3+</sup> components show

no significant shifts.

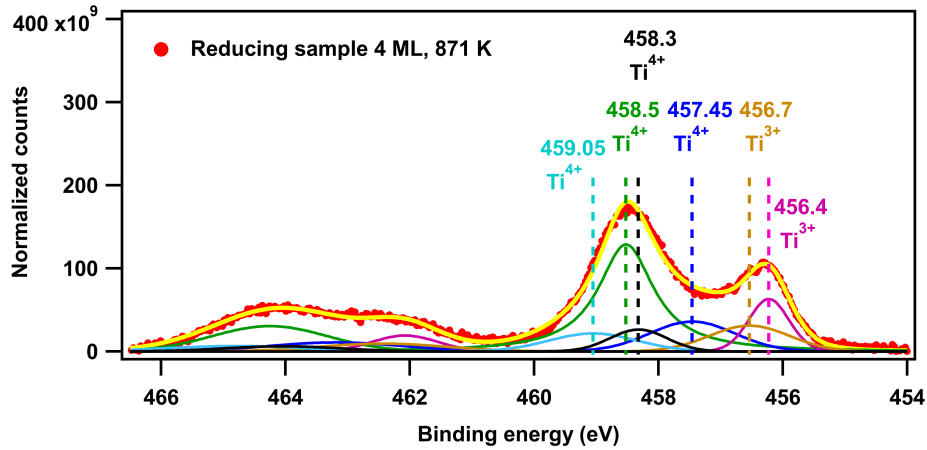


Figure 6.23: High resolution XPS spectrum of the Ti  $2p$  emission lines of the 4 ML BTO sample, taken at 871 K (while annealing in UHV) at a photon energy of 670 eV, in normal emission.

As mentioned, during the initial annealing in UHV (below 675 K), the 5-fold coordinated  $\text{Ti}^{4+}$  converts to 6-fold coordinated  $\text{Ti}^{4+}$ , while the  $\text{Ti}^{3+}$  components start to form in islands (Fig. 6.22). Further increase in temperature results in a slow and simultaneous decrease in both  $\text{Ti}^{4+}$  components and an increase in both  $\text{Ti}^{3+}$  components. In the temperature range between 950 and 1020 K, the small islands (with 6-fold coordinated  $\text{Ti}^{4+}$ ) collapse and form the OQC layer. The rewetting of the Pt surface by the layer in this temperature range is shown by the decrease in the surface component of the Pt  $4f$  signal (Fig. 6.24). The formation of the OQC layer leads to sudden increase in the orange  $\text{Ti}^{3+}$  component (456.75 eV binding energy at room temperature), which represents the binding energy of Ti in OQCs. The binding energy of this component in this sample with 4 ML coverage is comparable with that in the 1 ML sample (456.6 eV), discussed in Sec. 5.2.3.

The orange  $\text{Ti}^{3+}$  component at 456.75 eV in Fig. 6.22 dramatically increases in the temperature range of 950 to 1020 K, while the magenta component is almost constant. The increase is also visible in Fig. 6.21. This sudden increase also shows different behaviors of two  $\text{Ti}^{3+}$  components. At the end of the reduction ramp, the system returns to the reduced state in Fig. 6.3. In deed, the system can undergo the same oxidation reduction loops, several times.

As a result of rewetting of the Pt surface, an increase in the total Ti signal and a decrease in the total Pt signal are expected. The total Ti and Pt spectrum areas are presented in Fig. 6.24, which are obtained by normalizing the signals to the mirror currents (appended to the right axis, the axis values are not shown) and to the footpoints of the Pt spectra (appended to the left axis). For both normalizations the Pt curves show variations with time and temperature. However, the behavior does not really fit to the wetting process. The Ti curves show an increase in the last section, which fits to wetting of the pt surface by Ti.

The relative areas of the total  $\text{Ti}^{3+}$  and the total  $\text{Ti}^{4+}$  contributions of the Ti spectra are depicted in Fig. 6.24. In the last part of the ramp, where the temperature increases from 915 to 983 K, the relative area of  $\text{Ti}^{4+}$  undergoes a 20% decrease, while the relative area of  $\text{Ti}^{3+}$  increases by 45%.



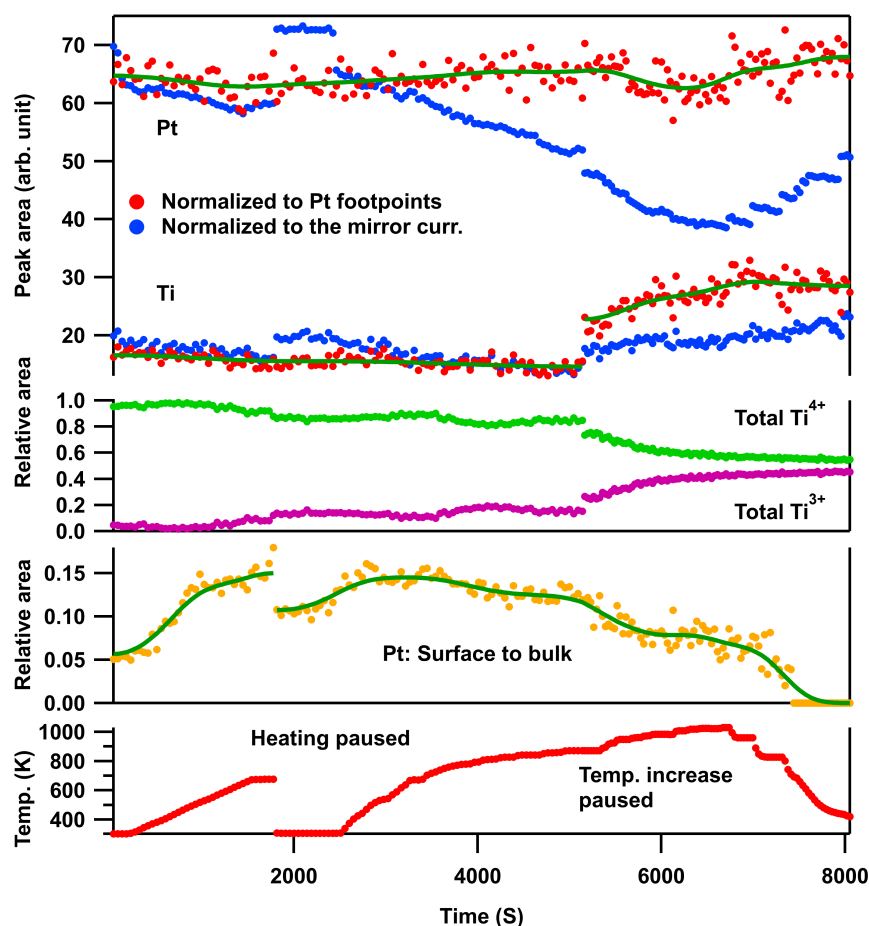


Figure 6.24: Relative areas of the total  $\text{Ti}^{3+}$  and the total  $\text{Ti}^{4+}$  contributions of the Ti  $2p$  emission lines of 4 ML BTO on Pt(111) during reduction in UHV, shown in Fig. 6.21, versus time, taken in normal emission. The total Ti and Pt areas are normalized to the mirror current and Pt footpoints and are appended to the right and left axis. The relative surface to bulk area of the Pt  $4f$  emission lines, recorded simultaneously in the reduction ramp (Fig. 6.25) is given, as well.

This can be assigned to rewetting of the Pt surface and the formation of OQCs. In summary, via reduction  $\text{Ti}^{4+}$  decreases from 95% of the total signal to 55%, while  $\text{Ti}^{3+}$  increases from 5% to 45%.

### Monitoring the Pt $4f$ emission lines during the growth of OQCs

The surface component of the  $4f$  emission lines of a clean Pt(111) surface shows a shift by 0.4 eV to lower binding energies than the bulk component at 71.2 eV [177]. The high resolution Pt  $4f$  spectrum of 4 ML BTO on Pt(111) in the oxidized state shows both components, which indicates the presence of bare Pt. Upon reduction in UHV, the Pt surface is covered with OQCs, which leads to vanish of the shift of the surface component. To increase the surface sensitivity, XPS measurements of the Pt  $4f$  emission lines were performed at a photon energy of 140 eV (Fig. 6.26 (a,b)). The spectra were obtained by subtracting a Shirley background and fitting with two doublets with Doniach-Sunjic line shapes [178], shifted by 0.4 eV [41].

During the reduction ramp of Fig. 6.21, the Ti  $2p$  and the Pt  $4f$  lines have been recorded in

normal emission, at a photon energy of 670 eV, to be more surface sensitive for the changes in Ti, which is less sensitive for Pt. Interestingly, it was still possible to resolve the surface component and monitor its variation during the reduction ramp. The Pt spectra in the reduction ramp are shown in Fig. 6.25. The Pt spectra are normalized to their footpoints. The change in relative area of the surface component to the bulk component is presented in Fig. 6.24. The details of the data analysis are discussed later.

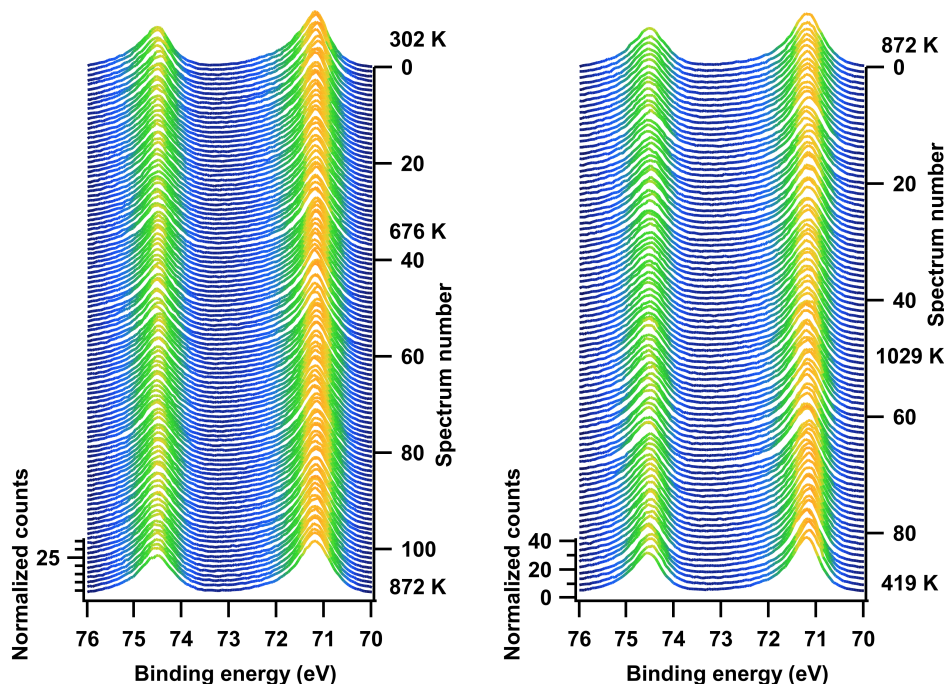


Figure 6.25: The Pt 4*f* spectra while reducing the 4 ML sample in UHV by heating up to 1029 K, taken in normal emission.

As mentioned in Sec. 6.1, the sample preparation in the further annealed state was followed by cooling in O<sub>2</sub> pressure. This results in the partial coverage of the bare Pt surface by O<sub>2</sub> (and other adsorbates), which leads to a decrease in the surface component and rise of the corresponding O<sub>2</sub>-adsorbed component. The presence of a strong surface component is approved by the O 1*s* emission line in grazing incidence at 532.55 eV (Fig. 8.4 (c)). Starting to anneal the sample in UHV from RT (Fig. 6.26 (c)) to 517 K (Fig. 6.26 (d)), the relative area of the surface component increases from 0.06 to 0.13, probably due to desorption of O<sub>2</sub> and other adsorbates. Due to the first pause at 676 K, the relative area of surface drops to 0.11. This can be explained by readsorption of residual gases, which desorbed by further heating in UHV.

While increasing the temperature from 871 to 982 K, the surface area ratio drops from 0.12 to 0.08, resulting from the rewetting of the Pt surface and formation of OQCs. However, the surface component is still present and reduces gradually during cooling the sample in UHV. The last distinguishable surface component is observed at 710 K. The existence of the surface component after the rewetting process implies the existence of bare Pt areas after covering the surface with

the OQC layer. This is in contradiction with the previously reported results, where a complete coverage of the surface by OQCs has been observed [41].

AFM measurements show that 35% to 47% of the surface is covered with large islands with a height of 10 to 17 nm (Sec. 6.1). It is interesting to determine the area of the small islands, which in principle, is possible to be calculated from the changes in the peak areas of the Pt  $4f$  emission lines. Qualitatively, there is an increase in the Pt signal in Fig. 6.26 (b), as a result of coalescence of the OQC layer and dewetting of the Pt surface. However, for a quantitative determination, three parameters enter the calculations, which cannot be given with sufficient precision. The area of the inelastic background, which needs to be subtracted from the spectrum, the density of atoms in the island and in particular, in the wetting layer and finally, photoelectron diffraction effects.

For fitting the spectra of the ramp (Fig. 6.25) three components have been used. For the bulk component a numerical line shape, derived from the last spectrum of the ramp at 419 K was used. For the surface component at 0.4 eV lower binding energies and the absorber component at 0.75 eV higher binding energies than the bulk, Doniach-Sunjic functions have been used. The components are shown for two spectra at 302 K (beginning of the ramp) and at 517 K in Fig. 6.26 (c,d). At the beginning, there is a considerable amount of adsorbates on the surface and the Pt surface component is small. By heating the sample in UHV, the contamination desorbs and the Pt surface component increases.

In summary, the formation of BTO-derived OQCs have been monitored by high resolution XPS measurements during reduction of 4 ML BTO on Pt(111) in UHV. The simultaneous increase in  $Ti^{3+}$  component at 456.75 eV and decrease in 6-fold coordinated  $Ti^{4+}$  originate from formation of OQCs, while rewetting the Pt surface. In addition to the reduction of  $Ti^{4+}$ , the rewetting process has been monitored using the surface component of the Pt  $4f$  emission lines. It is found that both processes occur simultaneously and not as a sequence of two.

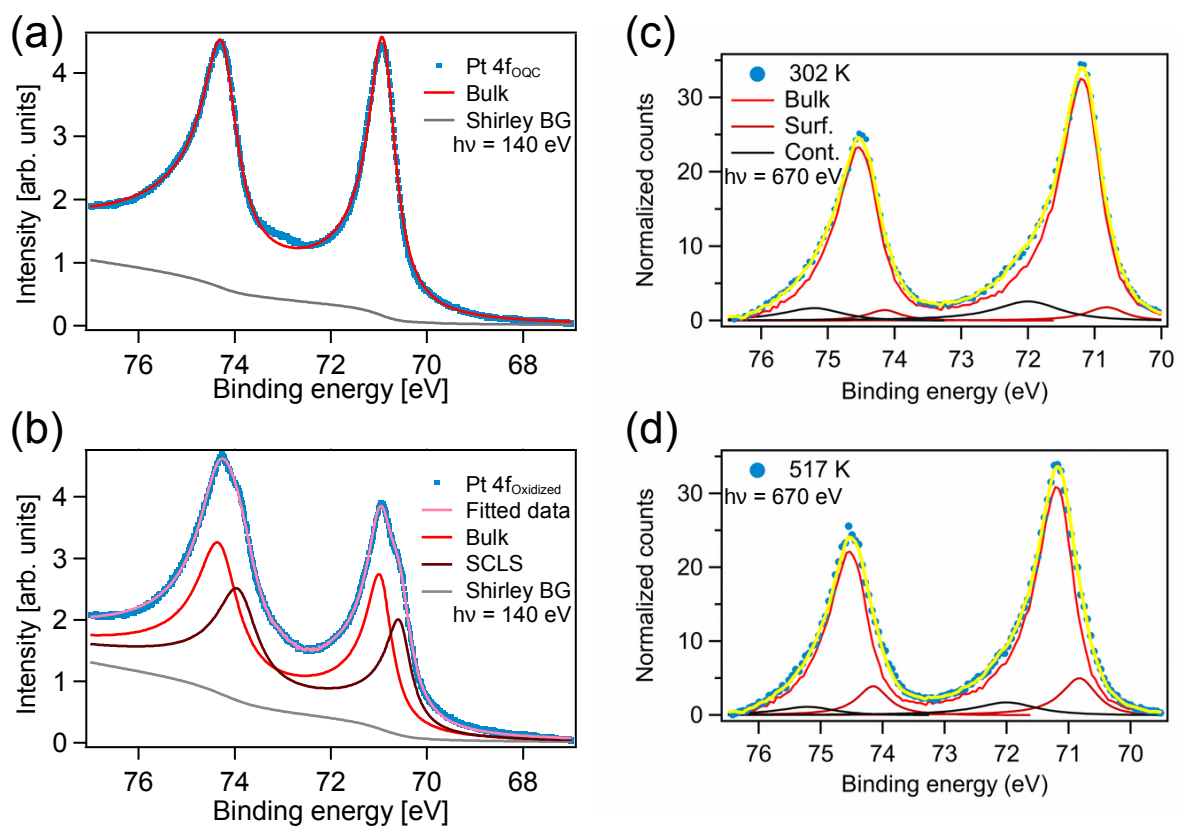


Figure 6.26: High resolution XPS spectra of the Pt 4f emission lines of 4 ML BTO on Pt(111) in normal emission in (a) the reduce and (b) the oxidized state, taken at a photon energy of 140 eV [41]. The Pt 4f emission lines are shown while reducing the sample in UHV, recorded (c) at 302 K (beginning of the reduction) and (d) at 517 K, taken at a photon energy of 670 eV in normal emission.

## 7 Summary

Within the scope of this thesis, developments in the data analysis in EXAFS have been done and presented in Ch. 4. A projection method has been initiated to decrease the uncertainty of the initial values of the nearest neighbor distances. This method has been tested successfully on an STO single crystal and results in a decrease in uncertainties from 40–80 pm (by Fourier transformation) to typically below 10 pm and only in unfortunate cases to 20 pm.

The geometrical structure of an ultrathin film of BaTiO<sub>3</sub>-derived oxide quasicrystals (OQC) is investigated and presented in Ch. 5 by performing XAS measurements in normal and grazing incidence, which unexpectedly, have not lead to any directional anisotropy. The EXAFS data analysis has resulted in two values for Ti-O bond-lengths: an in-plane O at 1.71 Å and an in- and out-of-plane O at 2.56 Å. The shorter in-plane and the out-of-plane O atoms were found to have small coordination numbers (0.23 and 0.38) with large errors, whereas the longer in-plane O is more prominent with a coordination number of 3. This indicates the presence of a majority arrangement with three in-plane O atoms at the long distance of 2.56 Å and the presence of a minority arrangement, where one O atom is at the small distance of 1.71 Å. Furthermore, some of these arrangements may have an additional adsorbate with an oxygen at 2.56 Å above the Ti. The low coordination number of the out-of-plane O indicates that the spectrum in grazing can be described almost completely by scatterings from the Pt substrate. The shortest Ti-Pt distance has been found as 2.69 Å. Although Ba is a strong scatterer, only small hints have been found of an in-plane Ba at 3.15 Å. The obtained values for the short in-plane Ti-O and the shortest Ti-Pt distance agree quite well with the bond-lengths in the Kepler-approximant, achieved by DFT calculations, whereas in case of the Ti-Ba distance, the agreement is not as good.

The quasicrystalline nature of the structure imposes the occupation of different sites above Pt by Ti atoms. Surprisingly, the presented cluster with only one site, off-3FH fcc, explains the experiment as well as averaging over all possible sites, or even slightly better. This indicates the presence of preferred sites of Pt for Ti. In addition, a pattern of occupation sites on the Pt surface has been found by back-folding Ti atoms in the QC structure to a Pt unit cell, which hints into the same direction. Due to the interaction between the OQC layer and the crystalline Pt substrate, the Ti-Pt bond-length has been found to be always constant, regardless of the site of Ti. This predicts height differences for Ti atoms in the OQC layer, as actually found by STM.

Studies of oxidation states in Ch. 6 reveal that Ti is in the 3+ state in the OQC layer. XPS measurements have enabled us to monitor the formation of the OQCs by following the intensity changes in the Ti 2*p* and the Pt 4*f* emission lines. The growth of the OQCs due to the decay

## 7 Summary

of small islands leads to a simultaneous rise in the  $\text{Ti}^{3+}$  component at 456.75 eV and fall in  $\text{Ti}^{4+}$  (459.25 eV at room temperature). Concurrently, the surface component of the Pt  $4f_{7/2}$  spectrum decays, which approves the rewetting of the Pt surface by OQCs.

NEXAFS of the Ti  $K$ -edge rules out more than 3-fold coordination of Ti by O atoms in OQCs. The coordination changes of the  $\text{Ti}^{4+}$  component in the islands from 6- to 5-fold while heating in oxygen atmosphere has been observed and is attributed to the transformation of the  $\text{Ti}^{3+}$  to the  $\text{Ti}^{4+}$  in large islands. The coordination changes of the  $\text{Ti}^{4+}$  component is found to be reversible and it changes back from 5- to 6-fold while annealing in UHV, during the formation of the  $\text{Ti}^{3+}$  in large islands.

In the absorption spectrum at the Ti  $K$ -edge of BTO-derived OQCs, only a short-range modulation function is available, due to the presence of the Ba  $L_3$ -edge. This points to future geometrical investigations of STO-derived OQC by EXAFS, where a long enough energy range is available in the Ti  $K$ -edge. In addition, the small directional anisotropy in the OQC system (seen at the Ti  $K$ - as well as the  $L$ -edge) can be addressed by further investigations on BTO- and STO-derived OQCs, using X-ray photoelectron diffraction (XPD). More information about the Ti-Ba distance may be obtained by adsorption of marker molecules, which adsorb specifically on Ti or Ba and image them with STM or AFM.

As conclusion, this thesis has successfully investigated the geometrical structure of a BTO-derived OQC system using state-of-the-art experimental methods, as well as data analysis. The current work is quite rich in monitoring the growth and the decay of OQCs and explaining the observed coordination changes in the islands via annealing in UHV, as well as in oxygen. Furthermore, major developments in the EXAFS data analysis have been achieved, which lead to more accurate initial structural models.

# Bibliography

- [1] M. S. Shumate. “Interferometric determination of the principal refractive indices of barium titanate single crystals”. In: *Appl. Phys. Lett.* 5 (1964), 178–179.
- [2] M. Woehlecke, V. Marrello, and A. Onton. “Refractive index of BaTiO<sub>3</sub> and SrTiO<sub>3</sub> films”. In: *J. Appl. Phys.* 48 (1977), 1748–1750.
- [3] W. Heywang. “Bariumtitanat als sperrschichtableiter”. In: *Solid-State Electron.* 3 (1961), 51–58.
- [4] O. Auciello, J. Scott, and R. Ramesh. “The physics of ferroelectric memories”. In: *Phys. Today* 51 (1998), 22–27.
- [5] M. Tomkiewicz and H. Fay. “Photoelectrolysis of water with semiconductors”. In: *Appl. Phys.* 18 (1979), 1–28.
- [6] T. Wolfram and F. Morin. “A conceptual model for surface states and catalysis on d-band perovskites”. In: *Appl. Phys.* 8 (1975), 125–141.
- [7] N. Yasuda, H. Murayama, Y. Fukuyama, J. Kim, S. Kimura, K. Toriumi, Y. Tanaka, Y. Moritomo, Y. Kuroiwa, K. Kato, H. Tanaka, and M. Takata. “X-ray diffractometry for the structure determination of a submicrometre single powder grain”. In: *J. Synchrotron Radiat.* 16 (2009), 352–357.
- [8] H. F. Kay and P. Vousden. “Symmetry changes in barium titanate at low temperatures and their relation to its ferroelectric properties”. In: *Lond. Edinb. Dubl. Phil. Mag.* 40 (1949), 1019–1040.
- [9] R. Gross and A. Marx. *Festkoerperphysik*. Oldenbourg Verlag, Muenchen, 2012.
- [10] P. Huth. “Untersuchungen zu elektronischen Bindungsenergien am ferroelektrisch- paraelektrischen Uebergang von Bariumtitanat und multiferroischen Schichtsystemen mit Bariumtitanat”. MA thesis. Universitaet Leipzig, 2015.
- [11] A. Berlich, H. Strauss, C. Langheinrich, A. Chasse, and H. Morgner. “Surface termination of BaTiO<sub>3</sub>(001) single crystals: A combined electron spectroscopic and theoretical study”. In: *Surf. Sci.* 605 (2011), 158–165.
- [12] A. Pancotti, J. Wang, P. Chen, L. Tortech, C.-M. Teodorescu, E. Frantzeskakis, and N. Barrett. “X-ray photoelectron diffraction study of relaxation and rumpling of ferroelectric domains in BaTiO<sub>3</sub>(001)”. In: *Phys. Rev. B* 87 (18 2013), p. 184116.

- [13] A. M. Kolpak, D. Li, R. Shao, A. M. Rappe, and D. A. Bonnell. “Evolution of the structure and thermodynamic stability of the BaTiO<sub>3</sub>(001) surface”. In: *Phys. Rev. Lett.* 101 (2008), p. 036102.
- [14] *Ferroelectric Materials*. URL: <http://www.doitpoms.ac.uk/tlplib/ferroelectrics/printall.php>.
- [15] H. D. Megaw. “Crystal structure of double oxides of the perovskite type”. In: *Proc. Phys. Soc.* 58 (1946), 133–152.
- [16] R. Mitchell, A. Chakhmouradian, and P. Woodward. “Crystal chemistry of perovskite-type compounds in the tausonite-loparite series, (Sr<sub>1-2x</sub>Na<sub>x</sub>La<sub>x</sub>)TiO<sub>3</sub>”. In: *Phys. Chem. Miner.* 27 (2000), 583–589.
- [17] R. Cowley. “The phase transition of strontium titanate”. In: *Philos. Trans. Royal Soc. A* 354 (1996), 2799–2814.
- [18] R. Loetzsch, A. Luebecke, I. Uschmann, E. Foerster, V. Grosse, M. Thuerk, T. Koettig, F. Schmidl, and P. Seidel. “The cubic to tetragonal phase transition in SrTiO<sub>3</sub> single crystals near its surface under internal and external strains”. In: *Appl. Phys. Lett.* 96 (2010).
- [19] E. Heifets, E. Kotomin, and V. A. Trepakov. “Calculations for antiferrodistortive phase of SrTiO<sub>3</sub> perovskite: hybrid density functional study”. In: *J. Phys. Condens. Matter.* 18 (2006), 4845–4851.
- [20] K. Krupski, M. Moors, P. Jozwik, T. Kobiela, and A. Krupski. “Structure Determination of Au on Pt111 Surface LEED STM and DFT Study”. In: *Materials* 8 (2015), 2935–2952.
- [21] S. Foerster and W. Widdra. “Growth, structure, and thermal stability of epitaxial BaTiO<sub>3</sub> films on Pt(111)”. In: *Surf. Sci.* 604 (2010), 2163–2169.
- [22] A. R. Sandy, S. G. J. Mochrie, D. M. Zehner, G. Gruebel, K. G. Huang, and D. Gibbs. “Reconstruction of the Pt(111) surface”. In: *Phys. Rev. Lett.* 68 (1992), 2192–2195.
- [23] N. Niizeki and H. Mitani. “Two-dimensional dodecagonal quasilattices”. In: *J. Phys. A: Math. Gen.* 20 (1987), L405–L410.
- [24] F. Gaehler. In: *Quasicrystalline Materials (eds Janot, D. & Dubois, J. M.)* (1988), 272–284.
- [25] P. J. Lu and P. J. Steinhardt. “Decagonal and quasi-crystalline tilings in medieval Islamic architecture”. In: *Science* 315 (2007), 1106–1110.
- [26] E. Makovicky. “Comment on “decagonal and quasi-crystalline tilings in medieval Islamic architecture””. In: *Science* 318 (2007).
- [27] P. J. Lu and P. J. Steinhardt. “Response to comment on “decagonal and quasi-crystalline tilings in medieval Islamic architecture””. In: *Science* 318 (2007), p. 1383.
- [28] P. M. de Wolff, T. Janssen, and A. Janner. “The superspace groups for incommensurate crystal structures with a one-dimensional modulation”. In: *Acta Cryst. A* 37 (1981), 625–636.



- [29] R. Penrose. “Pentaplexity A Class of Non-Periodic Tilings of the Plane”. In: *Math. Intelligencer* 2 (1979), 32–37.
- [30] S. Shechtman, I. Blech, D. Gratias, and J. W. Cahn. “Metallic Phase with Long-Range Orientational Order and No Translational Symmetry”. In: *Phys. Rev. Lett.* 53 (1984), 1951–1953.
- [31] N. Wang, H. Chen, and K. H. Kuo. “Two-dimensional quasicrystal with eightfold rotational symmetry”. In: *Phys. Rev. Lett.* 9 (1987), 1010–1013.
- [32] L. Bendersky. “Quasicrystal with One-Dimensional Translational Symmetry and a Tenfold Rotation Axis”. In: *Phys. Rev. Lett.* 55 (1985), 1461–1463.
- [33] T. Ishimasa, H.-U. Nissen, and Y. Fukano. “New ordered state between crystalline and amorphous in Ni-Cr particles”. In: *Phys. Rev. Lett.* 55 (1985), 511–513.
- [34] J. Mikhael, J. Roth, L. Helden, and C. Bechinger. “Archimedean-like tiling on decagonal quasicrystalline surfaces”. In: *Nature* 454 (2008), 501–504.
- [35] X. B. Zeng, G. Ungar, Y. Liu, V. Percec, S. E. Dulcey, and J. K. Hobbs. “Supramolecular dendritic liquid quasicrystals”. In: *Nature* 428 (2004), 157–160.
- [36] K. Hayashida, T. Dotera, A. Takano, and Y. Matsushita. “Polymeric Quasicrystal: Mesoscopic Quasicrystalline Tiling in *ABC* Star Polymers”. In: *Phys. Rev. Lett.* 98 (2007), p. 195502.
- [37] S. Fischer, A. Exner, K. Zielske, J. Perlich, S. Deloudi, W. Steurer, P. Lindner, and S. Foerster. “Colloidal quasicrystals with 12-fold and 18-fold diffraction symmetry”. In: *Proc. Natl. Acad. Sci. U.S.A.* 108 (2011), 1810–1814.
- [38] N. A. Wasio, R. C. Quardokus, R. P. Forrest, C. S. Lent, S. A. Corcelli, J. A. Christie, K. W. Henderson, and S. A. Kandel. “Self-assembly of hydrogen-bonded two-dimensional quasicrystals”. In: *NATURE* 507 (2014), 86–89.
- [39] J. I. Urgel, D. Eciija, G. Lyu, R. Zhang, C.-A. Palma, W. Auwaerter, N. Lin, and J. V. Barth. “Quasicrystallinity expressed in two-dimensional coordination networks”. In: *Nat. Chem.* 8 (2016), 657–662.
- [40] S. Foerster, K. Meinel, R. Hammer, M. Trautmann, and W. Widdra. “Quasicrystalline structure formation in a classical crystalline thin-film system”. In: *Nature* 502 (2013), 215–218.
- [41] S. Foerster, J. I. Flege, E. M. Zollner, F. O. Schumann, R. Hammer, A. Bayat, K.-M. Schindler, J. Falta, and W. Widdra. “Growth and decay of a two-dimensional oxide quasicrystal: High-temperature in situ microscopy”. In: *Ann. Phys.* 529 (2017), p. 1600250.
- [42] S. Schenk, S. Foerster, K. Meinel, R. Hammer, B. Leibundgut, M. Paleschke, J. Pantzer, C. Dresler, F. O. Schumann, and W. Widdra. “Observation of a dodecagonal oxide quasicrystal and its complex approximant in the SrTiO<sub>3</sub>-Pt(111) system”. In: *J. Phys. Condens. Matter.* 29 (2017), p. 134002.

- [43] J. Kepler. *Harmonices Mundi*. Linz, 1619.
- [44] S. Foerster, M. Trautmann, S. Roy, W. A. Adeagbo, E. M. Zollner, R. Hammer, F. O. Schumann, K. Meinel, S. K. Nayak, K. Mohseni, W. Hergert, H. L. Meyerheim, and W. Widdra. “Observation and Structure Determination of an Oxide Quasicrystal Approximant”. In: *Phys. Rev. Lett.* 117 (2016), p. 095501.
- [45] H. Wende. “Recent advances in x-ray absorption spectroscopy”. In: *Rep. Prog. Phys.* 67 (2004), 2105–2181.
- [46] J. Bahrtdt, W. Frentrup, A. Gaupp, M. Scheer, W. Gudat, G. Ingold, and S. Sasaki. “Elliptically polarizing insertion devices at BESSY II”. In: *Nucl. Instr. Meth. Phys. Res. A* 467 (2001), 21–29.
- [47] H. Onuki and P. Elleaume. *Undulators, Wigglers and Their Applications*. CRC Press, 2003.
- [48] P. Schmueser, M. Dohlus, J. Rossbach, and C. Behrens. “Undulator Radiation”. In: *Free-Electron Lasers in the Ultraviolet and X-Ray Regime: Physical Principles, Experimental Results, Technical Realization*. Springer International Publishing, 2014. Chap. 2, 11–23.
- [49] G. Margaritondo. *Introduction to synchrotron radiation*. Oxford University Press, 1988.
- [50] C. E. Webb. *Handbook of Laser Technology and Applications*. Ed. by C. E. Webb and J. D. C. Jones. Vol. II: Laser design and laser systems. Part B5. Institute of Physics Publishing, Bristol and Philadelphia, 2004.
- [51] F. Hippert, E. Geissler, J. Hodeau, E. Lelievre-Berna, and J. Regnard. *Neutron and X-ray Spectroscopy*. Springer Netherlands, 2005.
- [52] J. Stoehr and H. Siegmann. *Magnetism: From Fundamentals to Nanoscale Dynamics*. Springer Series in Solid-State Sciences. Springer Berlin Heidelberg, 2007.
- [53] R. K. Govind. “Growth, magnetic properties and interface effects of Fe and Fe-oxide ultrathin films on BaTiO<sub>3</sub>(001) substrates”. PhD thesis. Martin-Luther-Universitaet Halle-Wittenberg, 2013.
- [54] A. Tenderholt. 2016. URL: <http://en.wikipedia.org/wiki/File:XASEdges.svg>.
- [55] C. T. Chen, Y. U. Idzerda, H.-J. Lin, N. V. Smith, G. Meigs, E. Chaban, G. H. HO, E. Pellegrin, and F. Sette. “Experimental Confirmation of the X-Ray Magnetic Circular Dichroism Sum Rules for Iron and Cobalt”. In: *Phys. Rev. Lett.* 75 (1995), 152–155.
- [56] J. Stoehr. *NEXAFS Spectroscopy*. Springer-Verlag Berlin Heidelberg, 1992.
- [57] F. de Groot and A. Kotani. *Core Level Spectroscopy of Solids*. Advances in Condensed Matter Science. CRC Press, 2008.
- [58] M. Magnuson. “Electronic Structure Studies using Resonant X-Ray and photoemission Spectroscopy”. PhD thesis. Uppsala University, 1999.

- [59] M. P. Seah and W. A. Dench. “Quantitative electron spectroscopy of surfaces: A standard data base for electron inelastic mean free paths in solids”. In: *Surf. Interface Anal.* 1 (1979), 2–11.
- [60] K. Siegbahn and K. Edvarson. “ $\beta$ -Ray spectroscopy in the precision range of  $1 : 10^5$ ”. In: *Nucl. Phys.* 1 (1956), 137–159.
- [61] D. Curcio. “Growth and Properties of Graphene-Based Materials”. PhD thesis. University of Trieste, 2016-2017.
- [62] J. F. Moulder and J. Chastain. *Handbook of X-ray Photoelectron Spectroscopy: A Reference Book of Standard Spectra for Identification and Interpretation of XPS Data*. Physical Electronics, 1995.
- [63] P. Swift. “Adventitious carbon—the panacea for energy referencing?” In: *Surf. Interface Anal.* 4 (1982), 47–51.
- [64] V. V. Atuchin, V. G. Kesler, N. V. Pervukhina, and Z. Zhang. “Ti 2p and O 1s core levels and chemical bonding in titanium-bearing oxides”. In: *J. Electron. Spectrosc. Relat. Phenom.* 152 (2006), 18–24.
- [65] M. Grasserbauer, H. Dudek, and M. Ebel. *Angewandte Oberflaechenanalyse mit SIMS, AES und XPS*. Akademie-Verlag, 1986.
- [66] D. A. Shirley. “High-Resolution X-Ray Photoemission Spectrum of the Valence Bands of Gold”. In: *Phys. Rev. B* 5 (1972), 4709–4714.
- [67] S. Tougaard. “Quantitative analysis of the inelastic background in surface electron spectroscopy”. In: *Surf. Interface Anal.* 11 (1988), 453–472.
- [68] S. Huefner. *Photoelectron Spectroscopy, Principles and Applications*. Springer-Verlag Berlin Heidelberg, 2003.
- [69] F. Schaefers, M. Mertin, and M. Gorgoi. “KMC-1: A high resolution and high flux soft x-ray beamline at BESSY”. In: *Rev. Sci. Instrum.* 78 (2007), p. 123102.
- [70] M. Gorgoi, S. Svensson, F. Schaefers, G. Ohrwall, M. Mertin, P. Bressler, O. Karis, H. Siegbahn, A. Sandell, H. Rensmo, W. Doherty, C. Jung, W. Braun, and W. Eberhardt. “The high kinetic energy photoelectron spectroscopy facility at BESSY progress and first results”. In: *Nucl. Instr. Meth. Phys. Res. A* 601 (2009), 48–53.
- [71] W. Jark. “Soft x-ray monochromator configurations for the ELETTRA undulators: A stigmatic SX700 (invited)”. In: *Rev. Sci. Instrum.* 63 (1992), 1241–1246.
- [72] J. A. Prins. *Physics of non-crystalline solids: proceedings of the international conference*. Vol. 1964. North-Holland Pub. Co., 1965.
- [73] R. de L. Kronig. “Zur Theorie der Feinstruktur in den Roentgenabsorptionsspektren. III”. In: *Zeitschrift fuer Physik* 75 (1932), 468–475.
- [74] M. Newville. “Fundamentals of XAFS”. In: *Rev. Mineral. Geochem.* 78 (2014), 33–74.

- [75] G. Vlaic and L. Olivi. “EXAFS spectroscopy: a brief introduction”. In: *Croat. Chem. Acta* 77 (2004), 427–433.
- [76] J. Yano and V. K. Yachandra. “X-ray absorption spectroscopy”. In: *Photosynth. Res.* 102 (2009), 241–254.
- [77] B. K. Teo. *EXAFS: basic principles and data analysis*. Vol. 9. Inorganic chemistry concepts. Springer-Verlag, 1986.
- [78] D. Norman. “X-ray absorption spectroscopy (EXAFS and XANES) at surfaces”. In: *J. Phys. C: Solid State Phys.* 19 (1986), 3273–3311.
- [79] S. Calvin. *XAFS for Everyone*. Taylor & Francis, 2013.
- [80] E. A. A. Stern, B. A. Bunker, and S. M. Heald. “Many-body effects on extended x-ray absorption fine structure amplitudes”. In: *Phys. Rev. B* 21 (1980), 5521–5539.
- [81] D. Koningsberger and R. Prins. *X-Ray Absorption: Principles, Applications, Techniques of EXAFS, SEXAFS and XANES*. Chemical Analysis: A Series of Monographs on Analytical Chemistry and Its Applications. Wiley, 1988.
- [82] M. Vaccari and P. Fornasini. “Einstein and Debye models for EXAFS parallel and perpendicular mean-square relative displacements”. In: *J. Synchrotron Radiat.* 13 (2006), 321–325.
- [83] J. J. Rehr and R. C. Albers. “Theoretical approaches to x-ray absorption fine structure”. In: *Rev. Mod. Phys.* 72 (2000), 621–654.
- [84] E. A. Hudson, P. G. Allen, L. J. Terminello, M. A. Denecke, and T. Reich. “Polarized x-ray-absorption spectroscopy of the uranyl ion: Comparison of experiment and theory”. In: *Phys. Rev. B* 54 (1996), 156–165.
- [85] B. Ravel. *Artemis: EXAFS Data Analysis using Feff with Larch or Ifeffit*. URL: <https://bruceravel.github.io/demeter/documents/Artemis/index.html>.
- [86] B. Ravel and M. Newville. “ATHENA, ARTEMIS, HEPHAESTUS: data analysis for X-ray absorption spectroscopy using IFEFFIT”. In: *J. Synchrotron Radiat.* 12 (2005), 537–541.
- [87] S. I. Zabinsky, J. J. Rehr, A. Ankudinov, R. C. Albers, and M. J. Eller. “Multiple-scattering calculations of x-ray-absorption spectra”. In: *Phys. Rev. B* 52 (1995), 2995–3009.
- [88] A. L. Ankudinov, B. Ravel, J. J. Rehr, and S. D. Conradson. “Real-space multiple-scattering calculation and interpretation of x-ray-absorption near-edge structure”. In: *Phys. Rev. B* 58 (1998), 7565–7576.
- [89] J. J. Rehr, J. Mustre de Leon, S. I. Zabinsky, and R. C. Albers. “Theoretical x-ray absorption fine structure standards”. In: *J. Am. Chem. Soc.* 113 (1991), 5135–5140.
- [90] M. Newville. “IFEFFIT: interactive XAFS analysis and FEFF fitting”. In: *J. Synchrotron Radiat.* 8 (2001), 322–324.
- [91] M. Newville. *FEFFIT, Using FEFF to model XAFS data*. 1998. URL: <http://cars9.uchicago.edu/~newville/feffit/feffit.ps>.

- [92] B. Ravel. *Advanced Topics in EXAFS Analysis*. 2010. URL: <https://www.bnl.gov/ps/nsls/workshops/2010/exafs/files/Ravel.pdf>.
- [93] P. Pfalzer, J.-P. Urbach, M. Klemm, S. Horn, M. L. denBoer, A. I. Frenkel, and J. P. Kirkland. “Elimination of self-absorption in fluorescence hard-x-ray absorption spectra”. In: *Phys. Rev. B* 60 (1999), 9335–9339.
- [94] C. H. Booth and F. Bridges. “Improved self-absorption correction for fluorescence measurements of extended X-ray absorption fine-structure”. In: *Phys. Scr.* T115 (2005), 202–204.
- [95] Y. Iwasawa, K. Asakura, and M. Tada. *XAFS Techniques for Catalysts, Nanomaterials, and Surfaces*. Springer International Publishing, 2016.
- [96] M. Newville, P. Livins, Y. Yacoby, J. J. Rehr, and E. A. Stern. “Near-edge x-ray-absorption fine structure of Pb: A comparison of theory and experiment”. In: *Phys. Rev. B* 47 (1993), 14126–14131.
- [97] W. H. Press and W. T. Vetterling. *Numerical Recipes in C: The Art of Scientific Computing*. Book 4. Cambridge University Press, 1992.
- [98] P. Hofmann and K.-M. Schindler. “Direct adsorbate-structure determination by scanned-energy-mode photoelectron diffraction”. In: *Phys. Rev. B* 47 (1993), 13941–13943.
- [99] K.-M. Schindler and A. Bayat. “Projection Analysis of EXAFS Modulations”. In: (). Manuscript available.
- [100] D. P. Woodruff, P. Baumgaertel, J. T. Hoeft, M. Kittel, and M. Polcik. “Direct methods in photoelectron diffraction; experiences and lessons learnt based on the use of the projection method”. In: *J. Phys.: Condens. Matter* 13 (2001), 10625–10645.
- [101] L. Wang, A. Yoshiasa, M. Okube, and T. Takeda. “Titanium local structure in tektite probed by X-ray absorption fine structure spectroscopy”. In: *J. Synchrotron Radiat.* 18 (2011), 885–890.
- [102] A. Anspoks, D. Bocharov, J. Purans, F. Rocca, A. Sarakovskis, V. Trepakov, A. Dejneka, and M. Itoh. “Local structure studies of  $\text{SrTi}^{16}\text{O}_3$  and  $\text{SrTi}^{18}\text{O}_3$ ”. In: *Phys. Scr.* 89 (2014), p. 044002.
- [103] O. Lobacheva, M. Chavarha, Y. M. Yiu, T. K. Sham, and L. V. Goncharova. “The local structure and ferromagnetism in Fe-implanted  $\text{SrTiO}_3$  single crystals”. In: *J. Appl. Phys.* 116 (2014), p. 013901.
- [104] H. A. J. L. Mourao, O. F. Lopes, W. Avansi Jr., M. J. M. Pires, S. Souza, C. Ribeiro, and V. R. Mastelaro. “ $\text{SrTi}_{1-y}\text{Fe}_y\text{O}_3$  samples obtained by hydrothermal method: The effect of the amount of Fe on structural and photocatalytic properties”. In: *Mater. Sci. Semicond. Process.* 68 (2017), 140–146.

- [105] H. Stoecker, M. Zschornak, C. Richter, J. Hanzig, F. Hanzig, A. Hinze, K. Potzger, S. Gemming, and D. C. Meyer. “Surface-near Modifications of SrTiO<sub>3</sub> local symmetry due to nitrogen implantation investigated by grazing incidence XANES”. In: *Scr. Mater.* 86 (2014), 1–4.
- [106] T. Yamamoto, T. Mizoguchi, and I. Tanaka. “Core-hole effect on dipolar and quadrupolar transitions of SrTiO<sub>3</sub> and BaTiO<sub>3</sub> at Ti *K* edge”. In: *Phys. Rev. B* 71 (2005), p. 245113.
- [107] K. Yoshii, Y. Yoneda, I. Jarrige, T. Fukuda, Y. Nishihata, C. Suzuki, Y. Ito, T. Terashima, S. Yoshikado, and S. Fukushima. “Electronic structure of BaTiO<sub>3</sub> using resonant X-ray emission spectroscopy at the Ba-L<sub>3</sub> and Ti-K absorption edges”. In: *J. Phys. Chem. Solids* 75 (2014), 339–343.
- [108] B. Ravel, E. A. Stern, R. I. Vedrinskii, and V. Kraizman. “Local structure and the phase transitions of BaTiO<sub>3</sub>”. In: *Ferroelectrics* 206 (1998), 407–430.
- [109] N. Jiang, D. Su, and J. C. H. Spence. “Determination of Ti coordination from pre-edge peaks in Ti *K*-edge XANES”. In: *Phys. Rev. B* 76 (2007), p. 214117.
- [110] F. Farges, G. E. Brown, and J. J. Rehr. “Ti *K*-edge XANES studies of Ti coordination and disorder in oxide compounds: Comparison between theory and experiment”. In: *Phys. Rev. B* 56 (1997), 1809–1819.
- [111] A. Anspoks, J. Timoshenko, D. Bocharov, J. Purans, F. Rocca, A. Sarakovskis, V. Trepakov, A. Dejneka, and M. Itoh. “Local Structure Studies of Ti for SrTi<sup>16</sup>O<sub>3</sub> and SrTi<sup>18</sup>O<sub>3</sub> by Advanced X-ray Absorption Spectroscopy Data Analysis”. In: *Ferroelectrics* 485 (2015), 42–52.
- [112] A. Kuzmin and R. A. Evarestov. “Quantum mechanics-molecular dynamics approach to the interpretation of x-ray absorption spectra”. In: *J. Phys.: Condens. Matter* 21 (2009), p. 055401.
- [113] M. Fischer, A. Lahmar, M. Maglione, A. S. MigueL, J. P. Itie, A. Polian, and F. Baudelet. “Local disorder studied in SrTiO<sub>3</sub> at low-temperature by EXAFS spectroscopy”. In: *Phys. Rev. B* 49 (1994), 12451–12456.
- [114] O. Kamishima, Y. Nishihata, H. Maeda, T. Ishii, A. Sawada, and H. Terauchi. “EXAFS study on the local structure in strontium titanate”. In: *Physica B* 208 & 209 (1995), 303–304.
- [115] R. Dippel, K. U. Weiss, K.-M. Schindler, D. P. Woodruff, P. Gardner, V. Fritzsche, A. M. Bradshaw, and M. C. Asensio. “Multiple site coincidences and their resolution in photoelectron diffraction: PF<sub>3</sub> adsorbed on Ni(111)”. In: *Surf. Sci.* 287/288 (1993), 465–470.
- [116] A. Bootchanont, J. Jutimoosik, S. Chandarak, M. Unruan, P. Kidkhunthod, W. Klysubun, S. Rujirawat, R. Yimmirun, R. Guo, and A. Bhalla. “Synchrotron X-ray absorption spectroscopy study of local structure transformation behavior in perovskite Ba(Ti,Zr)O<sub>3</sub> system”. In: *J. Alloys Compd.* 616 (2014), 430–435.

- [117] M. Valant, I. Arcon, I. Mikulska, and D. Lisjak. “Cation Order-Disorder Transition in Fe-Doped 6H-BaTiO<sub>3</sub> for Dilute Room-Temperature Ferromagnetism”. In: *Chem. Mater.* 25 (2013), 3544–3550.
- [118] I. Mikulska, M. Valant, I. Arcon, and D. Lisjak. “X-ray Absorption Spectroscopy Studies of the Room-Temperature Ferromagnetic Fe-Doped 6H-BaTiO<sub>3</sub>”. In: *J. Am. Ceram. Soc.* 98 (2015), 1156–1161.
- [119] Y. Nishihata, O. Kamishima, K. Ojima, A. Sawada, H. Maeda, and H. Terauchi. “Temperature dependence of the local structure around the tantalum atom in potassium tantalate”. In: *J. Phys.: Condens. Matter.* 6 (1994), 9317–9328.
- [120] C. Dresler. “Niederenergetische Elektronenbeugung an oxidischen Quasikristallen im Submonologenbereich: BaTiO<sub>3</sub>/Pt(111)”. MA thesis. Martin-Luther-Universitaet Halle-Wittenberg, 2017.
- [121] R. O. Ansell, T. Dickinson, A. F. Povey, and P. M. A. Sherwood. “X-ray photoelectron spectroscopic studies of electrode surfaces using a new controlled transfer technique: Part II. Results for a molybdenum electrode and the curve fitting procedure”. In: *J. Electroanal. Chem.* 98 (1979), 79–89.
- [122] U. Gelius, C. J. Allan, G. Johansson, H. Siegbahn, D. A. Allison, and K. Siegbahn. “The ESCA Spectra of Benzene and the Iso-electronic Series, Thiophene, Pyrrole and Furan”. In: *Phys. Scr.* 3 (1971), 237–242.
- [123] *Compute inelastic mean free path of electron scattering*. URL: <http://electronsoftware.altervista.org/lab/IMFP.html>.
- [124] S. Tanuma, C. J. Powell, and D. R. Penn. “Calculations of electron inelastic mean free paths. V. Data for 14 organic compounds over the 50-2000 eV range”. In: *Surf. Interface Anal.* 21 (1994), 165–176.
- [125] K. Okada and A. Kotani. “Theory of core level X-ray photoemission and photoabsorption in Ti compounds”. In: *J. Electron. Spectrosc. Relat. Phenom.* 62 (1993), 131–140.
- [126] D. Gonbeau, C. Guimon, G. Pfister-Guillouzo, A. Levasseur, G. Meunier, and R. Dormoy. “XPS study of thin films of titanium oxysulfides”. In: *Surf. Sci.* 254 (1991), 81–89.
- [127] X. Xing, J. Deng, J. Chen, and G. Liu. “Phase evolution of barium titanate from alkoxide gel-derived precursor”. In: *J. Alloys Compd.* 384 (2004), 312–317.
- [128] D. S. Filimonov, Z.-K. Liu, and C. A. Randall. “Phase relations in the BaO-TiO<sub>2-δ</sub> system under highly reducing conditions”. In: *Mater. Res. Bull.* 38 (2003), 545–553.
- [129] D. E. Rase and R. Roy. “Phase Equilibria in the System BaO-TiO<sub>2</sub>”. In: *J. Am. Ceram. Soc.* 38 (1955), 102–113.

- [130] S. Lee, C. A. Randall, and Z.-K. Liu. “Modified phase diagram for the barium oxide-titanium dioxide system for the ferroelectric barium titanate”. In: *J. Am. Ceram. Soc.* 90 (2007), 2589–2594.
- [131] U. Diebold and T. E. Madey. “TiO<sub>2</sub> by XPS”. In: *Surf. Sci. Spectra* 4 (1996), 227–231.
- [132] M. Schneider, W. Richter, R. Keding, and C. Ruessel. “XPS investigations on coordination and valency of Ti in fresnoite glasses and glass ceramics”. In: *J. Non-Cryst. Solids* 226 (1998), 273–280.
- [133] C. N. Sayers and N. R. Armstrong. “X-ray photoelectron spectroscopy of TiO<sub>2</sub> and other titanate electrodes and various standard Titanium oxide materials: Surface compositional changes of the TiO<sub>2</sub> electrode during photoelectrolysis”. In: *Surf. Sci.* 77 (1978), 301–320.
- [134] P. A. W. van der Heide. “Surface core level shifts in photo-electron spectra from the Ca, Sr and Ba titanates”. In: *Surf. Sci.* 490 (2001), L619–L626.
- [135] J. L. Gland. “Molecular and atomic adsorption of oxygen on the Pt(111) and Pt(S)-12(111) × (111) surfaces”. In: *Surf. Sci.* 93 (1980), 487–514.
- [136] G. Kneringer and F. P. Netzer. “Adsorption studies of oxygen and carbon monoxide on a Pt(100) surface”. In: *Surf. Sci.* 49 (1975), 125–142.
- [137] M. Peuckert and H. P. Bonzel. “Characterization of oxidized platinum surfaces by X-ray photoelectron spectroscopy”. In: *Surf. Sci.* 145 (1984), 239–259.
- [138] J. A. T. Verhoeven and H. Van Doveren. “An XPS investigation of the interaction of CH<sub>4</sub>, C<sub>2</sub>H<sub>2</sub>, C<sub>2</sub>H<sub>4</sub> and C<sub>2</sub>H<sub>6</sub> with a barium surface”. In: *Surf. Sci.* 123 (1982), 369–383.
- [139] A. Tsami, F. Grillo, M. Bowker, and R. M. Nix. “Model NSR catalysts: Fabrication and reactivity of barium oxide layers on Cu(111)”. In: *Surf. Sci.* 600 (2006), 3403–3418.
- [140] C.-W. Yi and J. Szanyi. “Interaction of D<sub>2</sub>O with a Thick BaO Film: Formation of and Phase Transitions in Barium Hydroxides”. In: *J. Phys. Chem. C* 113 (2009), 15692–15697.
- [141] O. Karslioglu, L. Trotochaud, I. Zegkinoglou, and H. Bluhm. “X-Ray Spectroscopic Characterization of BaO, Ba(OH)<sub>2</sub>, BaCO<sub>3</sub>, and Ba(NO<sub>3</sub>)<sub>2</sub>”. In: *J. Electron. Spectrosc. Relat. Phenom.* 225 (2018), 55–61.
- [142] J. van Elp, J. L. Wieland, H. Eskes, P. Kuiper, G. A. Sawatzky, F. M. F. de Groot, and T. S. Turner. “Electronic structure of CoO, Li-doped CoO, and LiCoO<sub>2</sub>”. In: *Phys. Rev. B* 44 (1991), 6090–6103.
- [143] G. B. Fisher and B. A. Sexton. “Identification of an Adsorbed Hydroxyl Species on the Pt(111) Surface”. In: *Phys. Rev. Lett.* 44 (1980), 683–686.
- [144] A. Picolin, C. Busse, A. Redinger, M. Morgenstern, and T. Michely. “Desorption of H<sub>2</sub>O from Flat and Stepped Pt(111)”. In: *J. Phys. Chem. C* 113 (2009), 691–697.



- [145] P. R. Norton, J. W. Goodale, and E. B. Selkirk. “Adsorption of CO on Pt(111) studied by photoemission, thermal desorption spectroscopy and high resolution dynamic measurements of work function”. In: *Surf. Sci.* 83 (1979), 189–227.
- [146] L. T. Hudson, R. L. Kurtz, S. W. Robey, D. Temple, and R. L. Stockbauer. “Photoelectron spectroscopic study of the valence and core-level electronic structure of BaTiO<sub>3</sub>”. In: *Phys. Rev. B* 47 (1993), 1174–1180.
- [147] A. Gauzzi, H. J. Mathieu, J. H. James, and B. Kellett. “AES, XPS and SIMS characterization of YBa<sub>2</sub>Cu<sub>3</sub>O<sub>7</sub> superconducting high T<sub>C</sub> thin films”. English. In: *Vacuum* 41 (1990), 870–874.
- [148] S. Hofmann. *Auger- and X-Ray Photoelectron Spectroscopy in Materials Science: A User-Oriented Guide*. Springer Series in Surface Sciences. Springer Berlin Heidelberg, 2012.
- [149] C. Wagner and G. Muilenberg. *Handbook of X-ray Photoelectron Spectroscopy: A Reference Book of Standard Data for Use in X-ray Photoelectron Spectroscopy*. Perkin-Elmer, 1979.
- [150] M. P. Seah. “XPS reference procedure for the accurate intensity calibration of electron spectrometers- results of a BCR intercomparison co-sponsored by the VAMAS SCA TWA”. In: *Surf. Interface Anal.* 20 (1993), 243–266.
- [151] *Atomic Calculation of Photoionization Cross-Sections and Asymmetry Parameters*. URL: <https://vuo.elettra.eu/services/elements/WebElements.html>.
- [152] J.-J. Yeh. *Atomic Calculation of Photoionization Cross-sections and Asymmetry Parameters*. Gordon & Breach Science, Publishers, 1993.
- [153] J. J. Yeh and I. Lindau. “Atomic subshell photoionization cross sections and asymmetry parameters:  $1 \leq Z \leq 103$ ”. In: *At. Data Nucl. Data Tables* 32 (1985), 1–155.
- [154] B.-K. Teo and P. A. Lee. “Ab initio calculations of amplitude and phase functions for extended x-ray absorption fine structure spectroscopy”. In: *J. Am. Chem. Soc.* 101 (1979), 2815–2832.
- [155] D. Sun, W. Liu, Y. Fu, Z. Fang, F. Sun, X. Fu, Y. Zhang, and Z. Li. “Noble Metals Can Have Different Effects on Photocatalysis Over Metal-Organic Frameworks (MOFs): A Case Study on M/NH<sub>2</sub>-MIL-125(Ti) (M=Pt and Au)”. In: *Chem. Eur. J.* 20 (2014), 4780–4788.
- [156] B. Ravel. *Test the effect of self-consistent potentials on EXAFS analysis*. 2016. URL: <http://bruceravel.github.io/SCFtests/scf.html>.
- [157] A. L. Ankudinov, B. Ravel, and J. J. Rehr. *FEFF8-Lite Downloads*. Department of Physics University of Washington. 2002. URL: <http://monalisa.phys.washington.edu/feff/Bin-Source-feff8Lite/Bin-Source.html>.
- [158] A. L. Ankudinov, C. E. Bouldin, J. J. Rehr, J. Sims, and H. Hung. “Parallel calculation of electron multiple scattering using Lanczos algorithms”. In: *Phys. Rev. B* 65 (2002), p. 04107.

- [159] L. T. Hudson, R. L. Kurtz, S. W. Robey, D. Temple, and R. L. Stockbauer. “Surface core-level shifts of barium observed in photoemission of vacuum-fractured BaTiO<sub>3</sub>(100)”. In: *Phys. Rev. B* 47 (1993), 10832–10838.
- [160] E. H. P. Cordfunke, A. S. Booiij, R. J. M. Konings, R. R. van der Laan, V. M. SmitGreen, and P. van Vlaanderen. “A study of the phase transitions in Ba(OH)<sub>2</sub>, and a comment on the fusion of Sr(OH)<sub>2</sub>”. In: *Thermochim. Acta* 273 (1996), 1–9.
- [161] M. Oku. “X-ray photoelectron spectra of KMnO<sub>4</sub> and K<sub>2</sub>MnO<sub>4</sub> fractured in situ”. In: *J. Electron. Spectrosc. Relat. Phenom.* 74 (1995), 135–148.
- [162] S. C. Petitto, E. M. Marsh, G. A. Carson, and M. A. Langell. “Cobalt oxide surface chemistry: The interaction of CoO(100), Co<sub>3</sub>O<sub>4</sub>(110) and Co<sub>3</sub>O<sub>4</sub>(111) with oxygen and water”. In: *J. Mol. Catal. Chem.* 281 (2008), 49–58.
- [163] V. M. Jimenez, A. Fernandez, J. P. Espinos, and A. R. Gonzalez-Elipe. “The state of the oxygen at the surface of polycrystalline cobalt oxide”. In: *J. Electron. Spectrosc. Relat. Phenom.* 71 (1995), 61–71.
- [164] T. J. Chuang, C. R. Brundle, and D. Rice. “Interpretation of the x-ray photoemission spectra of cobalt oxides and cobalt oxide surfaces”. In: *Surf. Sci.* 59 (1976), 413–429.
- [165] P. Legare, L. Hilaire, and G. Maire. “Interaction of polycrystalline platinum and a platinum-silicon alloy with oxygen: An XPS study”. In: *Surf. Sci.* 141 (1984), 604–616.
- [166] J. Li, T. Liu, G. Sui, and D. Zhen. “Photocatalytic Performance of a Nd-SiO<sub>2</sub>-TiO<sub>2</sub> Nanocomposite for Degradation of Rhodamine B Dye Wastewater”. In: *J. Nanosci. Nanotechnol.* 15 (2015), 1408–1415.
- [167] A. A. Hermas, M. Nakayama, and K. Ogura. “Formation of stable passive film on stainless steel by electrochemical deposition of polypyrrole”. In: *Electrochim. Acta* 50 (2005), 3640–3647.
- [168] K. S. Kim and N. Winograd. “Charge transfer shake-up satellites in X-ray photoelectron spectra of cations and anions of SrTiO<sub>3</sub>, TiO<sub>2</sub> and Sc<sub>2</sub>O<sub>3</sub>”. In: *Chem. Phys. Lett.* 31 (1975), 312–317.
- [169] H. Chermette, P. Pertosa, and F. M. Michel-Calendini. “Molecular orbital study of satellites in XPS spectra of BaTiO<sub>3</sub> and TiO<sub>2</sub>”. In: *Chem. Phys. Lett.* 69 (1980), 240–245.
- [170] S. A. Chambers, M. H. Engelhard, L. Wang, T. C. Droubay, M. E. Bowden, M. J. Wahila, N. F. Quackenbush, L. F. J. Piper, T.-L. Lee, C. J. Nelin, and P. S. Bagus. “X-ray photoelectron spectra for single-crystal Ti<sub>2</sub>O<sub>3</sub>: Experiment and theory”. In: *Phys. Rev. B* 96 (2017), p. 205143.
- [171] A. Chasse, S. Borek, K.-M. Schindler, M. Trautmann, M. Huth, F. Steudel, L. Makhova, J. Graefe, and R. Denecke. “High-resolution x-ray absorption spectroscopy of BaTiO<sub>3</sub>: Experiment and first-principles calculations”. In: *Phys. Rev. B* 84 (2011), p. 195135.

- [172] V. S. Lusvardi, M. A. Barteau, J. G. Chen, J. Eng, B. Fruhberger, and A. Teplyakov. “An NEXAFS investigation of the reduction and reoxidation of  $\text{TiO}_2(001)$ ”. In: *Surf. Sci.* 397 (1998), 237–250.
- [173] C. E. Rice and W. R. Robinson. “Structural changes associated with the semiconductor-to-metal transition in  $\text{Ti}_2\text{O}_3$ ”. In: *Mater. Res. Bull.* 11 (1976), 1355–1359.
- [174] L. Cormier, O. Dargaud, N. Menguy, G. S. Henderson, M. Guignard, N. Trcera, and B. Watts. “Investigation of the Role of Nucleating Agents in  $\text{MgO-SiO}_2\text{-Al}_2\text{O}_3\text{-SiO}_2\text{-TiO}_2$  Glasses and Glass-Ceramics: A XANES Study at the Ti K- and  $L_{2,3}$ -Edges”. In: *Cryst. Growth Des.* 11 (2011), 311–319.
- [175] F. M. F. de Groot, M. Grioni, J. C. Fuggle, J. Ghijsen, G. A. Sawatzky, and H. Petersen. “Oxygen 1s x-ray-absorption edges of transition-metal oxides”. In: *Phys. Rev. B* 40 (1989), 5715–5723.
- [176] G. S. Henderson, X. Y. Liu, and M. E. Fleet. “Titanium coordination in silicate glasses investigated using O  $K$ -edge X-ray absorption spectroscopy”. In: *Mineral. Mag.* 67 (2003), 597–607.
- [177] R. C. Baetzold, G. Apai, E. Shustorovich, and R. Jaeger. “Surface core-level shifts for Pt single-crystal surfaces”. In: *Phys. Rev. B* 26 (1982), 4022–4027.
- [178] S. Doniach and M. Sunjic. “Many-electron singularity in X-ray photoemission and X-ray line spectra from metals”. In: *J. Phys. C: Solid State Phys.* 3 (1970), p. 285.

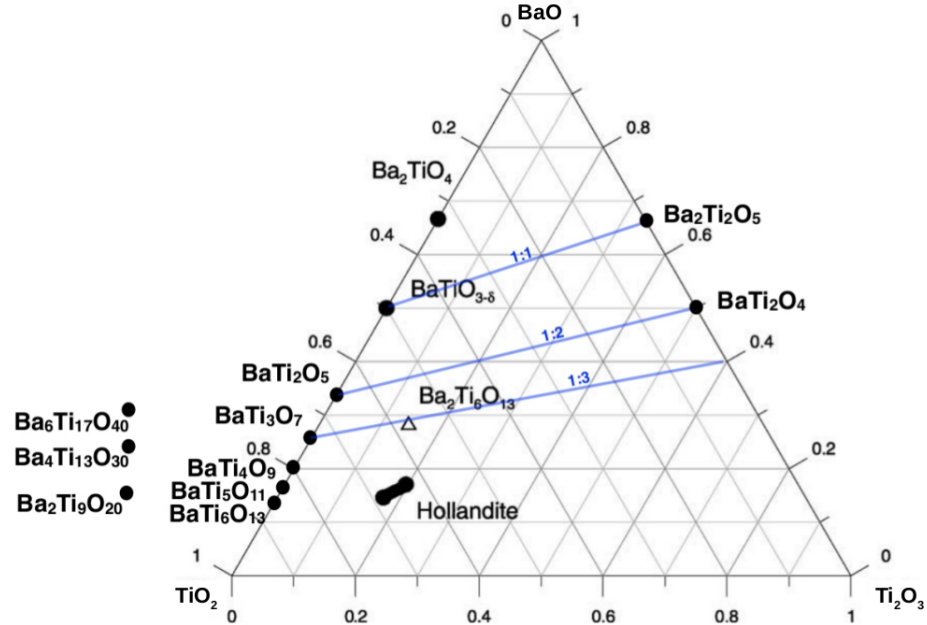


## 8 Appendix

Table 8.1: The line shapes of the components, employed for fitting the XPS spectra of 4 ML BTO on Pt(111) in the reduced state, presented in Sec. 6.3. In case of a modification in the corresponding peaks in the oxidized or the further annealed states, new parameters are given. The line shapes have been defined by using Eq. 5.1. In the table,  $E_B$  (eV) stands for the binding energy of the peak,  $M$ , the mixing ratio (0: pure Gaussian; 1: pure Lorentzian),  $\Gamma$  (eV), the FWHM of the peak, SOS (eV), the spin orbit splitting of the Ti doublet and AR and IR, the area and the intensity ratios of the peak in the Ti  $2p_{3/2}$  region to those in the Ti  $2p_{1/2}$  region. The peaks in Ti  $2p_{1/2}$  are Gaussian with the FWHM calculated so that they full fill the conditions of AR and IR.

| Emission line | State            | $E_B$  | $M$  | $\Gamma$ | SOS  | AR   | IR   |
|---------------|------------------|--------|------|----------|------|------|------|
| Ti $2p_{3/2}$ | Reduced          | 456.45 | 0.2  | 0.8      | 5.85 | 0.48 | 0.3  |
| Ti $2p_{3/2}$ | Reduced          | 456.75 | 0    | 1.5      | 5.9  | 0.48 | 0.3  |
| Ti $2p_{3/2}$ | Reduced          | 458.2  | 0    | 1.6      | 5.73 | 0.48 | 0.3  |
| Ti $2p_{3/2}$ | Reduced          | 459.25 | 0.99 | 1.1      | 5.73 | 0.48 | 0.24 |
| Ti $2p_{3/2}$ | Reduced          | 459.8  | 0    | 1.65     | 5.73 | 0.48 | 0.3  |
| Ti $2p_{3/2}$ | Oxidized         | 456.45 | 0.2  | 0.8      | 5.9  | 0.48 | 0.3  |
| Ti $2p_{3/2}$ | Further annealed | 456.45 | 0.2  | 0.8      | 5.9  | 0.48 | 0.3  |
| Ti $2p_{3/2}$ | Further annealed | 459.05 | 0    | 1.8      | 5.73 | 0.48 | 0.24 |
| O $1s$        | Reduced          | 529.75 | 0    | 1.15     | -    | -    | -    |
| O $1s$        | Reduced          | 530.1  | 0.75 | 0.85     | -    | -    | -    |
| O $1s$        | Reduced          | 531.3  | 0.05 | 2.2      | -    | -    | -    |
| O $1s$        | Reduced          | 533    | 0.96 | 1.85     | -    | -    | -    |
| O $1s$        | Reduced 999 K    | 529.75 | 0.86 | 1.15     | -    | -    | -    |
| O $1s$        | Reduced 999 K    | 530.1  | 0.6  | 1.25     | -    | -    | -    |
| O $1s$        | Reduced 999 K    | 531.3  | 0.51 | 2.35     | -    | -    | -    |
| O $1s$        | Oxidized         | 529.6  | 0    | 1.15     | -    | -    | -    |
| O $1s$        | Oxidized         | 529.9  | 0.75 | 0.85     | -    | -    | -    |
| O $1s$        | Oxidized         | 530.6  | 0.65 | 2.2      | -    | -    | -    |
| O $1s$        | Oxidized         | 531.9  | 0.27 | 1.85     | -    | -    | -    |
| O $1s$        | Further annealed | 529.5  | 0    | 1.15     | -    | -    | -    |
| O $1s$        | Further annealed | 529.8  | 0    | 0.85     | -    | -    | -    |
| O $1s$        | Further annealed | 530.7  | 0.05 | 2.2      | -    | -    | -    |
| O $1s$        | Further annealed | 532.55 | 0.44 | 1.85     | -    | -    | -    |
| O $1s$        | Further annealed | 530.45 | 0    | 0.9      | -    | -    | -    |
| Ba $3d_{5/2}$ | Reduced          | 780    | 0.76 | 1.6      | -    | -    | -    |
| Ba $3d_{5/2}$ | Reduced          | 781.35 | 0.76 | 2.05     | -    | -    | -    |
| Ba $3d_{5/2}$ | Oxidized         | 778.8  | 0.97 | 1.55     | -    | -    | -    |
| Ba $3d_{5/2}$ | Oxidized         | 779.65 | 0.23 | 1.6      | -    | -    | -    |
| Ba $3d_{5/2}$ | Oxidized         | 780.6  | 0.37 | 2.05     | -    | -    | -    |
| Ba $3d_{5/2}$ | Further annealed | 778.8  | 0.98 | 1.55     | -    | -    | -    |
| Ba $3d_{5/2}$ | Further annealed | 779.65 | 0.96 | 1.6      | -    | -    | -    |
| Ba $3d_{5/2}$ | Further annealed | 780.6  | 0.6  | 2.05     | -    | -    | -    |
| Ba $3d_{5/2}$ | Further annealed | 781.45 | 0.13 | 1.25     | -    | -    | -    |

(a)



(b)

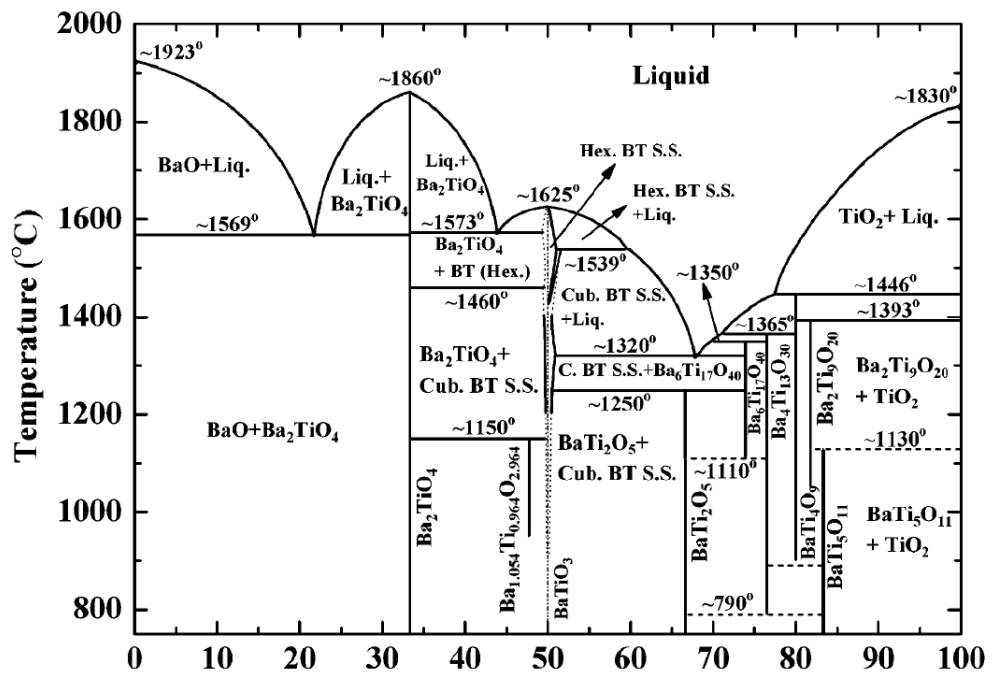


Figure 8.1: (a) Ternary phase diagram of BaO-TiO<sub>2-x</sub> systems above 1573 K [128]. The blue lines specify phases with the Ba:Ti ratios 1:1, 1:2 and 1:3. (b) Pseudo-binary phase diagram of BaO-TiO<sub>2</sub> systems under ambient air condition [130].

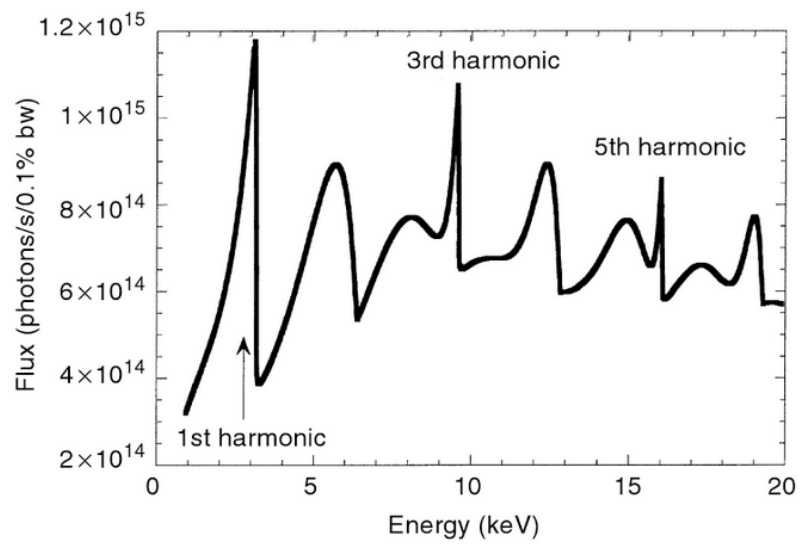


Figure 8.2: The typical spectrum of an undulator, taken from [47].



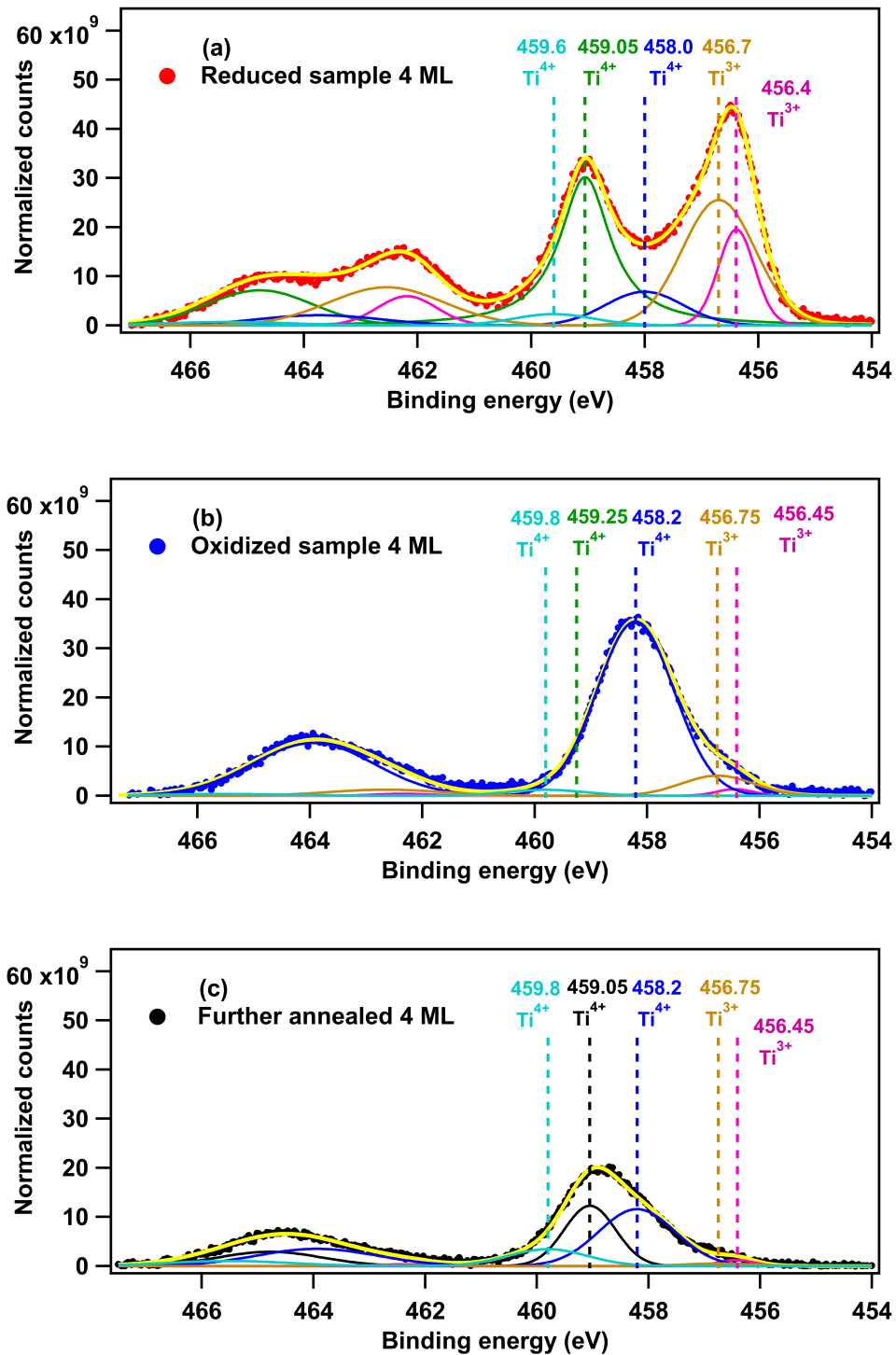


Figure 8.3: High resolution XPS spectrum of the Ti 2p emission lines, taken in 70° off normal emission at RT at a photon energy of 670 eV for 4 ML BTO sample (a) in the reduced state, annealed in UHV and (b) in the oxidized state, annealed in  $5 \times 10^{-7}$  mbar O<sub>2</sub> and (c) in the further annealed state, annealed in  $1 \times 10^{-5}$  mbar O<sub>2</sub>.

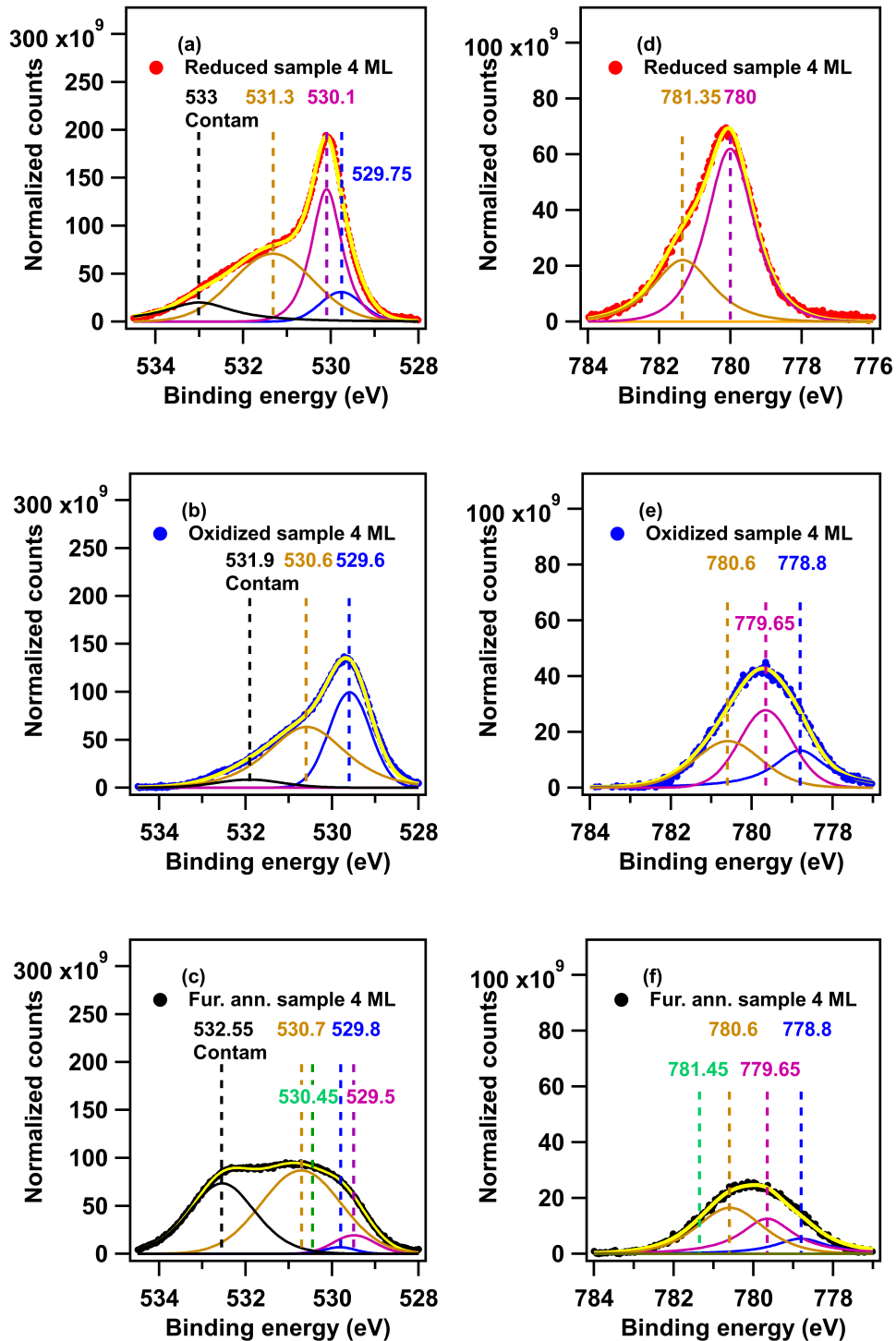


Figure 8.4: High resolution XPS spectrum of the O 1s and the Ba 3d<sub>5/2</sub> emission lines, taken in 70° off normal emission at RT at a photon energy of 670 for the O-1s and 1000 eV for the Ba 3d<sub>5/2</sub> emission line for 4 ML BTO sample (a,d) in the reduced state, annealed in UHV, (b,e) in the oxidized state, annealed in  $5 \times 10^{-7}$  mbar O<sub>2</sub> and (c,f) in the further annealed state, annealed in  $1 \times 10^{-5}$  mbar O<sub>2</sub>.

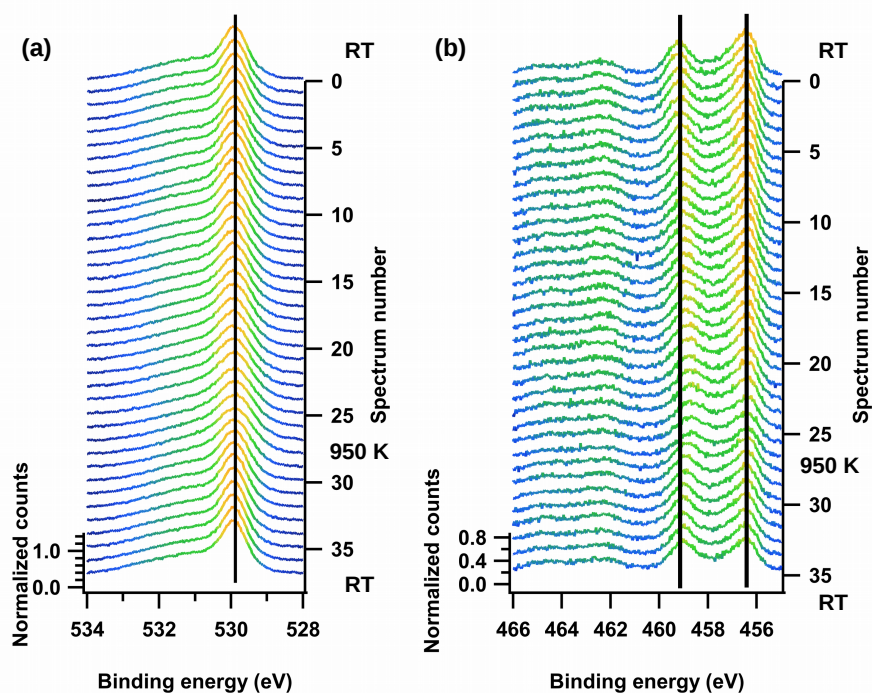


Figure 8.5: (a) The O 1s and (b) the Ti 2p spectra during reducing the 4 ML BTO sample in UHV, by heating up to 950 K. The spectra were taken at a photon energy of 670 eV, in normal emission.

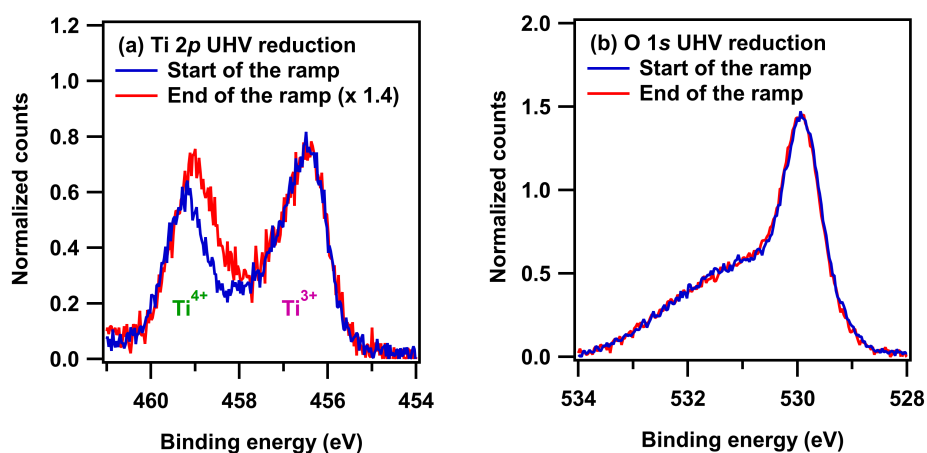


Figure 8.6: XPS spectra of (a) the Ti 2p and (b) the O 1s emission lines, taken at RT at the start and the end of heating 4 ML BTO sample in the reduced state in UHV up to 950 K, at a photon energy of 670 eV, taken in normal emission, shown in Fig. 8.5.

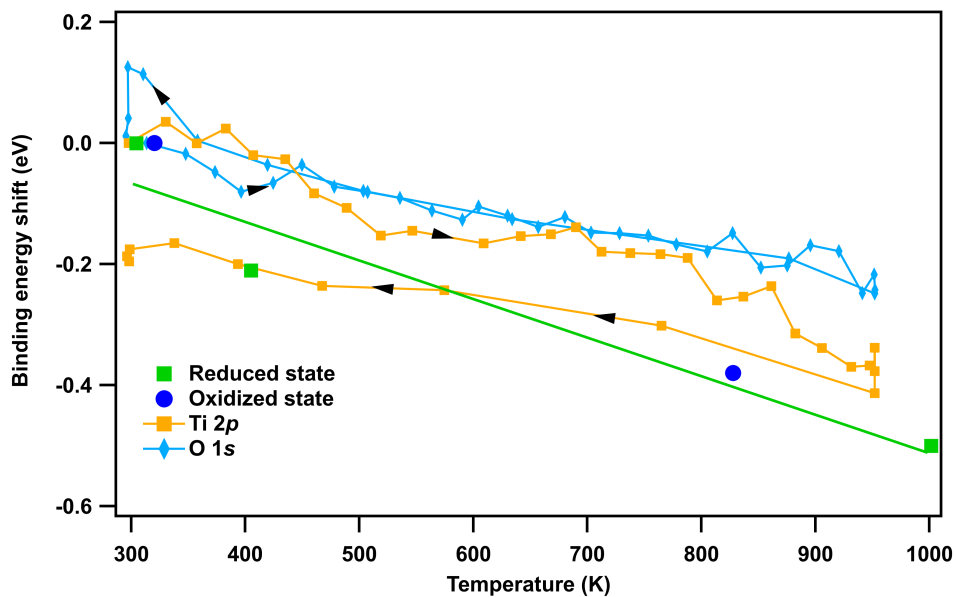


Figure 8.7: The combined plot of Fig. 6.12 and 6.16.

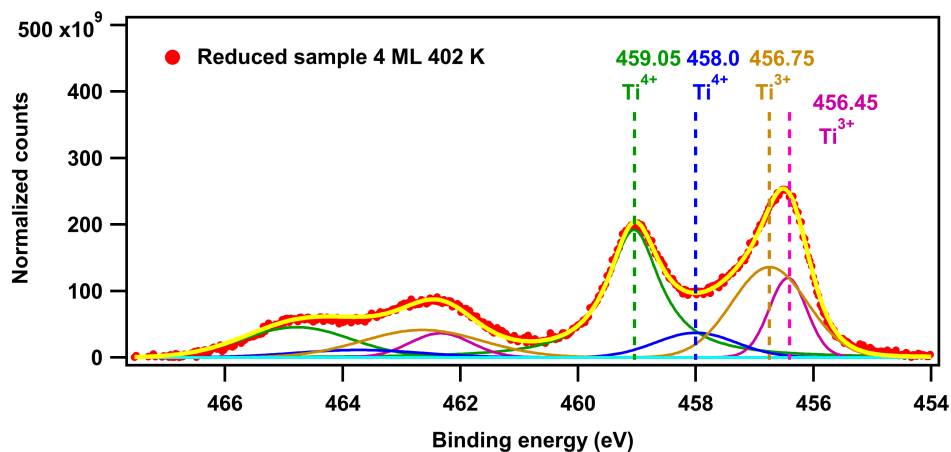


Figure 8.8: High resolution XPS spectrum of the Ti 2p emission lines of the 4 ML BTO sample in the reduced state, taken in normal emission at 402 K at a photon energy of 670 eV.

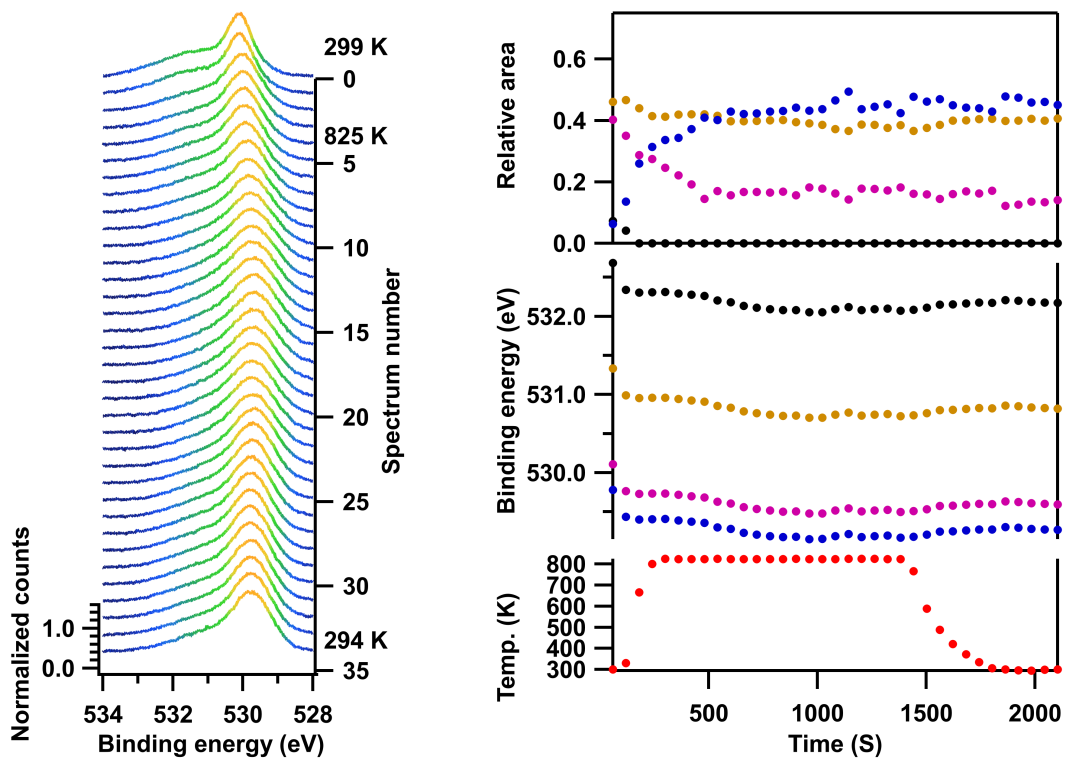


Figure 8.9: The O  $1s$  emission line of 4 ML BTO sample during oxidation in  $5 \times 10^{-7}$  mbar  $O_2$ , taken at a photon energy of 670 eV in normal emission. Temperature, relative areas and binding energies of the individual components are plotted versus time. The color codings of the components are the same as in Fig. 6.4 (a,b).



# Erklärung

Hiermit erkläre ich, dass ich, gemäß dem § 5 10 der Promotionsordnung der Naturwissenschaftlichen Fakultäten I, II und III der Martin-Luther-Universität Halle-Wittenberg vom 13.07.2016, die vorliegende Arbeit selbständig und ohne fremde Hilfe verfasst habe, keine anderen als die von mir angegebenen Quellen und Hilfsmittel benutzt habe und die den benutzten Werken wörtlich oder inhaltlich entnommenen Stellen als solche kenntlich gemacht habe, noch keine vergeblichen Promotionsversuche unternommen habe und die Dissertation weder in der gegenwärtigen noch in einer anderen Fassung bereits einer anderen Fakultät vorgelegt habe.

Halle (Saale), 01. August 2018

Alireza Bayat





# Curriculum Vitae

## Personal details

---

|                |               |
|----------------|---------------|
| Name           | Alireza Bayat |
| Marital birth  | 04. 08. 1986  |
| Place of birth | Tehran        |
| Nationality    | Iranian       |
| Marital status | Married       |

## Education

---

|                     |   |
|---------------------|---|
| Since 08. 2013      | PhD at Martin-Luther-Universität Halle-Wittenberg, Institut für Physik, Surface Science Group   |
| 09. 2008 – 11. 2011 | MSc, Solid state physics, Islamic Azad University, Science and Research Branch, Tehran, Iran (Thesis title: Size measurement metal nanoparticles using surface plasmon resonance) |
| 09. 2004 – 07. 2008 | BSc, Physics, Islamic Azad University, Varamin-Pishva Branch, Varamin, Iran   |
| 06. 2004            | Pre-University Studies, Tehran, Iran  |
| 06. 2003            | Highschool Degree, Tehran, Iran   |

## Publications

---

1. A. Bayat, et al., Monitoring the formation of the barium titanate derived quasicrystals on Pt(111) through high-resolution photoemission spectroscopy, in preparation
2. K.-M. Schindler, A. Bayat, et al., Direct projection analysis of EXAFS modulations in titanates, manuscript available
3. M. Trautmann, A. Bayat, et al., XAS calculations of quasicrystalline barium titanate, manuscript available
4. S. Förster, A. Bayat, et al., [Growth and decay of a two-dimensional oxide quasicrystal: High-temperature in situ microscopy](#), Annalen der Physik 529 (2016).
5. A. A. Ashkarran and A. Bayat, [Surface plasmon resonance of metal nanostructures as a complementary technique for microscopic size measurement](#), International Nano Letters 3 (2013).
6. A. A. Ashkarran, A. Bayat, et al., [Size measurement of gold and silver nanostructures based on their extinction spectrum: limitations and extensions](#), Iranian Journal of Physics Research 13 (2013).

## Talks

---

1. Direct projection analysis method of exafs modulations on ultrathinfilms, ECOSS 34<sup>th</sup>, Aarhus (2018).
2. X-Ray Absorption Study of a Barium Titanate Derived Quasicrystal on Pt(111), ECOSS 33<sup>rd</sup>, Szeged (2017).
3. NEXAFS and EXAFS Structure Determination within Quasicrystalline Barium Titanate on Pt(111), DPG-Frühjahrstagung, Dresden (2017).

## Talks

---

4. Influence of ferroelectric electron emission in BTO layer systems on measurements of core-level binding energies, DPG-Frühjahrstagung, Regensburg (2016).
5. Monitoring the Formation of Quasicrystalline Barium Titanate on Pt(111) using XPS and NEXAFS, DPG-Frühjahrstagung, Berlin (2015).
6. Investigations of magnetic properties of thin ferrimagnetic films on perovskite-like substrates, INTERMAG Europe 2014, Dresden (2014).

## Posters

---

1. X-ray Absorption of Ultrathin Titanate Layers, International Workshop: Functionality of Oxide Interfaces, Benedictine Abbey of Frauenwörth (2018).
2. Monitoring BaTiO<sub>3</sub> phase transitions in multiferroic layer systems through binding energy shifts in photoelectron spectroscopy, 20th International Conference on Ternary and Multinary Compounds, Halle (2016).
3. Influence of temperature-dependent charge redistributions in barium titanate on measurements of core-level binding energies, Condensed Matter in Groningen, Groningen (2016).
4. Ferroelectric Phase Transitions in Multiferroic Layer Systems, Spring School, Erlangen, (2016).
5. Monitoring the oxidation and reduction of islands of barium titanate on Pt(111) using XPS and NEXAFS during the formation of a quasi-crystalline layer, Nanospectroscopy for Two-dimensional Materials, Chemnitz (2015).
6. Magnetic anisotropy and magneto-electric coupling of thin ferrimagnetic films on Barium titanate, 580. WE-Heraeus-Seminar on Oxide Spintronics: Novel Materials, Transport and Engineering Phenomena, Bad Honnef (2015).
7. Ferroelectric Phase Transitions in Multiferroic Layer Systems, Sixth Joint BER II and BESSY II User Meeting, Berlin (2014).
8. Magneto-electric Coupling in Thin Ferrimagnetic Films on Perovskite-like Substrates, International Workshop: Functionality of Oxide Interfaces, Kloster Irsee/Augsburg (2014).
9. Size Measurement of Silver and Gold Nanoparticles Based on Their Optical Properties: Limitations and Extensions, 14th Iranian Inorganic Chemistry Conference in Sharif University of Technology, Tehran, Iran (2012).

Halle (Saale), 01. August 2018

## Acknowledgement

A Persian proverb says: even if you wish and do your very bests, you are not able to jam all the water of a sea into an urn. This sentence explains nicely my current feelings of inability to thank all, who have directly and indirectly supported me during the last five years, in only a few sentences. I express them my deep feelings and wish the best for them. Coming back to the words, I express my best thanks to PD Dr. Karl-Michael Schindler, my supervisor. I am grateful to him for his excellent scientific knowledge, his constant and effective supports, his encouragements, his tolerance and sense of humor, which made a nice and enjoyable working atmosphere for me in hard days. Without all his scientific supports, I would have never ever be able to accomplish my PhD. I have learned so much from him, also in the personal level, which definitely develops my future life by far.

I express my deepest feelings of acknowledgment to Prof. Dr. Wolf Widdra, the Head of the Surface Science Group, a kind and an excellent physicist, for everything. His scientific advice shined the light on my research path. His organized facilities made it possible to perform such state-of-the-art experiments. The friendly atmosphere in the group is undoubtedly due to his perfect leadership. And I thank him for giving me the opportunity to be one of his group members.

Beyond any question, Dr. Stefan Förster played a crucial role in my academic path. He is such a nice and patient scientist. I have followed his footsteps while my PhD. He was the one who has discovered BTO-derived OQC, the topic of this thesis and was always ready to help me at each stage.

I am sincerely grateful to Prof. Dr. Reinhard Denecke and PD Dr. Angelika Chassé for great discussions and all their supports during these years, through organizing the beamtimes and leading the experiments, as well as calculating my structural models. I have learned a lot from them, also on the personal level.

I am very grateful to Prof. Dr. Henning Neddermeyer, Assoc. Prof. Dr. Krassimir L. Kostov and Dr. Klaus Meinel for the brilliant discussions and nice advice. I am very thankful to Dr. Martin Trautmann and Dr. Waheed A. Adeagbo for nice discussions and performing calculations. I sincerely acknowledge Eva Maria Zollner and Christoph Dresler for their nice sample preparations and attending the beamtimes. I am extremely grateful to Dr. Maik Christl for AFM and PFM measurements and discussions and Robert Roth for support in the AFM data analysis, which played a key role in understanding the systems and interpreting the results. I am also very thankful to Dr. René Hammer and Paula Huth for supporting the beamtimes and taking part in discussions. I am very thankful to Dr. Florian Otto Schumann for EELS measurements and great sample preparations and to Sebastian Schenk for analyzing the STM image and calculations.

Of course performing such top-notch experiments would not have been possible without technical supports from the great engineer Ralf Kulla, who made major contributions in this thesis. I am also thankful to all members of workshops at the MLU, Halle. I am extremely thankful to Dr. Silvano Lizzit and Dr. Paolo Lacovig for their great supports during the beamtime in Super ESCA at Elettra, Trieste. Members of KMC-1 beamline at BESSY II, Berlin are also acknowledged.

I am specially grateful to Dr. Cheng-Tien Chiang for his extreme effective scientific support and discussions. I express my greatest acknowledgments to Dr. Remya K Govind, who has supported me a lot to come into this field. I am very thankful to Dr. Konrad Gillmeister and Erik Schreck for their great IT support. I sincerely acknowledge supports of Mathias Augstein and Bettina Allner during IT troubleshooting. I am extremely thankful to all members of Surface Science Group for their helpfulness and the nice, friendly and warm atmosphere in the group, which has particularly emotionally supported me.

In the personal level, I have always been and will be indebted to Effat Zandevakili and Hamid Bayat, my dear mother and father, whose brilliant moral characteristics have led and will lead me throughout my life. I thank them for everything and am proud to be their son, whose encouragements have motivated me not to give up in my life. I thank the soul of my father and ask God his blessings for him.

I am particularly grateful to Maryam Esmailzadeh Namini, my sweet love, my dear wife, who has patiently tolerated my impatience during those days. Without her understanding and emotional support I would never ever be able to accomplish my study. Who has always encouraged and supported me, whenever I needed her warm arms.

I am sincerely grateful to my family, Parvaneh, Mahboobeh, Farzaneh, Maryam and Banafsheh, my dear sisters and Masoud, my brother, whose marvelous supports enabled me to keep going. I am very thankful to Abbasali, my nephew and Sarina my niece. I am specially thankful to Hossein Esmailzadeh and Robabeh Vaziri, my father and my mother in law, for their extraordinary understanding and aids. I am extremely thankful to Assoc. Prof. Dr. Seyed Mohammad Elahi and Dr. Ali Akbar Ashkarran, supervisors of my MSc thesis for great advices and discussions. I am grateful to Hamidreza Shiravand and Saadollah Yazdani, my school teachers, who have motivated and encouraged me to continue my education in the world of physics. Finally, I am very thankful to all my friends and wish them all the best.